Politecnico di Torino

ScuDo
Scuola di Dottorato ~ Doctoral School
WHAT YOU ARE, TAKES YOU FAR

Doctoral Dissertation
Doctoral Program in Electrical, Electronics and Communications Engineering (27^{th}cycle)

Vertical-cavity surface-emitting lasers: computer-aided modal and polarization engineering

By

Valerio Torrelli

******

Supervisor(s):
Prof. Francesco Bertazzi, Supervisor
Pierluigi Debernardi, Co-Supervisor
Prof. Michele Goano, Co-Supervisor

Doctoral Examination Committee:
Prof. Connie Chang-Hasnain, Referee, Berxel Photonics Co.
Prof. Maciej Dems, Referee, Lodz University of Technology
Prof. Rainer Michalzik, Ulm University
Prof. Véronique Bardinal, LAAS-CNRS
Prof. Alberto Tibaldi, Politecnico di Torino

Politecnico di Torino
2025

Declaration

I hereby declare that, the contents and organization of this dissertation constitute my own original work and does not compromise in any way the rights of third parties, including those relating to the security of personal data.

Valerio Torrelli
2025

* This dissertation is presented in partial fulfillment of the requirements for **Ph.D. degree** in the Graduate School of Politecnico di Torino (ScuDo).

I would like to dedicate this thesis to my loving family

Acknowledgements

First and foremost, I would like to thank my co-supervisor and researcher Pierluigi Debernardi, who has been a true mentor throughout my PhD journey. He allowed me to grow both as a person and as a researcher, pushing my knowledge to an entirely new level. Truly, one of the most brilliant researchers I have ever met.

Similarly, I am deeply grateful to doctor Alberto Tibaldi, who passed on to me his passion for computational physics and his rigorous and theoretical approach. Without his guidance, I would have lost my way more than once during this PhD journey.

I would also like to thank the entire Microwave and Optoelectronic Group (MOG), in particular my supervisor Francesco Bertazzi, my co-supervisor Michele Goano, and my colleagues Martino, Alberto, Matteo and Lorenzo. Without them, this period would have been far less fruitful in terms of the innovation we brought forward together and the ideas we were able to explore.

On a more personal note, I wish to thank my family, my father Carmelo, my mother Marina, and my brother Emanuele, who have always supported me in every way throughout these long years spent away from home. It is only thanks to them that I was able to overcome the loneliness of the early days and make it this far.

A special thanks goes to my "adopted brother" Domenico, who stood by me during my lowest moments and helped me rise again. He is truly one of the kindest and most genuine people I've ever had the fortune to meet. My heartfelt thanks also go to my future fellow researcher Lorenzo, I eagerly look forward to writing a paper together, and to all my Abruzzese friends who, over the years, have become a second family to me.

I also want to thank my dear friends Samuele and Sara. Even though we haven't been able to see each other regularly, since you've been abroad for as long as I've

been in Turin, I still feel your presence close by. Your support has always reached me when it mattered most, and for that, I'm truly grateful.

A heartfelt thank you also to my friends in Turin, both old and new, from roommates to university colleagues and recent additions. Without you, my time away from home would have been significantly harder, and it is thanks to you that I can now imagine a future here.

Last but not least, I want to express my deep gratitude to Jermiah and his family. Even though we've known each other only recently, it feels like I've known him forever. A truly selfless, truly kind person and a real friend, who has given me multiple new perspectives on life and made me a much happier person over the past two years.

Thank you.

Abstract

In this work, we address the modeling and design of vertical-cavity surface-emitting lasers (VCSELs) featuring large-active-area non-circular geometries and elliptical polarization states. This is motivated by novel applications such as chip-scaled atomic clocks, quantum gyroscopes and atomic magnetometers, requiring high-power single-mode emission and circular polarization for optical atomic pumping. Traditional VCSELs, based on circular oxide apertures, featuring a relatively low optical power and linear polarization, are not suited for these needs, thus demanding new device architectures and accurate simulation tools.

To this end, a comprehensive and physics-based mathematical framework has been developed, capable of describing the electromagnetic modal behavior of VCSELs with arbitrary transverse geometries. The resulting simulation tool, our VCSEL ELectroMagnetic Suite (VELMS), supports both full-wave 3D simulations and simplified 1D scalar and vectorial formulations. The framework allows an efficient computation of optical modes and polarization states, only relying on the refractive index distribution of the VCSELs, and can also include self-heating and surface patterning effects.

The developed model was applied to two classes of VCSELs. The first focuses on large-area rectangular VCSELs for high-power single-mode operation. These devices exploit surface grating reliefs to achieve single-mode emission by matching the relief positions with the intensity peaks of the desired optical mode. High-power single-mode devices relying on this strategy were realized and measured in terms of near and far-field profiles, confirming our simulation results. Further optimizations involved far-field shaping for a better coupling with optical fibers and the modification of the grating reliefs' design at high bias currents, where thermal lensing strongly affects the topography of the optical modes.

The second application concerns VCSELs that can directly emit elliptically and circularly polarized light, targeting the elimination of bulky quarter waveplates in chip-scale atomic devices, needed to convert the polarization from linear to circular. A new approach to achieving polarization control was introduced, based on the concept of 3D cavity chirality, obtained from the interaction of tilted optical anisotropies. We simulated and measured a fabricated device, which combines the anisotropy arising from the electro-optic effect, aligned with the semiconductor crystal axes, and a tilted subwavelength grating. By doing so we confirmed the model's ability to predict the Stokes parameters associated to the lasing polarization, thus further validating the simulation tool. Parametric optimizations were performed to maximize the degree of circular polarization and explore the role of strain, which introduces additional optical anisotropies through the elasto-optic effect.

This work provides both a rigorous theoretical foundation and practical design strategies for next-generation VCSELs. Thanks to its generality, the developed framework is applicable to a wide variety of VCSEL architectures, including different wavelengths and material systems, making it a versatile asset for current and future photonic applications.

Contents

Publication list

1. V. Torrelli, L. Miri, M. D'Alessandro, A. Gullino, M. Zimmer, K. Dahler, M. Jetter, P. Michler, W. Elsäßer, F. Bertazzi, A. Tibaldi, and P. Debernardi, "Elliptical polarization in VCSELs via joint interaction of a tilted sub-wavelength grating and intrinsic semiconductor anisotropies", Opt. Lett. 50, 3082-3085 (2025).

2. V. Torrelli, M. D'Alessandro, L. Miri, A. Gullino, W. Elsässer, A. Tibaldi and P. Debernardi, "Mastering VCSEL polarization from linear to circular using subwavelength gratings", Proc. SPIE PC13384, Vertical-Cavity Surface-Emitting Lasers XXIX, PC1338407 (19 March 2025); https://doi.org/10.1117/12.3041898.

3. V. Torrelli, L. Miri, M. D'Alessandro, A. Gullino, R. de Gennaro, W. Elsäßer, A. Tibaldi and P. Debernardi, "Understanding polarization with gratings tilted to crystal axes: towards circularly-polarized VCSELs", 2024 IEEE Photonics Conference (IPC), Rome, Italy, 2024, pp. 1-2, doi: 10.1109/IPC60965.2024.10799509.

4. M. C. G. Alasio, V. Torrelli, S. Albano, L. Miri, A. Gullino, M. Goano and P. Debernardi, "Modeling self-heating in high-power non-circular VCSELs", 2024 IEEE Photonics Conference (IPC), Rome, Italy, 2024, pp. 1-2, doi: 10.1109/IPC60965.2024.10799821.

5. V. Torrelli, M. D'Alessandro, W. Elsäßer and P. Debernardi, "On-demand polarization by a vertical-cavity surface-emitting laser with two tilted sub-wavelength gratings", Opt. Lett. 49, 3773-3776 (2024).

6. V. Torrelli, A. Gullino, A. Tibaldi, F. Bertazzi, M. Goano and P. Debernardi, "High-Power Emission via Large-Area VCSELs With Single High-Order Mode Operation", in IEEE Photonics Journal, vol. 16, no. 2, pp. 1-7, April 2024, Art no. 0600507, doi: 10.1109/JPHOT.2024.3360992.

7. A. Gullino, V. Torrelli, M. D'Alessandro, A. Tibaldi, F. Bertazzi, M. Goano and P. Debernardi, "AlGaAs Tunnel Junction (TJ)-VCSELs: A NEGF–Drift-Diffusion Approach," in IEEE Photonics Journal, vol. 16, no. 2, pp. 1-9, April 2024, Art no. 0600409, doi: 10.1109/JPHOT.2024.3360897.

8. M. D'Alessandro, V. Torrelli, F. Bertazzi, M. Goano, N. N. Ledentsov, M. Lindemann, M. Gioannini, P. Debernardi and A. Tibaldi, "Transverse Coupled Cavity VCSELs: Bridging Ultrabroadband Dynamics to Optical Supermodes", in IEEE Photonics Journal, vol. 16, no. 2, pp. 1-7, April 2024, Art no. 0600807, doi: 10.1109/JPHOT.2024.3373171.

9. N. Ledentsov Jr., V. A. Shchukin, Ł. Chorchos, O. Yu. Makarov, J.-R. Kropp, I. E. Titkov, V. P. Kalosha, V. Zerova, M. Lindemann, N. C. Gerhardt, M. D'Alessandro, V. Torrelli, P. Debernardi, A. Tibaldi, M. R. Hofmann, N. N. Ledentsov, "Analysis of laterally-coupled-cavity VCSELs for ultra-high-frequency photon-photon resonance modulation", Proc. SPIE 12904, Vertical-Cavity Surface-Emitting Lasers XXVIII, 1290405 (13 March 2024); https://doi.org/10.1117/12.3001177.

10. V. Torrelli, A. Tibaldi, F. Bertazzi, M. Goano and P. Debernardi, "Modeling of single-mode high-power VCSEL arrays", 2023 International Conference on Numerical Simulation of Optoelectronic Devices (NUSOD), Turin, Italy, 2023, pp. 93-94, doi: 10.1109/NUSOD59562.2023.10273517.

11. V. Torrelli, M. D'Alessandro, L. Miri, P. Debernardi, F. Bertazzi, M. Goano, M. Gioannini and A. Tibaldi, "Analytical model of the Ultrabroadband Operation of Transverse-Coupled-Cavity VCSELs", 2023 International Conference on Numerical Simulation of Optoelectronic Devices (NUSOD), Turin, Italy, 2023, pp. 87-88, doi: 10.1109/NUSOD59562.2023.10273476.

12. A. Gullino, V. Torrelli, M. D'Alessandro, A. Tibaldi, F. Bertazzi, M. Goano and P. Debernardi, "Physics-based modeling of AlGaAs tunnel junction VCSELs: a comparative appraisal", 2023 International Conference on Numerical Simulation of Optoelectronic Devices (NUSOD), Turin, Italy, 2023, pp. 99-100, doi: 10.1109/NUSOD59562.2023.10273507.

13. V. Torrelli, J. A. Gonzalez Montoya, A. Tibaldi, P. Debernardi, A. Simaz, M. A. Belkin, M. Goano and F. Bertazzi, "Modeling carrier transport in mid-infrared VCSELs with type-II superlattices and tunnel junctions", 2022 International Conference on Numerical Simulation of Optoelectronic Devices (NUSOD), Turin, Italy, 2022, pp. 55-56, doi: 10.1109/NUSOD54938.2022.9894782.

Chapter 1

Introduction

1.1 Vertical-cavity surface-emitting lasers: targeting novel applications

Since their first presentation in 1977, vertical-cavity surface-emitting lasers (VCSELs) have come a long way [1], becoming the dominant light sources for short haul communication in data centers [2], gas sensing [3] and 3D-sensing [4], *e.g.*, face recognition applications, eventually opening the doors to LiDAR applications for the automotive market [5]. Initially, VCSELs featured a cylindrical geometry; however, their recent growth has been driven by breaking this paradigm, enabling a variety of alternative geometries. This diversification has led to distinct modifications in the emitted light's properties, including modulation speed, optical power, and polarization. According to the 2023 Yole Intelligence annual projection reported in www.yolegroup.com, the VCSEL market is expected to keep growing following Fig. 1.1.

Besides an expected increase in overall funds of 43%, a staggering increase of 84% is expected for telecommunication application. Indeed, short haul data transmission in data centers represents nowadays the bottleneck of internet speed, especially with streaming services and artificial-intelligence on the rise. In addition to system-level improvements [6], circular VCSEL geometries for high-speed applications must be designed accounting for several factors. Optimized commercial structures feature many oxide apertures and intracavity contacts to reduce the RC bandwidth

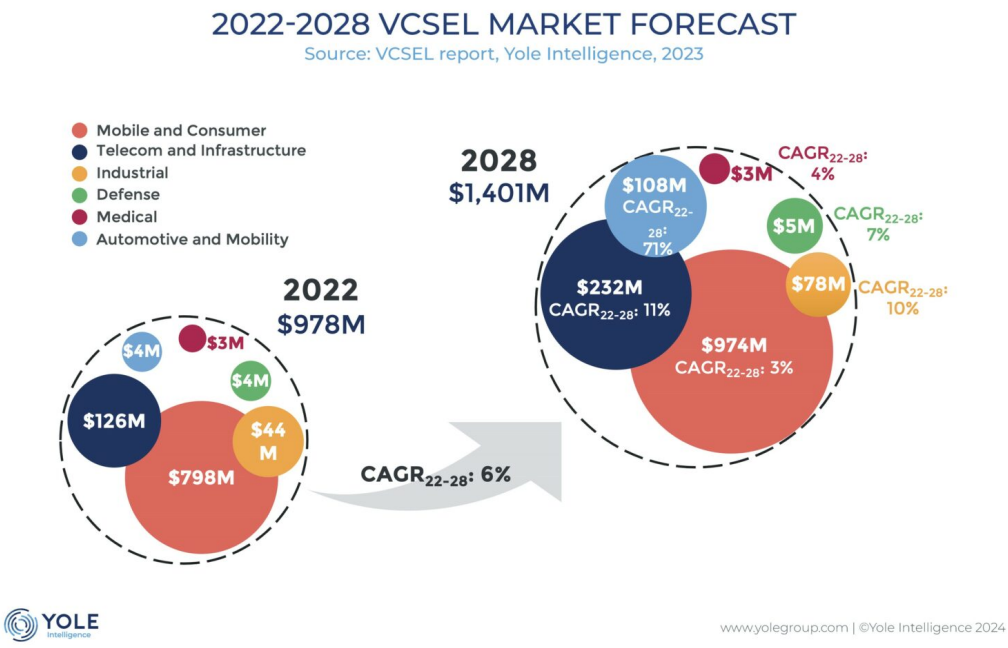

Fig. 1.1 Projection of the VCSEL market growth from 2022 to 2028, according to the 2023 Yole Intelligence report (www.yolegroup.com).

limitation and smaller oxide apertures to have the lowest possible optical volume [7]. However, more recent efforts aim at revolutionary designs relying on transverse coupled cavities (TCC), demonstrated more than a decade ago [8, 9] and recently regaining interest [10–13], harnessing the principle of photon-photon resonance (PPR). Despite being promising and demonstrated more than ten years ago, these devices are not currently on the market, highlighting the need to properly understand their electromagnetic properties for improved yield and reliability. To this aim, fast and efficient VCSEL simulators are needed, since TCC-VCSELs feature complex transverse shapes, deviating from the circular VCSEL geometry.

Furthermore, Fig. 1.1 suggests an exceptional expected increase in automotive and mobility, displaying investments growing from 4 G$ in 2022 to 108 G$ in 2028, targeting a massive employment of VCSEL-based LiDARs in vehicles. This is strictly linked to the realization of high-power VCSELs. The concept of a high-power VCSEL seems like an oxymoron, as VCSELs typically target a low threshold current and power consumption, which results in low optical output power. However, thanks to their versatility, vertical emission capability, and the possibility of realizing 2D planar arrays, VCSELs are also appealing for high-power applications, provided

their structure is properly modified, with current approaches including multi-tunnel junction VCSELs, leveraging the principle of carrier recycling [5], and large active area VCSELs [14–16]. It is remarkable how these two solutions for high power are independent, thus an optical power scale up is doable by combining the two methodologies.

As the optical power of VCSELs increased, their application extended to atomic clocks, atomic magnetometers, and quantum gyroscopes [17–28]. These advancements aim to miniaturize such devices to chip-scale levels by exploiting compact and efficient light sources. High optical power is essential for effective atomic pumping, while single-mode (SM) emission is crucial for exciting specific electronic transitions in targeted atomic species. In this context, the development of high-power SM VCSELs is pivotal for harnessing the inherent compactness and versatility of VCSELs in atomic applications [29].

In atomic devices, in addition to SM emission at the correct wavelength, polarization is also critical. Atomic transitions are activated exclusively by circularly polarized light, which serves as the pumping source. Consequently, a bulky quarter-wave plate, converting linear polarization to circular, is typically an essential component in such devices. To enhance compactness, numerous research efforts are focused on developing emitters capable of directly generating circularly polarized light, thereby eliminating the need for a quarter-wave plate.

This demand has given rise to a novel research area: circularly polarized (CP) VCSELs, which not only benefits atomic applications but also holds potential for spintronics, thanks to the selective interaction between spin-polarized carriers and circularly polarized photons [30]. CP VCSELs can be realized by embedding a two-dimensional chiral layer into the emitter's epitaxial structure, such as cholesteric liquid crystal layers [31] or 2D metastructures [32–36]. Alternatively, they can be achieved through three-dimensional cavity chirality, relying on misaligned optical anisotropies [37].

The potential applications and market relevance of a certain technology are closely tied to the scientific interest in new methodologies and advancements. By analyzing data from the Scopus database (www.scopus.com), we can trace how research groups have progressively engaged with this topics over time, as reflected in the annual number of publications shown in Fig. 1.2.

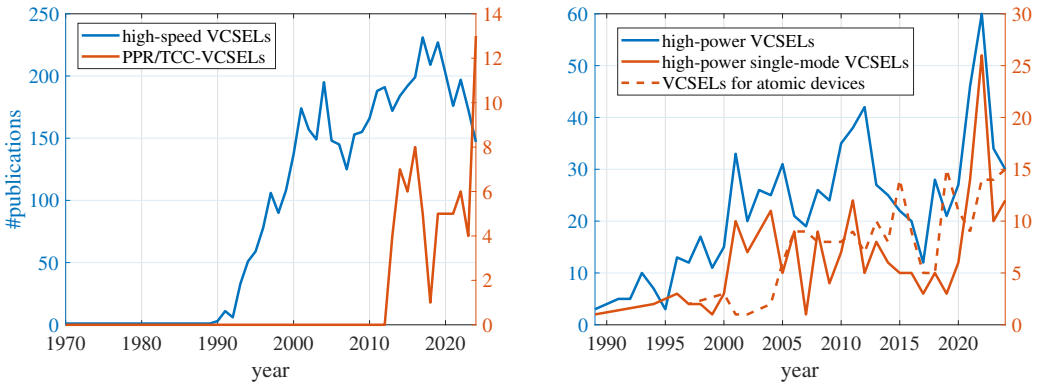

Fig. 1.2 Number of publications evolving in time for various VCSEL applications, from high-speed and PPR/TCC VCSELs (right) to high power VCSELs, high power SM VCSELs and VCSELs for atomic devices (left).

The graph on the left highlights that research on high-speed VCSELs began in the early 1990s, providing ample time for the development and optimization of bandwidth in standard circular devices, now supported by hundreds of publications per year. From the early 2010s, TCC-VCSELs have emerged as a promising approach to push these limits beyond the state of the art. However, the relatively low number of publications suggests that several aspects remain insufficiently understood, leaving room for improvement and making them an active area of interest in both academia and industry.

In contrast, high-power VCSELs, along with their byproducts such as high-power SM devices and VCSELs for atomic applications, have grown steadily over the past three decades, now reaching tens of publications per year and gaining increasing prominence in the laser industry. Beyond enabling advances in polarization control, like CP-VCSELs, their impact is evident across various industrial sectors.

For instance, the Qyro project [38] is developing an SM VCSEL with a output power exceeding 10 mW, intended as the optical source for a quantum gyroscope to be deployed in the first satellite utilizing quantum sensors, scheduled for launch by 2027 (see TRUMPF VCSELs for the Qyro Project). This project represents an application for the space industry, complementing the applications already explored in the automotive and mobility fields, as shown in Fig. 1.1.

Many VCSELs used in these novel areas depart from the conventional VCSEL paradigm, replacing the typical circular oxide confinement with other oxide

shapes and exploiting surface patterning techniques. This shift calls for a better understanding and an appropriate modeling of VCSEL designs.

Throughout this doctoral dissertation, we setup a fully tridimensional and vectorial mathematical framework based on coupled mode theory, capable of efficiently handling VCSELs of any shape, also accounting for self-heating of the device and surface patterning. This theory is embedded in our VCSEL Electromagnetic Suite (VELMS), a VCSEL optical mode solver originally published in [39] and successfully applied to a variety of cases [40, 14, 41–46, 37, 29, 13] for more than two decades.

The code was originally developed for conventional circular VCSELs, with a progressive addition of new transverse shapes, requiring a complex mathematical parametrization of non-circular shapes in polar coordinates. One of the strengths of this thesis relies in bypassing the analytical description of the shapes, making it fast and efficient for analyzing the impact of design variations on modal performances, also allowing for non-circular self-heating temperature profile. This feature represents a crucial point to analyze large rectangular active areas for high power applications [29], extremely dependent on confinement shape.

1.2 Circular VCSEL geometry

A sketch of a VCSEL structure is reported in Fig. 1.3. A short-haul VCSEL designed for intra-data center telecom applications, targeting a wavelength $\lambda_t = 850$ nm, is realized using $Al_xGa_{1-x}As$, where $x \in [0,1]$ represents the aluminum molar fraction. The device is built on an n-doped GaAs substrate, starting with the epitaxial growth of an n-doped distributed Bragg reflector (DBR) as the bottom mirror. This DBR consists of alternating AlGaAs layers with high and low aluminum molar fractions, creating a periodic variation in refractive index with low and high indices, respectively. The behavior of refractive index with Al molar fraction in AlGaAs is illustrated in Fig. 1.4. Transitions between high and low molar fraction layers are often graded to reduce resistivity at heterointerfaces. However, this approach compromises reflectivity, requiring a higher number of layer pairs compared to DBRs with sharp interfaces.

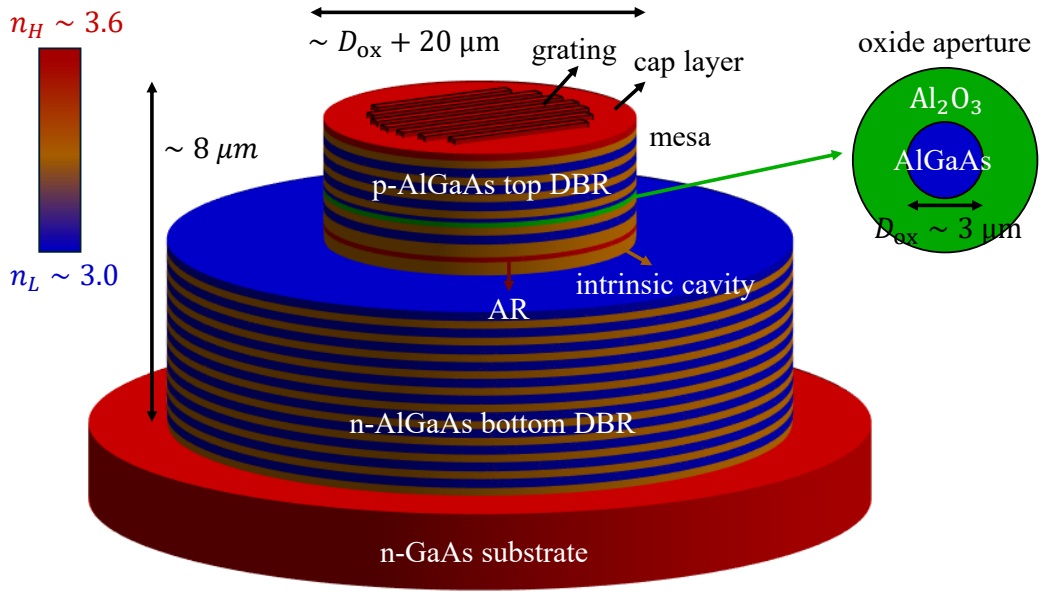

Fig. 1.3 3D sketch of a standard 850 nm VCSEL structure, together with typical dimensions and refractive index values.

Above the bottom DBR lies the intrinsic cavity, an AlGaAs region containing an active region (AR) with undoped GaAs quantum wells (QWs) that provide optical gain for stimulated emission. The cavity is capped by a p-doped DBR, forming the top mirror, which completes the vertical confinement of light. To allow light outcoupling at the top facet, the top DBR must feature fewer pairs than the bottom DBR, resulting in lower reflectivity. Usually the bottom and top graded AlGaAs DBRs feature around 35 and 20 pairs, respectively. The topmost layer of the top DBR, known as the cap layer, plays a crucial role in the performance and reliability of the VCSEL. This layer, typically composed of pure GaAs rather than AlGaAs, has three primary functions:

1. electrical: the cap layer interfaces with the top electrode and is heavily p-doped to facilitate efficient current injection. GaAs, with its superior hole mobility compared to AlGaAs, ensures excellent electrical contact with the electrode;

2. chemical: unlike AlGaAs, GaAs does not oxidize when exposed to air. Since the cap layer seals the VCSEL structure, this choice of material provides long-term stability to the device by preventing oxidation, which would otherwise degrade the performance over time;

3. optical: the thickness of the cap layer plays a critical role in determining the reflectivity of the top DBR. This, in turn, influences key optical properties such as the modal threshold and the light outcoupling efficiency. The reflectivity varies periodically with the cap layer thickness, with a spatial period of $\lambda_t/(2n_{cap})$, where n_{cap} is the refractive index of the cap layer. By carefully adjusting the cap layer thickness, the desired optical properties can be achieved.

In both DBRs, the layer thicknesses required for maximum reflectivity around λ_t are $\lambda_t/(4n_H)$ and $\lambda_t/(4n_L)$ for the high and low index layers, n_H and n_L being their indices, respectively [47]. Additionally, the cavity thickness required to ensure the emission at λ_t must be λ_t/n_{cav}, where n_{cav} is the cavity's refractive index[1]. The vertical stack is collectively referred to as the epitaxial structure of the VCSEL, which also functions electrically as a *pin* junction with heterointerfaces due to molar fraction changes.

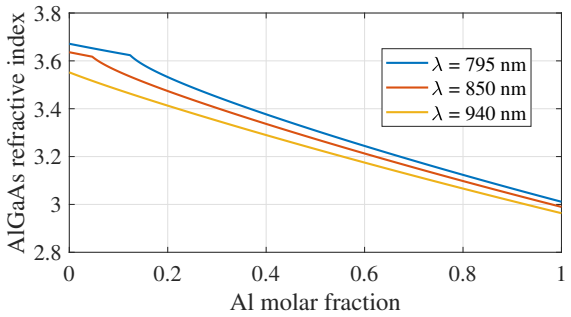

Fig. 1.4 AlGaAs refractive index as a function of the Al molar fraction for different relevant wavelengths [48].

While the epitaxial structure ensures longitudinal light confinement, additional measures are required for transverse confinement. Within the top DBR, one layer with a high aluminum content, typically > 0.98, located close to the cavity, serves as oxidation layer. The structure is partially etched from the top, stopping above the cavity but below the layer to be oxidized, leaving behind a mesa, *i.e.*, a pillar of the remaining top DBR. The device is then subjected to an oxidation process, converting the outermost part of the oxidation layer to aluminum oxide (Al_2O_3),

[1]This is an example of what is known as a λ-cavity VCSEL. It is not the only possibility, since also $\lambda/2$ cavities are employed for high-speed applications, bringing closer together the QWs and the oxide aperture and minimizing the spreading of carriers due to lateral diffusion.

while the central portion remains AlGaAs. Aluminum oxide has a significantly lower refractive index, ~ 1.6 at 850 nm, and negligible electrical conductivity, enabling the formation of a radially defined oxide aperture. This aperture confines both the optical mode and the current density transversely. For single transverse mode emission, a circular aperture diameter of approximately $3\,\mu$m is required. After the oxidation process, the mesa gets encapsulated by a passivation material.

For circular VCSELs, electrical contacts are formed by an annular electrode on top of the mesa and a planar electrode at the bottom of the substrate. The outcoupling facet of the VCSEL can also be patterned for additional functionality, such as etching a grating for polarization control.

1.3 Thesis Structure

This thesis focuses on developing a mathematical framework for the analysis of VCSELs, which is subsequently applied to their optimization across various applications. It moves from a general theoretical foundation to practical implementations, with a particular emphasis on VCSELs featuring non-circular transverse shapes and supporting the emission of different polarizations. The framework is completely general and potentially addresses all emerging applications discussed in Section 1.1. The approach combines fully vectorial three-dimensional (3D) simulations, simplified one-dimensional (1D) models, and a generalized vectorial interpretation of the Barkhausen criterion, which allows for a better understanding of polarization.

The initial part of the thesis establishes the theoretical framework. Firstly, we derive the coupled mode equations, which are obtained rigorously from the reciprocity theorem in the frequency domain. The framework is then applied to the 3D and 1D cases, extending the existing 1D model from scalar to vectorial, with emphasis on elliptically polarized single-transverse-mode VCSELs. The generalization of the Barkhausen criterion to the vectorial domain provides simple, intuitive rules and analytical expressions to determine the emitted polarization states. The correctness and predictive capability of the vectorial 1D theory and the vectorial Barkhausen criterion are validated by direct comparison with results obtained from fully vectorial 3D simulations of single-transverse-mode VCSELs, ensuring consistency and reliability of the simplified models.

A crucial aspect is the treatment of optical anisotropies, which in VCSELs can be introduced by:

- **Electro-optic effect (EOE)**: this effect allows modulation of the refractive index under the influence of an electrostatic field, introducing birefringence.
- **Elasto-optic effect**: this effect introduces birefringence through mechanical stress applied to the VCSEL structure.
- **Subwavelength grating (SWG)**: the most effective form of optical anisotropy from the engineering standpoint is the presence of a SWG at the outcoupling facet of the VCSEL. This grating introduces controllable birefringence and dichroism by acting as an equivalent anisotropic medium. Its effects are analyzed using two approaches, *i.e.*, the analytic Born-Wolf formulas [49] and a homogenization procedure based on rigorous coupled wave analysis (RCWA) [50, 51]. These methods enable the grating to be treated as a uniform anisotropic medium, provided its periodicity remains subwavelength.

Following the description of the theoretical framework, the latter is applied to two classes of VCSELs and validated against experimental results, as presented in the following chapters:

- **High-power single-mode rectangular VCSELs**: VELMS is employed to optimize modal parameters and beam profiles in large active-area rectangular VCSELs, designed for high-power single-mode operation. Experimental results are also presented, including light-current-voltage (LIV) characteristics, near-field patterns, and far-field distributions. These findings demonstrate the practical feasibility of the proposed designs and the ability to achieve partially collimated emission in non-circular geometries.
- **Elliptically and circularly polarized VCSELs**: The vectorial 1D framework and the generalized Barkhausen criterion are applied to VCSELs with misaligned optical anisotropies, allowing the design of devices capable of emitting elliptically or circularly polarized states. These polarization states are particularly valuable for advanced applications such as atomic pumping in atomic clocks, atomic magnetometers, and quantum gyroscopes. The theoretical predictions are supported by experimental data, including the first published

demonstration of elliptically polarized VCSELs achieved using a SWG tilted with respect to the electro-optic anisotropy, which is oriented along the crystal axes of the VCSEL. This unique configuration showcases the potential of SWGs in precisely tailoring the polarization characteristics of VCSELs.

A summary of the thesis structure is presented below:

- **Chapter 1:** Introduction.
- **Chapter 2:** Fully vectorial three-dimensional framework: derivation of coupled mode equations and setup of 3D simulations.
- **Chapter 3:** Simplified one-dimensional models for normal incidence: scalar and vectorial analysis for single-mode VCSELs. Study of the optical anisotropies associated with electro-optic, elasto-optic effects and subwavelength gratings.
- **Chapter 4:** Application of 3D simulations. High-power single-mode rectangular VCSELs: numerical results, experimental characterization (LIV, near field, far field), and design optimizations, including the impact of thermal lensing.
- **Chapter 5:** Generalization of the Barkhausen criterion to the vectorial case: analytic rules for polarization control. Applications to elliptically and circularly polarized VCSELs, exploiting both the vectorial Barkhausen criterion and vectorial 1D simulations.
- **Chapter 6:** Conclusions.

Chapter 2

Rigorous coupled mode theory

To provide an overview of the numerical approaches available for simulating VCSELs [52], it is useful to mention several established methodologies. Full-wave expansion techniques include Rigorous Coupled-Wave Analysis (RCWA) [53], although rarely applied to entire VCSELs, as well as the Plane-Wave Admittance Method [54–56] and Coupled Mode Theory [39], all of which rely on modal expansions of the electromagnetic field. Other strategies include the Method of Lines [57], which attacks directly Maxwell's differential equations along the VCSEL transverse plane without modal decomposition, and more computationally intensive finite-element methods [58]. Among these, our focus is on Coupled Mode Theory (CMT), which has been successfully applied to VCSEL modeling since [39] and has since been extended to a wide range of device configurations. Its principal strength lies in its computational efficiency, which makes it particularly well suited for the analysis of complex structures.

In electromagnetism, CMT is typically used in the context of perturbation theory, where the few optical modes of a fully characterized structure are analyzed to determine how they are influenced by small changes in the refractive index. The original modes act as a basis, and the perturbed modes are described as a linear combination. The approach in [39] is different. It starts from the infinitely many modes of a uniform medium, represented as cylindrical waves. These modes, through the formulation of a proper eigenvalue problem, are combined to compute the modes supported by a device, without assuming it to be a "small perturbation" relative to

the uniform medium. This makes the method both full-wave and applicable to a wide range of electromagnetic structures.

In this work, the theory introduced in [39] is further developed, allowing the use of any set of basis functions to expand the electric field in the VCSEL structure. Simulations are carried out by bypassing some of the analytical calculations required for different geometries, relying instead on the computational power of modern personal computers. This enables the rapid determination of the modal properties of fully three-dimensional VCSELs in just a few minutes, only requiring the knowledge of the VCSEL refractive index and geometry, without the need for any additional parameters.

We restrict our analysis to the calculation of cold-cavity modes. Temperature effects are only indirectly accounted for by explicitly modifying the VCSEL refractive index profile. However, we do not include carrier dynamics, and, consequently, spatial-hole-burning effects are not considered. A more comprehensive treatment can be achieved by using the cold-cavity modes, along with their associated properties such as emission wavelength and threshold gain, as input parameters for a dynamical model that includes carrier interactions, as done in [13].

2.1 Integral form of the reciprocity theorem

Within the mathematical formulations, bold letters represent non-scalar quantities, *i.e.*, vectors, matrices and operators. The space to which a non-scalar quantity belongs will be specified at its definition.

Let us consider the Maxwell's equations in the frequency domain[1] with unknown electric field phasor $\mathbf{E}(\mathbf{r}) \in \mathbb{C}^3$ (V/m) and magnetic field phasor $\mathbf{H}(\mathbf{r}) \in \mathbb{C}^3$ (A/m), together with the known input dielectric permittivity $\boldsymbol{\varepsilon}(\mathbf{r}) \in \mathbb{C}^{3\times3}$ (F/m), magnetic permeability $\boldsymbol{\mu}(\mathbf{r}) \in \mathbb{C}^{3\times3}$ (H/m), electric current density $\mathbf{J}_e(\mathbf{r}) \in \mathbb{C}^3$ (A/m^2) and magnetic current density $\mathbf{J}_m(\mathbf{r}) \in \mathbb{C}^3$ (V/m^2)[2]:

$$\begin{cases} \nabla \times \mathbf{E} = -j\omega\boldsymbol{\mu}\mathbf{H} - \mathbf{J}_m, \\ \nabla \times \mathbf{H} = j\omega\boldsymbol{\varepsilon}\mathbf{E} + \mathbf{J}_e. \end{cases} \tag{2.1}$$

[1] We are now considering the phasors of the fields. The time dependency is assumed to be as $\exp(j\omega t)$, ω being the optical frequency, thus time derivatives become multiplications by $j\omega$.

[2] The space dependency is implied.

Let us also consider a related problem with unknowns $\bar{\mathbf{E}}$ and $\bar{\mathbf{H}}$, without sources and with input dielectric permittivity and magnetic permeability which are the adjoint (transpose and complex conjugate) to the ones in (2.1) [59, 60], *i.e.*,

$$\begin{cases} \nabla \times \bar{\mathbf{E}} = -j\omega \boldsymbol{\mu}^{\dagger} \bar{\mathbf{H}}, \\ \nabla \times \bar{\mathbf{H}} = j\omega \boldsymbol{\varepsilon}^{\dagger} \bar{\mathbf{E}}. \end{cases} \tag{2.2}$$

In order to proceed we will need to exploit the well known vector calculus property which states:

$$\nabla \cdot (\mathbf{A} \times \mathbf{B}) = \mathbf{B} \cdot \nabla \times \mathbf{A} - \mathbf{A} \cdot \nabla \times \mathbf{B}, \tag{2.3}$$

$\mathbf{A}$ and $\mathbf{B}$ being generic vector fields in $\mathbb{C}^3$. Let us apply (2.3) to the quantity

$$\begin{aligned} &\nabla \cdot \left(\mathbf{E} \times \bar{\mathbf{H}}^* + \bar{\mathbf{E}}^* \times \mathbf{H} \right) = \nabla \cdot \left(\mathbf{E} \times \bar{\mathbf{H}}^* \right) + \nabla \cdot \left(\bar{\mathbf{E}}^* \times \mathbf{H} \right) = \\ &= \bar{\mathbf{H}}^* \cdot \nabla \times \mathbf{E} - \mathbf{E} \cdot \nabla \times \bar{\mathbf{H}}^* + \mathbf{H} \cdot \nabla \times \bar{\mathbf{E}}^* - \bar{\mathbf{E}}^* \cdot \nabla \times \mathbf{H} = \\ &= \bar{\mathbf{H}}^* \cdot \nabla \times \mathbf{E} - \mathbf{E} \cdot \left(\nabla \times \bar{\mathbf{H}} \right)^* + \mathbf{H} \cdot \left(\nabla \times \bar{\mathbf{E}} \right)^* - \bar{\mathbf{E}}^* \cdot \nabla \times \mathbf{H}. \end{aligned} \tag{2.4}$$

Noticing that all the curls in (2.4) can be determined starting from (2.1) and (2.2), it follows that[3]

$$\begin{aligned} &\nabla \times \left(\mathbf{E} \times \bar{\mathbf{H}}^* + \bar{\mathbf{E}}^* \times \mathbf{H} \right) = \bar{\mathbf{H}}^* \cdot (-j\omega \boldsymbol{\mu} \mathbf{H} - \mathbf{J}_m) + \\ &- \mathbf{E} \cdot \left(-j\omega \boldsymbol{\varepsilon}^T \bar{\mathbf{E}}^* \right) + \mathbf{H} \cdot \left(+j\omega \boldsymbol{\mu}^T \bar{\mathbf{H}}^* \right) - \bar{\mathbf{E}}^* \cdot (j\omega \boldsymbol{\varepsilon} \mathbf{E} + \mathbf{J}_e) = \\ &= -j\omega \bar{\mathbf{H}}^* \cdot (\boldsymbol{\mu} \mathbf{H}) - \bar{\mathbf{H}}^* \cdot \mathbf{J}_m + j\omega \mathbf{E} \cdot \left(\boldsymbol{\varepsilon}^T \bar{\mathbf{E}}^* \right) + j\omega \mathbf{H} \cdot \left(\boldsymbol{\mu}^T \bar{\mathbf{H}}^* \right) + \\ &- j\omega \bar{\mathbf{E}}^* \cdot (\boldsymbol{\varepsilon} \mathbf{E}) - \bar{\mathbf{E}}^* \cdot \mathbf{J}_e. \end{aligned}$$

If the medium is reciprocal, *i.e.* $\boldsymbol{\varepsilon} = \boldsymbol{\varepsilon}^T$ and $\boldsymbol{\mu} = \boldsymbol{\mu}^T$, true for typical semiconductor lasers, the red red and blue terms in the previous equation simplify, giving

$$\nabla \cdot \left(\mathbf{E} \times \bar{\mathbf{H}}^* + \bar{\mathbf{E}}^* \times \mathbf{H} \right) = - \left(\bar{\mathbf{H}}^* \cdot \mathbf{J}_m + \bar{\mathbf{E}}^* \cdot \mathbf{J}_e \right). \tag{2.5}$$

Let us now consider a field whose Poynting vector is aligned with $\hat{z}$, chosen as the longitudinal direction for a VCSEL. In this view, we can identify a transverse coordinate $\boldsymbol{\rho} \in \mathbb{R}^2$ and a propagation coordinate $z \in \mathbb{R}$. In this way, it is possible to decompose the ∇ operator as

$$\nabla = \nabla_t + \hat{z} \partial_z, \tag{2.6}$$

[3] Note that the complex conjugate applied on an adjoint matrix simply yields the transposed matrix.

with $\nabla_t = \partial_x \hat{x} + \partial_y \hat{y}$ in cartesian coordinates. Considering (2.5) with a fixed value of z and integrating the remaining $\boldsymbol{\rho}$-dependent quantity over the entire plane $\mathbb{R}^2$, it is possible to obtain:

$$\int_{\mathbb{R}^2} (\nabla_t + \hat{z}\partial_z) \cdot \left(\mathbf{E} \times \bar{\mathbf{H}}^* + \bar{\mathbf{E}}^* \times \mathbf{H}\right) \mathrm{d}^2\boldsymbol{\rho} = -\int_{\mathbb{R}^2} \left(\bar{\mathbf{H}}^* \cdot \mathbf{J}_m + \bar{\mathbf{E}}^* \cdot \mathbf{J}_e\right) \mathrm{d}^2\boldsymbol{\rho}. \tag{2.7}$$

The left-hand side of (2.7) gives rise to two integrals, let us focus on the first one featuring ∇_t and let us apply the 2D divergence theorem, *i.e.*,

$$\int_D \nabla_t \cdot \left(\mathbf{E} \times \bar{\mathbf{H}}^* + \bar{\mathbf{E}}^* \times \mathbf{H}\right) \mathrm{d}^2\boldsymbol{\rho} = \oint_{\partial D} \hat{n} \cdot \left(\mathbf{E} \times \bar{\mathbf{H}}^* + \bar{\mathbf{E}}^* \times \mathbf{H}\right) \mathrm{d}l = 0, \tag{2.8}$$

∂D representing the boundary of D, with $D = \mathbb{R}^2$. Indeed the latter expression requires the evaluation of the fields at the boundaries of $D = \mathbb{R}^2$ (fields must be evaluated at infinite), which are zero due to the Poynting theorem. Finally, inserting (2.8) into (2.7), the integral form of the reciprocity theorem for a field propagating along z is obtained. We can further notice that the projection along z in the left-hand side makes uninfluent any z-component of the fields. By defining $\mathbf{E}_t$ the transverse component of $\mathbf{E}$ (and similarly for the other fields), the final result reads

$$\int_{\mathbb{R}^2} \frac{\partial}{\partial z} \left(\mathbf{E}_t \times \bar{\mathbf{H}}_t^* + \bar{\mathbf{E}}_t^* \times \mathbf{H}_t\right) \cdot \hat{z}\, \mathrm{d}^2\boldsymbol{\rho} = -\int_{\mathbb{R}^2} \left(\bar{\mathbf{H}}^* \cdot \mathbf{J}_m + \bar{\mathbf{E}}^* \cdot \mathbf{J}_e\right) \mathrm{d}^2\boldsymbol{\rho}. \tag{2.9}$$

Typically the magnetic currents are not considered and one simply assumes $\mathbf{J}_e = \mathbf{J}$, further simplifying (2.9).

2.2 Relation between longitudinal and transverse components of the fields

The goal of this section is to show that the transverse and longitudinal components of the fields are not independent. Indeed, it is possible to derive the longitudinal component as a function of the transverse one. Starting from a sourceless version of (2.1) and exploiting the decomposition of differential operators in longitudinal and

transverse components, assuming no magnetic materials, Maxwell's equations read

$$\begin{cases} \nabla \times \mathbf{E} = (\nabla_t + \partial_z \hat{z}) \times (\mathbf{E}_t + E_z \hat{z}) = -j\omega\mu_0 (\mathbf{H}_t + H_z \hat{z}), \\ \nabla \times \mathbf{H} = (\nabla_t + \partial_z \hat{z}) \times (\mathbf{H}_t + H_z \hat{z}) = +j\omega \boldsymbol{\varepsilon} \mathbf{E}. \end{cases} \tag{2.10}$$

Defining

$$\boldsymbol{\varepsilon} = \begin{bmatrix} \varepsilon_{xx} & \varepsilon_{xy} & \varepsilon_{xz} \\ \varepsilon_{yx} & \varepsilon_{yy} & \varepsilon_{yz} \\ \varepsilon_{zx} & \varepsilon_{zy} & \varepsilon_{zz} \end{bmatrix}, \tag{2.11}$$

with $\boldsymbol{\varepsilon} = \boldsymbol{\varepsilon}^T$, the term in $\boldsymbol{\varepsilon}\mathbf{E}$ in (2.10) can be written as

$$\boldsymbol{\varepsilon}\mathbf{E} = \begin{bmatrix} \varepsilon_{xx} & \varepsilon_{xy} & \varepsilon_{xz} \\ \varepsilon_{yx} & \varepsilon_{yy} & \varepsilon_{yz} \\ \varepsilon_{zx} & \varepsilon_{zy} & \varepsilon_{zz} \end{bmatrix} \begin{bmatrix} E_x \\ E_y \\ E_z \end{bmatrix} = \begin{bmatrix} \varepsilon_{xx}E_x + \varepsilon_{xy}E_y + \varepsilon_{xz}E_z \\ \varepsilon_{yx}E_x + \varepsilon_{yy}E_y + \varepsilon_{yz}E_z \\ \varepsilon_{zx}E_x + \varepsilon_{zy}E_y + \varepsilon_{zz}E_z \end{bmatrix}. \tag{2.12}$$

The z component of the vector $\boldsymbol{\varepsilon}\mathbf{E}$ defined in (2.12) can be written in a more compact way by defining the vector

$$\boldsymbol{\varepsilon}_{tz} = \begin{bmatrix} \varepsilon_{xz} \\ \varepsilon_{yz} \\ 0 \end{bmatrix} \tag{2.13}$$

and noticing that, due to the reciprocity of $\boldsymbol{\varepsilon}$,

$$\begin{bmatrix} \varepsilon_{zx} & \varepsilon_{zy} & 0 \end{bmatrix} = \boldsymbol{\varepsilon}_{tz}^T.$$

With these definitions, the z component of $\boldsymbol{\varepsilon}\mathbf{E}$ can be written as

$$\boldsymbol{\varepsilon}\mathbf{E} \cdot \hat{z} = \boldsymbol{\varepsilon}_{tz}^T \mathbf{E}_t + \varepsilon_{zz} E_z = \boldsymbol{\varepsilon}_{tz} \cdot \mathbf{E}_t + \varepsilon_{zz} E_z. \tag{2.14}$$

Projecting both equations of (2.10) onto the longitudinal direction we obtain:

$$\begin{cases} \hat{z} \cdot \nabla_t \times \mathbf{E}_t = -j\omega\mu_0 H_z, \\ \hat{z} \cdot \nabla_t \times \mathbf{H}_t = j\omega \left(\boldsymbol{\varepsilon}_{tz}^T \mathbf{E}_t + \varepsilon_{zz} E_z \right), \end{cases}$$

from which the z components of the fields can be easily written in terms of the transverse ones as:

$$\begin{cases} H_z = -(j\omega\mu_0)^{-1}\,\hat{z}\cdot\nabla_t\times\mathbf{E}_t, \\ E_z = (j\omega\varepsilon_{zz})^{-1}\,\hat{z}\cdot\nabla_t\times\mathbf{H}_t - \dfrac{1}{\varepsilon_{zz}}\boldsymbol{\varepsilon}_{tz}^T\mathbf{E}_t. \end{cases} \tag{2.15}$$

The demonstration can be easily generalized in the case of a more general problem which also icnludes $\mathbf{J}_e$. In this case the equations for the z components become:

$$\begin{cases} H_z = -(j\omega\mu_0)^{-1}\,\hat{z}\cdot\nabla_t\times\mathbf{E}_t, \\ E_z = (j\omega\varepsilon_{zz})^{-1}\,[\hat{z}\cdot\nabla_t\times\mathbf{H}_t - J_{e,z}] - \dfrac{1}{\varepsilon_{zz}}\boldsymbol{\varepsilon}_{tz}^T\mathbf{E}_t. \end{cases} \tag{2.16}$$

2.3 Reference medium basis

2.3.1 Treatment of the dielectric constant profile as an equivalent source of a reference problem

At this stage, the core of the theory can be addressed. To determine the optical modes of a VCSEL, we need to consider the source-free problem characterized by a position-dependent dielectric tensor profile $\boldsymbol{\varepsilon}(\mathbf{r})$, representing the VCSEL structure. The corresponding Maxwell's equations are identical to those presented in (2.10). We can consider the simpler problem of a certain reference medium described by a lossless dielectric constant ε_{ref} or, equivalently, by a refractive index r so that $\varepsilon_{\text{ref}} = r^2\varepsilon_0$, where ε_0 is the vacuum dielectric constant. Since this is arbitrary, the simplest possible choice is a uniform ε_{ref}, however, the general theory is not limited by this assumption[4]. For instance, in [7] the reference medium is chosen to be an unperturbed optical fiber. With this view, fixing the z coordinate, the actual dielectric tensor can be thought of as

$$\boldsymbol{\varepsilon}(\boldsymbol{\rho}) = \varepsilon_{\text{ref}}\mathbf{I} + \Delta\boldsymbol{\varepsilon}(\boldsymbol{\rho}), \tag{2.17}$$

[4]The important requirement for the reference medium is that we are able to determine, possibly analytically, the optical modes that it supports, as they will be used as a basis. A uniform reference dielectric constant supports the very well-known modes of free space.

with

$$\Delta\boldsymbol{\varepsilon} = \boldsymbol{\varepsilon} - \boldsymbol{\varepsilon}_{\text{ref}}\mathbf{I}, \tag{2.18}$$

$\mathbf{I}$ being the identity matrix. The $\mathbf{H}$ curl equation of (2.10) can be rewritten as

$$\nabla \times \mathbf{H} = j\omega\varepsilon_{\text{ref}}\mathbf{E} + \mathbf{J}_{eq}, \tag{2.19}$$

where

$$\mathbf{J}_{\text{eq}} = j\omega\Delta\boldsymbol{\varepsilon}\mathbf{E}. \tag{2.20}$$

We can interpret the spatial distribution of the dielectric tensor as an equivalent source, $\mathbf{J}_{\text{eq}}$, within the context of a uniform reference problem characterized by ε_{ref}, simply reading

$$\begin{cases} \nabla \times \mathbf{E}_{\boldsymbol{\mu}} = -j\omega\mu_0\mathbf{H}_{\boldsymbol{\mu}}, \\ \nabla \times \mathbf{H}_{\boldsymbol{\mu}} = +j\omega\varepsilon_{\text{ref}}\mathbf{E}_{\boldsymbol{\mu}}, \end{cases} \tag{2.21}$$

$\boldsymbol{\mu}$ being the label identifying the various modes. CMT aims to express the solution of this problem as a linear combination of the modes of the uniform reference medium, whose transverse $\boldsymbol{\rho}$-dependent components form a complete vectorial basis.

2.3.2 Modes of the reference medium for any basis choice

The modes of the reference medium defined in (2.21), which must be pre-determined or known analytically, are central to the formulation of the theory. Each mode is identified by a multi-dimensional label $\boldsymbol{\mu}$ consisting of N_l components. These components are further divided into N_c continuous labels, grouped into $\boldsymbol{\mu}_c$, such as the transverse wavevector, and N_d discrete labels, grouped into $\boldsymbol{\mu}_d$, representing properties like forward/backward propagation or TE/TM polarization. The forward/backward propagation label, present for all bases, denoted by α, only specifies the dependency on the propagation coordinate z, either $\exp\left(-j\beta_{\boldsymbol{\mu}}z\right)$ or $\exp\left(+j\beta_{\boldsymbol{\mu}}z\right)$, where $\beta_{\boldsymbol{\mu}}$ is the longitudinal component of the wavevector for the mode labeled by $\boldsymbol{\mu}$, also denoted as modal propagation constant. The norm of the total wavevector in the reference medium, k_r, is determined by the dispersion relation of light, while the transverse component k_t is embedded in $\boldsymbol{\mu}$. This reads:

$$k_r = \frac{2\pi}{\lambda}r \tag{2.22}$$

and

$$\beta_{\boldsymbol{\mu}} = \sqrt{k_r^2 - k_t^2}, \tag{2.23}$$

with λ being the considered wavelength. The type of propagation can be compactly expressed using a functional form for the z-dependency as $\exp\left(-js_\alpha\beta_{\boldsymbol{\mu}}z\right)$, with

$$s_{\boldsymbol{\mu}} = \begin{cases} +1, & \alpha = \text{forward}, \\ -1, & \alpha = \text{backward}. \end{cases} \tag{2.24}$$

To account for forward/backward propagation explicitly, α can be placed as the last element of $\boldsymbol{\mu}_d$, i.e., $\mu_d^{(N_d)} = \alpha$. Thus, the decomposition of $\boldsymbol{\mu}$ is expressed as:

$$\boldsymbol{\mu} = \begin{bmatrix} \boldsymbol{\mu}_c \\ \boldsymbol{\mu}_d \end{bmatrix} = \begin{bmatrix} \mu_c^{(1)} \\ \vdots \\ \mu_c^{(N_c)} \\ \mu_d^{(1)} \\ \vdots \\ \mu_d^{(N_d-1)} \\ \alpha \end{bmatrix}. \tag{2.25}$$

Having defined the modal label $\boldsymbol{\mu}$, the vector basis describing the electric and magnetic fields of the reference medium can be generally expressed as

$$\mathbf{E}_{\boldsymbol{\mu}} = \mathbf{E}_{t,\boldsymbol{\mu}} + \hat{z}E_{z,\boldsymbol{\mu}} = \left[\mathbf{e}_{\boldsymbol{\mu}}(\boldsymbol{\rho}) + \hat{z}e_{z,\boldsymbol{\mu}}(\boldsymbol{\rho})\right]\exp\left(-js_{\boldsymbol{\mu}}\beta_{\boldsymbol{\mu}}z\right), \tag{2.26}$$

$$\mathbf{H}_{\boldsymbol{\mu}} = \mathbf{H}_{t,\boldsymbol{\mu}} + \hat{z}H_{z,\boldsymbol{\mu}} = \left[\mathbf{h}_{\boldsymbol{\mu}}(\boldsymbol{\rho}) + \hat{z}h_{z,\boldsymbol{\mu}}(\boldsymbol{\rho})\right]\exp\left(-js_{\boldsymbol{\mu}}\beta_{\boldsymbol{\mu}}z\right), \tag{2.27}$$

with

- $\mathbf{E}_{t,\boldsymbol{\mu}}$ and $\mathbf{H}_{t,\boldsymbol{\mu}}$ representing the transverse components of the modal fields,
- $E_{z,\boldsymbol{\mu}}$ and $H_{z,\boldsymbol{\mu}}$ representing the longitudinal components of the modal fields,
- $\mathbf{e}_{\boldsymbol{\mu}}$ and $\mathbf{h}_{\boldsymbol{\mu}}$ representing the z-independent transverse components of the modal fields,
- $e_{z,\boldsymbol{\mu}}$ and $h_{z,\boldsymbol{\mu}}$ representing the z-independent longitudinal components of the modal fields.

The z-independent transverse components $\mathbf{e}_{\boldsymbol{\mu}}$ and $\mathbf{h}_{\boldsymbol{\mu}}$ are related by the modal impedance $Z_{\boldsymbol{\mu}}$, defined as the quantity such that:

$$\mathbf{h}_{\boldsymbol{\mu}} = \frac{\left(s_{\boldsymbol{\mu}}\hat{z}\right) \times \mathbf{e}_{\boldsymbol{\mu}}}{Z_{\boldsymbol{\mu}}}. \tag{2.28}$$

2.3.3 Modes of the adjoint reference medium

When applying (2.9) to the perturbed reference problem defined in (2.19), the solutions of the sourceless adjoint reference problem are needed. Having defined $\mathbf{E}_{\boldsymbol{\mu}}$ and $\mathbf{H}_{\boldsymbol{\mu}}$ in (2.26)–(2.27) as the $\boldsymbol{\mu}$-th mode of the reference problem in (2.21), completely determined by:

- the transverse components $\mathbf{e}_{\boldsymbol{\mu}}$ and $\mathbf{h}_{\boldsymbol{\mu}}$,
- the longitudinal components $e_{z,\boldsymbol{\mu}}$ and $h_{z,\boldsymbol{\mu}}$,
- the sign $s_{\boldsymbol{\mu}} = \pm 1$ determined by the type of propagation along $\pm\hat{z}$,
- the propagation constant $\beta_{\boldsymbol{\mu}}$,

we can define the corresponding $\boldsymbol{\mu}$-th mode of the adjoint problem as

$$\bar{\mathbf{E}}_{\boldsymbol{\mu}} = \bar{\mathbf{E}}_{t,\boldsymbol{\mu}} + \hat{z}\bar{E}_{z,\boldsymbol{\mu}} = \left[\bar{\mathbf{e}}_{\boldsymbol{\mu}}(\boldsymbol{\rho}) + \hat{z}\bar{e}_{z,\boldsymbol{\mu}}(\boldsymbol{\rho})\right] \exp\left(-j\bar{s}_{\boldsymbol{\mu}}\bar{\beta}_{\boldsymbol{\mu}} z\right), \tag{2.29}$$

$$\bar{\mathbf{H}}_{\boldsymbol{\mu}} = \bar{\mathbf{H}}_{t,\boldsymbol{\mu}} + \hat{z}\bar{H}_{z,\boldsymbol{\mu}} = \left[\bar{\mathbf{h}}_{\boldsymbol{\mu}}(\boldsymbol{\rho}) + \hat{z}\bar{h}_{z,\boldsymbol{\mu}}(\boldsymbol{\rho})\right] \exp\left(-j\bar{s}_{\boldsymbol{\mu}}\bar{\beta}_{\boldsymbol{\mu}} z\right), \tag{2.30}$$

determined by an equivalent set of parameters. The goal of this subsection is to link the parameters describing $\bar{\mathbf{E}}_{\boldsymbol{\mu}}$ and $\bar{\mathbf{H}}_{\boldsymbol{\mu}}$ with the ones of the modes of the reference problems in (2.26) and (2.27). To do so, one can start by plugging the expressions of the modes $\mathbf{E}_{\boldsymbol{\mu}}$ and $\mathbf{H}_{\boldsymbol{\mu}}$ into (2.21) splitting the gradient operator into $\nabla = \nabla_t + \hat{z}\partial_z$. Doing so, we can consider the exponential propagation along z, resulting in $\partial_z = -js_{\boldsymbol{\mu}}\beta_{\boldsymbol{\mu}}$. Simplifying the complex exponential propagation functions in both sides and defining $\mathbf{e}^{\text{tot}}_{\boldsymbol{\mu}} = \mathbf{e}_{\boldsymbol{\mu}} + \hat{z}e_{z,\boldsymbol{\mu}}$ and $\mathbf{h}^{\text{tot}}_{\boldsymbol{\mu}} = \mathbf{h}_{\boldsymbol{\mu}} + \hat{z}h_{z,\boldsymbol{\mu}}$, one remains with

$$\begin{cases} \nabla_t \times \mathbf{e}^{\text{tot}}_{\boldsymbol{\mu}} - js_{\boldsymbol{\mu}}\beta_{\boldsymbol{\mu}}\hat{z} \times \mathbf{e}^{\text{tot}}_{\boldsymbol{\mu}} = -j\omega\mu_0\mathbf{h}^{\text{tot}}_{\boldsymbol{\mu}}, \\ \nabla_t \times \mathbf{h}^{\text{tot}}_{\boldsymbol{\mu}} - js_{\boldsymbol{\mu}}\beta_{\boldsymbol{\mu}}\hat{z} \times \mathbf{h}^{\text{tot}}_{\boldsymbol{\mu}} = j\omega\varepsilon_{\text{ref}}\mathbf{e}^{\text{tot}}_{\boldsymbol{\mu}}. \end{cases} \tag{2.31}$$

Similarly, the equations defining the parameters of $\bar{\mathbf{E}}_{\boldsymbol{\mu}}$ and $\bar{\mathbf{H}}_{\boldsymbol{\mu}}$ will be exactly the same, with $\varepsilon^*_{\text{ref}}$ instead of ε_{ref}[5]:

$$\begin{cases} \nabla_t \times \bar{\mathbf{e}}^{\text{tot}}_{\boldsymbol{\mu}} - j\bar{s}_{\boldsymbol{\mu}}\bar{\beta}_{\boldsymbol{\mu}}\hat{z} \times \bar{\mathbf{e}}^{\text{tot}}_{\boldsymbol{\mu}} = -j\omega\mu_0\bar{\mathbf{h}}^{\text{tot}}_{\boldsymbol{\mu}}, \\ \nabla_t \times \bar{\mathbf{h}}^{\text{tot}}_{\boldsymbol{\mu}} - j\bar{s}_{\boldsymbol{\mu}}\bar{\beta}_{\boldsymbol{\mu}}\hat{z} \times \bar{\mathbf{h}}^{\text{tot}}_{\boldsymbol{\mu}} = j\omega\varepsilon^*_{\text{ref}}\bar{\mathbf{e}}^{\text{tot}}_{\boldsymbol{\mu}}. \end{cases} \tag{2.32}$$

Splitting (2.31) into longitudinal and transverse components it is possible to rewrite:

$$\begin{cases} \nabla_t \times \mathbf{e}_{\boldsymbol{\mu}} = -j\omega\mu_0 h_{z,\boldsymbol{\mu}}\hat{z}, & \text{longitudinal}, \\ \nabla_t \times \mathbf{h}_{\boldsymbol{\mu}} = j\omega\varepsilon_{\text{ref}} e_{z,\boldsymbol{\mu}}\hat{z}, & \text{longitudinal}, \\ \nabla_t e_{z,\boldsymbol{\mu}} \times \hat{z} - js_{\boldsymbol{\mu}}\beta_{\boldsymbol{\mu}}\hat{z} \times \mathbf{e}_{\boldsymbol{\mu}} = -j\omega\mu_0\mathbf{h}_{\boldsymbol{\mu}}, & \text{transverse}, \\ \nabla_t h_{z,\boldsymbol{\mu}} \times \hat{z} - js_{\boldsymbol{\mu}}\beta_{\boldsymbol{\mu}}\hat{z} \times \mathbf{h}_{\boldsymbol{\mu}} = j\omega\varepsilon_{\text{ref}}\mathbf{e}_{\boldsymbol{\mu}}, & \text{transverse}. \end{cases} \tag{2.33}$$

From the latter, by complex conjugating both sides one has:

$$\begin{cases} \nabla_t \times \mathbf{e}^*_{\boldsymbol{\mu}} = j\omega\mu_0 h^*_{z,\boldsymbol{\mu}}\hat{z}, & \text{longitudinal}, \\ \nabla_t \times \mathbf{h}^*_{\boldsymbol{\mu}} = -j\omega\varepsilon^*_{\text{ref}} e^*_{z,\boldsymbol{\mu}}\hat{z}, & \text{longitudinal}, \\ \nabla_t e^*_{z,\boldsymbol{\mu}} \times \hat{z} + js_{\boldsymbol{\mu}}\beta^*_{\boldsymbol{\mu}}\hat{z} \times \mathbf{e}^*_{\boldsymbol{\mu}} = j\omega\mu_0\mathbf{h}^*_{\boldsymbol{\mu}}, & \text{transverse}, \\ \nabla_t h^*_{z,\boldsymbol{\mu}} \times \hat{z} + js_{\boldsymbol{\mu}}\beta^*_{\boldsymbol{\mu}}\hat{z} \times \mathbf{h}^*_{\boldsymbol{\mu}} = -j\omega\varepsilon^*_{\text{ref}}\mathbf{e}^*_{\boldsymbol{\mu}}, & \text{transverse}. \end{cases} \tag{2.34}$$

Similarly, splitting (2.32), we can write:

$$\begin{cases} \nabla_t \times \bar{\mathbf{e}}_{\boldsymbol{\mu}} = -j\omega\mu_0 \bar{h}_{z,\boldsymbol{\mu}}\hat{z}, & \text{longitudinal}, \\ \nabla_t \times \bar{\mathbf{h}}_{\boldsymbol{\mu}} = j\omega\varepsilon^*_{\text{ref}} \bar{e}_{z,\boldsymbol{\mu}}\hat{z}, & \text{longitudinal}, \\ \nabla_t \bar{e}_{z,\boldsymbol{\mu}} \times \hat{z} - j\bar{s}_{\boldsymbol{\mu}}\bar{\beta}_{\boldsymbol{\mu}}\hat{z} \times \bar{\mathbf{e}}_{\boldsymbol{\mu}} = -j\omega\mu_0\bar{\mathbf{h}}_{\boldsymbol{\mu}}, & \text{transverse}, \\ \nabla_t \bar{h}_{z,\boldsymbol{\mu}} \times \hat{z} - j\bar{s}_{\boldsymbol{\mu}}\bar{\beta}_{\boldsymbol{\mu}}\hat{z} \times \bar{\mathbf{h}}_{\boldsymbol{\mu}} = j\omega\varepsilon_{\text{ref}}\bar{\mathbf{e}}_{\boldsymbol{\mu}}, & \text{transverse}. \end{cases} \tag{2.35}$$

Comparing (2.35) and (2.34), one can infer that the barred parameters of the adjoint structure to be substituted into (2.35) to obtain (2.34) are

$$\bar{\mathbf{e}}_{\boldsymbol{\mu}} = \mathbf{e}^*_{\boldsymbol{\mu}}, \tag{2.36}$$

$$\bar{e}_{z,\boldsymbol{\mu}} = -e^*_{z,\boldsymbol{\mu}}, \tag{2.37}$$

[5]Having chosen an isotropic reference medium, its dielectric constant is represented by a scalar quantity, thus the adjoint operation (transposition and complex conjugation) simply equates to a complex conjugation operation.

$$\bar{\mathbf{h}}_{\boldsymbol{\mu}} = \mathbf{h}^*_{\boldsymbol{\mu}}, \tag{2.38}$$

$$\bar{h}_{z,\boldsymbol{\mu}} = -h^*_{z,\boldsymbol{\mu}}, \tag{2.39}$$

$$\bar{\beta}_{\boldsymbol{\mu}} = \beta^*_{\boldsymbol{\mu}}, \tag{2.40}$$

$$\bar{s}_{\boldsymbol{\mu}} = s_{\boldsymbol{\mu}}. \tag{2.41}$$

2.3.4 Orthogonality between the modes of the reference medium

The orthogonality condition between different modes of the reference medium is given by the integral form of the reciprocity theorem expressed in (2.9), which must be expressed by targeting the reference problem in (2.21). This means that one can plug any mode of the reference problem in place of **E** and **H** and any mode of the adjoint reference problem in place of $\bar{\mathbf{E}}$ and $\bar{\mathbf{H}}$. Considering the modes $\boldsymbol{\nu}$ and $\boldsymbol{\mu} \neq \boldsymbol{\nu}$, the left-hand side of (2.9) for the reference problem in (2.21) reads:

$$\begin{aligned}
&\int_{\mathbb{R}^2} \partial_z \left(\mathbf{E}_{t,\boldsymbol{\nu}} \times \bar{\mathbf{H}}^*_{t,\boldsymbol{\mu}} + \bar{\mathbf{E}}^*_{t,\boldsymbol{\mu}} \times \mathbf{H}_{t,\boldsymbol{\nu}} \right) \cdot \hat{z}\, \mathrm{d}^2\rho = \\
&\int_{\mathbb{R}^2} \partial_z \left[\left(\mathbf{e}_{\boldsymbol{\nu}} e^{-j s_{\boldsymbol{\nu}} \beta_{\boldsymbol{\nu}} z} \right) \times \left(\bar{\mathbf{h}}_{\boldsymbol{\mu}} e^{-j \bar{s}_{\boldsymbol{\mu}} \bar{\beta}_{\boldsymbol{\mu}} z} \right)^* + \left(\bar{\mathbf{e}}_{\boldsymbol{\mu}} e^{-j \bar{s}_{\boldsymbol{\mu}} \bar{\beta}_{\boldsymbol{\mu}} z} \right)^* \times \left(\mathbf{h}_{\boldsymbol{\nu}} e^{-j s_{\boldsymbol{\nu}} \beta_{\boldsymbol{\nu}} z} \right) \right] \cdot \hat{z}\, \mathrm{d}^2\rho = \\
&= \left[\partial_z e^{-j \left(s_{\boldsymbol{\nu}} \beta_{\boldsymbol{\nu}} - \bar{s}_{\boldsymbol{\mu}} \bar{\beta}^*_{\boldsymbol{\mu}} \right) z} \right] \int_{\mathbb{R}^2} \left(\mathbf{e}_{\boldsymbol{\nu}} \times \bar{\mathbf{h}}^*_{\boldsymbol{\mu}} + \bar{\mathbf{e}}^*_{\boldsymbol{\mu}} \times \mathbf{h}_{\boldsymbol{\nu}} \right) \cdot \hat{z}\, \mathrm{d}^2\rho = \\
&= -j \left(s_{\boldsymbol{\nu}} \beta_{\boldsymbol{\nu}} - \bar{s}_{\boldsymbol{\mu}} \bar{\beta}^*_{\boldsymbol{\mu}} \right) e^{-j \left(s_{\boldsymbol{\nu}} \beta_{\boldsymbol{\nu}} - \bar{s}_{\boldsymbol{\mu}} \bar{\beta}^*_{\boldsymbol{\mu}} \right) z} \int_{\mathbb{R}^2} \left(\mathbf{e}_{\boldsymbol{\nu}} \times \bar{\mathbf{h}}^*_{\boldsymbol{\mu}} + \bar{\mathbf{e}}^*_{\boldsymbol{\mu}} \times \mathbf{h}_{\boldsymbol{\nu}} \right) \cdot \hat{z}\, \mathrm{d}^2\rho.
\end{aligned} \tag{2.42}$$

Being (2.21) a sourceless problem, the right-hand side of (2.9) is identically zero, thus yielding the condition:

$$\left(s_{\boldsymbol{\nu}} \beta_{\boldsymbol{\nu}} - \bar{s}_{\boldsymbol{\mu}} \bar{\beta}^*_{\boldsymbol{\mu}} \right) \int_{\mathbb{R}^2} \left(\mathbf{e}_{\boldsymbol{\nu}} \times \bar{\mathbf{h}}^*_{\boldsymbol{\mu}} + \bar{\mathbf{e}}^*_{\boldsymbol{\mu}} \times \mathbf{h}_{\boldsymbol{\nu}} \right) \cdot \hat{z}\, \mathrm{d}^2\rho = 0. \tag{2.43}$$

Recalling (2.41)–(2.40) and considering non-evanescent modes with real propagation constants, the latter becomes:

$$\left(s_{\boldsymbol{\nu}} \beta_{\boldsymbol{\nu}} - s_{\boldsymbol{\mu}} \beta_{\boldsymbol{\mu}} \right) \int_{\mathbb{R}^2} \left(\mathbf{e}_{\boldsymbol{\nu}} \times \bar{\mathbf{h}}^*_{\boldsymbol{\mu}} + \bar{\mathbf{e}}^*_{\boldsymbol{\mu}} \times \mathbf{h}_{\boldsymbol{\nu}} \right) \cdot \hat{z}\, \mathrm{d}^2\rho = 0. \tag{2.44}$$

If $\boldsymbol{\mu} = \boldsymbol{\nu}$, the equation is satisfied due to the first factor, $\left(s_{\boldsymbol{\mu}} \beta_{\boldsymbol{\mu}} - s_{\boldsymbol{\nu}} \beta_{\boldsymbol{\nu}} \right)$, independently on the value of the integral, although for different modes the equation must be satisfied due to the second integral being zero. In other words, the integral must be

zero when $\boldsymbol{\mu} \neq \boldsymbol{\nu}$, with the possibility of it being different from zero only for $\boldsymbol{\mu} = \boldsymbol{\nu}$. Mathematically, this translates to:

$$\int_{\mathbb{R}^2} \left(\mathbf{e}_{\boldsymbol{\nu}} \times \bar{\mathbf{h}}^*_{\boldsymbol{\mu}} + \bar{\mathbf{e}}^*_{\boldsymbol{\mu}} \times \mathbf{h}_{\boldsymbol{\nu}} \right) \cdot \hat{z} \, \mathrm{d}^2\rho = C_{\boldsymbol{\mu}} \prod_{i=1}^{N_c} \delta \left(\mu_c^{(i)} - \nu_c^{(i)} \right) \prod_{i=1}^{N_d} \delta_{\mu_d^{(i)} \nu_d^{(i)}}, \tag{2.45}$$

having defined $C_{\boldsymbol{\mu}}$ the power normalization constant of mode $\boldsymbol{\mu}$, $\delta \left(\mu_c^{(i)} - \nu_c^{(i)} \right)$ the Dirac delta function describing the continuous labels and $\delta_{\mu_d^{(i)} \nu_d^{(i)}}$ the Krönecker delta describing discrete labels[6]. The latter is useful to determine the power normalization constant $C_{\boldsymbol{\mu}}$ for any given basis.

All deltas (both Kröneker and Dirac) that do not describe propagation type must arise due to the specific chosen basis. In this view, they arise from the specific expressions for the z-independent transverse components of the modes. However, the Kröneker delta in relation to propagation arises at a more general level, directly from the left-hand side of (2.45), which can be rewritten exploiting (2.36)–(2.38), obtaining:

$$\begin{aligned}
&\int_{\mathbb{R}^2} \left[\mathbf{e}_{\boldsymbol{\nu}} \times \left(\mathbf{h}^*_{\boldsymbol{\mu}} \right)^* + \left(\mathbf{e}^*_{\boldsymbol{\mu}} \right)^* \times \mathbf{h}_{\boldsymbol{\nu}} \right] \cdot \hat{z} \, \mathrm{d}^2\rho = \\
&= \int_{\mathbb{R}^2} \left(\mathbf{e}_{\boldsymbol{\nu}} \times \mathbf{h}_{\boldsymbol{\mu}} + \mathbf{e}_{\boldsymbol{\mu}} \times \mathbf{h}_{\boldsymbol{\nu}} \right) \cdot \hat{z} \, \mathrm{d}^2\rho \overset{(2.28)}{=} \\
&= \int_{\mathbb{R}^2} \left(\mathbf{e}_{\boldsymbol{\nu}} \times \frac{(s_{\boldsymbol{\mu}} \hat{z}) \times \mathbf{e}_{\boldsymbol{\mu}}}{Z_{\boldsymbol{\mu}}} + \mathbf{e}_{\boldsymbol{\mu}} \times \frac{(s_{\boldsymbol{\nu}} \hat{z}) \times \mathbf{e}_{\boldsymbol{\nu}}}{Z_{\boldsymbol{\nu}}} \right) \cdot \hat{z} \, \mathrm{d}^2\rho = \\
&= \left(\frac{s_{\boldsymbol{\mu}}}{Z_{\boldsymbol{\mu}}} + \frac{s_{\boldsymbol{\nu}}}{Z_{\boldsymbol{\nu}}} \right) \int_{\mathbb{R}^2} \mathbf{e}_{\boldsymbol{\mu}} \cdot \mathbf{e}_{\boldsymbol{\nu}} \, \mathrm{d}^2\rho.
\end{aligned} \tag{2.46}$$

With this new expression, the orthogonality between the modes can be expressed as:

$$\left(\frac{s_{\boldsymbol{\mu}}}{Z_{\boldsymbol{\mu}}} + \frac{s_{\boldsymbol{\nu}}}{Z_{\boldsymbol{\nu}}} \right) \int_{\mathbb{R}^2} \mathbf{e}_{\boldsymbol{\mu}} \cdot \mathbf{e}_{\boldsymbol{\nu}} \, \mathrm{d}^2\rho = C_{\boldsymbol{\mu}} \prod_{i=1}^{N_c} \delta \left(\mu_c^{(i)} - \nu_c^{(i)} \right) \prod_{i=1}^{N_d} \delta_{\mu_d^{(i)} \nu_d^{(i)}}. \tag{2.47}$$

Consider for instance two identical modes except for the propagation type. Defining $\alpha_{\boldsymbol{\mu}}$ and $\alpha_{\boldsymbol{\nu}}$ the propagation label for modes $\boldsymbol{\mu}$ and $\boldsymbol{\nu}$ respectively, then the result is identically zero if $\alpha_{\boldsymbol{\mu}} \neq \alpha_{\boldsymbol{\nu}}$. This explains the presence of the Kroñeker deltas for

[6]Notice that all Dirac delta functions are dimensional quantities, whose unit is the reciprocal of the unit of their argument. On the other hand, Krönecker deltas are adimensional. The unit of the power normalization constant $C_{\boldsymbol{\mu}}$ will depend both on the unit of the basis and on the unit of the continuous labels.

all discrete labels in (2.45), including the propagation label. On the contrary, for $\alpha_{\boldsymbol{\mu}} = \alpha_{\boldsymbol{\nu}}$, the two terms in the left-hand side sum up, from which a factor of $2\frac{s_{\boldsymbol{\mu}}}{Z_{\boldsymbol{\mu}}}$ arises, yielding:

$$C_{\boldsymbol{\mu}} \propto s_{\boldsymbol{\mu}}. \tag{2.48}$$

As expected from the physical intuition, (2.48) confirms that the sign of the power propagation constant is determined by whether the considered mode is forwardly or backwardly propagating.

This general framework accommodates all of the bases which are solution of the reference problem in (2.21). For instance, it can represent both the plane wave basis of a uniform medium, where two transverse wavevector components are needed, and the cylindrical wave basis, only involving one radial component for the transverse wavevector, offering a more theoretical description compared to [39]. We choose to work with cylindrical waves primarily for computational efficiency. Indeed, reducing the number of continuous labels minimizes the number of required basis functions that are needed to accurately represent the fields.

2.3.5 Basis of cylindrical waves

In this thesis, the unknown transverse components of the electric field within the VCSEL are expanded using the cylindrical wave basis defined in [61]. Employing a basis that aligns with the symmetries of the geometry of the investigated structure is crucial to reduce the number of basis functions required to achieve an accurate representation. This makes the cylindrical wave basis highly efficient for modeling standard circular VCSELs. Nevertheless, it can also be applied to VCSELs of other shapes, although at the cost of increasing the number of basis functions needed. This basis features a multi-label $\boldsymbol{\mu}$ with five entries, among which one is continuous and four are discrete:

$$\boldsymbol{\mu}_c = k_t, \quad \boldsymbol{\mu}_d = \begin{bmatrix} m \\ p \\ l \\ \alpha \end{bmatrix} \quad \rightarrow \quad \boldsymbol{\mu} = \begin{bmatrix} k_t \\ m \\ p \\ l \\ \alpha \end{bmatrix}, \tag{2.49}$$

with their meaning expressed in Tab. 2.1.

Symbol	Type	Values	Description
k_t	Continuous	$\mathbb{R}_+$	Transverse wavevector component in the reference medium with reference index r, dimensionally $[\text{length}]^{-1}$.
m	Discrete	$\{0,1,2,3,\ldots\}$	Azimuthal order of the modes, related to the number of angular zeros of the mode, dimensionless.
p	Discrete	TE, TM	Polarization of the mode: either TE (transverse electric) or TM (transverse magnetic), dimensionless.
l	Discrete	Even, Odd	Determines the choice of angular functions (sine or cosine) used for the mode, dimensionless.
α	Discrete	Forward, Backward	Type of propagation: forward or backward, dimensionless.

Table 2.1 Description of the labels identifying the basis of cylindrical waves.

To define the analytical expression of cylindrical waves, we first introduce $J_m(x)$ as the Bessel function of the first kind of order m calculated at an adimensional argument x. These well-known functions exhibit numerous mathematical properties including [62, 63]:

$$J_m(x) = \frac{x}{2m}\left[J_{m-1}(x) + J_{m+1}(x)\right], \tag{2.50}$$

$$\frac{\partial J_m(x)}{\partial x} = \frac{1}{2}\left[J_{m-1}(x) - J_{m+1}(x)\right], \tag{2.51}$$

$$J_{m+1}(x) = \frac{m}{x}J_m(x) - \frac{\partial J_m(x)}{\partial x}, \tag{2.52}$$

$$J_{m-1}(x) = \frac{m}{x}J_m(x) + \frac{\partial J_m(x)}{\partial x}, \tag{2.53}$$

$$J_{-2m}(x) = J_{2m}(x), \tag{2.54}$$

$$J_{-(2m+1)}(x) = -J_{2m+1}(x), \tag{2.55}$$

$$J_m(x) \sim \frac{2^{-m}}{m!}x^m, \quad x \to 0, \tag{2.56}$$

$$J_m(x) \sim \sqrt{\frac{2}{\pi x}} \cos\left(x - \frac{2m+1}{4}\pi\right), \quad x \to \infty, \tag{2.57}$$

$$\int_0^\infty x dx J_m(k_1 x) J_m(k_2 x) = \frac{\delta(k_1 - k_2)}{k_1} \quad \text{(orthogonality)}. \tag{2.58}$$

Furthermore, modal angular functions[7] can be defined as

$$f_m(\phi) = \begin{cases} \cos(m\phi), & l = \text{even} \\ \sin(m\phi), & l = \text{odd} \end{cases} \tag{2.59}$$

and

$$g_m(\phi) = \begin{cases} -\sin(m\phi), & l = \text{even} \\ \cos(m\phi), & l = \text{odd} \end{cases}. \tag{2.60}$$

With these definitions, the modal electric fields $\mathbf{e}_{\boldsymbol{\mu}} = \mathbf{e}_{x,\boldsymbol{\mu}}\hat{x} + \mathbf{e}_{y,\boldsymbol{\mu}}\hat{y}$ and $e_{z,\boldsymbol{\mu}}$ of (2.26) can be written for the basis of the cylindrical wave as a function of the transverse coordinate $\boldsymbol{\rho}$ expressed in the polar coordinates (ρ, ϕ). This is reported in Tab. 2.2.

p value	Component	Expression
TE	x	$e_x = J_{m+1}(k_t\rho) f_{m+1}(\phi) + J_{m-1}(k_t\rho) f_{m-1}(\phi)$
	y	$e_y = -J_{m+1}(k_t\rho) g_{m+1}(\phi) + J_{m-1}(k_t\rho) g_{m-1}(\phi)$
	z	$e_z = 0$
TM	x	$e_x = J_{m+1}(k_t\rho) f_{m+1}(\phi) - J_{m-1}(k_t\rho) f_{m-1}(\phi)$
	y	$e_y = -J_{m+1}(k_t\rho) g_{m+1}(\phi) - J_{m-1}(k_t\rho) g_{m-1}(\phi)$
	z	$e_z = 2 s_{\boldsymbol{\mu}} j \frac{k_t}{\beta_{\boldsymbol{\mu}}} J_m(k_t\rho) f_m(\phi)$

Table 2.2 Expressions for the electric field components of cylindrical waves for TE and TM modes.

The easiest case we could try is $m = 0$, $p = \text{TE}$, $l = \text{even}$. We would obtain

$$e_x = J_1(k_t\rho)\cos(\phi) + J_{-1}(k_t\rho)\cos(-\phi) = \cos(\phi)\left(J_1(k_t\rho) + J_{-1}(k_t\rho)\right) \overset{(2.55)}{=} 0,$$

[7] Notice that these angular functions also depend on l even if the explicit dependency is not reported to be coherent with [61].

(with the same result for e_y) meaning that this specific combination does not lead to an actual mode. This implies that a brute force approach for the field expansion could result in useless contributions, only increasing computational time.

For this basis, magnetic fields can be calculated using (2.28), knowing that the modal impedance reads:

$$Z_{\boldsymbol{\mu}} = \frac{Z_0}{r} \cdot \begin{cases} k_r/\beta_{\boldsymbol{\mu}}, & p = \mathrm{TE}, \\ \beta_{\boldsymbol{\mu}}/k_r, & p = \mathrm{TM}, \end{cases} \tag{2.61}$$

Z_0 being the vacuum impedance.

2.3.6 Calculation of the power normalization constant for cylindrical waves

Considering labels k_t, m, p, l and α for mode $\boldsymbol{\mu}$ and k_t', m', p', l' and α' for mode $\boldsymbol{\nu}$, the definition of the power normalization constant $C_{\boldsymbol{\mu}}$ in (2.47) reads for cylindrical waves:

$$\left(\frac{s_{\boldsymbol{\mu}}}{Z_{\boldsymbol{\mu}}} + \frac{s_{\boldsymbol{\nu}}}{Z_{\boldsymbol{\nu}}}\right) \int_{\mathbb{R}^2} \mathbf{e}_{\boldsymbol{\mu}} \cdot \mathbf{e}_{\boldsymbol{\nu}} \, \mathrm{d}^2\rho = C_{\boldsymbol{\mu}} \delta\left(k_t - k_t'\right) \delta_{mm'} \delta_{pp'} \delta_{ll'} \delta_{\alpha\alpha'}. \tag{2.62}$$

We can consider just forward modes, recalling that a factor $s_{\boldsymbol{\mu}}$ should be added to the final result as a consequence of (2.48). Since the basis functions must satisfy (2.62), thanks to the Krönecker deltas, we can set all discrete labels to be the same, as they do not lead to divergent integrals and only contribute with a finite term. Thus, we focus solely on distinct continuous variables. Specifically we can consider the case

where $k_t \neq k_t'$, while keeping $m = m'$, $p = p'$, and $l = l'$. Defining

$$\begin{aligned}
J_\pm &= J_{m\pm1}(k_t\rho),\\
J'_\pm &= J_{m\pm1}(k'_t\rho),\\
f_\pm &= f_{m\pm1}(\phi),\\
g_\pm &= g_{m\pm1}(\phi),\\
e_{x,\mathrm{TE}} &= J_+ f_+ + J_- f_-,\\
e'_{x,\mathrm{TE}} &= J'_+ f_+ + J'_- f_-,\\
e_{y,\mathrm{TE}} &= -J_+ g_+ + J_- g_-,\\
e'_{y,\mathrm{TE}} &= -J'_+ g_+ + J'_- g_-
\end{aligned} \tag{2.63}$$

for sake of compactness, starting with $p = \mathrm{TE}$, the double integral on the left-hand side of (2.62) can be evaluated as

$$\begin{aligned}
&\int_0^{2\pi} d\phi \int_0^\infty \rho d\rho \left(e_{x,\mathrm{TE}} e'_{x,\mathrm{TE}} + e_{y,\mathrm{TE}} e'_{y,\mathrm{TE}}\right) =\\
&\int_0^{2\pi} d\phi \int_0^\infty \rho d\rho \left(J_+ J'_+ f_+^2 + J_+ J'_- f_+ f_- + J_- J'_+ f_- f_+ + J_- J'_- f_-^2 + \right.\\
&\left. + J_+ J'_+ g_+^2 - J_+ J'_- g_+ g_- - J_- J'_+ g_- g_+ + J_- J'_- g_-^2\right).
\end{aligned} \tag{2.64}$$

Noticing that $f_\pm^2 + g_\pm^2 = 1$, that

$$\int_0^\infty \rho d\rho \left(J_+ J'_+ + J_- J'_-\right) \overset{(2.58)}{=} \frac{2\delta\left(k_t - k'_t\right)}{k_t} \tag{2.65}$$

and computing the trivial angular integrals, (2.64) becomes

$$\frac{4\pi\delta\left(k_t - k'_t\right)}{k_t} + \int_0^{2\pi} d\phi \left(f_+ f_- - g_+ g_-\right) \int_0^\infty \rho d\rho \left(J_+ J'_- + J_- J'_+\right). \tag{2.66}$$

The remaining angular integral can be computed analytically for the various cases (different m and l values), whose results are summarized in Fig. 2.1. Finally, the remaining radial integral has to be evaluated only for $m = 0$. In that case $J_\pm = J_{\pm1}(k_t\rho)$ and $J'_\pm = J_{\pm1}(k'_t\rho)$, for which

$$J_{\pm1}(k_t\rho) \overset{(2.55)}{=} -J_{\mp1}(k_t\rho),$$

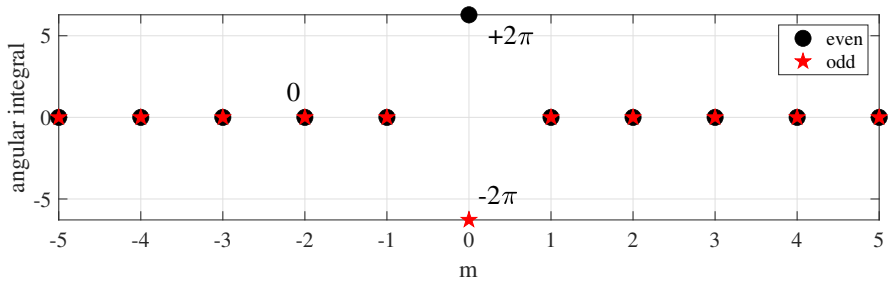

Fig. 2.1 Angular integral defined in (2.66) for the TE case, evaluated for different values of m and l, either even or odd.

leading to

$$\int_0^\infty \rho d\rho \left[J_{+1}(k_t\rho)J_{-1}(k_t'\rho)+J_{-1}(k_t\rho)J_{+1}(k_t'\rho)\right] =$$
$$\int_0^\infty \rho d\rho \left[-J_{-1}(k_t\rho)J_{-1}(k_t'\rho)-J_{+1}(k_t\rho)J_{+1}(k_t'\rho)\right] \overset{(2.58)}{=} -\frac{2\delta\left(k_t-k_t'\right)}{k_t}.$$

Finally, for the TE case, it holds:

$$\int_0^{2\pi} d\phi \int_0^\infty \rho\, d\rho \left(e_{x,\mathrm{TE}}e'_{x,\mathrm{TE}}+e_{y,\mathrm{TE}}e'_{y,\mathrm{TE}}\right) = \begin{cases} \dfrac{4\pi\delta\left(k_t-k_t'\right)}{k_t}, & m\neq 0, \\ 0, & m=0,\ l=\text{even}, \\ \dfrac{8\pi\delta\left(k_t-k_t'\right)}{k_t}, & m=0,\ l=\text{odd}. \end{cases} \tag{2.67}$$

Ignoring the case $m=0$ and $l=$ even, yielding a trivial mode, not able to carry any power, recalling (2.62) and defining

$$n_m = \begin{cases} 1, & m\neq 0, \\ 2, & m=0, \end{cases} \tag{2.68}$$

we finally obtain for the forward TE case:

$$C_{\boldsymbol{\mu}}\Big|_{\text{forward, TE}} = \frac{8\pi n_m}{Z_{\boldsymbol{\mu}}k_t}. \tag{2.69}$$

Repeating the same calculations for the TM case, considering

$$\begin{aligned} e_{x,\mathrm{TM}} &= J_+ f_+ - J_- f_-, \\ e'_{x,\mathrm{TM}} &= J'_+ f_+ - J'_- f_-, \\ e_{y,\mathrm{TM}} &= -J_+ g_+ - J_- g_-, \\ e'_{y,\mathrm{TM}} &= -J'_+ g_+ - J'_- g_-, \end{aligned} \tag{2.70}$$

we end up with

$$\begin{aligned} &\int_0^{2\pi} d\phi \int_0^{\infty} \rho \, d\rho \, \left(e_{x,\mathrm{TM}} e'_{x,\mathrm{TM}} + e_{y,\mathrm{TM}} e'_{y,\mathrm{TM}} \right) = \\ &= \frac{4\pi\delta\left(k_t - k'_t\right)}{k_t} + \int_0^{2\pi} d\phi \, \left(g_+ g_- - f_+ f_- \right) \int_0^{\infty} \rho d\rho \, \left(J_+ J'_- + J_- J'_+ \right). \end{aligned} \tag{2.71}$$

Noticing that the remaining radial integral is exactly the same as the one for the TE case in (2.66), while the angular part differs for a minus sign, the final result is

$$\int_0^{2\pi} d\phi \int_0^{\infty} \rho \, d\rho \, \left(e_{x,\mathrm{TM}} e'_{x,\mathrm{TM}} + e_{y,\mathrm{TM}} e'_{y,\mathrm{TM}} \right) = \begin{cases} \dfrac{4\pi\delta\left(k_t - k'_t\right)}{k_t}, & m \neq 0, \\ 0, & m = 0, \, l = \text{odd}, \\ \dfrac{8\pi\delta\left(k_t - k'_t\right)}{k_t}, & m = 0, \, l = \text{even}. \end{cases} \tag{2.72}$$

Once again, neglecting the powerless case $m = 0$ and $l = \text{odd}$, the power normalization constant in the forward TM case is exactly the same as the TE case, eventually yielding the final result of

$$C_{\boldsymbol{\mu}} = s_{\boldsymbol{\mu}} \frac{8\pi n_m}{Z_{\boldsymbol{\mu}} k_t}, \tag{2.73}$$

considering both forward and backward modes. A summary of the combinations of modal indices which give rise to powerless modes is reported in Tab. 2.3.

p	m	l
TE	0	even
TM	0	odd

Table 2.3 Powerless modes of the cylindrical wave basis. It doesn't make sense to consider them in the basis expansion.

2.4 Coupled mode equations

Consider the unknown fields of the structure under study defined in (2.10), with the reference dielectric constant and equivalent source further specified in (2.19). We can expand their transverse component in terms of the chosen basis of the reference medium as:

$$\mathbf{E}_t(\boldsymbol{\rho},z) = \sum_{\boldsymbol{\mu}_d} \int \mathrm{d}^{N_c}\mu_c \, a_{\boldsymbol{\mu}}(z)\mathbf{e}_{\boldsymbol{\mu}}(\boldsymbol{\rho}), \tag{2.74}$$

$$\mathbf{H}_t(\boldsymbol{\rho},z) = \sum_{\boldsymbol{\mu}_d} \int \mathrm{d}^{N_c}\mu_c \, a_{\boldsymbol{\mu}}(z)\mathbf{h}_{\boldsymbol{\mu}}(\boldsymbol{\rho}), \tag{2.75}$$

where we used the compact notation for the multi-dimensional integral

$$\int \mathrm{d}^{N_c}\mu_c = \int \mathrm{d}\mu_c^{(1)} \ldots \int \mathrm{d}\mu_c^{(N_c)}, \tag{2.76}$$

with each integral extended over the support of the corresponding continuous label.

2.4.1 Left-hand side of the reciprocity theorem

We can plug these expansions in the integral form of the reciprocity theorem (2.9). To do so, one has to consider $\mathbf{E}$ and $\mathbf{H}$ as the actual solutions representing the fields within the VCSEL, whose transverse component can be expanded using (2.74)–(2.75), while $\bar{\mathbf{E}}$ and $\bar{\mathbf{H}}$ are the solutions of the sourceless adjoint problem as defined in (2.29)–(2.30). The left-hand side (LHS) of (2.9) becomes:

$$\begin{aligned}
\mathrm{LHS} &= \int_{\mathbb{R}^2} \mathrm{d}^2\rho \, \partial_z \cdot \\
&\cdot \left[\left(\sum_{\boldsymbol{\nu}_d} \int \mathrm{d}^{N_c}\nu_c \, a_{\boldsymbol{\nu}}\mathbf{e}_{\boldsymbol{\nu}} \right) \times \bar{\mathbf{h}}^*_{\boldsymbol{\mu}} e^{+j\bar{s}_{\boldsymbol{\mu}}\bar{\beta}_{\boldsymbol{\mu}}z} + \bar{\mathbf{e}}^*_{\boldsymbol{\mu}} e^{+j\bar{s}_{\boldsymbol{\mu}}\bar{\beta}^*_{\boldsymbol{\mu}}z} \times \left(\sum_{\boldsymbol{\nu}_d} \int \mathrm{d}^{N_c}\nu_c \, a_{\boldsymbol{\nu}}\mathbf{h}_{\boldsymbol{\nu}} \right) \right] \cdot \hat{z} = \\
&= \sum_{\boldsymbol{\nu}_d} \int \mathrm{d}^{N_c}\nu_c \, \partial_z \left[a_{\boldsymbol{\nu}} e^{j\bar{s}_{\boldsymbol{\mu}}\bar{\beta}^*_{\boldsymbol{\mu}}z} \int_{\mathbb{R}^2} \mathrm{d}^2\rho \, \left(\mathbf{e}_{\boldsymbol{\nu}} \times \bar{\mathbf{h}}^*_{\boldsymbol{\mu}} + \bar{\mathbf{e}}^*_{\boldsymbol{\mu}} \times \mathbf{h}_{\boldsymbol{\nu}} \right) \cdot \hat{z} \right].
\end{aligned}$$

Exploiting the mode orthogonality in (2.45), it is possible to write:

$$\mathrm{LHS} = \sum_{\boldsymbol{\nu}_d} \int \mathrm{d}^{N_c}\nu_c \left[\frac{d}{dz} \left(a_{\boldsymbol{\nu}} e^{j\bar{s}_{\boldsymbol{\mu}}\bar{\beta}^*_{\boldsymbol{\mu}}z} \right) C_{\boldsymbol{\mu}} \prod_{i=1}^{N_c} \delta\left(\mu_c^{(i)} - \nu_c^{(i)} \right) \prod_{i=1}^{N_d} \delta_{\mu_d^{(i)}\nu_d^{(i)}} \right].$$

Considering that:

- $\prod_{i=1}^{N_c} \delta\left(\mu_c^{(i)} - \nu_c^{(i)}\right)$ removes the continuous integrals while imposing all continuous labels to be equal, *i.e.*, $\boldsymbol{\nu}_c = \boldsymbol{\mu}_c$,
- $\prod_{i=1}^{N_d} \delta_{\mu_d^{(i)} \nu_d^{(i)}}$ removes summations for all discrete labels while imposing all discrete labels to be equal, *i.e.*, $\boldsymbol{\nu}_d = \boldsymbol{\mu}_d$,

the LHS becomes

$$\text{LHS} = C_{\boldsymbol{\mu}} \frac{d}{dz}\left(a_{\boldsymbol{\mu}} e^{j\bar{s}_{\boldsymbol{\mu}}\bar{\beta}^*_{\boldsymbol{\mu}} z}\right) = C_{\boldsymbol{\mu}}\left(\frac{da_{\boldsymbol{\mu}}}{dz} + j\bar{s}_{\boldsymbol{\mu}}\bar{\beta}^*_{\boldsymbol{\mu}} a_{\boldsymbol{\mu}}\right) e^{j\bar{s}_{\boldsymbol{\mu}}\bar{\beta}^*_{\boldsymbol{\mu}} z}. \tag{2.77}$$

The final expression for the LHS is obtained by recalling (2.41)–(2.40), *i.e.*, $\bar{\beta}_{\boldsymbol{\mu}} = \beta^*_{\boldsymbol{\mu}}$ and $\bar{s}_{\boldsymbol{\mu}} = s_{\boldsymbol{\mu}}$, yielding:

$$\text{LHS} = C_{\boldsymbol{\mu}}\left(\frac{da_{\boldsymbol{\mu}}}{dz} + j s_{\boldsymbol{\mu}}\beta_{\boldsymbol{\mu}} a_{\boldsymbol{\mu}}\right) e^{j s_{\boldsymbol{\mu}}\beta_{\boldsymbol{\mu}} z}. \tag{2.78}$$

2.4.2 Right-hand side of the reciprocity theorem

Concerning the right-hand side (RHS) of (2.9), one must consider:

$$\text{RHS} = -\int_{\mathbb{R}^2}\left[\left(\bar{\mathbf{e}}^*_{\boldsymbol{\mu}} + \hat{z}\bar{e}^*_{z,\boldsymbol{\mu}}\right) e^{+j\bar{s}_{\boldsymbol{\mu}}\bar{\beta}^*_{\boldsymbol{\mu}} z}\right] \cdot \mathbf{J}_{eq}\, \mathrm{d}^2\boldsymbol{\rho}, \tag{2.79}$$

where $\mathbf{J}_{eq}$ is the one defined in (2.20), featuring the field to be expanded. We can write:

$$\mathbf{J}_{eq} = j\omega\Delta\boldsymbol{\varepsilon}\left(\mathbf{E}_t + E_z\hat{z}\right) \overset{(2.74)}{=} j\omega\Delta\boldsymbol{\varepsilon}\left(\sum_{\boldsymbol{\nu}_d}\int \mathrm{d}^{N_c}\nu_c\, a_{\boldsymbol{\nu}}\mathbf{e}_{\boldsymbol{\nu}} + E_z\hat{z}\right), \tag{2.80}$$

where

$$E_z \overset{(2.16)}{=} \frac{1}{j\omega\varepsilon_{\text{ref}}}\left(\hat{z}\cdot\nabla_t \times \mathbf{H}_t - J_{eq,z}\right). \tag{2.81}$$

Considering the expansion of the transverse component of the magnetic field (2.75) together with

$$\frac{1}{j\omega\varepsilon_{\text{ref}}}\hat{z}\cdot\nabla_t \times \mathbf{h}_{\boldsymbol{\nu}} \overset{(2.21)}{=} e_{z,\boldsymbol{\mu}}, \tag{2.82}$$

it is possible to rewrite E_z in (2.81) as

$$E_z = \sum_{\boldsymbol{\nu}_d}\int \mathrm{d}^{N_c}\nu_c\, a_{\boldsymbol{\nu}} e_{z,\boldsymbol{\nu}} - \frac{J_{eq,z}}{j\omega\varepsilon_{\text{ref}}}. \tag{2.83}$$

Consequently:

$$\begin{aligned}
&\mathbf{J}_{eq} = j\omega\Delta\boldsymbol{\varepsilon}\left(\sum_{\boldsymbol{\nu}_d}\int \mathrm{d}^{N_c}\nu_c\, a_{\boldsymbol{\nu}}\mathbf{e}_{\boldsymbol{\nu}} + \sum_{\boldsymbol{\nu}_d}\int \mathrm{d}^{N_c}\nu_c\, a_{\boldsymbol{\nu}} e_{z,\boldsymbol{\nu}}\hat{z} - \frac{J_{eq,z}}{j\omega\varepsilon_{\mathrm{ref}}}\hat{z}\right) = \\
&\overset{\mathbf{e}^{\mathrm{tot}}_{\boldsymbol{\nu}}=\mathbf{e}_{\boldsymbol{\nu}}+e_{z,\boldsymbol{\nu}}\hat{z}}{=} j\omega\Delta\boldsymbol{\varepsilon}\left(\sum_{\boldsymbol{\nu}_d}\int \mathrm{d}^{N_c}\nu_c\, a_{\boldsymbol{\nu}}\mathbf{e}^{\mathrm{tot}}_{\boldsymbol{\nu}} - \frac{J_{eq,z}}{j\omega\varepsilon_{\mathrm{ref}}}\hat{z}\right) = \\
&= j\omega\sum_{\boldsymbol{\nu}_d}\int \mathrm{d}^{N_c}\nu_c\, a_{\boldsymbol{\nu}}\Delta\boldsymbol{\varepsilon}\mathbf{e}^{\mathrm{tot}}_{\boldsymbol{\nu}} - \frac{J_{eq,z}}{\varepsilon_{\mathrm{ref}}}\Delta\boldsymbol{\varepsilon}\hat{z} = \\
&= j\omega\sum_{\boldsymbol{\nu}_d}\int \mathrm{d}^{N_c}\nu_c\, a_{\boldsymbol{\nu}}\left(\Delta\boldsymbol{\varepsilon}\mathbf{e}^{\mathrm{tot}}_{\boldsymbol{\nu}}\right)_t + j\omega\sum_{\boldsymbol{\nu}_d}\int \mathrm{d}^{N_c}\nu_c\, a_{\boldsymbol{\nu}}\left(\Delta\boldsymbol{\varepsilon}\mathbf{e}^{\mathrm{tot}}_{\boldsymbol{\nu}}\right)_z\hat{z} - \frac{J_{eq,z}}{\varepsilon_{\mathrm{ref}}}\Delta\boldsymbol{\varepsilon}\hat{z},
\end{aligned}$$

where the subscript t stands for the transverse component of the original vector, while the subscript z refers to the z component of the vector, which is a scalar. Focusing on the last product and using a cartesian reference system we can write

$$\begin{aligned}
\Delta\boldsymbol{\varepsilon}\hat{z} &= \begin{bmatrix}\Delta\varepsilon_{xx} & \Delta\varepsilon_{xy} & \Delta\varepsilon_{xz}\\ \Delta\varepsilon_{yx} & \Delta\varepsilon_{yy} & \Delta\varepsilon_{yz}\\ \Delta\varepsilon_{zx} & \Delta\varepsilon_{zy} & \Delta\varepsilon_{zz}\end{bmatrix}\begin{bmatrix}0\\0\\1\end{bmatrix} = \begin{bmatrix}\Delta\varepsilon_{xz}\\ \Delta\varepsilon_{yz}\\ \Delta\varepsilon_{zz}\end{bmatrix} = \\
&= \begin{bmatrix}\Delta\varepsilon_{xz}\\ \Delta\varepsilon_{yz}\\ 0\end{bmatrix} + \Delta\varepsilon_{zz}\hat{z} = \Delta\boldsymbol{\varepsilon}_{t,z} + \Delta\varepsilon_{zz}\hat{z}.
\end{aligned} \tag{2.84}$$

Summing up:

$$\begin{aligned}
&\mathbf{J}_{eq} = \mathbf{J}_{eq,t} + J_{eq,z}\hat{z} = \\
&= j\omega\sum_{\boldsymbol{\nu}_d}\int \mathrm{d}^{N_c}\nu_c\, a_{\boldsymbol{\nu}}\left(\Delta\boldsymbol{\varepsilon}\mathbf{e}^{\mathrm{tot}}_{\boldsymbol{\nu}}\right)_t + j\omega\sum_{\boldsymbol{\nu}_d}\int \mathrm{d}^{N_c}\nu_c\, a_{\boldsymbol{\nu}}\left(\Delta\boldsymbol{\varepsilon}\mathbf{e}^{\mathrm{tot}}_{\boldsymbol{\nu}}\right)_z\hat{z} - \frac{J_{eq,z}}{\varepsilon_{\mathrm{ref}}}\left(\Delta\boldsymbol{\varepsilon}_{t,z} + \Delta\varepsilon_{zz}\hat{z}\right).
\end{aligned} \tag{2.85}$$

Projecting (2.85) onto $\hat{z}$ we obtain a linear equation for $J_{eq,z}$:

$$J_{eq,z} = j\omega\sum_{\boldsymbol{\nu}_d}\int \mathrm{d}^{N_c}\nu_c\, a_{\boldsymbol{\nu}}\left(\Delta\boldsymbol{\varepsilon}\mathbf{e}^{\mathrm{tot}}_{\boldsymbol{\nu}}\right)_z - \frac{\Delta\varepsilon_{zz}}{\varepsilon_{\mathrm{ref}}}J_{eq,z},$$

from which

$$J_{eq,z} = \frac{j\omega\varepsilon_{\text{ref}}}{\varepsilon_{\text{ref}} + \Delta\varepsilon_{zz}} \sum_{\boldsymbol{\nu}_d} \int \mathrm{d}^{N_c} \nu_c \, a_{\boldsymbol{\nu}} \left(\Delta\boldsymbol{\varepsilon}\mathbf{e}_{\boldsymbol{\nu}}^{\text{tot}}\right)_z . \tag{2.86}$$

Knowing the longitudinal component of the equivalent current density, projecting (2.85) onto the transverse plane allows to determine the transverse component as well as

$$\begin{aligned}
\mathbf{J}_{eq,t} &= j\omega \sum_{\boldsymbol{\nu}_d} \int \mathrm{d}^{N_c} \nu_c \, a_{\boldsymbol{\nu}} \left(\Delta\boldsymbol{\varepsilon}\mathbf{e}_{\boldsymbol{\nu}}^{\text{tot}}\right)_t - \frac{J_{eq,z}}{\varepsilon_{\text{ref}}} \Delta\boldsymbol{\varepsilon}_{t,z} = \\
&\overset{(2.86)}{=} j\omega \sum_{\boldsymbol{\nu}_d} \int \mathrm{d}^{N_c} \nu_c \, a_{\boldsymbol{\nu}} \left(\Delta\boldsymbol{\varepsilon}\mathbf{e}_{\boldsymbol{\nu}}^{\text{tot}}\right)_t - j\omega \frac{1}{\varepsilon_{\text{ref}} + \Delta\varepsilon_{zz}} \Delta\boldsymbol{\varepsilon}_{t,z} \sum_{\boldsymbol{\nu}_d} \int \mathrm{d}^{N_c} \nu_c \, a_{\boldsymbol{\nu}} \left(\Delta\boldsymbol{\varepsilon}\mathbf{e}_{\boldsymbol{\nu}}^{\text{tot}}\right)_z = \\
&= j\omega \sum_{\boldsymbol{\nu}_d} \int \mathrm{d}^{N_c} \nu_c \, a_{\boldsymbol{\nu}} \left[\left(\Delta\boldsymbol{\varepsilon}\mathbf{e}_{\boldsymbol{\nu}}^{\text{tot}}\right)_t - \frac{\Delta\boldsymbol{\varepsilon}_{t,z} \left(\Delta\boldsymbol{\varepsilon}\mathbf{e}_{\boldsymbol{\nu}}^{\text{tot}}\right)_z}{\varepsilon_{\text{ref}} + \Delta\varepsilon_{zz}} \right] .
\end{aligned} \tag{2.87}$$

2.4.3 Calculation of the transmission operator

Putting together (2.78), (2.79), (2.86), (2.87) and simplifying the exponential $e^{+j\bar{s}_{\boldsymbol{\mu}}\bar{\beta}_{\boldsymbol{\mu}}^* z}$ from both sides, the integral form of the reciprocity theorem reads

$$\begin{aligned}
&\frac{da_{\boldsymbol{\mu}}}{dz} + j\bar{s}_{\boldsymbol{\mu}}\bar{\beta}_{\boldsymbol{\mu}}^* a_{\boldsymbol{\mu}} = -\frac{1}{C_{\boldsymbol{\mu}}} \int_{\mathbb{R}^2} \left(\bar{\mathbf{e}}_{\boldsymbol{\mu}}^* + \hat{z}\bar{e}_{z,\boldsymbol{\mu}}^* \right) \cdot \left(\mathbf{J}_{eq,t} + \hat{z} J_{eq,z} \right) \mathrm{d}^2\rho = \\
&= -\frac{1}{C_{\boldsymbol{\mu}}} \int_{\mathbb{R}^2} \left(\bar{\mathbf{e}}_{\boldsymbol{\mu}}^* \cdot \mathbf{J}_{eq,t} + \bar{e}_{z,\boldsymbol{\mu}} J_{eq,z} \right) \mathrm{d}^2\rho = \\
&= -\frac{j\omega}{C_{\boldsymbol{\mu}}} \sum_{\boldsymbol{\nu}_d} \int \mathrm{d}^{N_c} \nu_c \, a_{\boldsymbol{\nu}} \int_{\mathbb{R}^2} \left\{ \bar{\mathbf{e}}_{\boldsymbol{\mu}}^* \cdot \left[\left(\Delta\boldsymbol{\varepsilon}\mathbf{e}_{\boldsymbol{\nu}}^{\text{tot}}\right)_t - \frac{\Delta\boldsymbol{\varepsilon}_{t,z} \left(\Delta\boldsymbol{\varepsilon}\mathbf{e}_{\boldsymbol{\nu}}^{\text{tot}}\right)_z}{\varepsilon_{\text{ref}} + \Delta\varepsilon_{zz}} \right] + \bar{e}_{z,\boldsymbol{\mu}}^* \frac{\varepsilon_{\text{ref}}}{\varepsilon_{\text{ref}} + \Delta\varepsilon_{zz}} \left(\Delta\boldsymbol{\varepsilon}\mathbf{e}_{\boldsymbol{\nu}}^{\text{tot}}\right)_z \right\} \mathrm{d}^2\rho .
\end{aligned} \tag{2.88}$$

Finally, defining

$$K_{\boldsymbol{\mu}\boldsymbol{\nu}} = -\frac{j\omega}{C_{\boldsymbol{\mu}}} \int_{\mathbb{R}^2} \left\{ \bar{\mathbf{e}}_{\boldsymbol{\mu}}^* \cdot \left[\left(\Delta\boldsymbol{\varepsilon}\mathbf{e}_{\boldsymbol{\nu}}^{\text{tot}}\right)_t - \frac{\Delta\boldsymbol{\varepsilon}_{t,z} \left(\Delta\boldsymbol{\varepsilon}\mathbf{e}_{\boldsymbol{\nu}}^{\text{tot}}\right)_z}{\varepsilon_{\text{ref}} + \Delta\varepsilon_{zz}} \right] + \bar{e}_{z,\boldsymbol{\mu}}^* \frac{\varepsilon_{\text{ref}}}{\varepsilon_{\text{ref}} + \Delta\varepsilon_{zz}} \left(\Delta\boldsymbol{\varepsilon}\mathbf{e}_{\boldsymbol{\nu}}^{\text{tot}}\right)_z \right\} \mathrm{d}^2\rho \tag{2.89}$$

as the coupling matrix, the coupled mode equations for each mode, recalling (2.41)–(2.40), *i.e.*, $\bar{\beta}_{\boldsymbol{\mu}} = \beta_{\boldsymbol{\mu}}^*$ and $\bar{s}_{\boldsymbol{\mu}} = s_{\boldsymbol{\mu}}$, read

$$\frac{da_{\boldsymbol{\mu}}(z)}{dz} + j s_{\boldsymbol{\mu}} \beta_{\boldsymbol{\mu}} a_{\boldsymbol{\mu}}(z) = \sum_{\boldsymbol{\nu}_d} \int \mathrm{d}^{N_c} \nu_c \, K_{\boldsymbol{\mu}\boldsymbol{\nu}} a_{\boldsymbol{\nu}}(z) . \tag{2.90}$$

For isotropic distribution of refractive indices, then $\Delta\boldsymbol{\varepsilon} = \Delta\varepsilon\mathbf{I}$, greatly simplifying (2.89), which becomes

$$K_{\boldsymbol{\mu}\boldsymbol{\nu}} = -\frac{j\omega}{C_{\boldsymbol{\mu}}}\int_{\mathbb{R}^2}\Delta\varepsilon\left(\bar{\mathbf{e}}^*_{\boldsymbol{\mu}}\cdot\mathbf{e}_{\boldsymbol{\nu}} + \frac{\varepsilon_{\text{ref}}}{\varepsilon_{\text{ref}}+\Delta\varepsilon}\bar{e}^*_{z,\boldsymbol{\mu}}e_{z,\boldsymbol{\nu}}\right)\mathrm{d}^2\rho = K^t_{\boldsymbol{\mu}\boldsymbol{\nu}} + K^z_{\boldsymbol{\mu}\boldsymbol{\nu}}, \tag{2.91}$$

where we have defined the transverse and longitudinal coupling matrices $K^t_{\boldsymbol{\mu}\boldsymbol{\nu}}$ and $K^z_{\boldsymbol{\mu}\boldsymbol{\nu}}$. Wanting to express the latter just as a functions of the modes of the reference medium, exploiting (2.36)–(2.37), *i.e.*, $\bar{\mathbf{e}}_{\boldsymbol{\mu}} = \mathbf{e}^*_{\boldsymbol{\mu}}$ and $\bar{e}_{z,\boldsymbol{\mu}} = -e^*_{z,\boldsymbol{\mu}}$, we can write[8]:

$$K_{\boldsymbol{\mu}\boldsymbol{\nu}} = -\frac{j\omega}{C_{\boldsymbol{\mu}}}\int_{\mathbb{R}^2}\Delta\varepsilon\left(\mathbf{e}_{\boldsymbol{\mu}}\cdot\mathbf{e}_{\boldsymbol{\nu}} - \frac{\varepsilon_{\text{ref}}}{\varepsilon_{\text{ref}}+\Delta\varepsilon}e_{z,\boldsymbol{\mu}}e_{z,\boldsymbol{\nu}}\right)\mathrm{d}^2\rho. \tag{2.92}$$

Choosing a proper ordering for the modal labels contained $\boldsymbol{\mu}$, all modal expansion coefficients $a_{\boldsymbol{\mu}}$ can be collected into the vector $\mathbf{a}$, which belongs to an infinitely dimensional Hilbert space, with both continuous and discrete indices (if the modal basis is not truncated). Similarly, coefficients related to propagation and coupling can be organized into operators of such Hilbert space, leading to the coupled mode equations in vectorial form:

$$\frac{\mathrm{d}\mathbf{a}(z)}{\mathrm{d}z} = (\mathbf{B}+\mathbf{K})\,\mathbf{a}(z), \tag{2.93}$$

where $\mathbf{B}$ is a diagonal multiplicative operator with elements $B_{\boldsymbol{\mu}\boldsymbol{\mu}} = -js_{\boldsymbol{\mu}}\beta_{\boldsymbol{\mu}}$, and $\mathbf{K} = \mathbf{K}^t + \mathbf{K}^z$ is the coupling operator. Solving this system of differential equations provides the transmission operator of a layer with thickness L. The solution of (2.93) is given by the exponential of the operator $(\mathbf{B}+\mathbf{K})L$, yielding the transmission operator or propagator $\mathbf{T}$:

$$\mathbf{T} = \exp\left[(\mathbf{B}+\mathbf{K})L\right]. \tag{2.94}$$

[8] See [52, 64] to further characterize this methodology in terms of a direct/inverse factorization rule, a common terminology in electromagnetic numerical simulations. This choice is usually associated to convergence issues of the reconstructed field, especially close to discontinuities of the dielectric constant, however, as one can see in Subsection 2.6.4, convergence is achieved with a relatively low number of employed basis functions.

2.5 Coupling operator

While the propagation operator **B** is straightforward, this is not the case for the coupling operator **K**. In this section, we investigate the latter, both its transverse and its longitudinal component, for a uniform layer and for a layer featuring transverse variations. We will also provide manageable expressions that can be implemented by properly truncating the basis representation.

2.5.1 Transverse coupling operator for an isotropic uniform layer

Consider an isotropic uniform layer, *i.e.*, $\nabla_t(\Delta\varepsilon) = \mathbf{0}$, $\Delta\varepsilon$ being the difference of the dielectric constant of the layer in question and the reference dielectric constant defined in (2.18). In this view, the transverse component of (2.92) becomes

$$K^t_{\boldsymbol{\mu}\boldsymbol{\nu}} = -\frac{j\omega\Delta\varepsilon}{C_{\boldsymbol{\mu}}} \int_{\mathbb{R}^2} \mathbf{e}_{\boldsymbol{\mu}} \cdot \mathbf{e}_{\boldsymbol{\nu}} \, \mathrm{d}^2\rho. \tag{2.95}$$

Recalling the calculation of the normalization constant (2.47), one can see that the integral on the right-hand side becomes

$$\int_{\mathbb{R}^2} \mathbf{e}_{\boldsymbol{\mu}} \cdot \mathbf{e}_{\boldsymbol{\nu}} \, \mathrm{d}^2\rho = \frac{Z_{\boldsymbol{\mu}} C_{\boldsymbol{\mu}}}{2 s_{\boldsymbol{\mu}}} \prod_{i=1}^{N_c} \delta\left(\mu_c^{(i)} - \nu_c^{(i)}\right) \prod_{i=1}^{N_d-1} \delta_{\mu_d^{(i)} \nu_d^{(i)}}, \tag{2.96}$$

where we no longer consider the Kröneker delta associated to the type of propagation, $\delta_{\mu_d^{(N_d)} \nu_d^{(N_d)}}$, and we annul the dependency of $C_{\boldsymbol{\mu}}$ from the propagation type by dividing from $s_{\boldsymbol{\mu}}$. Indeed, both $\delta_{\mu_d^{(N_d)} \nu_d^{(N_d)}}$ and the fact that $C_{\boldsymbol{\mu}} \propto s_{\boldsymbol{\mu}}$ derived from the factor $\left(\frac{s_{\boldsymbol{\mu}}}{Z_{\boldsymbol{\mu}}} + \frac{s_{\boldsymbol{\nu}}}{Z_{\boldsymbol{\nu}}}\right)$, which is not present at the left-hand side of (2.96), as opposed to (2.47). Furthermore, we accounted for the fact that, as shown in (2.28), the modal impedance does not depend on the type of propagation, so that on the right-hand side one must consider the factor $C_{\boldsymbol{\mu}} Z_{\boldsymbol{\mu}} / (2 s_{\boldsymbol{\mu}})$ in front of the deltas. Finally, the power normalization constant simplifies, $s_{\boldsymbol{\mu}}^{-1} = s_{\boldsymbol{\mu}}$ and (2.95) becomes

$$K^t_{\boldsymbol{\mu}\boldsymbol{\nu}} = -s_{\boldsymbol{\mu}} \frac{j\omega\Delta\varepsilon Z_{\boldsymbol{\mu}}}{2} \prod_{i=1}^{N_c} \delta\left(\mu_c^{(i)} - \nu_c^{(i)}\right) \prod_{i=1}^{N_d-1} \delta_{\mu_d^{(i)} \nu_d^{(i)}}, \tag{2.97}$$

implying that the only remaining coupling is between forward and backward modes.

2.5.2 Longitudinal coupling operator for an isotropic uniform layer using the cylindrical wave basis

Unfortunately, the power normalization constant does not feature the z-components of the basis fields, thus an explicit expression for $K^z_{\boldsymbol{\mu}\boldsymbol{\nu}}$ must be derived in accordance with the chosen basis, which in our case is the cylindrical wave basis. Also in this case, the same product of both Dirac and Kröneker deltas present in (2.97) arise due to the properties of the basis functions, which should arise independently on the basis choice, as dictated by physical intuition. However the constant in front must be explicitly calculated. Let us consider the cylindrical wave basis defined in Tab. 2.2, specifically two modes $\boldsymbol{\mu} = [k_t, m, p, l, \alpha]^T$ and $\boldsymbol{\nu} = [k_t', m', p', l', \alpha']^T$ featuring:

- $m' = m$ since the term $\delta_{mm'}$ would arise due to trigonometric properties, thus two modes with the same m give rise to a finite contribution,
- $p = p' = \mathrm{TM}$, since the the z-component of cylindrical waves is different from zero only for TM modes,
- $l = l'$ since the term $\delta_{ll'}$ would arise due to trigonometric properties, thus two modes with the same l give rise to a finite contribution.

With these assumptions, considering a $\boldsymbol{\rho}$-independent $\Delta\varepsilon$ and defining for sake of compactness

$$
\begin{aligned}
&J = J_m\left(k_t\rho\right),\\
&J' = J_m\left(k_t'\rho\right),\\
&f = f_m(\phi),\\
&e_{z,\mathrm{TM}} = 2s_{\boldsymbol{\mu}} j\frac{k_t}{\beta_{\boldsymbol{\mu}}} Jf,\\
&e'_{z,\mathrm{TM}} = 2s_{\boldsymbol{\nu}} j\frac{k_t'}{\beta_{\boldsymbol{\nu}}} J'f,
\end{aligned}
\tag{2.98}
$$

the z-component of (2.92) becomes

$$\begin{aligned} K^z_{\boldsymbol{\mu}\boldsymbol{\nu}} &= +\frac{j\omega}{C_{\boldsymbol{\mu}}}\frac{\varepsilon_{\text{ref}}\Delta\varepsilon}{\varepsilon_{\text{ref}}+\Delta\varepsilon}\int_{\mathbb{R}^2} e_{z,\text{TM}}e'_{z,\text{TM}}\,\mathrm{d}^2\rho = \\ &= +\frac{j\omega}{C_{\boldsymbol{\mu}}}\frac{\varepsilon_{\text{ref}}\Delta\varepsilon}{\varepsilon_{\text{ref}}+\Delta\varepsilon}\int_0^\infty \rho d\rho \int_0^{2\pi} d\phi \left(2s_{\boldsymbol{\mu}} j\frac{k_t}{\beta_{\boldsymbol{\mu}}}Jf\cdot 2\boldsymbol{\nu} j\frac{k'_t}{\beta_{\boldsymbol{\nu}}}J'f\right) = \\ &= -\frac{j\omega}{C_{\boldsymbol{\mu}}}\frac{\varepsilon_{\text{ref}}\Delta\varepsilon}{\varepsilon_{\text{ref}}+\Delta\varepsilon}s_{\boldsymbol{\mu}}s_{\boldsymbol{\nu}}\frac{4k_tk'_t}{\beta_{\boldsymbol{\mu}}\beta_{\boldsymbol{\nu}}}\int_0^\infty \rho d\rho\, JJ' \int_0^{2\pi} d\phi\, f^2. \end{aligned} \tag{2.99}$$

Analytic results for the angular integral are reported in Fig. 2.2, while the radial integral can be solved considering the orthogonality of Bessel functions expressed in (2.58), from which the Dirac delta $\delta(k_t - k'_t)$ arises, forcing $k_t = k'_t$, from which $\beta_{\boldsymbol{\mu}} = \beta_{\boldsymbol{\nu}}$. Finally, the longitudinal component of the coupling operator for a cylindrical

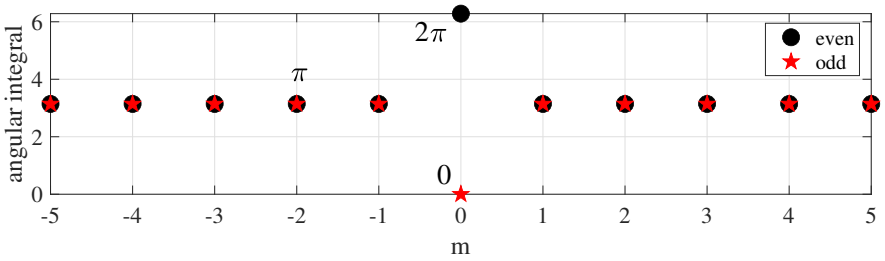

Fig. 2.2 Angular integral defined in (2.99) for the TM case, evaluated for different values of $m \in \mathbb{Z}$ and l, either even or odd.

wave basis reads:

$$K^z_{\boldsymbol{\mu}\boldsymbol{\nu}} = \begin{cases} 0, & p = \text{TE} \vee p' = \text{TE}, \\ -\dfrac{j\omega}{C_{\boldsymbol{\mu}}}\dfrac{\varepsilon_{\text{ref}}\Delta\varepsilon}{\varepsilon_{\text{ref}}+\Delta\varepsilon}s_{\boldsymbol{\mu}}s_{\boldsymbol{\nu}}\dfrac{4\pi k_t}{\beta^2_{\boldsymbol{\mu}}}\delta(k_t-k'_t)\delta_{mm'}\delta_{ll'}, & p = p' = \text{TM}, m \neq 0, \\ -\dfrac{j\omega}{C_{\boldsymbol{\mu}}}\dfrac{\varepsilon_{\text{ref}}\Delta\varepsilon}{\varepsilon_{\text{ref}}+\Delta\varepsilon}s_{\boldsymbol{\mu}}s_{\boldsymbol{\nu}}\dfrac{8\pi k_t}{\beta^2_{\boldsymbol{\mu}}}\delta(k_t-k'_t)\delta_{mm'}\delta_{ll'}, & p = p' = \text{TM}, m = 0, l = \text{even}, \\ 0, & p = p' = \text{TM}, m = 0, l = \text{odd}. \end{cases} \tag{2.100}$$

Once again, we end up with the trivial case of $p = \text{TM}$, $m = 0$ and $l = \text{odd}$ as obtained in (2.72), corresponding to a powerless case. Plugging the explicit expression of $C_{\boldsymbol{\mu}}$ defined in (2.73) into (2.100), ignoring all powerless cases summed up in Tab. 2.3

and considering that $s_{\boldsymbol{\mu}}^2 = 1$, one gets:

$$K^z_{\boldsymbol{\mu}\boldsymbol{\nu}} = \begin{cases} 0, & p = \mathrm{TE} \vee p' = \mathrm{TE}, \\ -s_{\boldsymbol{\nu}} \dfrac{j\omega}{2} \dfrac{\varepsilon_{\mathrm{ref}}\Delta\varepsilon}{\varepsilon_{\mathrm{ref}}+\Delta\varepsilon} Z_{\boldsymbol{\mu}} \dfrac{k_t^2}{\beta^2_{\boldsymbol{\mu}}} \delta(k_t - k_t')\delta_{mm'}\delta_{ll'}, & p = p' = \mathrm{TM}. \end{cases} \tag{2.101}$$

Thanks to the propagation signs in the general definition of the coupling operator in (2.92), specifically recalling that $C_{\boldsymbol{\mu}} \propto s_{\boldsymbol{\mu}}$ and that $e_{z,\boldsymbol{\mu}} \propto s_{\boldsymbol{\mu}}$ (see Tab. 2.2), it holds that $K^t_{\boldsymbol{\mu}\boldsymbol{\nu}} \propto s_{\boldsymbol{\mu}}$, while $K^z_{\boldsymbol{\mu}\boldsymbol{\nu}} \propto s^2_{\boldsymbol{\mu}} s_{\boldsymbol{\nu}} = s_{\boldsymbol{\nu}}$, as confirmed also from the uniform case in (2.97) and (2.101). Subdividing the whole coupling operator into its forward and backward components as

$$\mathbf{K} = \begin{bmatrix} \mathbf{K}_{\mathrm{FF}} & \mathbf{K}_{\mathrm{FB}} \\ \mathbf{K}_{\mathrm{BF}} & \mathbf{K}_{\mathrm{BB}} \end{bmatrix} = \begin{bmatrix} (\mathbf{K}^t_{\mathrm{FF}} + \mathbf{K}^z_{\mathrm{FF}}) & (\mathbf{K}^t_{\mathrm{BF}} + \mathbf{K}^z_{\mathrm{BF}}) \\ (\mathbf{K}^t_{\mathrm{BF}} + \mathbf{K}^z_{\mathrm{BF}}) & (\mathbf{K}^t_{\mathrm{BB}} + \mathbf{K}^z_{\mathrm{BB}}) \end{bmatrix}, \tag{2.102}$$

one can see that

$$\mathbf{K}^t_{\mathrm{FB}} = +\mathbf{K}^t_{\mathrm{FF}}, \tag{2.103}$$

$$\mathbf{K}^t_{\mathrm{BF}} = -\mathbf{K}^t_{\mathrm{FF}}, \tag{2.104}$$

$$\mathbf{K}^t_{\mathrm{BB}} = -\mathbf{K}^t_{\mathrm{FF}}, \tag{2.105}$$

$$\mathbf{K}^z_{\mathrm{FB}} = -\mathbf{K}^z_{\mathrm{FF}}, \tag{2.106}$$

$$\mathbf{K}^z_{\mathrm{BF}} = +\mathbf{K}^z_{\mathrm{FF}}, \tag{2.107}$$

$$\mathbf{K}^z_{\mathrm{BB}} = -\mathbf{K}^z_{\mathrm{FF}}. \tag{2.108}$$

In other words, the overall coupling operator can be obtain from the forward-forward components only as:

$$\mathbf{K} = \begin{bmatrix} (\mathbf{K}^t_{\mathrm{FF}} + \mathbf{K}^z_{\mathrm{FF}}) & (\mathbf{K}^t_{\mathrm{FF}} - \mathbf{K}^z_{\mathrm{FF}}) \\ (-\mathbf{K}^t_{\mathrm{FF}} + \mathbf{K}^z_{\mathrm{FF}}) & (-\mathbf{K}^t_{\mathrm{FF}} - \mathbf{K}^z_{\mathrm{FF}}) \end{bmatrix}. \tag{2.109}$$

2.5.3 Coupling operator for layers with transverse variations

Consider a layer featuring the following dielectric constant profile:

$$\varepsilon(\boldsymbol{\rho}) = \varepsilon_b + \delta\varepsilon S(\boldsymbol{\rho}), \tag{2.110}$$

where:

- ε_b represent a uniform background dielectric constant,
- $S(\boldsymbol{\rho}) \in [0,1]$, represents a normalized function describing the shape of the non-uniform layer, which is non-zero over a certain support $D_S \subseteq \mathbb{R}^2$,
- $\delta\varepsilon$ represents the maximum deviation of the dielectric constant of the layer with respect to the background dielectric constant.

In this case, $\Delta\varepsilon$, *i.e.*, the difference between the dielectric constant of the layer and the reference index, is $\boldsymbol{\rho}$-dependent and reads:

$$\Delta\varepsilon(\boldsymbol{\rho}) = (\varepsilon_b - \varepsilon_{\text{ref}}) + \delta\varepsilon S(\boldsymbol{\rho}). \tag{2.111}$$

With such an expression, the coupling operator for such a layer can be evaluated as:

$$K^t_{\boldsymbol{\mu}\boldsymbol{\nu}} = -\frac{j\omega\,(\varepsilon_b - \varepsilon_{\text{ref}})}{C_{\boldsymbol{\mu}}} \int_{\mathbb{R}^2} \mathbf{e}_{\boldsymbol{\mu}} \cdot \mathbf{e}_{\boldsymbol{\nu}}\, \mathrm{d}^2\rho - \frac{j\omega\delta\varepsilon}{C_{\boldsymbol{\mu}}} \int_{D_S} S(\rho)\, \mathbf{e}_{\boldsymbol{\mu}} \cdot \mathbf{e}_{\boldsymbol{\nu}}\, \mathrm{d}^2\rho. \tag{2.112}$$

The first integral corresponds to the transverse coupling operator of a uniform layer with dielectric constant ε_b, which can be evaluated analytically using (2.97). Conversely, the second integral requires numerical evaluation, as it depends on the specific shape under consideration, resulting in a full operator. From an implementation perspective, the numerical evaluation of the second integral introduces a key difference compared to [39] and other works employing VELMS, where analytical or semi-analytical approaches were used. A fully numerical computation enables extensive parametric studies across different shapes, which is crucial for accounting for technological tolerances in VCSELs or thermal lensing effects. This approach comes with a slightly increased computational cost; however, with modern personal computers, this overhead is negligible, still allowing for a full 3D modal analysis of complete VCSEL structures within a few minutes.

Similarly, for the longitudinal component one has:

$$K^z_{\boldsymbol{\mu}\boldsymbol{\nu}} = +\frac{j\omega}{C_{\boldsymbol{\mu}}}\int_{\mathbb{R}^2}\frac{\varepsilon_{\text{ref}}\left[(\varepsilon_b-\varepsilon_{\text{ref}})+\delta\varepsilon S(\boldsymbol{\rho})\right]}{\varepsilon_b+\delta\varepsilon S(\boldsymbol{\rho})}e_{z,\boldsymbol{\mu}}e_{z,\boldsymbol{\nu}}\,\mathrm{d}^2\rho = \\ \overset{S(\boldsymbol{\rho})=0,\,\boldsymbol{\rho}\notin D_S}{=} +\frac{j\omega}{C_{\boldsymbol{\mu}}}\frac{\varepsilon_{\text{ref}}\left(\varepsilon_b-\varepsilon_{\text{ref}}\right)}{\varepsilon_b}\int_{\mathbb{R}^2\setminus D_S}e_{z,\boldsymbol{\mu}}e_{z,\boldsymbol{\nu}}\,\mathrm{d}^2\rho + \\ +\frac{j\omega}{C_{\boldsymbol{\mu}}}\int_{D_S}\frac{\varepsilon_{\text{ref}}\left[(\varepsilon_b-\varepsilon_{\text{ref}})+\delta\varepsilon S(\boldsymbol{\rho})\right]}{\varepsilon_b+\delta\varepsilon S(\boldsymbol{\rho})}e_{z,\boldsymbol{\mu}}e_{z,\boldsymbol{\nu}}\,\mathrm{d}^2\rho. \tag{2.113}$$

Adding and subtracting the term

$$\frac{j\omega}{C_{\boldsymbol{\mu}}}\frac{\varepsilon_{\text{ref}}\left(\varepsilon_b-\varepsilon_{\text{ref}}\right)}{\varepsilon_b}\int_{D_S}e_{z,\boldsymbol{\mu}}e_{z,\boldsymbol{\nu}}\,\mathrm{d}^2\rho,$$

equation (2.113) becomes:

$$K^z_{\boldsymbol{\mu}\boldsymbol{\nu}} = \frac{j\omega}{C_{\boldsymbol{\mu}}}\frac{\varepsilon_{\text{ref}}\left(\varepsilon_b-\varepsilon_{\text{ref}}\right)}{\varepsilon_b}\int_{\mathbb{R}^2}e_{z,\boldsymbol{\mu}}e_{z,\boldsymbol{\nu}}\,\mathrm{d}^2\rho + \\ +\frac{j\omega}{C_{\boldsymbol{\mu}}}\int_{D_S}\left\{\frac{\varepsilon_{\text{ref}}\left[(\varepsilon_b-\varepsilon_{\text{ref}})+\delta\varepsilon S(\boldsymbol{\rho})\right]}{\varepsilon_b+\delta\varepsilon S(\boldsymbol{\rho})}-\frac{\varepsilon_{\text{ref}}\left(\varepsilon_b-\varepsilon_{\text{ref}}\right)}{\varepsilon_b}\right\}e_{z,\boldsymbol{\mu}}e_{z,\boldsymbol{\nu}}\,\mathrm{d}^2\rho. \tag{2.114}$$

Also in this case, the first integral represents the longitudinal coupling operator of a uniform layer with dielectric constant ε_b, which can be evaluated analytically using (2.101). In contrast, the second integral requires a numerical evaluation, giving rise to a full operator.

2.5.4 Basis truncation and visualization of the matrices

From an implementation perspective, the basis must be truncated to maintain manageable expressions and matrices of finite dimensions. Specifically, the continuous labels can be discretized as:

$$\int d\mu_c^{(i)} \simeq \Delta\mu_c^{(i)}\sum_k, \quad i\in\{1,\ldots,N_c\}, \tag{2.115}$$

where a uniformly spaced set of values $\left\{\left(\mu_c^{(i)}\right)_1,\left(\mu_c^{(i)}\right)_2,\ldots,\left(\mu_c^{(i)}\right)_k,\ldots\right\}$ is chosen for the i-th continuous label, with spacing $\Delta\mu_c^{(i)}$. With this discretization, the right-hand side of the coupled mode equations in (2.90) only features summations,

which can be truncated at a suitable threshold. For the cylindrical wave basis, the truncation can be further refined by selecting specific subsets of modes, such as only even or odd modes, restricting certain azimuthal orders, or setting a proper threshold for the transverse wavevector with a corresponding proper spacing Δk_t. These choices should align with the geometry of the VCSEL and the properties of the modes under investigation.

Additionally, since the second integrals in (2.112) and (2.114) are limited to the support D_S, they do not generate neither Dirac nor Kronecker deltas. Consequently, the differentials associated with continuous labels in (2.90) remain significant and are not canceled by the properties of Dirac delta functions. Therefore, when computing the coupling matrix for transverse variations, all integrals over a finite domain must be multiplied by Δk_t in the cylindrical wave basis. Ultimately, this procedure reduces the original infinite-dimensional Hilbert space to $\mathbb{C}^{N_{\text{tot}}}$, where N_{tot} is the total number of labels retained after discretization and truncation. Notably, this is the only approximation introduced so far, and it remains entirely justified as long as the chosen basis adequately represents the desired VCSEL modes.

Finally, being $\boldsymbol{\mu}$ a multi-dimensional label, one must choose a proper ordering for the expansion coefficients $a_{\boldsymbol{\mu}}$, in order to express them into a unique vector $\mathbf{a} \in \mathbb{C}^{N_{\text{tot}}}$. The convention that is followed throughout all 3D analyses of this thesis for the basis of cylindrical waves is the following:

- the vector is split into its forward and backward components,
- forward and backward components are divided into the even and odd components,
- even and odd components are divided into TE and TM components,
- TE and TM components are divided into different azimuthal components, labeled by different m values ranging in $\{m_1, m_2 \ldots, m_{N_m}\}$,
- each azimuthal component is split into different k_t components, ranging in $\left\{k_{t_1}, k_{t_2} \ldots, k_{t_{N_k}}\right\}$.

This method eventually subdivides the vector $\mathbf{a}$ according to a Matrioska-like structure, displayed in Fig. 2.3.

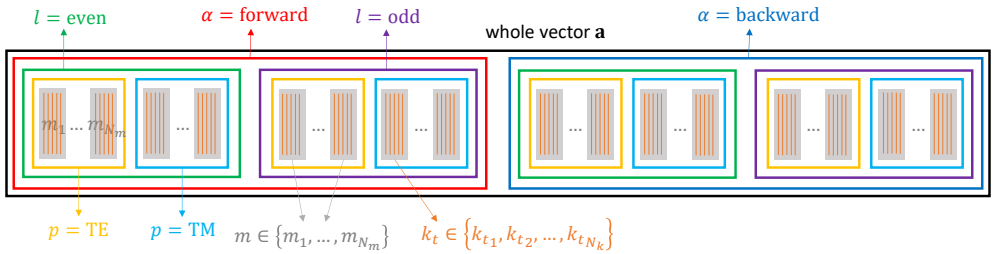

Fig. 2.3 Matrioska-like structure of the vector of expansion coefficients **a**, here reported as a row vector instead of a column vector just for visualization purposes.

To give a real example of how the corresponding matrices could look like, consider the following parameters:

- $\lambda = 850$ nm, from which one can calculate

$$\omega = ck_0, \tag{2.116}$$

with

$$k_0 = \frac{2\pi}{\lambda}, \tag{2.117}$$

- a reference refractive index $r = 1.6$, from which $\varepsilon_{\text{ref}} = \varepsilon_0 r^2$, mimicking the refractive index of the Al_2O_3 oxide,
- a uniform layer with a refractive index of $n = 3.5$, mimicking a GaAs layer,
- a non-uniform layer featuring a background refractive index of $n_b = 1.6$, so that $\varepsilon_b = \varepsilon_0 n_b^2$, and a circular variation in the center with radius $R = 1.5\,\mu$m and index $n_{\text{center}} = 3$, so that $\delta\varepsilon = \varepsilon_0 \left(n_{\text{center}}^2 - n_b^2\right)$. Consider the shape to be defined by a port function, *i.e.*,

$$S(\boldsymbol{\rho}) = \begin{cases} 1, & |\boldsymbol{\rho}| \leq R \\ 0, & \text{otherwise,} \end{cases}$$

mimicking the oxidation layer in VCSELs in Al_2O_3/AlGaAs,

- $k_t \in \{1\Delta k_t, 2\Delta k_t, \dots, N_k \Delta k_t\}$, where $N_k = 15$ and $\Delta k_t = 0.15 \cdot k_r/(N_k + 1)$, k_r being the one in (2.22),
- $m \in \{1\}$,

- $p \in \{\text{TE, TM}\}$,
- $l \in \{\text{even}\}$,
- $\alpha \in \{\text{forward, backward}\}$.

The chosen subset of cylindrical waves is enough to represent the fundamental mode of a standard VCSEL.

Having defined both the dielectric constants and the considered discretization and truncation of the cylindrical wave basis, we must now consider that all matrices can be obtained just from their forward-forward components. Indeed, for the propagation matrix it holds

$$\mathbf{B} = \begin{bmatrix} \mathbf{B}_{\text{FF}} & \mathbf{0} \\ \mathbf{0} & -\mathbf{B}_{\text{FF}} \end{bmatrix} \tag{2.118}$$

as a direct consequence of (2.90), while for the coupling matrix one can exploit (2.109). In this view, the forward-forward component of the propagation matrix and the coupling matrices are reported in Fig. 2.4 and Fig. 2.5, respectively. Only the imaginary part is shown, as the real part is identically zero.

Figure 2.5 illustrates how the longitudinal component of the coupling matrix is generally much smaller than its transverse counterpart both for uniform and non-uniform layers. Additionally, to obtain the matrices of the non-uniform layer, the second terms of (2.112) and (2.114) were employed, where the double integration was performed numerically.

On the other hand, the first terms of (2.112) and (2.114), associated with the coupling matrix of a uniform layer with the same index as the background, were not considered, since in this example $\varepsilon_b = \varepsilon_{\text{ref}}$, making them identically zero. Furthermore, the k_t discretization was accounted for by multiplying the integrals by the k_t spacing, Δk_t, which unifies the units of all matrices, expressed as the inverse of a length.

Finally, for a truncated and discretized basis of cylindrical waves, the formulas for all of the needed matrices is summed up in Fig. 2.6. The generalization to the anisotropic case can be obtained starting from (2.89). It is reported in Appendix A.

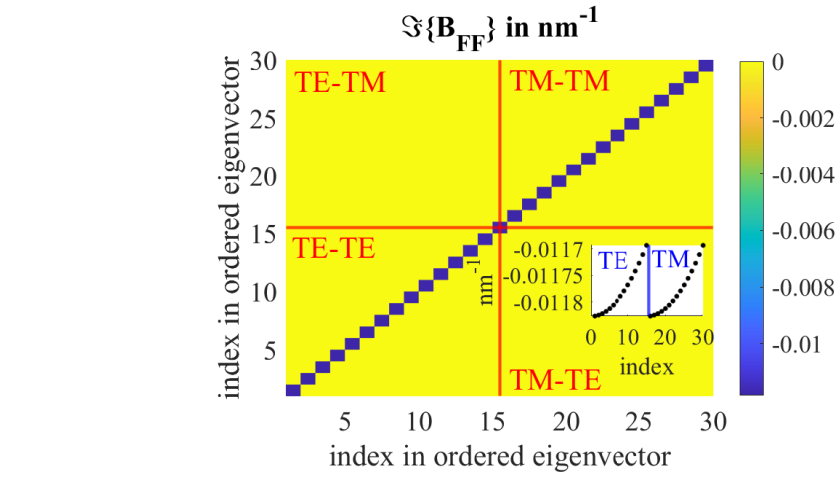

Fig. 2.4 Imaginary part of the forward-forward component of the propagation matrix.

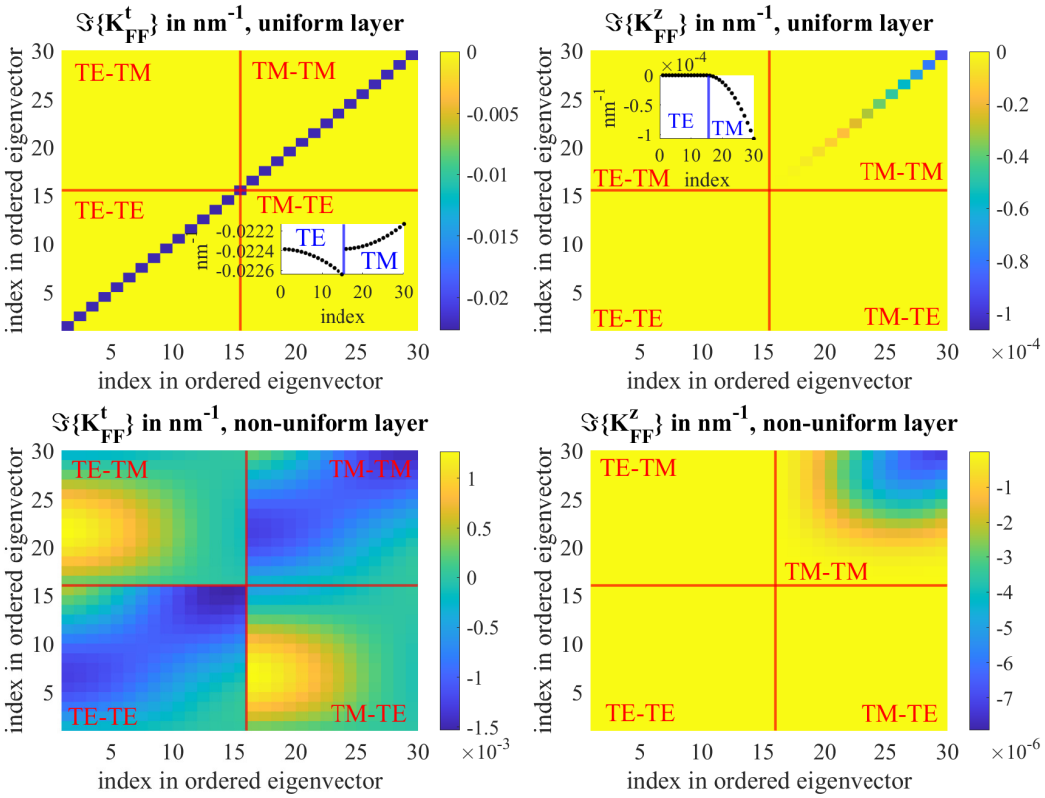

Fig. 2.5 Imaginary part of the forward-forward components of the transverse and longitudinal propagation matrices, both for a uniform and a non-uniform layer. Insets in the first two plots represent the diagonal values of the matrices.

Quantity	Expression
$C_{\boldsymbol{\mu}}$	$s_{\boldsymbol{\mu}} \frac{8\pi n_m}{Z_{\boldsymbol{\mu}} k_t}$
$\left(B_{\boldsymbol{\mu\mu}}\right)_{\mathrm{FF}}$ (diagonal)	$-j\beta_{\boldsymbol{\mu}}$
$\left(K^t_{\boldsymbol{\mu\mu}}\right)_{\mathrm{FF}}$ uniform layer (diagonal)	$\begin{cases} 0, & \text{if } (m=0, p=\mathrm{TE}, l=\text{even}) \; or \; (m=0, p=\mathrm{TM}, l=\text{odd}) \\ -\frac{j\omega\Delta\epsilon Z_{\boldsymbol{\mu}}}{2}, & \text{otherwise} \end{cases}$
$\left(K^z_{\boldsymbol{\mu\mu}}\right)_{\mathrm{FF}}$ uniform layer (diagonal)	$\begin{cases} 0, & \text{if } (p=TE) \; or \; (m=0, p=\mathrm{TM}, l=\text{odd}) \\ -\frac{j\omega}{2}\frac{\varepsilon_{\mathrm{ref}}\Delta\varepsilon}{\varepsilon_{\mathrm{ref}}+\Delta\varepsilon} Z_{\boldsymbol{\mu}} \frac{k_t^2}{\beta_{\boldsymbol{\mu}}^2}, & \text{otherwise} \end{cases}$
$K^t_{\boldsymbol{\mu\nu}}$ non-uniform layer	$\left(K^t_{\boldsymbol{\mu\nu}}\right)_{\mathrm{uniform}} + \left(K^t_{\boldsymbol{\mu\nu}}\right)_{\mathrm{non-uniform}}$, where • $\left(K^t_{\boldsymbol{\mu\nu}}\right)_{\mathrm{uniform}}$ is the one for a uniform layer with the same index as the background • $\left(K^t_{\boldsymbol{\mu\nu}}\right)_{\mathrm{non-uniform}} = -\frac{j\omega\delta\varepsilon\Delta k_t}{c_\mu}\int_{D_S} S(\boldsymbol{\rho})\, \boldsymbol{e_\mu}\cdot\boldsymbol{e_\nu}\, d^2\rho$
$K^z_{\boldsymbol{\mu\nu}}$ non-uniform layer	$\left(K^z_{\boldsymbol{\mu\nu}}\right)_{\mathrm{uniform}} + \left(K^z_{\boldsymbol{\mu\nu}}\right)_{\mathrm{non-uniform}}$, where • $\left(K^z_{\boldsymbol{\mu\nu}}\right)_{\mathrm{uniform}}$ is the one for a uniform layer with the same index as the background • $\left(K^z_{\boldsymbol{\mu\nu}}\right)_{\mathrm{non-uniform}} = +\frac{j\omega\Delta k_t}{c_\mu}\int_{D_S}\left\{\frac{\varepsilon_{\mathrm{ref}}[(\varepsilon_b-\varepsilon_{\mathrm{ref}})+\delta\varepsilon S(\boldsymbol{\rho})]}{\varepsilon_b+\delta\varepsilon S(\boldsymbol{\rho})} - \frac{\varepsilon_{\mathrm{ref}}(\varepsilon_b-\varepsilon_{\mathrm{ref}})}{\varepsilon_b}\right\} e_{z,\boldsymbol{\mu}} e_{z,\nu}\, d^2\rho$
$\mathbf{B}$	$\begin{bmatrix} \mathbf{B}_{\mathrm{FF}} & \mathbf{0} \\ \mathbf{0} & -\mathbf{B}_{\mathrm{FF}} \end{bmatrix}$
$\mathbf{K}$	$\begin{bmatrix} \mathbf{K}^t_{\mathrm{FF}} + \mathbf{K}^z_{\mathrm{FF}} & \mathbf{K}^t_{\mathrm{FF}} - \mathbf{K}^z_{\mathrm{FF}} \\ -\mathbf{K}^t_{\mathrm{FF}} + \mathbf{K}^z_{\mathrm{FF}} & -\mathbf{K}^t_{\mathrm{FF}} - \mathbf{K}^z_{\mathrm{FF}} \end{bmatrix}$
$\boldsymbol{T}$	$\exp[(\mathbf{B}+\mathbf{K})L]$

Fig. 2.6 Most relevant formulas for the calculation of the coupling and transmission matrix for both a uniform and a non-uniform layer, using a truncated and discretized cylindrical wave basis. The effect of the discretization can be noticed by the factor Δk_t, present in the non-uniform components of the coupling matrices.

2.5.5 Application to optical fibers and criteria for basis truncation

Consider an optical fiber characterized by a specific distribution of the dielectric constant, as defined in (2.110). From Fig. 2.6, we now understand how to compute the transmission operator associated with such a structure. Let **a** represent one of the modes supported by the optical fiber, linked to the transverse field through (2.74). By definition, the propagation of **a** through the fiber over a distance L must result in the same mode, phase-shifted by a factor $\exp(-j\beta_{\text{eff}}L)$, where β_{eff} is the modal propagation constant. Mathematically, this condition translates into the following eigenvalue equation:

$$\mathbf{Ta} = e^{-j\beta_{\text{eff}}L}\mathbf{a}. \tag{2.119}$$

Being the propagation operator defined through an operator exponentiation, **T** and $(\mathbf{B}+\mathbf{K})L$ are diagonalized by the same set of eigenvectors, with the eigenvalues of $(\mathbf{B}+\mathbf{K})L$ simply being $-j\beta_{\text{eff}}L$. In this view, (2.119) can be rewritten as

$$(\mathbf{B}+\mathbf{K})\,\mathbf{a} = -j\beta_{\text{eff}}\mathbf{a}. \tag{2.120}$$

We can further define the modal effective refractive index n_{eff} as

$$\beta_{\text{eff}} = n_{\text{eff}}k_0. \tag{2.121}$$

Equation (2.120) is capable of determining the modes of an optical fiber of any shape with relatively low computational cost, provided that an appropriately truncated basis of cylindrical waves is employed. By selecting a suitable basis, it is possible to numerically verify that the results remain independent of the choice of the reference index, as expected from physical intuition.

As a final remark, the choice of a suitable subset of the basis functions must always align with the symmetry properties of the given structure. A common approach is to initially consider an extensive set of basis modes, including both even and odd modes, multiple azimuthal orders, and a broad range of k_t values. By analyzing the coupling matrix and the eigenvectors corresponding to the modes of interest, one can identify the impact of symmetries in the structure. Specifically, certain mode combinations will result in null elements in the coupling matrix due to the symmetry properties of the angular functions of cylindrical waves over the

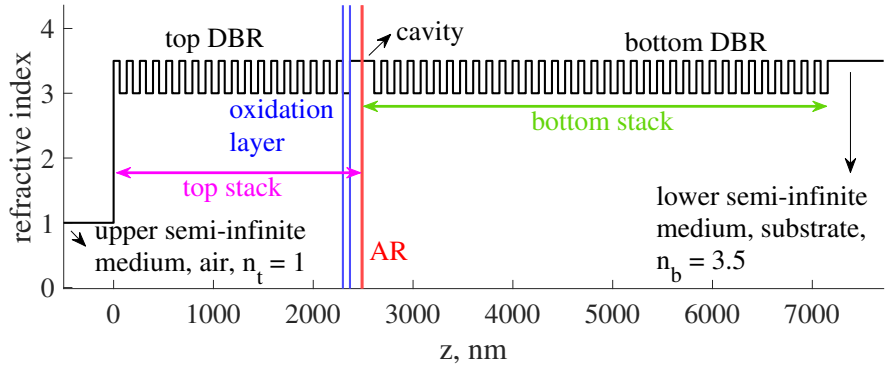

Fig. 2.7 Typical longitudinal structure of a VCSEL.

integration domain. Consequently, the eigenvectors associated with these modes will exhibit null components for specific labels. Based on this observation, the basis can be systematically reduced to optimize computational efficiency. This reasoning justifies why the basis considered in Subsection 2.5.4 is sufficient to represent the fundamental mode of a circular fiber or a circular VCSEL, despite including only even modes and the first azimuthal order.

2.6 Calculation of the VCSEL modes

2.6.1 Generalized Barkhausen criterion

Consider a VCSEL structure with a longitudinal refractive index distribution as sketched in Fig. 2.7. The VCSEL can be divided into multiple layers, each with a constant refractive index along the z axis. These layers can be conceptually grouped into five distinct regions, from top to bottom:

1. An upper semi-infinite medium acting as a top boundary condition, typically air. Let us denote the refractive index of this layer as n_t.

2. A top stack of N_t layers extending from the cap layer to the first half of the cavity, including the entire top DBR. This stack typically contains layers with transverse variations due to the presence of one or more oxidation layers, defined by a certain transverse shape $S(\boldsymbol{\rho})$. Transverse variations could also

arise from the patterning of the cap layer or from the top electrode, when placed transversely close to the oxide aperture.

3. An AR, responsible for providing gain through stimulated emission to support the optical modes. This region usually consists of QWs. However, for modeling purposes, we consider it as a single layer. In real devices, multiple QWs exist, but electromagnetically, one can assume that all the gain is concentrated in a single well and then redistributed among the various QWs according to the standing wave (SW) profile, *i.e.*, the normalized longitudinal profile of the squared modulus of the supported electric field. The dielectric constant of the AR can be expressed as:

$$\tilde{\varepsilon}_a(\boldsymbol{\rho}) = \varepsilon_a + \Delta\tilde{\varepsilon}_a S(\boldsymbol{\rho}), \tag{2.122}$$

where ε_a is the nominal dielectric constant of the AR material, while $\Delta\tilde{\varepsilon}_a S(\boldsymbol{\rho})$ represents the modification required to support the optical modes. This modification approximately follows the spatial profile of the oxide aperture, in the absence of strong carrier diffusion, which is a reasonable assumption when oxides are placed close to the AR. For standard VCSELs, the dielectric constant modification of the active layer is a small perturbation to the overall dielectric constant, so it holds that

$$|\Delta\tilde{\varepsilon}_a| << |\varepsilon_a|. \tag{2.123}$$

If diffusion is considered, the shape should have a larger support than the oxide aperture, as done in [45], which couples optical simulations with drift-diffusion simulations, with access to the transverse distribution of carriers. The parameter n_a is an input, whereas $\Delta\tilde{n}_a$ is an unknown that must be determined, as it directly influences both the emission frequency and the threshold gain of the optical mode.

4. A bottom stack of N_b layers extending from the second half of the cavity to the end of the bottom DBR, typically consisting of uniform layers.

5. A lower semi-infinite medium acting as a bottom boundary condition, typically a GaAs substrate for 850 nm VCSELs. Let us denote its refractive index as n_b.

At this point, we can calculate the transmission operator associated to the top stack ($\mathbf{T}_t$), the AR ($\mathbf{T}_a$) and the bottom stack ($\mathbf{T}_b$) of the VCSEL structure. Since $\mathbf{T}_t$ and

$\mathbf{T}_b$ comprise more than one layer, they can be evaluated relying the product of the transmission operators of the single layers as

$$\mathbf{T}_t = \mathbf{T}_t^{(N_t)} \cdot \mathbf{T}_t^{(N_t-1)} \cdot \ldots \cdot \mathbf{T}_t^{(2)} \cdot \mathbf{T}_t^{(1)} = \prod_{i=N_t}^{1} \mathbf{T}_t^{(i)}, \tag{2.124}$$

where $\mathbf{T}_t^{(i)}$ represents the transmission operator of the i-th layer of the top stack,

$$\mathbf{T}_b = \mathbf{T}_b^{(N_b)} \cdot \mathbf{T}_b^{(N_b-1)} \cdot \ldots \cdot \mathbf{T}_b^{(2)} \cdot \mathbf{T}_b^{(1)} = \prod_{i=N_b}^{1} \mathbf{T}_b^{(i)}, \tag{2.125}$$

where $\mathbf{T}_b^{(i)}$ represents the transmission operator of the i-th layer of the bottom stack. The transmission operator of the whole VCSEL is in turn calculated as

$$\mathbf{T} = \mathbf{T}_b \mathbf{T}_a \mathbf{T}_t. \tag{2.126}$$

If L represents the total longitudinal extension of the VCSEL and $\mathbf{a}(z)$ the field expansion coefficients within the VCSEL structure, from the outcoupling facet to the substrate, then it holds that

$$\mathbf{a}(L^-) = \mathbf{T}\mathbf{a}(0^+), \tag{2.127}$$

where $\mathbf{a}(0^+)$ represents the field at the beginning of the resonator, still embedded in the reference medium and before exiting into the upper semi-infinite medium (air), while $\mathbf{a}(L^-)$ represents the field at the end of the resonator, still embedded in the reference medium and before exiting into the lower semi-infinite medium (substrate). Splitting (2.127) into the forward and backward components, considering

$$\mathbf{a}(z) = \begin{bmatrix} \mathbf{a}_\mathrm{F}(z) \\ \mathbf{a}_\mathrm{B}(z) \end{bmatrix} \tag{2.128}$$

and

$$\mathbf{T} = \begin{bmatrix} \mathbf{T}_\mathrm{FF} & \mathbf{T}_\mathrm{FB} \\ \mathbf{T}_\mathrm{BF} & \mathbf{T}_\mathrm{BB} \end{bmatrix}, \tag{2.129}$$

one gets

$$\begin{cases} \mathbf{a}_\mathrm{F}(L^-) = \mathbf{T}_\mathrm{FF}\mathbf{a}_\mathrm{F}(0^+) + \mathbf{T}_\mathrm{FB}\mathbf{a}_\mathrm{B}(0^+) \\ \mathbf{a}_\mathrm{B}(L^-) = \mathbf{T}_\mathrm{BF}\mathbf{a}_\mathrm{F}(0^+) + \mathbf{T}_\mathrm{BB}\mathbf{a}_\mathrm{B}(0^+) \end{cases}. \tag{2.130}$$

At this point, one can consider that $\mathbf{a}_{\mathrm{F}}(0^+)$ is linked to $\mathbf{a}_{\mathrm{B}}(0^+)$ through the reflection operator $\mathbf{\Gamma}_t$ acting on the modes impinging from the reference medium to the semi-infinite upper medium. Specifically:

$$\mathbf{a}_{\mathrm{F}}(0^+) = \mathbf{\Gamma}_t \mathbf{a}_{\mathrm{B}}(0^+). \tag{2.131}$$

Similarly, $\mathbf{a}_{\mathrm{B}}(L^-)$ is linked to $\mathbf{a}_{\mathrm{F}}(L^-)$ through the bottom reflection operator $\mathbf{\Gamma}_b$ as

$$\mathbf{a}_{\mathrm{B}}(L^-) = \mathbf{\Gamma}_b \mathbf{a}_{\mathrm{F}}(L^-). \tag{2.132}$$

The reflection operators are diagonal multiplicative operators, which can be obtained as [65]

$$\left(\Gamma_{t,b}\right)_{\boldsymbol{\mu}\boldsymbol{\mu}} = \frac{Z_{\boldsymbol{\mu}}^{t,b} - Z_{\boldsymbol{\mu}}}{Z_{\boldsymbol{\mu}}^{t,b} + Z_{\boldsymbol{\mu}}}. \tag{2.133}$$

In (2.133) $Z_{\boldsymbol{\mu}}$ represents the modal impedance in the reference medium, as defined in (2.61), and $Z_{\boldsymbol{\mu}}^{t,b}$ is the modal impedance in the top/bottom semi-infinite medium, which can be evaluated as

$$Z_{\boldsymbol{\mu}}^{t,b} = \frac{Z_0}{n_{t,b}} \times \begin{cases} k^{(t,b)}/\beta_{\boldsymbol{\mu}}^{(t,b)}, & p = \mathrm{TE}, \\ \beta_{\boldsymbol{\mu}}^{(t,b)}/k^{(t,b)}, & p = \mathrm{TM}, \end{cases} \tag{2.134}$$

where

$$k^{(t,b)} = n_{t,b} k_0 \tag{2.135}$$

and

$$\beta_{\boldsymbol{\mu}}^{(t,b)} = \sqrt{\left[k^{(t,b)}\right]^2 - k_t^2}. \tag{2.136}$$

Using the same basis, reference index ($n_{\mathrm{ref}} = 1.6$) and wavelength ($\lambda = 850$ nm) defined in Subsection 2.5.4, considering $n_t = 1$ and $n_b = 3.5$, the resulting $\mathbf{\Gamma}_t$ and $\mathbf{\Gamma}_b$ are reported in Fig. 2.8.

Equations (2.132), (2.131) and (2.130) represent a system of four equations in four unknowns, namely $\mathbf{a}_{\mathrm{F}}(0^+)$, $\mathbf{a}_{\mathrm{F}}(L^-)$, $\mathbf{a}_{\mathrm{B}}(0^+)$ and $\mathbf{a}_{\mathrm{B}}(L^-)$. Substituting (2.130) into (2.132), thus remaining with $\mathbf{a}_{\mathrm{F}}(0^+)$ and $\mathbf{a}_{\mathrm{B}}(0^+)$ only, and using (2.131) to express $\mathbf{a}_{\mathrm{F}}(0^+)$ as a function of $\mathbf{a}_{\mathrm{B}}(0^+)$, one remains with an expression for $\mathbf{a}_{\mathrm{B}}(0^+)$ only, *i.e.*, the expansion of the transverse field exiting the outcoupling facet of the laser, or the so called near field (NF). This expression can be interpreted as a generalized Barkhausen criterion, relying on both propagation throughout the

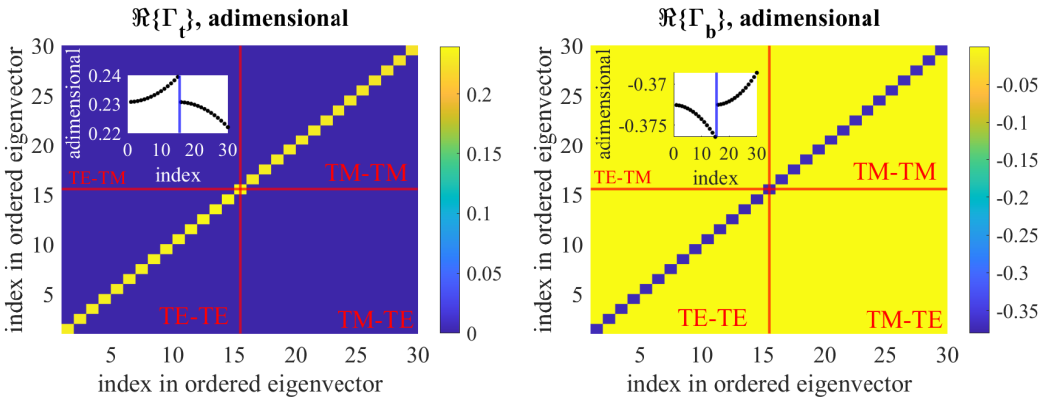

Fig. 2.8 Real part of the reflection matrices for both the top semi-infinite medium and the bottom semi-infinite medium. Insets represent the diagonal values of the matrices.

structure and reflections at the two boundaries. It reads:

$$(\mathbf{T}_{\mathrm{BF}}\boldsymbol{\Gamma}_t + \mathbf{T}_{\mathrm{BB}})\,\mathbf{a}_{\mathrm{B}}(0^+) = \boldsymbol{\Gamma}_b\,(\mathbf{T}_{\mathrm{FF}}\boldsymbol{\Gamma}_t + \mathbf{T}_{\mathrm{FB}})\,\mathbf{a}_{\mathrm{B}}(0^+). \tag{2.137}$$

2.6.2 Transmission operator of the active layer

To obtain the VCSEL modes, we must explicitly derive an equation that determines $\Delta\tilde{n}_a$. Notably, the operator $\mathbf{T}$ depends on $\Delta\tilde{n}_a$, as it appears in both the coupling and transmission operators of the active layer. Consequently, equation (2.137) inherently contains information about both $\Delta\tilde{n}_a$ and $\mathbf{a}_{\mathrm{B}}(0^+)$. However, the dependence on $\Delta\tilde{n}_a$ is nonlinear, making the equation impractical for direct use. To obtain a more convenient expression, we can write the coupling operator of the active $\mathbf{K}_a$ layer using (2.91) and (2.122) as[9]

$$\begin{aligned}(K_a)_{\boldsymbol{\mu}\boldsymbol{\nu}} = &-\frac{j\omega}{C_{\boldsymbol{\mu}}}\int_{\mathbb{R}^2}\left[(\varepsilon_a - \varepsilon_{\mathrm{ref}}) + \Delta\tilde{\varepsilon}_a S(\boldsymbol{\rho})\right]\mathbf{e}_{\boldsymbol{\mu}}\cdot\mathbf{e}_{\boldsymbol{\nu}}\,\mathrm{d}^2\rho + \\ &+\frac{j\omega\varepsilon_{\mathrm{ref}}}{C_{\boldsymbol{\mu}}}\int_{\mathbb{R}^2}\frac{(\varepsilon_a - \varepsilon_{\mathrm{ref}}) + \Delta\tilde{\varepsilon}_a S(\boldsymbol{\rho})}{\varepsilon_a + \Delta\tilde{\varepsilon}_a S(\boldsymbol{\rho})}e_{z,\boldsymbol{\mu}}e_{z,\boldsymbol{\nu}}\,\mathrm{d}^2\rho.\end{aligned} \tag{2.138}$$

[9]Notice that here we are considering an isotropic active layer and an isotropic gain, which is the case of AlGaAs VCSELs. As long as the gain is isotropic, described by $\Delta\tilde{\varepsilon}_a\mathbf{I}$, the following treatment can be done following the same procedure, even if the nominal active layer is anisotropic, thus using the equations defined in Appendix A.

Neglecting the red term with respect to the blue term in (2.138) thanks to (2.123), the previous equation can be rewritten as

$$(K_a)_{\boldsymbol{\mu\nu}} = \left(K_a^{(0)}\right)_{\boldsymbol{\mu\nu}} + \frac{\Delta\tilde{\varepsilon}_a}{\varepsilon_{\text{ref}}} (\Delta K_a)_{\boldsymbol{\mu\nu}}, \tag{2.139}$$

where the operator $\mathbf{K}_a^{(0)}$ is the coupling operator associated to the unmodified uniform active layer and

$$\begin{aligned}(\Delta K_a)_{\boldsymbol{\mu\nu}} = &-\frac{j\omega\varepsilon_{\text{ref}}}{C_{\boldsymbol{\mu}}} \int_{D_S} S(\boldsymbol{\rho}) \mathbf{e}_{\boldsymbol{\mu}} \cdot \mathbf{e}_{\boldsymbol{\nu}} \, \mathrm{d}^2\rho + \\ &+ \frac{j\omega\varepsilon_{\text{ref}}^2}{C_{\boldsymbol{\mu}}\varepsilon_a} \int_{D_S} S(\boldsymbol{\rho}) e_{z,\boldsymbol{\mu}} e_{z,\boldsymbol{\nu}} \, \mathrm{d}^2\rho.\end{aligned} \tag{2.140}$$

In this way, we have made the coupling operator of the active layer explicitly dependent in a linear manner on the modification of the dielectric constant. Please notice that when considering a discretized and truncated basis, the matrix $\Delta\boldsymbol{K}_a$ must include the multiplication by the selected spacing of continuous labels (Δk_t for the basis of cylindrical waves), as remarked in the finite integrals in Fig. 2.6.

Moving on to the corresponding transmission operator for an active layer of thickness L_a, we can write

$$\mathbf{T}_a = \exp\left[\left(\mathbf{B} + \mathbf{K}_a^{(0)} + \frac{\Delta\tilde{\varepsilon}_a}{\varepsilon_{\text{ref}}} \Delta\mathbf{K}_a\right) L_a\right], \tag{2.141}$$

where the nonlinear dependence on $\Delta\tilde{\varepsilon}_a$ is evident. Assuming that the last term, proportional to $\Delta\tilde{\varepsilon}_a$, represents a small perturbation, we can perform a Taylor expansion of (2.141) up to the first order to obtain a linear approximation in $\Delta\tilde{\varepsilon}_a$, yielding

$$\mathbf{T}_a \simeq \exp\left[\left(\mathbf{B} + \mathbf{K}_a^{(0)}\right) L_a\right] + \frac{\Delta\tilde{\varepsilon}_a}{\varepsilon_{\text{ref}}} \exp\left[\left(\mathbf{B} + \mathbf{K}_a^{(0)}\right) L_a\right] \Delta\mathbf{K}_a L_a. \tag{2.142}$$

The latter holds true for thin active layers, *i.e.* small L_a. Further details regarding the linearization procedure can be found in Appendix B. Noticing that

$$\mathbf{T}_a^{(0)} = \exp\left[\left(\mathbf{B} + \mathbf{K}_a^{(0)}\right) L_a\right] \tag{2.143}$$

represents the transmission operator of the unmodified active layer, then one can write $\mathbf{T}_a$ as

$$\mathbf{T}_a = \mathbf{T}_a^{(0)} + \frac{\Delta\tilde{\varepsilon}_a}{\varepsilon_{\text{ref}}}\mathbf{T}_a^{(0)}\Delta\mathbf{K}_a L_a. \tag{2.144}$$

2.6.3 VCSEL modes equation

Substituting the linearization of the transmission operator of the active layer (2.144) into the transmission operator of the whole structure (2.126) one gets

$$\begin{aligned}\mathbf{T} &= \mathbf{T}_b\left(\mathbf{T}_a^{(0)} + \frac{\Delta\tilde{\varepsilon}_a}{\varepsilon_{\text{ref}}}\mathbf{T}_a^{(0)}\Delta\mathbf{K}_a L_a\right)\mathbf{T}_t = \\ &= \mathbf{T}_b\mathbf{T}_a^{(0)}\mathbf{T}_t + \frac{\Delta\tilde{\varepsilon}_a}{\varepsilon_{\text{ref}}}\mathbf{T}_b\mathbf{T}_a^{(0)}\Delta\mathbf{K}_a\mathbf{T}_t L_a.\end{aligned} \tag{2.145}$$

Defining

$$\mathbf{T}^{(1)} = \mathbf{T}_b\mathbf{T}_a^{(0)}\mathbf{T}_t \tag{2.146}$$

as the transmission operator of the whole VCSEL with the unmodified active layer and

$$\mathbf{T}^{(2)} = \mathbf{T}_b\mathbf{T}_a^{(0)}\Delta\mathbf{K}_a\mathbf{T}_t L_a, \tag{2.147}$$

the total transmission operator eventually reads

$$\mathbf{T} = \mathbf{T}^{(1)} + \frac{\Delta\tilde{\varepsilon}_a}{\varepsilon_{\text{ref}}}\mathbf{T}^{(2)}. \tag{2.148}$$

The generalized Barkhausen condition in (2.137) can be rewritten using this new expression for $\mathbf{T}$ as

$$\begin{aligned}&\left[\left(\mathbf{T}_{\text{BF}}^{(1)} + \frac{\Delta\tilde{\varepsilon}_a}{\varepsilon_{\text{ref}}}\mathbf{T}_{\text{BF}}^{(2)}\right)\boldsymbol{\Gamma}_t + \mathbf{T}_{\text{BB}}^{(1)} + \frac{\Delta\tilde{\varepsilon}_a}{\varepsilon_{\text{ref}}}\mathbf{T}_{\text{BB}}^{(2)}\right]\mathbf{a}_{\text{B}}(0^+) = \\ &= \boldsymbol{\Gamma}_b\left[\left(\mathbf{T}_{\text{FF}}^{(1)} + \frac{\Delta\tilde{\varepsilon}_a}{\varepsilon_{\text{ref}}}\mathbf{T}_{\text{FF}}^{(2)}\right)\boldsymbol{\Gamma}_t + \mathbf{T}_{\text{FB}}^{(1)} + \frac{\Delta\tilde{\varepsilon}_a}{\varepsilon_{\text{ref}}}\mathbf{T}_{\text{FB}}^{(2)}\right]\mathbf{a}_{\text{B}}(0^+).\end{aligned} \tag{2.149}$$

Bringing all operators with index (1) to the left-hand side and all operators with index (2) to the right-hand side we obtain:

$$\begin{aligned}&\left(\mathbf{T}_{\mathrm{BF}}^{(1)}\boldsymbol{\Gamma}_t+\mathbf{T}_{\mathrm{BB}}^{(1)}-\boldsymbol{\Gamma}_b\mathbf{T}_{\mathrm{FF}}^{(1)}\boldsymbol{\Gamma}_t-\boldsymbol{\Gamma}_b\mathbf{T}_{\mathrm{FB}}^{(1)}\right)\mathbf{a}_B(0^+)=\\&=-\frac{\Delta\tilde{\varepsilon}_a}{\varepsilon_{\mathrm{ref}}}\left(\mathbf{T}_{\mathrm{BF}}^{(2)}\boldsymbol{\Gamma}_t+\mathbf{T}_{\mathrm{BB}}^{(2)}-\boldsymbol{\Gamma}_b\mathbf{T}_{\mathrm{FF}}^{(2)}\boldsymbol{\Gamma}_t-\boldsymbol{\Gamma}_b\mathbf{T}_{\mathrm{FB}}^{(2)}\right)\mathbf{a}_{\mathrm{B}}(0^+).\end{aligned}\tag{2.150}$$

Finally, defining the operators

$$\mathbf{N}^{(1,2)}=\mathbf{T}_{\mathrm{BF}}^{(1,2)}\boldsymbol{\Gamma}_t+\mathbf{T}_{\mathrm{BB}}^{(1,2)}-\boldsymbol{\Gamma}_b\mathbf{T}_{\mathrm{FF}}^{(1,2)}\boldsymbol{\Gamma}_t-\boldsymbol{\Gamma}_b\mathbf{T}_{\mathrm{FB}}^{(1,2)}\tag{2.151}$$

and the scalar quantity

$$\gamma=-\frac{\varepsilon_{\mathrm{ref}}}{\Delta\tilde{\varepsilon}_a},\tag{2.152}$$

equation (2.150) can be cast into a generalized eigenvalue problem, also known as VCSEL modes equation, reading

$$\gamma\mathbf{N}^{(1)}\mathbf{a}_{\mathrm{B}}(0+)=\mathbf{N}^{(2)}\mathbf{a}_{\mathrm{B}}(0^+).\tag{2.153}$$

The latter allows for the evaluation of the supported $\Delta\tilde{\varepsilon}_a$ (from the eigenvalues γ) and the supported NF profiles $\mathbf{a}_{\mathrm{B}}(0^+)$ (from the eigenstates) at different wavelengths. Specifically, $\gamma=\gamma(\lambda)$ and $\Delta\tilde{\varepsilon}_a=\Delta\tilde{\varepsilon}_a(\lambda)=-\varepsilon_{\mathrm{ref}}/\gamma(\lambda)$ for all possible supported eigenstates. The real and imaginary parts of these as a function of the wavelength, for all supported modes, are usually referred to as dispersion curves of the VCSEL. We want to obtain the cold-cavity modes, *i.e.*, the modes that are supported by the resonator by only introducing a certain gain in the QWs, affecting the imaginary part of the active refractive index, without considering any modification of the corresponding real part. For this reason, the emission frequency of the various modes, λ_{e}, is the frequency for which:

$$\Re\left\{\Delta\tilde{\varepsilon}_a(\lambda_{\mathrm{e}})\right\}=0,\tag{2.154}$$

[10]Once the emission wavelength for a specific mode is evaluated, typically numerically, according to (2.154), the corresponding modal threshold gain can be obtained considering the maximum modification of the refractive index of the active layer. Defining $\tilde{n}_a$ the maximally modified refractive index of the active layer and $n_a = \sqrt{\varepsilon_a/\varepsilon_0}$ the corresponding unmodified refractive index, the index modification $\Delta\tilde{n}_a$ can be obtain exploiting (2.123):

$$\tilde{n}_a = \sqrt{\frac{\varepsilon_a + \Delta\tilde{\varepsilon}_a}{\varepsilon_0}} = \sqrt{\frac{\varepsilon_a}{\varepsilon_0}}\sqrt{1 + \frac{\Delta\tilde{\varepsilon}_a}{\varepsilon_a}} \simeq n_a\left(1 + \frac{1}{2}\frac{\Delta\tilde{\varepsilon}_a}{\varepsilon_a}\right) = n_a + \frac{\Delta\tilde{\varepsilon}_a}{2n_a\varepsilon_0}, \quad (2.155)$$

so that

$$\Delta\tilde{n}_a = \frac{\Delta\tilde{\varepsilon}_a}{2n_a\varepsilon_0}. \quad (2.156)$$

The field threshold gain, g_{field}, can be defined through the imaginary part of the refractive index of the active layer as

$$\tilde{n}_a = n_a + j\frac{g_{\text{field}}}{k_0}, \quad (2.157)$$

while the power threshold gain, or simply modal threshold gain g, is

$$g = 2g_{\text{field}}. \quad (2.158)$$

Comparing (2.158)–(2.157) with (2.156) evaluated at $\lambda = \lambda_e$, one gets

$$g = \frac{k_0\Im\left\{\Delta\tilde{\varepsilon}_a(\lambda_e)\right\}}{n_a\varepsilon_0}. \quad (2.159)$$

Once λ_e and g are known for each mode, the eigenstates at λ_e can be taken into account. The field that is obtained by reconstructing the state

$$\mathbf{a}_{\text{NF}} = \begin{bmatrix} \mathbf{0} \\ \mathbf{a}_{\text{B}}(0^+) \end{bmatrix} \quad (2.160)$$

[10]One could also account for a modification of the real part of the dielectric constant of the active layers. This is known as anti-guiding effect. To properly account for that, usually, the considered figure of merit is the ratio between the real and imaginary parts of the modification of the refractive index of the active layer, which can be interpreted as a non-differential version of the Henry alpha factor, α_{ND}. In this way, the condition for the emission wavelength becomes $\Re\left\{\Delta\tilde{n}_a(\lambda_e)\right\}/\Im\left\{\Delta\tilde{n}_a(\lambda_e)\right\} = \alpha_{\text{ND}}$, which yields the previous condition if $\alpha_{\text{ND}} = 0$.

using (2.74). This can be interpreted as the spatial NF profile right before exiting the resonator. Using transmission operators evaluated at λ_c, including the one of the active layer, whose refractive index is now completely characterized, one can propagate the field from the outcoupling facet anywhere both inside and outside of the resonator[11] (relying for instance on the transmission operator of free space). In this way, for each mode, one can get the far field (FF) profile by propagating the field in air or the field profile at the active layer simply exploiting $\mathbf{T}_t$. In general, this procedure allows for a fully vectorial and three-dimensional reconstruction of the modal fields supported by the VCSEL.

Aiming at implementing these equations, one must follow the following steps:

1. Select a set of wavelengths around the design target wavelength of the VCSEL[12]. Notice that each of the selected wavelengths can be solved in parallel.

2. Select a certain basis with an appropriate truncation and discretization, tailored according to the investigated geometry.

3. For each wavelength, calculate the operators $\mathbf{N}^{(1)}$ and $\mathbf{N}^{(2)}$ and solve the generalized eigenvalue problem.

4. For each wavelength, a subset of modes, typically those with the lowest threshold gain, is selected. It is essential to ensure that the same physical modes are consistently tracked across different wavelengths. For instance, if modes 1, 2, and 3 are selected at the first wavelength, the corresponding modes at the next wavelength should represent the same spatial field distributions. However, since eigenvalue problems do not guarantee a consistent ordering of eigenvectors, a mismatch may occur. To correctly associate corresponding modes across wavelengths, a correlation analysis is required: the spatial overlap between the field distributions of two modes at adjacent wavelengths must exceed a given threshold. A low overlap would indicate that the modes do not correspond. Within our problem, the spatial overlap can be easily estimated by the scalar product between the eigenvectors associated to the

[11] To do so, one must account for the fact that all the layers of the resonators are embedded in the reference medium. To pass from the reference medium to one of the two semi-infinite media embedding the VCSEL one must consider the transmission across an interface.

[12] A more precise starting point would be a wavelength interval around the emission wavelength obtained through a 1D simulation, further discussed in Section 3.1.

various modes. Once the modes are selected and tracked across all considered wavelengths, compute the corresponding dispersion curves.

5. From the dispersion curves, determine the emission wavelength of each mode and the corresponding threshold gain. The mode with the lowest threshold corresponds to the lasing mode of the VCSEL.

6. Evaluate the eigenvectors at the emission wavelengths of the selected modes, either by interpolation of the closest available eigenvectors or by solving the eigenvalue problem again. Reconstruct the NF profile over the desired spatial domain and/or propagate the field to the desired longitudinal section of the structure.

Please note that the only theoretical approximation in this treatment stems from the linearization of the transmission operator of the active layer[13]. As a result, the estimated values of λ_e and g for the desired modes are approximate. For instance, if one directly substitutes the imaginary modification of the dielectric constant of the active layer at λ_e (obtained as an output) back into the nominal dielectric constant ε_a, the expectation is that no further modifications should be necessary to support that specific mode. However, this is usually not the case, as a slight adjustment may still be required. To address this issue, one can iterate this procedure while gradually restricting the investigated range of wavelengths until the required modification falls below a certain threshold.

Using as an example the modal basis defined in Subsection 2.5.4 (R representing the radius of the oxide aperture in this case) and the VCSEL stack defined in Fig. 2.7, the dispersion curves with the lowest threshold are reported in Fig. 2.9. The latter reports both $\Re\{\Delta\tilde{\varepsilon}_a\}$ and $\Im\{\Delta\tilde{\varepsilon}_a\}$ (and thus the threshold gain) as a function of the wavelength, demonstrating how to apply (2.154) and (2.159). Furthermore, the fundamental mode of the structure that is linearly polarized along x is reported in Fig. 2.10 in terms of eigenvector, near field (NF, all three vectorial components), far field (FF, squared norm), field at the active layer (x component), threshold gain, and emission wavelength. Notice that the z-component of the NF was obtained from the transverse component according to (2.15). All NF profiles are normalized with respect to the maximum value of the x component. Had one chosen $l =$ odd instead

[13] From the point of view of the practical implementation, an addition approximation is represented by the basis truncation and discretization in k_t.

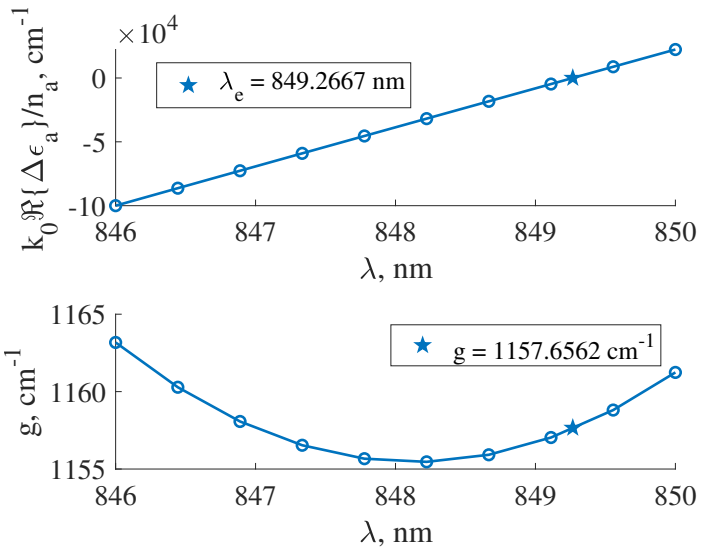

Fig. 2.9 Dispersion curves obtained using the modal basis defined in Subsection 2.5.4.

of $l =$ even, a degenerate mode with a dominant y component instead of x would have been obtained. This demonstrates how the modal label l in cylindrical waves determines the investigated linear polarization of the VCSEL modes. The degeneracy is lifted when anisotropies are introduced. The difference in emission wavelength between modes with the same spatial profile but different polarization is referred to as birefringence, while the difference in threshold gain is known as dichroism, both of which are related to the optical anisotropy sources in the structure.

The modal basis must include both $l =$ even and $l =$ odd when chiral structures are analyzed so that elliptically polarized states can emerge. Further details on this will be explored in Chapter 5.

2.6.4 Impact of the truncation and discretization of the transverse wavevector on convergence

In order to properly implement the algorithm described in the previous subsection, a key aspect lies in the choice of a suitable set of basis functions capable of accurately representing the electric field phasor. Focusing on the x-polarized fundamental mode of a circular VCSEL, as selected in Sec. 2.5.4, we restrict ourselves to $m = 1$ and $l =$ even, with $p \in \{\text{TE}, \text{TM}\}$. However, special care must be taken in the truncation and subsequent discretization of the transverse wavevector k_t. In this subsection, we

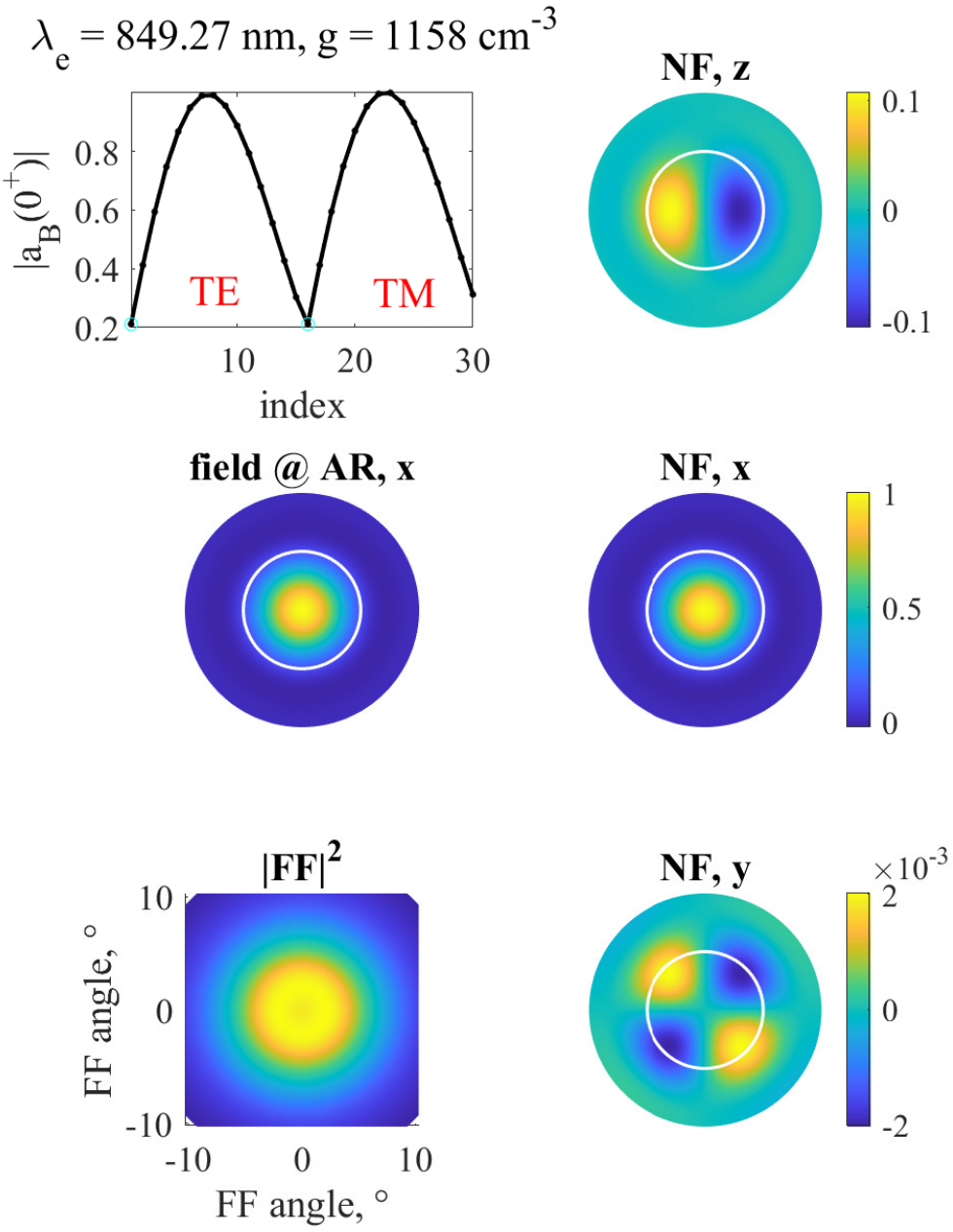

Fig. 2.10 Example of the fundamental mode of a circular VCSEL linearly polarized along the *x* direction, showcasing all the information which can be extracted with our methodology. White circles represent the oxide aperture.

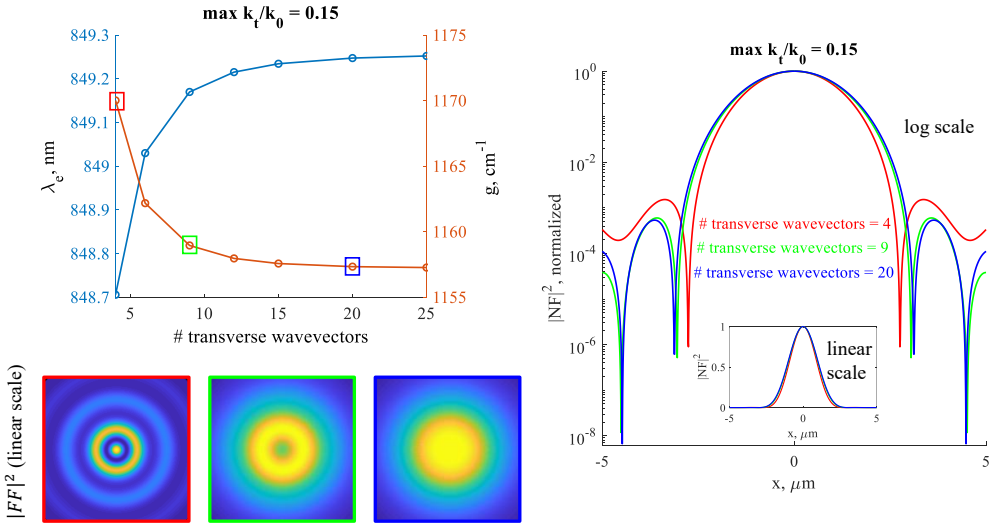

Fig. 2.11 Emission wavelength, threshold gain, NF (both in linear and log scales, to highlight the differences) and FF (only in linear scale, since differences are already evident) profiles of the fundamental mode of a circular VCSEL for $k_t^{\max} = 0.15k_0$ as a function of the number of transverse wavevectors. The x and y axes of the FF maps range from $-10°$ to $10°$.

analyze how these choices affect the threshold gain and the emission wavelength of the VCSEL fundamental mode, as well as the NF and FF profiles.

Specifically, we consider two different values for the maximum transverse wavevector: $k_t^{\max} = 0.15k_0$ and $k_t^{\max} = 0.25k_0$. For each case, a different number of discretization points N_k is employed. The results for $k_t^{\max} = 0.15, k_0$ are shown in Fig.2.11, while those for $k_t^{\max} = 0.25, k_0$ are reported in Fig. 2.12.

One can observe that λ_e and g, associated with the eigenvalues of (2.153), converge significantly faster than the NF profile, which depends on the corresponding eigenvector. Moreover, the propagation of the NF in air to compute the FF requires an even larger number of modes to achieve convergence and represents the most sensitive quantity overall. A typical indicator of insufficient discretization of the transverse wavevector is the absence of a central peak in the FF profile, at least for the fundamental mode.

By comparing Fig. 2.11 and Fig. 2.12, it becomes evident that convergence is achieved more rapidly for the lower value of $k_t^{\max}$. However, the quality of the NF profile ultimately improves with the higher $k_t^{\max}$, showing reduced side lobes. These lobes are residual artifacts due to the oscillations of the Bessel functions and are better compensated as the basis becomes more complete.

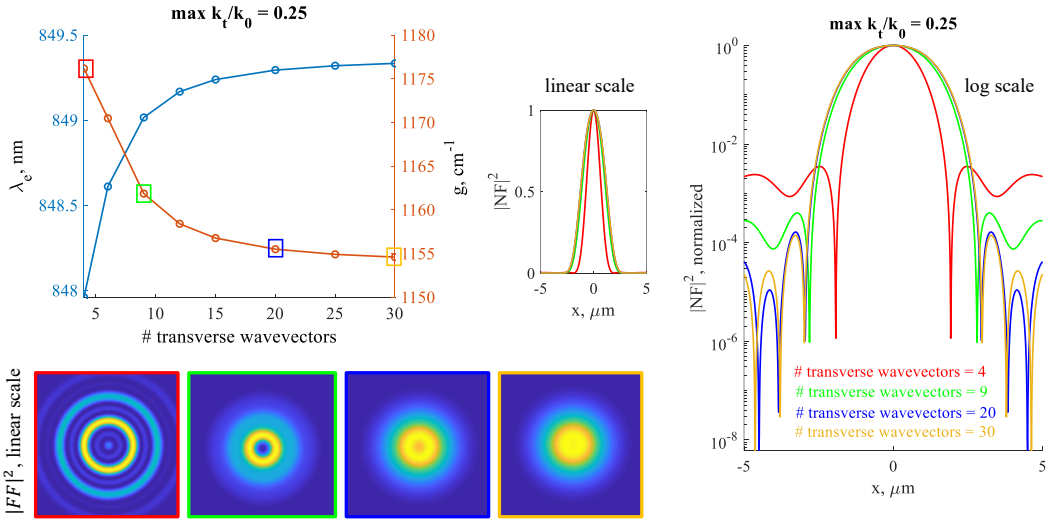

Fig. 2.12 Same as Fig. 2.11, but for $k_t^{\max} = 0.25k_0$.

For particularly complex structures, featuring for instance strong scattering losses [66], a non-uniform discretization of the transverse wavevector [67] can be employed, properly modifying (2.115).

Chapter 3

1D modeling of VCSELs

3.1 Scalar 1D simulations of VCSELs

If for some reason we already know that the VCSEL that we want to investigate is SM with a specific polarization, *e.g.*, due to a small oxide aperture or to the presence of a surface grating relief, we can significantly simplify the problem discussed in the previous chapter. This simplification is achieved by reducing the subset of chosen basis functions and considering only normal incidence.

Let us specifically investigate a SM-VCSEL which is linearly polarized and let us denote with x the polarization direction. We focus solely on the longitudinal stack of the VCSEL, ignoring any transverse variation. This is referred to as 1D scalar approximation. The simplest basis that we can use features a scalar label μ, only containing the forward/backward nature of the mode, *i.e.*, $\mu = \alpha$. Since we are considering normal incidence ($k_t = 0$), there is not difference between TE and TM modes, and the modes never feature a z-component. Furthermore, the modal impedance defined in (2.61) no longer depends on the modal label, simply becoming:

$$Z_\perp = \frac{Z_0}{r}, \tag{3.1}$$

since the normal propagation constant is:

$$\beta_\perp = \sqrt{k_r^2 - k_t^2} = k_r. \tag{3.2}$$

The modal electric field simply reads

$$e_{x,\mu} = e_0, \quad e_{y,\mu} = 0, \quad e_{z,\mu} = 0, \tag{3.3}$$

where e_0 is an arbitrary function used in the definition of the power normalization constant. The 2×2 coupling matrix, full in the 1D scalar case, is obtained entirely from from (2.97), since $K^z_{\mu\nu} = 0$, as:

$$K_{\mu\nu} = -s_\mu \frac{j\omega\Delta\varepsilon Z_\perp}{2}. \tag{3.4}$$

On the other hand, the propagation matrix reads

$$\mathbf{B} = \begin{bmatrix} -j\beta_\perp & 0 \\ 0 & j\beta_\perp \end{bmatrix}. \tag{3.5}$$

We have now everything we need to evaluate the 2×2 transmission matrix of any layer characterized by a certain $\Delta\varepsilon$. To treat the whole VCSEL stack as done in Section 2.6, we need to linearize the transmission matrix of the active layer. To do so, similarly to (2.138), one can write:

$$(K_a)_{\mu\nu} = -s_\mu \frac{j\omega\left[(\varepsilon_a - \varepsilon_{\text{ref}}) + \Delta\tilde{\varepsilon}_a\right] Z_\perp}{2} = \left(K_a^{(0)}\right)_{\mu\nu} + \frac{\Delta\tilde{\varepsilon}_a}{\varepsilon_{\text{ref}}} (\Delta K_a)_{\mu\nu}, \tag{3.6}$$

where $\left(K_a^{(0)}\right)_{\mu\nu}$ is the coupling matrix of the unmodified active layer, while

$$(\Delta K_a)_{\mu\nu} = -s_\mu \frac{j\omega\varepsilon_{\text{ref}} Z_\perp}{2}. \tag{3.7}$$

Finally, the scalar reflection coefficients at the top and bottom interfaces between the reference medium and the two boundary semi-infinite media for normal incidence read:

$$\Gamma_{t,b} = \frac{r - n_{t,b}}{r + n_{t,b}}. \tag{3.8}$$

At this point, the VCSEL mode equation (2.153) becomes much simpler. Indeed being the operators that feature in (2.153) are obtained from the forward-forward, forward-backward, backward-forward and backward-backward components of the

transmission matrices, thus they become scalar quantities, yielding the solution:

$$a_{\mathrm{B}}(0+) = 1, \tag{3.9}$$

defined up to a multiplicative constant, and

$$\gamma(\lambda) = -\frac{\varepsilon_{\mathrm{ref}}}{\Delta\tilde{\varepsilon}_a(\lambda)} = \frac{N^{(2)}(\lambda)}{N^{(1)}(\lambda)}. \tag{3.10}$$

Once the emission wavelength and threshold gain are found, the refractive index profile is completely characterized, thus one can propagate the field at the outcoupling facet up to any longitudinal section of the VCSEL, using the fully determined transmission matrices and obtaining the SW profile as:

$$\mathrm{SW}(z) = \left|a_{\mathrm{F}}(z) + a_{\mathrm{B}}(z)\right|^2, \tag{3.11}$$

also defined up to a multiplicative constant.

To evaluate the SW properly, one must account for the the transition between the top semi-infinite medium to the reference medium, in which all VCSEL layers are embedded. This can be done by considering the transmission matrix across the interface between such media. Specifically, the field right outside of the VCSEL outcoupling facet is:

$$\mathbf{a}_{\mathrm{NF}} = \mathbf{a}(0^-) = \begin{bmatrix} 0 \\ 1 \end{bmatrix}, \tag{3.12}$$

which is made entirely of a backward component, since, at $z = 0^-$, the field is exiting the device from the top without facing any more reflections. To propagate such a field inside, we must consider that

$$\mathbf{a}(0^+) = \mathbf{T}_{\mathrm{enter}}\mathbf{a}_{\mathrm{NF}}, \tag{3.13}$$

where [68]

$$\mathbf{T}_{\mathrm{enter}} = \frac{1}{\sqrt{1-\Gamma_t^2}} \begin{bmatrix} 1 & \Gamma_t \\ \Gamma_t & 0 \end{bmatrix}. \tag{3.14}$$

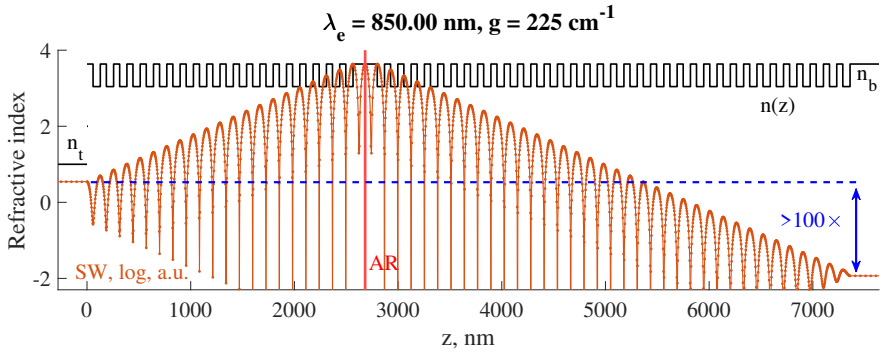

Fig. 3.1 Example of a scalar 1D simulation. The refractive index profile is reported, alongside the standing wave in logarithmic scale, normalized so that its maximum matches the refractive index profile. At the top, the emission wavelength and the threshold gain are reported.

Once $\mathbf{a}(0^+)$ is known, it can be propagated throughout the device. Similarly, at the bottom medium ($z = L$), it holds that

$$\mathbf{a}(L^+) = \mathbf{T}_{\text{exit}}\mathbf{a}(L^-), \tag{3.15}$$

where [68]

$$\mathbf{T}_{\text{enter}} = \frac{1}{\sqrt{1-\Gamma_b^2}}\begin{bmatrix} 1 & -\Gamma_b \\ -\Gamma_b & 0 \end{bmatrix}. \tag{3.16}$$

An example of a 1D scalar simulation for a VCSEL designed to emit at a target wavelength of $\lambda_t = 850$ nm is presented in Fig. 3.1. The simulation highlights the emission wavelength, the threshold gain, and the SW profile in logarithmic scale. The results show that, at the outcoupling facet, the SW intensity is more than 100 times higher than its corresponding value at the substrate. This confirms the appropriate choice of the number of pairs in both the top and bottom DBRs, as an intensity contrast of at least two orders of magnitude between the outcoupling facet and the non-emitting facet is typically required.

It is now possible to investigate how the optical properties of the VCSEL such as threshold gain and emission wavelength vary with respect to the thickness of the cap layer, *i.e.*, the topmost layer of the top DBR, previously discussed in discussed in Section 1.2. Let us define L_{cap} as its thickness and n_{cap} as its refractive index. In the results of Fig. 3.1, L_{cap} was set at $\lambda_t/(4n_{\text{cap}})$, and we aim to demonstrate that this is the best possible choice in terms of minimum threshold gain.

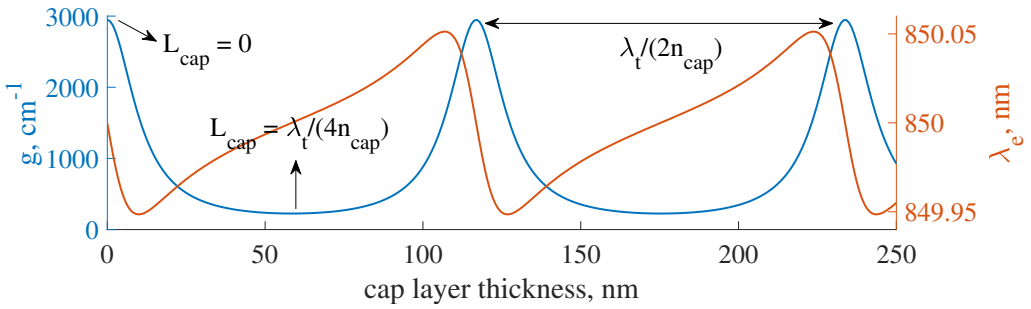

Fig. 3.2 Threshold gain and emission wavelength of the VCSEL structure defined in Fig. 3.1 as a function of the cap layer thickness, showing a periodic behavior.

The threshold gain and the emission wavelength as functions of L_{cap} are reported in Fig. 3.2, displaying a periodicity with a period of $\lambda_t/(2n_{\text{cap}})$. The first minimum threshold gain, due to the highest reflectivity of the top DBR, is obtained for $L_{\text{cap}} = \lambda_t/(4n_{\text{cap}})$, confirming the optimal design of Fig. 3.1.

A notable feature is that the valleys corresponding to the minima of the threshold gain are broad, providing room for technological tolerances. In contrast, at points where the threshold gain is maximum, due to the poorer reflectivity of the top DBR, the variation is sharper. This periodic behavior of the cap layer is crucial for designing a surface relief, as will be discussed in Chapter 4.

If optical losses in the cap layer are taken into account, the behavior is no longer perfectly periodic, and the minimum values of the threshold gain slightly increase with increasing cap layer thicknesses.

3.1.1 Reflectivity spectrum of a distributed Bragg reflector

A useful application of the scalar 1D formalism is the calculation of the reflectivity spectrum of a DBR for normal incidence. In general, given a stack of N layers with refractive indices n_i and thicknesses L_i, embedded between two semi-infinite media with indices n_{in} and n_{out}, it is possible to calculate the overall transmission matrix of a field impinging from the input medium n_{in}. From this it is possible to evaluate the scattering matrix and thus the reflection coefficient. To do so, one must first calculate the transmission matrix from the input medium to the reference medium $\mathbf{T}_{n_{\text{in}}\to r}$, then the transmission matrices of all layers $\mathbf{T}_i$ (using the CMT formalism), and finally the transmission matrix between the reference medium and the output medium $\mathbf{T}_{r\to n_{\text{out}}}$.

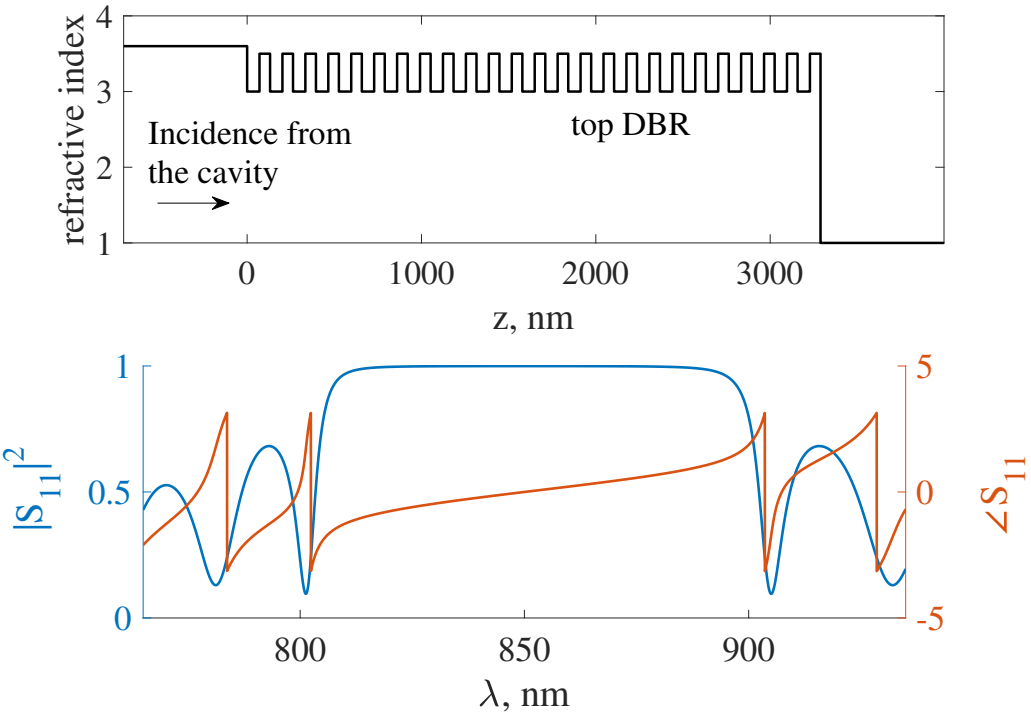

Fig. 3.3 Top: considered DBR structure. Light is impinging from the input medium on the left, representing the cavity, while air represents the output medium on the right. This is the case of a top DBR. The thickness of a layer with index n is set at $\lambda_t/(4n)$, with $\lambda_t = 850$ nm, aiming at achieving maximum reflectivity at λ_t. Bottom: power reflectivity and phase of the reflectivity as a function of the wavelength.

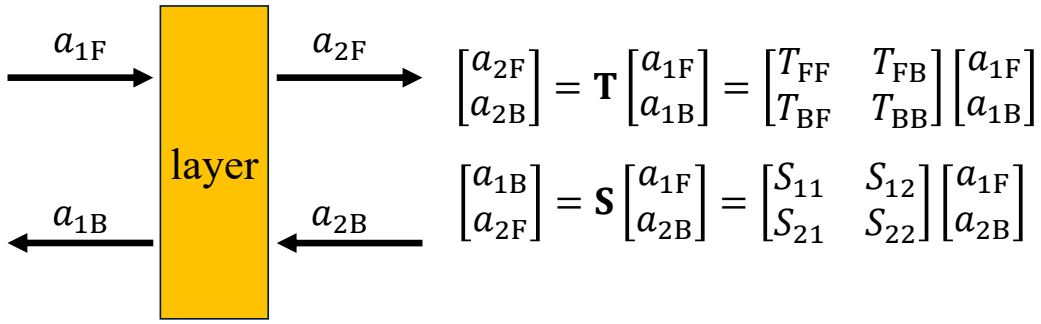

Fig. 3.4 Chosen convention for the definition of the scattering matrix **S**.

The needed matrices read:

$$\mathbf{T}_{n_{\text{in}} \to r} = \begin{bmatrix} 1 & \Gamma_{\text{in}} \\ \Gamma_{\text{in}} & 1 \end{bmatrix}, \tag{3.17}$$

$$\mathbf{T}_{r \to n_{\text{out}}} = \begin{bmatrix} 1 & -\Gamma_{\text{out}} \\ -\Gamma_{\text{out}} & 1 \end{bmatrix}, \tag{3.18}$$

where

$$\Gamma_{\text{in,out}} = \frac{r - n_{\text{in,out}}}{r + n_{\text{in,out}}}, \tag{3.19}$$

$$\mathbf{T}_i = \exp\left[(\mathbf{B} + \mathbf{K}_i) L_i\right], \tag{3.20}$$

with $\mathbf{K}_i$ obtained for each layer according to (3.4), exploiting n_i when calculating $\Delta\varepsilon$ for the different layers. Similarly, **B** can be calculated using (3.5). The overall transmission matrix for the stack reads:

$$\mathbf{T} = \mathbf{T}_{r \to n_{\text{out}}} \left(\prod_{i=N}^{1} \mathbf{T}_i \right) \mathbf{T}_{n_{\text{in}} \to r}. \tag{3.21}$$

Finally, according to the convention chosen in Fig. 3.4, the scattering matrix can be calculated as a function of the transmission matrix as [68]:

$$\mathbf{S} = \begin{bmatrix} -T_{\text{BF}}/T_{\text{BB}} & 1/T_{\text{BB}} \\ T_{\text{FF}} - \dfrac{T_{\text{FB}} T_{\text{BF}}}{T_{\text{BB}}} & T_{\text{FB}}/T_{\text{BB}} \end{bmatrix}, \tag{3.22}$$

from which one can extract the reflection coefficient S_{11}[1]. Doing this as a function of the wavelength can provide the reflection spectrum of a DBR, as reported in Fig. 3.3 optimized for maximum reflectivity at $\lambda_t = 850$ nm. One can notice that the broadness of the the reflectivity spectrum is of the order of 100 nm, much larger than the typical variations of emission wavelengths in VCSELs, in the order of ~ 0.5 nm as shown in Fig. 3.2. For this reason, mirror dispersion can be neglected in VCSELs.

The definition of the scattering matrix in (3.22) is useful for highlighting a possible criticality of our methodology. Indeed, the inverse relation of (3.22), *i.e.*, expressing a generic transmission matrix **T** as a function of **S**, using the convention in Fig. 3.4, is given by:

$$\mathbf{T} = \begin{bmatrix} S_{21} - \dfrac{S_{11}S_{22}}{S_{12}} & S_{22}/S_{12} \\ -S_{11}/S_{12} & 1/S_{12} \end{bmatrix}. \tag{3.23}$$

Our algorithm is based on transmission matrices, however, when a layer exhibits very strong reflectivity or high absorption, *e.g.*, metallic layers that may support evanescent fields, the element S_{12} can approach zero. As a result, **T** may become nearly singular, leading to numerical instabilities and errors. To address this issue, metallic layers in our implementation are treated directly via their scattering matrix, even in 3D.

3.2 Vectorial 1D simulations of VCSELs

To account for optical anisotropies while remaining within the normal incidence case and neglecting all transverse variations, we must slightly modify the procedure presented in Section 3.1. This vectorial 1D analysis remains significantly simpler than the full 3D problem discussed in Chapter 2 and proves useful for studying VCSELs that support two different modes sharing the same transverse spatial profile but exhibiting distinct polarization characteristics. This approach is particularly valuable for assessing the impact of gratings and intrinsic semiconductor anisotropies on the laser's dichroism and birefringence.

Practically, also in this case the basis must be simplified. The modal basis must consider fields that are linearly polarized either along x or y, which serve as a basis

[1] Similarly, one can also extract the transmission coefficient from S_{21}.

for all kinds of different polarizations, including elliptical and circular, given the possibility of having complex expansion coefficients. In this way, the bi-dimensional modal label reads:

$$\boldsymbol{\mu} = \begin{bmatrix} i \\ \alpha \end{bmatrix}, \tag{3.24}$$

where $i \in \{x, y\}$ represents the polarization and $\alpha \in \{\text{forward, backward}\}$ represents the type of propagation. In this case, all matrices are 4×4 complex matrices.While the modal impedance $Z_\perp$ and the normal propagation constant $\beta_\perp$ remain the same as (3.1)–(3.2), the modal fields read:

$$e_{x,\boldsymbol{\mu}} = \begin{cases} e_0, & i = x, \\ 0, & i = y, \end{cases} \tag{3.25}$$

$$e_{y,\boldsymbol{\mu}} = \begin{cases} 0, & i = x, \\ e_0, & i = y, \end{cases} \tag{3.26}$$

$$e_{z,\boldsymbol{\mu}} = 0, \tag{3.27}$$

e_0 being arbitrary and linked to the power normalization constant. Starting from the general result expressed in (2.96), given two modes labeled by $\boldsymbol{\mu} = [i, \alpha]^T$ and $\boldsymbol{\nu} = [i', \alpha']^T$, we can calculate:

$$\int_{\mathbb{R}^2} \mathbf{e}_{\boldsymbol{\mu}} \cdot \mathbf{e}_{\boldsymbol{\nu}} \, \mathrm{d}^2\rho = \frac{Z_\perp C_{\boldsymbol{\mu}}}{2 s_{\boldsymbol{\mu}}} \delta_{ii'}. \tag{3.28}$$

From the latter, one can obtain the link between e_0 and $C_{\boldsymbol{\mu}}$. For instance, choosing $i = i' = x$, one obtains that

$$\int_{\mathbb{R}^2} e_0^2 \, \mathrm{d}^2\rho = \frac{Z_\perp C_{\boldsymbol{\mu}}}{2 s_{\boldsymbol{\mu}}}, \tag{3.29}$$

from which it is evident that $C_{\boldsymbol{\mu}}$ only depends on the propagation type and not on the polarization label.

At this point, consider an anisotropic layer described by the parameters defined in Appendix A, namely the dielectric constants along the principal axes ε_{XX} and ε_{YY}, together with the tilting angle θ. Having defined ε_{iso} and ε_{ani} as:

$$\varepsilon_{\text{iso}} = \frac{\varepsilon_{XX} + \varepsilon_{YY}}{2}, \tag{3.30}$$

$$\varepsilon_{\text{ani}} = \frac{\varepsilon_{XX} - \varepsilon_{YY}}{2}, \tag{3.31}$$

the whole coupling matrix can be calculated as (see Appendix A, equation (A.26) for further details):

$$\begin{aligned} K_{\boldsymbol{\mu\nu}} = &-\frac{j\omega}{C_{\boldsymbol{\mu}}} (\varepsilon_{\text{iso}} - \varepsilon_{\text{ref}}) \int_{\mathbb{R}^2} \left(e_{x,\boldsymbol{\mu}} e_{x,\boldsymbol{\nu}} + e_{y,\boldsymbol{\mu}} e_{y,\boldsymbol{\nu}} \right) \mathrm{d}^2\boldsymbol{\rho} + \\ &-\frac{j\omega}{C_{\boldsymbol{\mu}}} \varepsilon_{\text{ani}} \cos(2\theta) \int_{\mathbb{R}^2} \left(e_{x,\boldsymbol{\mu}} e_{x,\boldsymbol{\nu}} - e_{y,\boldsymbol{\mu}} e_{y,\boldsymbol{\nu}} \right) \mathrm{d}^2\boldsymbol{\rho} + \\ &-\frac{j\omega}{C_{\boldsymbol{\mu}}} \varepsilon_{\text{ani}} \sin(2\theta) \int_{\mathbb{R}^2} \left(e_{x,\boldsymbol{\mu}} e_{y,\boldsymbol{\nu}} + e_{y,\boldsymbol{\mu}} e_{x,\boldsymbol{\nu}} \right) \mathrm{d}^2\boldsymbol{\rho}, \end{aligned} \tag{3.32}$$

recalling that $\mathbf{K}^z$ is identically zero due to (3.27). Let us denote the three terms as $(K_{\text{iso}})_{\boldsymbol{\mu\nu}}$, $\left(K_{\text{ani}}^{\cos}\right)_{\boldsymbol{\mu\nu}}$ and $\left(K_{\text{ani}}^{\sin}\right)_{\boldsymbol{\mu\nu}}$, respectively. We are now able to calculate all of the double integrals for the various combinations of i and i'. Specifically:

$$\int_{\mathbb{R}^2} e_{x,\boldsymbol{\mu}} e_{x,\boldsymbol{\nu}} \, \mathrm{d}^2\boldsymbol{\rho} = \begin{cases} \int_{\mathbb{R}^2} e_0^2 \, \mathrm{d}^2\boldsymbol{\rho} \overset{(3.29)}{=} \dfrac{Z_\perp C_{\boldsymbol{\mu}}}{2 s_{\boldsymbol{\mu}}}, & i = x,\ i' = x, \\ 0, & i = y,\ i' = x, \\ 0, & i = x,\ i' = y, \\ 0, & i = y,\ i' = y, \end{cases} \tag{3.33}$$

$$\int_{\mathbb{R}^2} e_{y,\boldsymbol{\mu}} e_{x,\boldsymbol{\nu}} \, \mathrm{d}^2\boldsymbol{\rho} = \begin{cases} 0, & i = x,\ i' = x, \\ \int_{\mathbb{R}^2} e_0^2 \, \mathrm{d}^2\boldsymbol{\rho} \overset{(3.29)}{=} \dfrac{Z_\perp C_{\boldsymbol{\mu}}}{2 s_{\boldsymbol{\mu}}}, & i = y,\ i' = x, \\ 0, & i = x,\ i' = y, \\ 0, & i = y,\ i' = y, \end{cases} \tag{3.34}$$

$$\int_{\mathbb{R}^2} e_{x,\boldsymbol{\mu}} e_{y,\boldsymbol{\nu}} \, \mathrm{d}^2\boldsymbol{\rho} = \begin{cases} 0, & i = x,\ i' = x, \\ 0, & i = y,\ i' = x, \\ \int_{\mathbb{R}^2} e_0^2 \, \mathrm{d}^2\boldsymbol{\rho} \overset{(3.29)}{=} \dfrac{Z_\perp C_{\boldsymbol{\mu}}}{2 s_{\boldsymbol{\mu}}}, & i = x,\ i' = y, \\ 0, & i = y,\ i' = y, \end{cases} \tag{3.35}$$

$$\int_{\mathbb{R}^2} e_{y,\boldsymbol{\mu}} e_{y,\boldsymbol{\nu}} \, \mathrm{d}^2\rho = \begin{cases} 0, & i = x,\, i' = x, \\ 0, & i = y,\, i' = x, \\ 0, & i = x,\, i' = y, \\ \int_{\mathbb{R}^2} e_0^2 \, \mathrm{d}^2\rho \overset{(3.29)}{=} \dfrac{Z_\perp C_{\boldsymbol{\mu}}}{2 s_{\boldsymbol{\mu}}}, & i = y,\, i' = y. \end{cases} \tag{3.36}$$

Using these relations, considering that $s_{\boldsymbol{\mu}}^{-1} = s_{\boldsymbol{\mu}}$ and simplifying $C_{\boldsymbol{\mu}}$, one entirely calculate the coupling matrix as:

$$(K_{\mathrm{iso}})_{\boldsymbol{\mu}\boldsymbol{\nu}} = \begin{cases} -s_{\boldsymbol{\mu}} \dfrac{j\omega\,(\varepsilon_{\mathrm{iso}} - \varepsilon_{\mathrm{ref}}) Z_\perp}{2}, & i = x,\, i' = x, \\ 0, & i = y,\, i' = x, \\ 0, & i = x,\, i' = y, \\ -s_{\boldsymbol{\mu}} \dfrac{j\omega\,(\varepsilon_{\mathrm{iso}} - \varepsilon_{\mathrm{ref}}) Z_\perp}{2}, & i = y,\, i' = y, \end{cases} \tag{3.37}$$

$$(K_{\mathrm{ani}}^{\cos})_{\boldsymbol{\mu}\boldsymbol{\nu}} = \begin{cases} -s_{\boldsymbol{\mu}} \dfrac{j\omega\varepsilon_{\mathrm{ani}} \cos(2\theta) Z_\perp}{2}, & i = x,\, i' = x, \\ 0, & i = y,\, i' = x, \\ 0, & i = x,\, i' = y, \\ +s_{\boldsymbol{\mu}} \dfrac{j\omega\varepsilon_{\mathrm{ani}} \cos(2\theta) Z_\perp}{2}, & i = y,\, i' = y, \end{cases} \tag{3.38}$$

$$\left(K_{\mathrm{ani}}^{\sin}\right)_{\boldsymbol{\mu}\boldsymbol{\nu}} = \begin{cases} 0, & i = x,\, i' = x, \\ -s_{\boldsymbol{\mu}} \dfrac{j\omega\varepsilon_{\mathrm{ani}} \sin(2\theta) Z_\perp}{2}, & i = y,\, i' = x, \\ -s_{\boldsymbol{\mu}} \dfrac{j\omega\varepsilon_{\mathrm{ani}} \sin(2\theta) Z_\perp}{2}, & i = x,\, i' = y, \\ 0, & i = y,\, i' = y. \end{cases} \tag{3.39}$$

Nothing changes concerning the propagation matrix, which now will be a diagonal 4×4 matrix with identical values for the *xx* and *yy* components, and for the reflection matrices, which now will be diagonal 2×2 matrices, with identical values along the diagonal since the reference medium and the semi-infinite boundary media are isotropic. The active layer is also considered isotropic, so (3.6)–(3.7) are still formally valid, but now all matrices will be 4×4 with identical values for their *xx* and *yy* components and with null values for their *xy* and *yx* components. The VCSEL mode equation in (2.153) is now a 2×2 generalized eigenvalue problem, from which the modal properties of the two modes with different polarization features can be

extracted. Besides the two threshold gains, whose difference determines dichroism, and the two emission wavelengths, whose difference determines birefringence, the normalized $\mathbf{E}_{\text{out}} = \mathbf{a}_{\text{B}}(0^+) \in \mathbb{C}^2$ for both modes, featuring an x and a y components, represents the Jones vector of the supported modes at the outcoupling facet[2]. This complex vector embeds all the polarization information of the supported modes at the output facet. Starting from $\mathbf{E}_{\text{out}}$, it is possible to calculate the Stokes parameters of the mode and to represent them on the Poincaré sphere as done in [37].

If all VCSEL layers exhibit the same principal axes (X,Y), the reference system (x,y) can simply be chosen to align with said axes, fully decoupling the two polarizations. In this simplified case, two separate scalar simulations can be performed: one considering the refractive indices along the x-axis and the other along the y-axis. The resulting modes are linearly polarized along x and y, respectively.

The general methodology presented in this section is particularly useful when different VCSEL layers exhibit distinct sets of principal axes, rotated relative to one another. This occurs, for instance, in a VCSEL with intrinsic semiconductor anisotropies aligned with the GaAs crystalline axes and a subwavelength grating tilted with respect to these axes. The vectorial 1D model enables the analysis of interactions between misaligned optical anisotropies, facilitating possible VCSEL deigns devoted to polarization control across the entire Poincaré sphere, as will be discussed in the following chapters.

The vectorial 1D model is particularly well-suited for engineering polarization control, offering significant simplifications compared to full 3D simulations. This approach allows for a deeper understanding and extensive parametric studies, which would otherwise be computationally prohibitive using a full 3D solver.

[2]The eigenvector $\mathbf{a}_{\text{B}}(0^+)$, defined up to a multiplicative constant, represents the NF exiting the device, without any forward component, since $\mathbf{a}_{\text{B}}(0^-) \propto \mathbf{a}_{\text{B}}(0^+)$ according to the scalar transmission coefficient from the reference medium to the top semi-infinite medium. This vector of $\mathbb{C}^4$ (the two obtained backward components and null forward components) can be transmitted from 0^- to 0^+ using the scalar transmission coefficient from the top semi-infinite medium to the reference medium, then it can be propagated using the 4×4 transmission matrices up to any section z of the VCSEL. This allows the evaluation of the standing wave as $\text{SW}(z) = |E_x(z)|^2 + |E_y(z)|^2$, where $E_x(z) = a_{x\text{F}}(z) + a_{x\text{B}}(z)$ (similarly for E_y), and the spatially-resolved Stokes parameters according to [37].

3.3 Optical anisotropies in VCSELs

In Section 3.2 and Appendix A, we discussed the effects of anisotropies in VCSELs, particularly their impact on the calculation of coupling operators. This analysis extends the work of [69] to the case of rotated principal axes. At this stage, it is essential to examine the specific mechanisms that introduce optical anisotropies in VCSELs. These mechanisms can be categorized as either **intrinsic** or **extrinsic**:

- intrinsic anisotropies arise from the optical properties of semiconductors and include effects such as:
  - the elasto-optic effect, induced by applied mechanical strain [70],
  - the electro-optic effect (EOE), caused by the electrostatic field at the doped DBR hetero-interfaces and from which the VCSEL modes typically exhibit a birefringence of around $10 \div 20$ GHz [69],
- extrinsic optical anisotropies result from the presence of anisotropic layers or subwavelength gratings, which can be effectively modeled as a uniform anisotropic medium.

In the following, we quantify such optical anisotropies in terms of dielectric constants along the different principal axes.

3.3.1 Electro- and elasto-optic effects

AlGaAs is an isotropic material when it is not subjected to an electrostatic field or mechanical strain. Let us denote by n_{iso} the isotropic refractive index of AlGaAs, which depends on the aluminum molar fraction as depicted in Fig. 1.4. The corresponding dielectric constant is $\varepsilon_{\text{iso}} = \varepsilon_0 n_{\text{iso}}^2$. Electrically pumped VCSELs have doped DBRs to ensure electrical injection in the AR, resulting in strong electrostatic field peaks at the DBR heterointerfaces, which in turn makes the material anisotropic through the EOE. This introduces a birefringence in the VCSEL modes, removing the degeneracy between different polarizations and leading to the possible emission of different linearly polarized modes with extremely similar threshold gain, which can cause polarization switching [37].

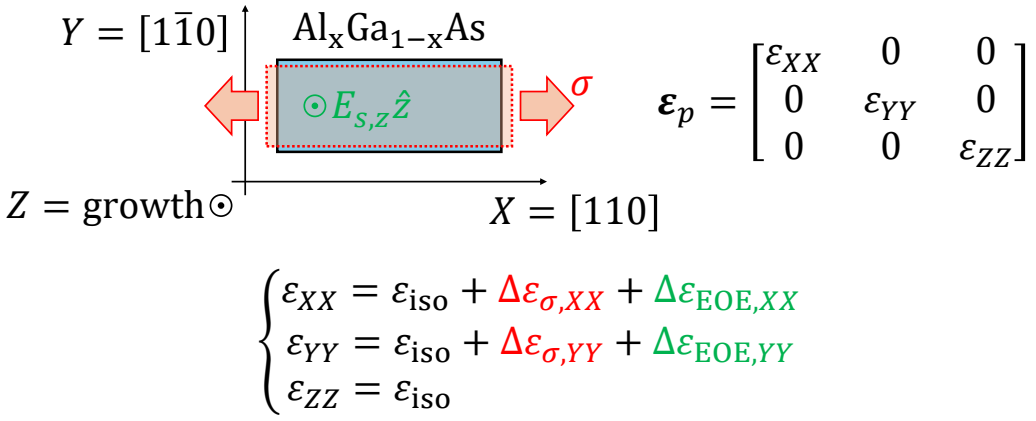

Fig. 3.5 Impact of electro- and elasto-optic effects on the anisotropic dielectric tensor.

The application of mechanical strain also causes an additional anisotropy through the elasto-optic effects, which can either be unintentional due to the VCSEL packaging and manufacturing processes, or it can be used to control the birefringence, which is a key parameter for spin dynamics [71, 70].

We can denote the principal axes of an AlGaAs layer using the crystallographic Miller indices, *i.e.*, $X = [110]$ and $Y = [1\bar{1}0]$, with Z being the longitudinal growth direction. If a strain σ is induced along X (positive if the strain is tensile) and an electrostatic field featuring a z-component $E_{s,z}$ is present, the electro- and elasto-optic effects impact on the dielectric tensor as reported in Fig. 3.5, where [69]:

$$\Delta\varepsilon_{\sigma,XX}/\varepsilon_0 = -n_{\text{iso}}^4 p_{44}\sigma/2, \quad \text{elasto-optic effect,} \tag{3.40}$$

$$\Delta\varepsilon_{\sigma,YY}/\varepsilon_0 = +n_{\text{iso}}^4 p_{44}\sigma/2, \quad \text{elasto-optic effect,} \tag{3.41}$$

$$\Delta\varepsilon_{\text{EOE},XX}/\varepsilon_0 = +n_{\text{iso}}^4 r_{41}E_{s,z}, \quad \text{electro-optic effect,} \tag{3.42}$$

$$\Delta\varepsilon_{\text{EOE},YY}/\varepsilon_0 = -n_{\text{iso}}^4 r_{41}E_{s,z}, \quad \text{electro-optic effect.} \tag{3.43}$$

In the latter, $p_{44} = 0.072$ [69], while $r_{41} = 1.6$ pm/V for GaAs [72] and 0.78 pm/V for AlAs [73]. For intermediate aluminum molar fractions, the values of r_{41} can be linearly interpolated. In (3.40)–(3.41), a sign change occurs if the strain is applied along Y instead of X.

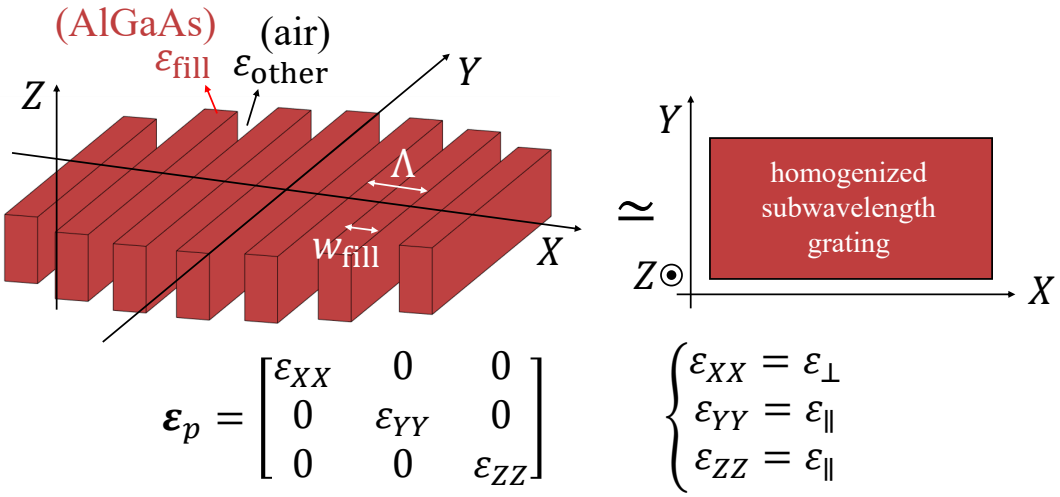

Fig. 3.6 Illustration of the homogenization procedure: a subwavelength grating, which is an inhomogeneous medium, can be treated as an equivalent anisotropic homogeneous medium described a unique dielectric tensor.

3.3.2 Subwavelength gratings

Grating VCSELs, *i.e.*, VCSELs with a grating etched in their cap layer, were originally introduced to fix the VCSEL emitted polarization [41, 74–76]. From the optical standpoint, a grating that is aligned with respect to the AlGaAs crystalline axes introduces a large dichroism between the two linear polarizations associated to each transverse mode, thus enabling single-polarization emission. A grating can be represented by an inhomogeneous medium, featuring alternating parallel bars made out of two materials, typically AlGaAs and air, if the cap layer is not encapsulated in further cover layers. We can define:

- $\varepsilon_{\text{fill}}$ and $\varepsilon_{\text{other}}$ as the dielectric constants of the two materials used for the bars,
- n_{fill} and n_{other} as the corresponding refractive indices,
- w_{fill} as the width of one of the bars characterized by n_{fill}, typically the semiconductor bars,
- Λ as the spatial period of the grating,
- $\eta_{\text{DC}} = w_{\text{fill}}/\Lambda$ as the spatial duty cycle of the grating, as reported in the top left sketch of Fig. 3.6.

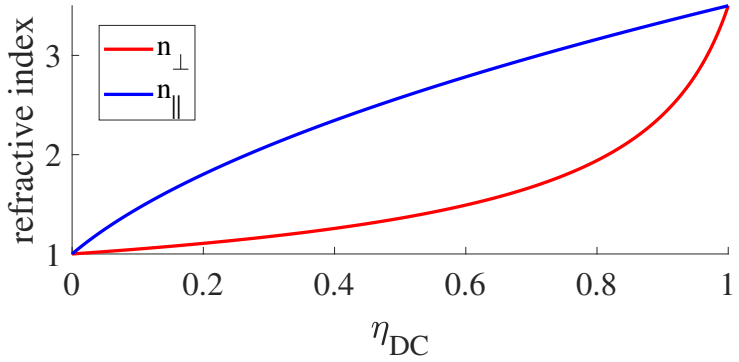

Fig. 3.7 Born-Wolf formulas to evaluate the anisotropic indices of a subwavelength grating, valid for $\Lambda << \lambda / \max(n_{\text{fill}}, n_{\text{other}})$. In this example, $n_{\text{fill}} = 3.5$ and $n_{\text{other}} = 1$.

To properly account for such a layer, one should consider it as a layer with transverse variations, however the bars can have very different spatial dimensions with respect to the oxide. When different spatial scales are present, one should use a large number of basis functions to expand the fields, thus significantly increasing the computational effort.

Fortunately, with increasing precision of lithographic masks, gratings became subwavelength [77], resulting in the elimination of scattering losses since the higher order diffractions are suppressed. If λ is the wavelength of the light interacting with the grating, a subwavelength grating features a spatial period such that

$$\Lambda < \frac{\lambda}{\max(n_{\text{fill}}, n_{\text{other}})}, \tag{3.44}$$

with state of the art dimensions being $\Lambda \sim 100 \div 200$ nm for 850 nm VCSELs. A subwavelength grating can be approximated as an anisotropic homogeneous medium with a dielectric tensor as the one represented in Fig. 3.6. This procedure is referred to as grating homogenization.

The simplest way to evaluate $\varepsilon_{\perp}$ and $\varepsilon_{\parallel}$ and their corresponding refracrive indices $n_{\perp}$ and $n_{\parallel}$ is to use the Born-Wolf formulas [49], holding their validity in the limit $\Lambda << \lambda / \max(n_{\text{fill}}, n_{\text{other}})$ and reading:

$$n_{\perp} = \frac{1}{\sqrt{\dfrac{\eta_{\text{DC}}}{\varepsilon_{\text{fill}}/\varepsilon_0} + \dfrac{1-\eta_{\text{DC}}}{\varepsilon_{\text{other}}/\varepsilon_0}}}, \tag{3.45}$$

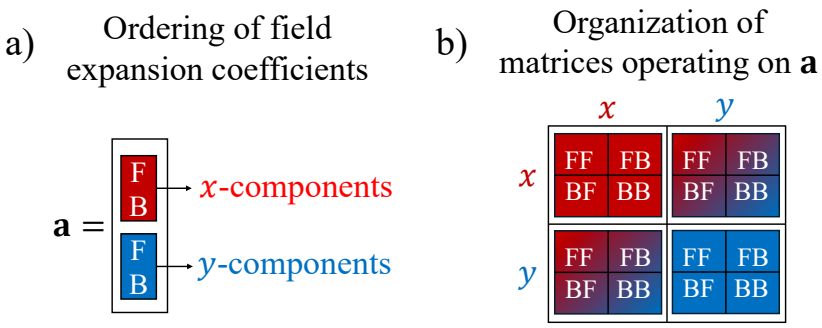

Fig. 3.8 Ordering of vectors (a) and matrices (b) in the 1D vectorial analysis.

$$n_{\parallel} = \sqrt{\eta_{\mathrm{DC}} \cdot \frac{\varepsilon_{\mathrm{fill}}}{\varepsilon_0} + (1-\eta_{\mathrm{DC}}) \cdot \frac{\varepsilon_{\mathrm{other}}}{\varepsilon_0}}. \tag{3.46}$$

Notice how (3.45)–(3.46) do not depend explicitly on Λ, nor on the grating bar thickness t_{grat}, which start to matter for larger values of Λ. The Born-Wolf formulas are represented in Fig. 3.7.

Let us now develop an alternative way to obtain the homogenized indices and to test the Born-Wolf formulas. Consider the 1D coupling matrix of an anisotripc layer described in (3.37)–(3.38)–(3.39). We can arbitrarily order the vector of expansion coefficients $\mathbf{a}$, which comprises all $a_{\boldsymbol{\mu}}$ with $\boldsymbol{\mu} = [i, \alpha]^T$, $i \in \{x, y\}$, $\alpha \in$ {forward (F), backward (B)}, and all matrices acting on it. For instance, we can choose the ordering described in Fig. 3.8. Defining the auxiliary matrices

$$\mathbf{A}_1 = \begin{bmatrix} 1 & 0 \\ 0 & -1 \end{bmatrix}, \tag{3.47}$$

$$\mathbf{A}_2 = \begin{bmatrix} 1 & 1 \\ -1 & -1 \end{bmatrix}, \tag{3.48}$$

we can rewrite the propagation and coupling matrices of the 1D vectorial analysis with this new ordering as

$$\mathbf{B} = -j\beta_{\perp} \begin{bmatrix} \mathbf{A}_1 & \mathbf{0} \\ \mathbf{0} & \mathbf{A}_1 \end{bmatrix}, \tag{3.49}$$

$$\mathbf{K}_{\mathrm{iso}} = -\frac{j\omega\,(\varepsilon_{\mathrm{iso}} - \varepsilon_{\mathrm{ref}})\,Z_{\perp}}{2} \begin{bmatrix} \mathbf{A}_2 & \mathbf{0} \\ \mathbf{0} & \mathbf{A}_2 \end{bmatrix}, \tag{3.50}$$

$$\mathbf{K}_{\text{ani}} = \mathbf{K}_{\text{ani}}^{\cos} + \mathbf{K}_{\text{ani}}^{\sin} = -\frac{j\omega\varepsilon_{\text{ani}} Z_{\perp}}{2} \begin{bmatrix} \cos(2\theta)\mathbf{A}_2 & \sin(2\theta)\mathbf{A}_2 \\ \sin(2\theta)\mathbf{A}_2 & -\cos(2\theta)\mathbf{A}_2 \end{bmatrix}, \tag{3.51}$$

so that the overall transmission matrix of an anisotropic layer of thickness L within the reference medium reads:

$$\mathbf{T} = \exp\left[\left(\mathbf{B} + \mathbf{K}_{\text{iso}} + \mathbf{K}_{\text{ani}}\right) L\right]. \tag{3.52}$$

The transmission matrix of a grating sandwiched between two semi-infinite media can also be obtained by rigorous coupled wave analysis (RCWA) [50, 51], which will not be discussed as it is beyond the scopes of this dissertation. Supposing to have access to said transmission matrix[3], namely $\mathbf{T}_{\text{RCWA}}$, by extracting its matrix logarithm it is possible to have a set of 4×4 equations involving both ε_{iso} and ε_{ani} reading:

$$\left(\mathbf{B} + \mathbf{K}_{\text{iso}} + \mathbf{K}_{\text{ani}}\right) L = \log\left(\mathbf{T}_{\text{RCWA}}\right). \tag{3.53}$$

Focusing on the components $(1,1)$ and $(3,3)$ of the previous matrix equation, it is possible to derive a 2×2 system of equations with unknowns ε_{iso} and ε_{ani}, in turn linked to the ε_{XX} and ε_{YY} of the homogenized grating according to (A.20)–(A.21), simply representing $\varepsilon_{\perp}$ and $\varepsilon_{\parallel}$, respectively. Fixing the grating thickness $t_{\text{grat}} = 60$ nm, the duty cycle $\eta_{\text{DC}} = 0.5$ and for a varying grating period, the results of this new homogenization procedure, compared with the Born-Wolf formulas are reported in Fig. 3.9, showing that for typical grating periods there is a significant deviation from the Born-Wolf results, especially concerning $n_{\perp}$. One could use the RCWA transmission matrix directly, however the homogenization procedure is crucial when wanting to consider grating reliefs, *i.e.*, gratings with a finite transverse shape, since RCWA is only able to provide the transmission matrix of an infinite layer.

Subwavength gratings represent a source of optical anisotropy which can be easily engineered by varying the grating design parameters. Such a strategy will be further discussed in the following chapters (see Chapter 5), especially useful for polarization control [37].

[3] Our optical mode solver, VELMS, is able to calculate a grating transmission matrix using RCWA.

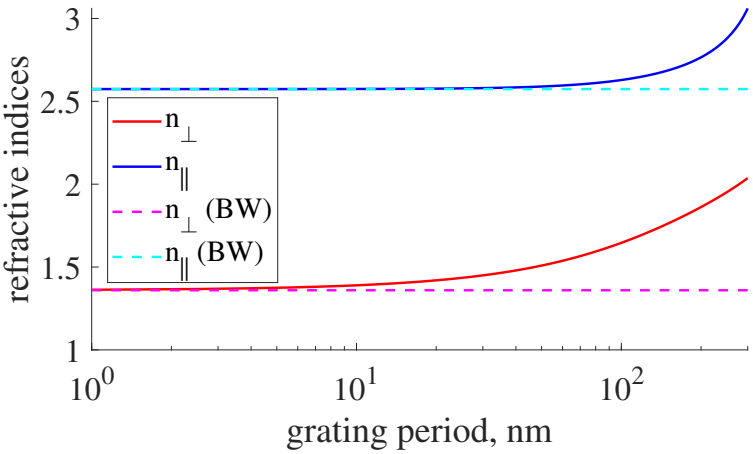

Fig. 3.9 Grating homogenization starting from the grating transmission matrix calculated via RCWA, obtained fixing the grating thickness and duty cycle, while varying the period. The results are compared with the Born-Wolf formulas (BW), which are only accurate at lower periods.

3.3.3 3D vs 1D vectorial simulations

Consider a VCSEL supporting two modes sharing the same intensity profile associated to the fundamental mode (see Fig. 2.10), with the same epitaxial structure defined in Fig. 3.1. Let us analyze the modal properties of this device using both a full 3D analysis and the vectorial 1D analysis. Consider the application of a uniform strain along one of the GaAs principal axes throughout the entire structure, so that two linearly polarized modes are supported along $x = X$ and $y = Y$, respectively. Defining the lasing and superior modes as the mode with the lower and higher threshold gains, respectively, we can denote g_l and g_s as the lasing and superior threshold gains, $\lambda_{\mathrm{e,l}}$ and $\lambda_{\mathrm{e,s}}$ as the lasing and superior emission wavelengths and f_l and f_s as the lasing and superior emission frequencies. The absolute birefringence Δf between the two modes can be expressed as:

$$\Delta f = |f_\mathrm{s} - f_\mathrm{l}| = c \left| \frac{1}{\lambda_{\mathrm{e,s}}} - \frac{1}{\lambda_{\mathrm{e,l}}} \right|, \tag{3.54}$$

c being the speed of light. Furthermore, the absolute relative dichroism between the modes reads:

$$\Delta g = \frac{|g_\mathrm{s} - g_\mathrm{l}|}{g_\mathrm{l}}, \tag{3.55}$$

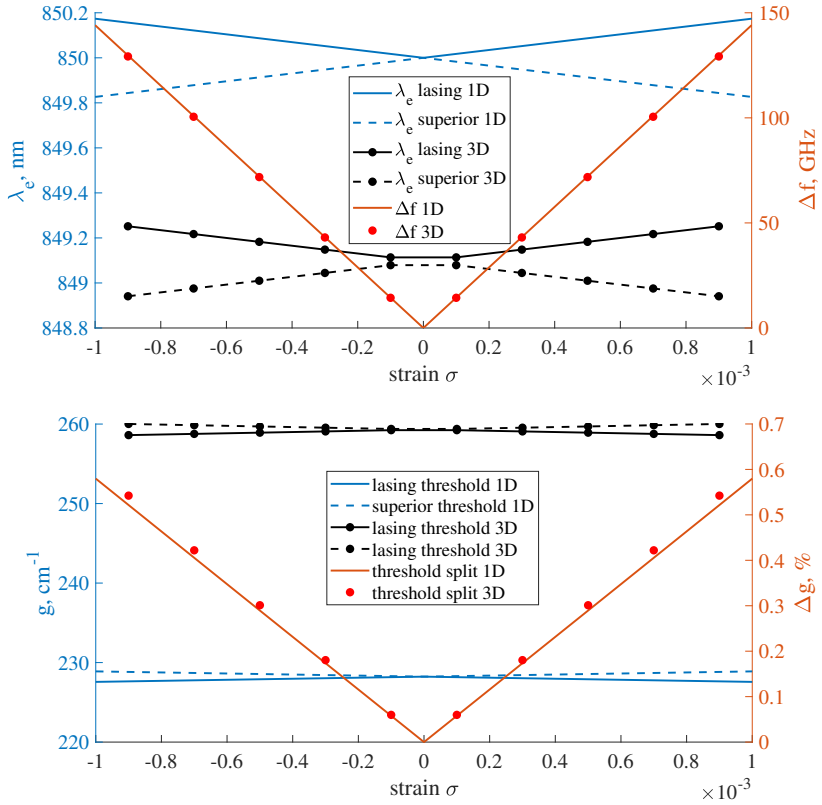

Fig. 3.10 Top: emission wavelength for both modes and corresponding birefringence calculated for a 1D vectorial simulation and a full 3D simulation. Bottom: threshold gain for both modes and corresponding relative dichroism calculated for a 1D vectorial simulation and a full 3D simulation. At $\sigma = 0$, the linear lasing polarization switches from x to y, which is predicted from both the 3D and 1D vectorial model.

which can be expressed as a percentage. The results for varying strain values in the cases of 3D and 1D vectorial simulations are reported in Fig. 3.10. It can be seen that the wavelengths in the 3D case are lower with respect to the vectorial 1D case, due to the fact that the 1D simulation only accounts for $k_t = 0$, while larger values of k_t are employed in the 3D case. In addition, the 3D thresholds are higher. However, both the birefringence Δf and the dichroism Δg are in perfect agreement[4], confirming how useful the fast and computationally light 1D model can be, especially when a single transverse mode is selected and the focus is entirely on the polarization features.

[4]The slight disagreement appearing in Δg is due to the fact that the dichroism is usually defined in relation to g_l. If one uses an absolute definition for the dichroism, *i.e.*, $\Delta g_{\mathrm{abs}} = |g_{\mathrm{s}} - g_{\mathrm{l}}|$, the agreement between the 3D and 1D vectorial case would be perfect.

Chapter 4

High-power single-mode VCSELs

A SM circular VCSEL features an oxide radius of $\sim 1.5\,\mu$m and a relatively low optical power, limited to $4 \div 6$ mW [20, 43, 78]. Aiming at a higher output power, one can rely on larger apertures at the cost of losing the SM emission. Large-active-area (LAA) VCSELs are employed for applications that do not require a coherent emission of a pure spectral line, *e.g.*, plastic welding, industrial heating processes or skin treatment [15]. The most critical aspect to be considered when designing LAA devices is self-heating, *i.e.*, the internal heating of the VCSEL due to current injection. Typical heat sources are Joule heating, non-radiative carrier recombination mechanisms and thermalization of carriers in the QWs, creating a non-uniform temperature distribution in the device that peaks at the QWs [45, 79] and that increases with the VCSEL bias point.

Self-heating has several effects, and represents the main cause of the VCSEL roll-over. Indeed, self-heating causes a thermal lensing due to the empirical dependence of the refractive index profile on temperature [79], causing a shift in emission towards longer wavelengths [45]. On the other hand, the gain provided by the QWs, besides depending on carrier population, depends on both wavelength and temperature. The gain peak also shifts towards higher wavelengths with increasing temperature, but with a faster shift rate with respect to the VCSEL emission wavelength[1] [80]. In an optimal design, the QWs gain peak should be aligned with the emission wavelength,

[1]The gain spectra are determined by the structure of the quantum wells (QWs), in particular by the thickness of both wells and barriers, their molar fractions, the number of confined carriers, the operating temperature, and the optical wavelength. A quantitative description of these dependencies can be derived using the Fermi Golden Rule [45], which, for example, allows one to predict the temperature-induced shift of the gain spectra. Conversely, the resonant emission wavelength is

thus introducing a dependence of the VCSEL design on the target bias point. As the bias point increases, the peak of the gain spectrum gets more and more misaligned with the emission wavelength, thus degrading the QWs gain and eventually turning off the laser[2]. The goal is to push the roll-over point towards higher and higher currents, so that the maximum optical output power of the laser is increased as much as possible.

In LAA-VCSELs self-heating depends on the transverse shape of the oxide, as demonstrated experimentally in [15] and interpreted with thermal simulations in [79]. They key message is that VCSELs with elongated active shapes show the roll-over point for higher currents and can achieve higher output power and wall-plug efficiency compared to standard circular or quadratic VCSELs with the same area. This is due to a better thermal dissipation along the shorter side of the elongated oxide. This is the reason why multi-mode large-area rectangular VCSELs are typically employed.

In this thesis, LAA-VCSELs represent the starting point, aiming to add SM emission on top of a higher-out power. This is what we refer to as modal engineering, relying on surface patterning techniques based for instance on arrays of surface grating reliefs, generalizing the concept of circular grating VCSELs. Possible designs and associated issues are investigated in the following sections.

Most of the results of this chapter have been published by our group in [81, 29, 79].

4.1 Modal engineering of rectangular large-active-area VCSELs

Atomic devices such as atomic clocks, quantum gyroscopes and atomic magnetometers call for the optical pumping of a specific atomic species, which can only be excited at specific wavelengths due to the electronic transitions, furthermore, the input light needs to be circularly polarized. This requires a SM light source with a stable linear polarization, which can be later converted into a circular polarization

determined by electromagnetic considerations: it depends on the properties of the optical cavity, the mirrors, and the temperature, which affects the refractive index profile.

[2]This phenomenon happens in conjunction with a worsening of the injection efficiency in the QWs with temperature, which also contributes to the device turn-off.

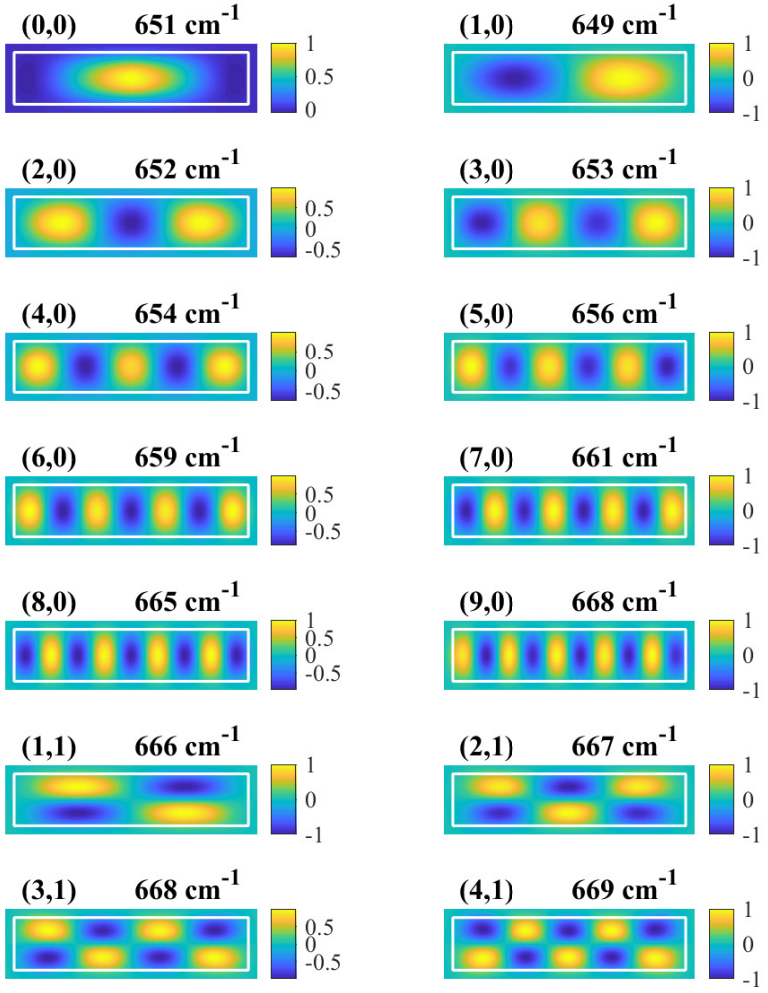

Fig. 4.1 Calculated mode profiles at the outcoupling facet of a rectangular VCSEL with their corresponding threshold gain. Only x-polarization is displayed; y-polarization features exactly the same threshold gain, wavelength and field profile, since in the simulation no intrinsic anisotropy is included. Each mode is indexed by the number of nodes along x and y. Emission wavelengths are closely packed: all the modes in the figure lie within a wavelength interval of 0.5 nm.

through a quarter waveplate [27]. VCSELs are emerging as a compact semiconductor light source, which, however, must target tens of milliwatts of single-mode power (see TRUMPF VCSELs for the Qyro Project) for a good efficiency of the atomic pumping process [38]. As stated in [20], several designs have been proposed to increase the output power whilst remaining within the SM regime, such as surface-relief based circular VCSELs [43, 78] or circular devices whose epi-structure features a particular alignment between the oxide and the standing wave, obtained by modifying few p-DBR pairs [20]. Both solutions present an insufficient SM power of around $4 \div 6$ mW. A much more promising solution relies in modal engineering of LAA devices.

The goal of this section is to give design guidelines for a SM linearly polarized LAA rectangular VCSEL tailored for atomic pumping of rubidium atoms [18, 20, 24, 82], targeting an emission wavelength of $\lambda_t = 795$ nm and compatible with AlGaAs VCSEL technology [38]. The SM emission is achieved through surface patterning of the outcoupling facet. Complementary measurements were performed on SM rectangular VCSELs featuring a standard emission at 850 nm, which are in agreement with numerical simulations, thus validating the design and optimization strategies.

4.1.1 Optical modes of a large-active-area rectangular VCSEL without surface patterning: multi-mode emission

Given an epitaxial structre that is compatible with the emission at $\lambda_t = 795$ nm, we focus on simulating a LAA-VCSEL with a rectangular oxide aperture (and therefore a rectangular active area) of $26\,\mu$m along the x axis and $6\,\mu$m along the y axis, with an aspect ratio of 4.33.

We can calculate the optical modes supported by this structure using the procedure described in Chapter 2, employing a much larger number of basis functions with respect to Fig. 2.10, given the non-circular shape.

Each supported mode is indexed by a two dimensional label of integer numbers, (n_x, n_y), n_x and n_y being the number of nodes along x and y, respectively. In Fig. 4.1 we are reporting the normalized dominant component of the modes at the outcoupling facet of the laser, namely the NF profiles, together with their threshold gains. Since

design	G_0^x, cm^{-1}	G_0^y, cm^{-1}	G_1, cm^{-1}	η_o
A	884	879	1080	0.55
B	1192	1634	1536	0.94

Table 4.1 Parameters characterizing designs A and B.

mode discrimination solutions are not applied here, they have similar threshold gains, which is compatible with the expected multi-mode emission.

4.1.2 Surface patterning for single-mode emission: metallic grid and grating relief array

Now, we present design strategies aimed at SM operation based on selecting a high-order mode by introducing threshold gain penalties for all its competitors. The fundamental idea is to introduce a patterning at the VCSEL aperture, which mimics the topography of the mode. Such patterning can be designed on the basis of the preliminary simulations presented in Fig. 4.1.

We discard the idea of selecting the modes with $n_y > 0$. Indeed, with such an aspect ratio, the patterned structures needed to select a mode with $n_y > 0$ should be quite small and thus more challenging from the manufacturing standpoint. The situation would be different for squared geometries like the one investigated in [14], for which modes with $n_x = n_y$ become a reasonable choice.

Among the modes with $n_y = 0$, considering that the aspect ratio of the rectangle is about 4, the mode $(4,0)$ is the one featuring the most circular field spots, while the others are quite elliptical (see the limit cases with $n_x = 0$ and $n_x = 9$ featuring the highest ellipticity). For this reason, the target of the designs will be achieving SM, single-polarization (*e.g.*, x) operation with the $(4,0)$ mode. In the following, we will present different possibilities to achieve this target.

The SM solutions investigated in this subsection rely on a metallic grid and a grating relief array at the VCSEL outcoupling facet, respectively, presented in Fig. 4.2. In view of a comparative appraisal between the design strategies, four parameters are investigated, which are summarized in Tab 4.1. These are:

- the threshold gain per QW of the selected mode for both polarizations, G_0^x, and its y-polarized counterpart G_0^y,

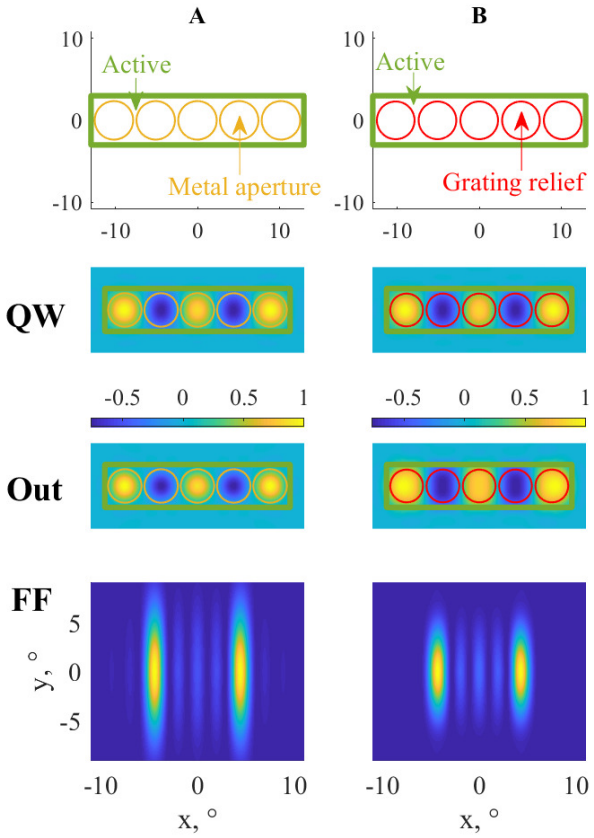

Fig. 4.2 Overview of the investigated designs (A and B) achieving the SM emission. Each column represents one of the designs, described in terms of transverse geometry (first row, axes are expressed in μm), dominant component of the mode with the lowest threshold at the QW section (second row), at the output section, *i.e.*, the NF profile (third row), and FF profile. More in detail, design A features the oxide aperture sketched by the green line and is covered with metal everywhere except for the metal opening depicted in yellow. Design B instead features circular grating surface reliefs within the red circles.

- the threshold gain per QW of the first superior (in gain) mode G_1,
- the outcoupling efficiency η_o, defined as the ratio of the optical power emitted by the device to that generated in the QW active region.

Design A: metallic grid

The first investigated solution to retrieve the single-mode emission (design A), similarly to that simulated, realized and characterized in [14], is based on patterning the outcoupling facet with a metallic grid, consisting of a 50 nm Pt layer featuring 5 uniformly spaced apertures in correspondence to the field spots of the mode $(4,0)$. For the design A, the first column of Fig. 4.2 shows the transverse features of the investigated geometry, the dominant component of the mode with the lowest threshold both at the QW section and at the outcoupling facet (NF), and the FF profile. The parameters characterizing the design are reported in the first row of Tab. 4.1.

Design A features a relative difference between G_0^y and G_1 of 23.4%, therefore much higher than the situation depicted in Fig. 4.1, where the maximum relative threshold difference between the modes is around 3%. Besides the optical advantages, this solution can also improve dramatically the electrical injection and its uniformity in the QWs, especially useful for very large apertures.

This design lacks any polarization control (nearly equal G_0^x and G_0^y) and features a strong metal absorption (low outcoupling efficiency). If polarization control is not an issue, then efficiency can be improved by using elliptical metal apertures and this design can be used.

Design B: grating relief array

The second investigated solution (design B) consists of a grating relief array, where each grating relief is aligned with one of the field spots of the mode $(4,0)$. As displayed in Fig. 3.2, the reflectivity of the *p*-DBR depends strongly on the thickness of the cap layer. For a standard design, this thickness is optimized to have the maximum DBR reflectivity and the lowest threshold gain. In relief-based designs, the cap layer is grown longer, targeting the highest threshold gain, and subsequently etched, with a depth corresponding to the optimal design, following the transverse profile of the mode to be selected. This procedure strongly increases

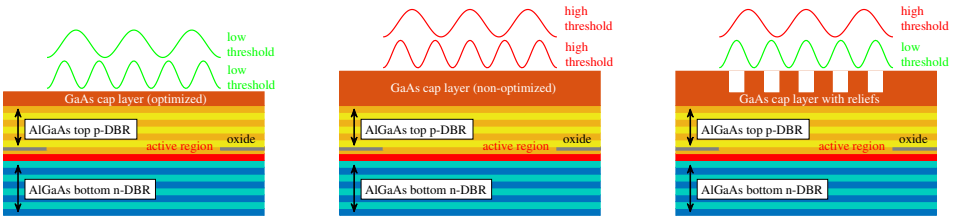

Fig. 4.3 Schematic of the relief design. For a standard VCSEL, the cap layer thickness is optimized to have the lowest threshold for all the modes such as $(4,0)$ and $(2,0)$, whose intensity is sketched above the laser (left). To only select the mode $(4,0)$, it is possible to raise the cap layer thickness to a point where the threshold is high for all the modes (middle) and then etch in correspondence to the peaks of the mode $(4,0)$ (right).

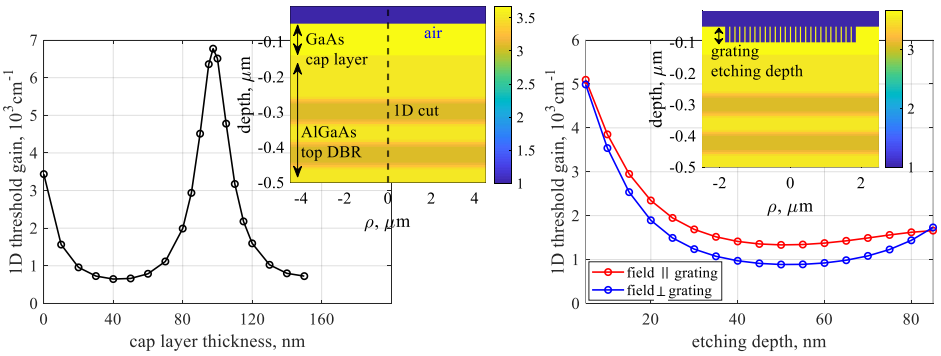

Fig. 4.4 Left: calculated threshold gain from 1D simulations as a function of the cap layer thickness. The inset represents the refractive index map of the structure, highlighting the 1D cut. Right: calculated threshold gain for the fields parallel and orthogonal to the grating bars with a fixed value of cap layer thickness of 90 nm. The inset shows the investigated sub-wavelength grating.

the thresholds for all the modes less than the selected one, hence acting as a mode selector. This design also allows for polarization control. Indeed, it is possible to etch a subwavelength grating in the regions where the relief is needed, which can be treated using the homogenization procedure described in Subsection 3.3.2. A sketch of the working principle is reported in Fig. 4.3.

From a quantitative standpoint, the thicknesses can be designed by computing the 1D threshold gain (see Chapter 3.1) as done in Fig. 4.4. Aiming at maximizing the threshold gain *a priori* of the patternings, we choose a cap layer thickness of 90 nm. From there, the right image shows how the threshold gain decreases as we etch into the cap layer, favoring the field orthogonal to the grating bars. We selected a grating etching depth of 50 nm, yielding the lowest threshold for the orthogonal field. Now, the full three-dimensional simulation can be carried out using the transverse geometry reported in the second column of Fig. 4.2. The parameters of this design are reported in the second row of Tab. 4.1.

This geometry performs well as mode selector, yielding a satisfactory relative difference between G_0^x and G_1 of 29.9% and an excellent control on the selected polarization given the high value of G_0^y. Furthermore, the absence of metal at the output facet improves the outcoupling efficiency significantly with respect to design A, raising it as high as 0.94. The only downside of such a design is the higher threshold even for the wanted mode $(4,0)$, due to the reduced DBR reflectivity introduced by the portions of non-optimized cap layer and by the absence of metal (note that a metallic layer, besides introducing optical losses, increases the overall reflectivity of the DBR, reducing the threshold).

Design B was experimentally tested on a similar 850 nm double-junction [83] LAA rectangular VCSEL with an aspect ratio of around 7 and used to select the mode $(7,0)$[3]. Light-current-voltage (LIV), NF and FF measurements are reported in Fig. 4.5, showing how the laser is able to retain the SM emission for a large current range, with a peak SM power exceeding 20 mW. The author performed the measurements in the TRUMPF laboratories using the VTC 4000 near-field camera, manufactured by Instrument Systems. Both the NF and FF profiles are in qualitative agreement with our simulated modes. In addition, one can notice that the experimental NF profile features stronger external peaks at higher currents, which reflects in stronger

[3]Specific details regarding the VCSEL structure cannot be disclosed due to confidentiality reasons.

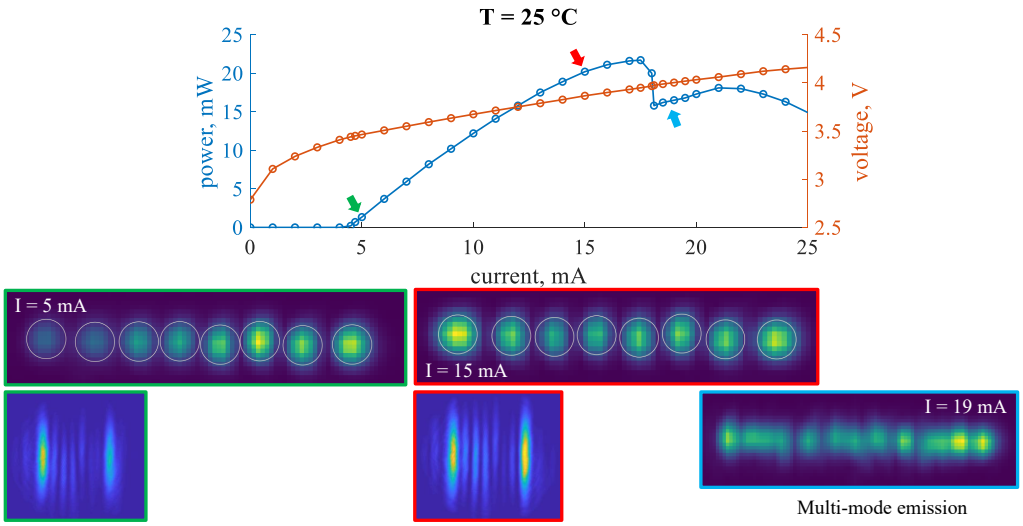

Fig. 4.5 Experimental LIV, NF and FF profiles for an 850 nm double-junction LAA rectangular VCSEL adopting design B to successfully select the mode $(7,0)$ for a large current range. White circles in the NF plots represent the regions associated to the various peaks, automatically detected by the NF camera software.

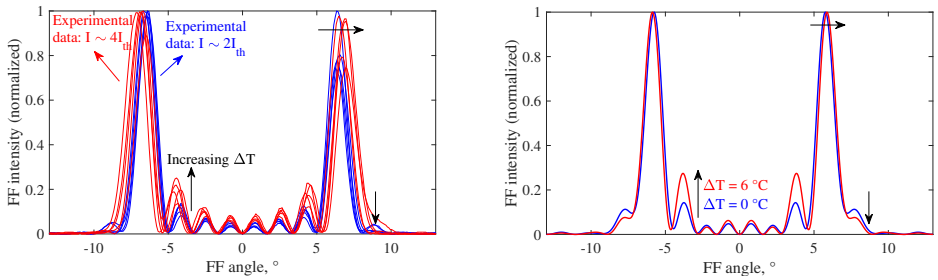

Fig. 4.6 Left: horizontal cuts of the FF data for an 850 nm AlGaAs VCSEL adopting design B to select the mode $(7,0)$. Multiple curves of the same color refer to nominally equal devices in different positions of the wafer, while blue and red curves differ in terms of injection current, set at twice and four times the threshold current, respectively. Right: 3D optical simulations of the same structure with a peak self-heating temperature ΔT of 0 and 6 °C. They provide the best fit with the experimental results after a parametric variation of ΔT.

inner peaks of the FF. This behavior is due to self-heating and is further addressed in Section 4.2.

Aiming at a more quantitative comparison, the FF of a specific 850 nm VCSEL using design B to select the mode $(7,0)$ was simulated and measured for different values of the bias current. Results are displayed in Fig. 4.6. To simulate the effect of temperature, a self-heating temperature distribution was used to modify the input refractive index profile of the VCSEL optical simulations. Further details about the thermal profile are presented in Section 4.2. Experimental results and simulations are in excellent agreement, validating our 3D optical mode solver and SM design strategies. A more detailed analysis of self-heating is reported in Section 4.2.

Further technological implementations of this solution for quantum gyroscopes are discussed in [38].

4.1.3 Maximizing axial power: shaping of the emitted far field

Both designs A and B investigated in Subsection 4.1.2 are able to select the desired transverse mode, with design B also providing polarization control. However, one can see from both simulated and experimental FF profiles that the axial power, *i.e.*, optical power emitted along a null FF angle, of these single-higher-order-mode devices is quite low, as shown in Fig. 4.2, Fig. 4.5 and Fig. 4.6.

This leads to two possible issues. In fiber applications, external and bulky optics are needed to collimate the beam, which, taken as it is, would feature poor coupling efficiency with the fiber [84, 28, 22]. On the other hand, in free-space applications, one should only rely on one of the two FF peaks, yielding the loss of half the optical power. In both cases, having an FF with high axial power would be beneficial.

The low axial power is due to the alternating positive and negative peaks in the NF profile, resulting in a destructive interference effect. Looking at Fig. 4.1, it is possible to see that the positive and negative peak values are exactly symmetric for the modes with an odd n_x, while slightly asymmetric for the modes with an even n_x, for which the destructive interference is less significant. This leads the corresponding FF profile to show more radiated power in the axial direction, another valid reason to focus on selecting the mode $(4,0)$ instead of the mode $(3,0)$, which also presents pretty circular contour lines. In general, mitigating destructive interference is a

design	G_0^x, cm^{-1}	G_0^y, cm^{-1}	G_1, cm^{-1}	η_o
C	1145	1944	1399	0.65
D	1314	2363	1735	0.92

Table 4.2 Parameters characterizing designs C and D.

way to retrieve more power in central FF region, but from Fig. 4.2 we can see that choosing an even n_x is not enough.

The solutions proposed in this subsection (designs C and D) aim at achieving the single-mode emission while simultaneously inhibiting the destructive interference effect resulting from the NF profile, overall retrieving a central peak in the FF.

Design C: grating relief array partially covered with metal

Design C combines designs A and B. Specifically, a grating relief array corresponding only to the three positive field spots of the mode $(4,0)$ is used for mode selection and polarization discrimination, while a 50 nm thick Pt layer is deposited on top of the outcoupling facet. The latter features three rectangular apertures in correspondence to the positive field spots where the reliefs are localized, while simultaneously covering the negative field spots. The results are reported in the first column of Fig. 4.7. It can be noticed that, at the QW section, the field profile is exactly the expected profile of the mode $(4,0)$, featuring both positive negative spots. However, at the output section, the NF is strongly affected by the metallic cover layer, yielding a strong reduction of the negative field, whilst leaving the positive regions mostly unaffected. This heavily inhibits the destructive interference phenomena, yielding a FF profile with a central peak, much better for fiber coupling applications.

The figures of merit qualifying this design are summarized in the first row of Tab. 4.2, showing a good relative separation between G_0^x and G_1 of 22.2%, together with an excellent polarization control and an improved electrical injection with respect to design B thanks to the presence of the metal. Notice that the value of G_0^x for the design C is lower with respect to the corresponding value for the design B, once again confirming that the metal layer is able to reduce the VCSEL threshold gain due to the increased reflectivity. Of course, the outcoupling efficiency is worsened due to the increased optical losses.

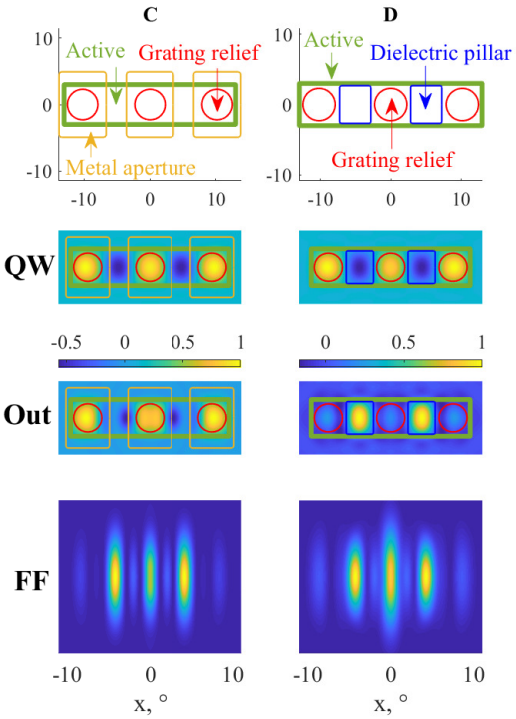

Fig. 4.7 Overview of the investigated designs (C and D) achieving the single-mode emission and optimizing the FF pattern, retrieving a central peak along the axial direction. The designs are described in the same terms as the ones in Fig. 4.2. Specifically, design C combines grating surface reliefs (indicated red circles) with metal apertures (indicated with yellow rectangles). Design D instead combines grating surface reliefs (withing red circles) with square dielectric pillars indicated in blue.

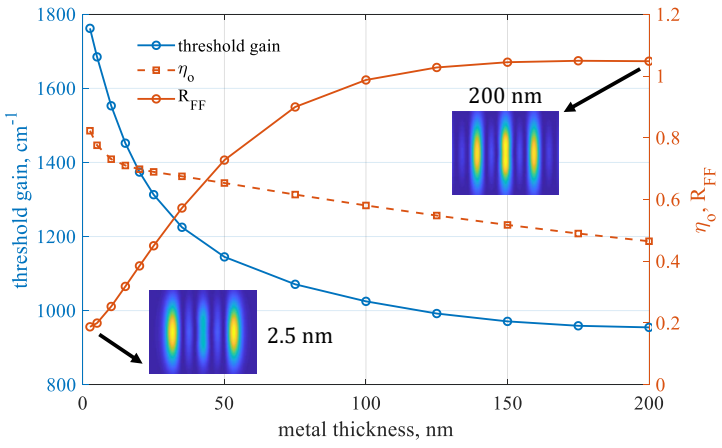

Fig. 4.8 Impact of the metal thickness on the threshold gain G_0^x, outcoupling efficiency η_o and FF ratio R_{FF} for the design C.

To quantify the strength of the central FF peak, it is possible to introduce the FF ratio R_{FF}, defined as the ratio between the central FF peak to one of the two side peaks. One can imagine that a thicker metallic layer induces a stronger inhibition of destructive interference, yielding a larger R_{FF}, a reduction of G_0^x due to the added reflectivity, and a reduction of η_{o} due to the added losses. This is investigated in Fig. 4.8.

As expected, G_0^x is a decreasing function of the metal thickness, with most of its variation taking place within the first 100 nm, η_o is a decreasing function with a linear behavior after 50 nm and R_{FF} shows an increasing behavior, saturating after 150 nm. A trade-off between $\boldsymbol{\eta_{\mathrm{o}}}$ and R_{FF} is highlighted. One can notice that choosing a metal thickness of 50 nm already provides a FF ratio of 73%, with an outcoupling efficiency of 65%. Exceeding this value of the metal thickness could lead to an excessive worsening of η_{o}, however, this depends on the specific application.

Design D: grating relief array with dielectric pillars

Finally, the last investigated solution (design D) aims at achieving the central FF peak without worsening the outcoupling efficiency, at the cost of a higher threshold gain G_0^x. To achieve this, three grating reliefs in correspondence to the positive field spots are used for mode and polarization selection just like in design C. However, the negative field spots are not inhibited via a lossy metallic layer, but rephased by means of a 100 nm thick Si_3N_4 pillars grown on top of the outcoupling facet in correspondence to the negative field spots. The refractive index of Si_3N_4 at $\lambda_{\mathrm{t}} = 795$ nm is $n_{Si_3N_4} = 2$. The results are reported in the last column of Fig. 4.2.

Once again, it is possible to see the usual profile of the mode $(4,0)$ at the QW section, which dramatically changes at the outcoupling facet. Indeed, the color bar displays an extreme reduction of the negative portion of the field, with the second and fourth NF peaks now being positive and dominant with respect to the others. This in turns reduces the destructive interference, yielding a strong central peak in the FF profile. The characteristics of this design are reported in the second row of Tab. 4.2. It features a great relative difference between G_0^x and G_1 of 32.0%, an excellent polarization control and an almost unaffected outcoupling efficiency with respect to design B. The only downsides with respect to design C (linked to the absence of a metallic layer) are a worsened electrical injection and a relevant

increase of G_0^x of 14.8%, translating into a higher threshold current, which is not an issue for high-power applications.

Although already promising, design D can be further optimized in future work in terms of FF emission by parametrically changing the thicknesses and the widths of the dielectric pillars, with the aim of a perfectly axial FF emission.

4.2 Effects of self-heating

Our goal in this section is to analyze the behavior of optical modes as the bias current and therefore the VCSEL self-heating increases, which can lead to the misalignment of the target optical mode with respect to the surface patterning used for modal discrimination. This misalignment is the primary cause of loss of SM emission. Focusing on design B, *i.e.*, the grating relief array, used for both modal and polarization control, we will provide design guidelines for both low and high self-heating temperature regimes.

In doing so, we will also investigate an effect already observable in Fig. 4.5, *i.e.*, the reduction in relative intensity of the innermost peaks of the NF profile as the current (and consequently self-heating) increases. Additional experimental evidence of both this phenomenon and the shift of the peak positions with increasing current is presented in Fig. 4.9, where a VCSEL selecting the $(7,0)$ mode is analyzed. By comparing the outermost and innermost peaks of the NF profile, it becomes clear that, on average, the outermost peaks become increasingly dominant with rising current, while the innermost ones progressively weaken. This effect will be interpreted by incorporating the computed self-heating temperature profile into optical modal simulations and will be considered in the design of the grating relief array for devices operating at higher self-heating temperatures.

4.2.1 Setup and calibration of thermal simulations

To simulate self-heating in VCSELs, the heat equation must be solved self-consistently with carrier transport and optical mode simulations, as done in [45]. The approach in [45] relies on an in-house VCSEL solver for circular geometries and is already computationally demanding despite leveraging the cylindrical symmetry to reduce

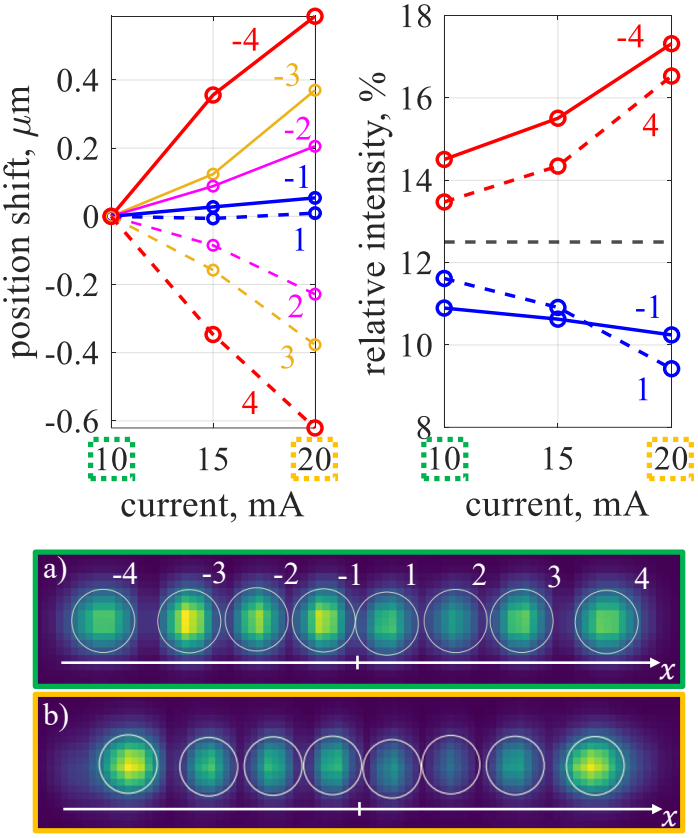

Fig. 4.9 Experimental evidence of peak position shifts (top left) and relative intensities (top right) for the innermost and outermost peaks for a VCSEL selecting the $(7,0)$ mode. Relative intensities are normalized to the total intensity and the dashed black line represents the ideal case where power is equally distributed among all peaks (12.5% of the total power for each NF lobe). The data represent averages over multiple devices. At the bottom, NF profiles of a specific device are shown for $I = 10\,\text{mA}$ (a) and $I = 20\,\text{mA}$ (b). White circles represent the regions associated to the various peaks, automatically detected by the NF camera software. Peak position shifts are calculated relative to their positions at $I = 10\,\text{mA}$, with the sign convention defined according to the reference frame used in the NF plots.

Layer	κ ($\mathrm{Wm^{-1}{}^{\circ}C^{-1}}$)
Substrate	46
DBRs, active region, mesa (transverse)	15
DBRs, active region, mesa (longitudinal)	12
Passivation	0.5

Table 4.3 Thermal conductivity values for different sections of AlGaAs VCSELs.

the 3D drift-diffusion (DD) problem to an equivalent 2D one, expressed in cylindrical coordinates. Extending this approach to non-circular geometries, as the ones in Section 4.1, would require the solution of the full 3D problem, making the computation even more complex. To address this issue, in this subsection, we adopt a simplified approach [79] for computing the self-heating temperature profile in VCSELs, which is important for computing the modified refractive index profile.

Defining $T(\mathbf{r})$ as the VCSEL internal temperature, $\kappa(\mathbf{r})$ as the thermal conductivity and $Q(\mathbf{r})$ as the heat source, the heat equation reads:

$$\nabla \cdot (\kappa \nabla T) = -Q. \tag{4.1}$$

The latter can be solved numerically using either a finite element method (FEM), as done in this thesis, or the methodology described in [45, 85], relying on spectral elements for a faster computation. In both cases, we can apply a Dirichlet boundary condition at the bottom of the VCSEL substrate imposing a null temperature, so that T in (4.1) can be interpreted as a temperature rise with respect to the thermal reservoir. In other words, T directly represents the self-heating temperature profile. Typical values of κ for AlGaAs VCSELs are reported in Tab. 4.3 [79, 45].

On the other hand, Q is the sum of different contributions such as Joule heating, heating induced from recombination of carriers and heating derived from carrier thermalization in the QWs [45, 85]. In an effort to conduct an extensive simulation campaign on VCSELs with different geometries, we use and test a simplified heat source, based on the knowledge of LIV data. Indeed, we may consider a piece-wise

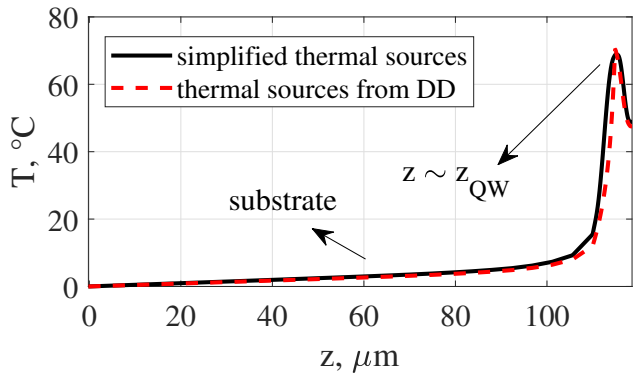

Fig. 4.10 Self-heating temperature profile along the longitudinal direction z for a conventional circular VCSEL using both the actual thermal sources from [45, 85] and the simplified source define in (4.2).

constant source, defined as

$$Q(\mathbf{r}) = \begin{cases} P_{\text{loss}}/V, & \mathbf{r} \in V, \\ 0, & \mathbf{r} \notin V, \end{cases} \tag{4.2}$$

where

$$P_{\text{loss}} = V_{\text{bias}} I_{\text{bias}} - P_{\text{opt}} \tag{4.3}$$

is the dissipated thermal power, $V_{\text{bias}} I_{\text{bias}}$ the input electrical power, P_{opt} the output optical power, while V is the volume associated with the constant source. The source is transversely defined by the oxide aperture and vertically placed at the QW section.

This simplified heat source model is first tested on the circular VCSEL described in [45, 85], showing that the self-heating temperature profile is well reproduced for a heat source thickness of $4\,\mu$m, as illustrated in Fig. 4.10. Similar results can be obtained even with different values of this parameter. Although not rigorous, this approach provides useful qualitative insight into the self-heating temperature distribution, which is crucial for evaluating thermal lensing.

For a more accurate description, the physics-based heat source distribution presented in [45, 85], obtained for cylindrical structures, can be fitted and adapted to devices with non-circular oxide apertures, although this goes beyond the scope of this work.

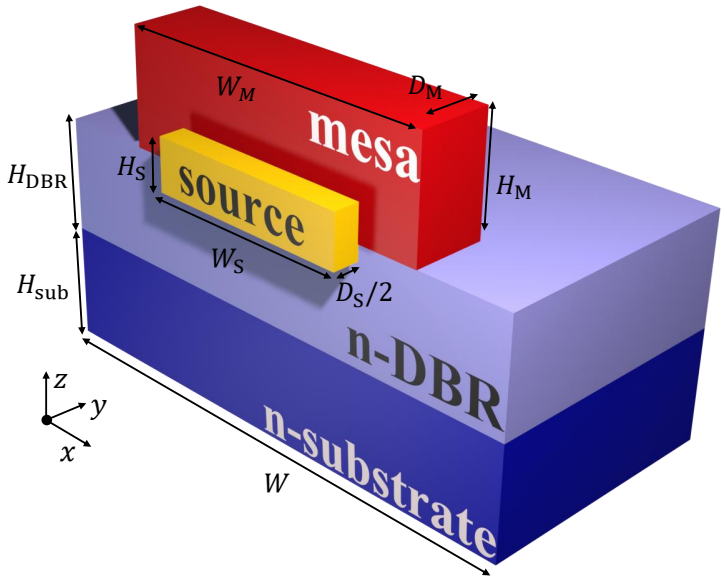

Fig. 4.11 Perspective view of the simulation domain and the simplified heat source, also indicating key geometrical parameters. The mesa is encapsulated within a passivation layer, which is not shown in the figure.

This simplified heat source can now be extended to rectangular structures, as the one reported in Fig. 4.11. In this subsection, the method is tested against three 850 nm rectangular VCSEL structures inspired by [15], since this work shows experimental emission spectra, which can be used to calibrate our thermal solver. Using the nomenclature defined in Fig. 4.11, we will consider for all structures $H_{\text{sub}} = 120\,\mu\text{m}$, $H_{\text{DBR}} = 6.7\,\mu\text{m}$, $H_{\text{M}} = 2\,\mu\text{m}$, $W_{\text{M}} = W_{\text{S}} + 20\,\mu\text{m}$, $D_{\text{M}} = D_{\text{S}} + 20\,\mu\text{m}$, with W_{S} and D_{S} representing the oxide aperture, and consequently the source size, for all the considered variants.

As a validation, the first case with $W_{\text{S}} = 125$ µm and $D_{\text{S}} = 5$ µm was simulated with substrate size $W = 240$ µm, obtaining a maximum temperature rise of $T_{\text{max}} \sim 85$ °C. Experimental spectral intensity data in [15] allow to cross-check the computed temperature profile.

From [15], at rollover $P_{\text{loss}} \sim 200$ mW, the wavelength shift is $\Delta\lambda \sim 5$ nm and the emission wavelength is $\lambda_{\text{e}} \sim 860$ nm. Knowing that the refractive index variation rate with temperature, $\text{d}n/\text{d}T$, is linked to the maximum self-heating temperature

rise $T_{\max}$ and wavelength shift according to [85] as

$$\frac{\mathrm{d}n}{\mathrm{d}T} = \frac{\bar{n}}{\lambda_{\mathrm{e}}} \frac{\Delta\lambda}{T_{\max}}, \tag{4.4}$$

where $\bar{n} = 3.25$ represent an effective index for AlGaAs VCSELs as stated in [85], we can infer a $\mathrm{d}n/\mathrm{d}T \sim 2 \times 10^{-4}\ (^{\circ}\mathrm{C})^{-1}$, in accordance with typical values for 850 nm VCSELs [45, 85], validating the soundness of the methodology.

The second and third investigated structures present lower aspect ratios [15], thus allowing a lower number of FEM mesh points and reducing the computational time. Specifically, a rectangular structure with $W_{\mathrm{S}} = 40$ µm and $D_{\mathrm{S}} = 10$ µm and a squared structure with $W_{\mathrm{S}} = D_{\mathrm{S}} = 20$ µm were simulated with substrate size $W = 140$ µm, resulting in an equal area of 400 µm^2. P_{loss} was set for the rectangular case to 135 mW in correspondence of the roll-over point at 66 mA, and 152 mW for the square case to keep the same current [15].

Results are reported in Fig. 4.12. The maximum temperature rise for the rectangular case is ~ 140 °C, lower than the square case at ~ 160 °C, confirming the experimental trends in [15], for which larger aspect ratios allow for better heat dissipation, thus pushing roll-over towards higher currents and justifying the need for elongated oxide apertures in high-power applications. The isothermal contour lines for these rectangular structures can be approximated by ellipses, whose corresponding semi-major and minor axes and ellipticity can be estimated as done in Fig. 4.12 (first column).

4.2.2 Design guidelines for single-mode emission in the presence of self-heating

Thermal simulations described in Subsection 4.2.1 can now be applied to our device under study for high-power SM emission, namely the 795 nm VCSEL described in Subsections 4.1.1–4.1.2 with a rectangular active area of $26 \times 6\,\mu\mathrm{m}^2$. In this case, the geometrical parameters employed for thermal simulations are reported in Tab. 4.4, using the nomenclature defined in Fig. 4.11. Using the thermal source in (4.2) with a dissipated power of $P_{\mathrm{loss}} = 5$ mW, chosen as a case study, we obtain the self-heating temperature profile reported in Fig. 4.13, featuring a maximum temperature rise of $T_{\max} = 10.1$ °C. Since the heat equation in (4.1) is linear, by changing P_{loss} the

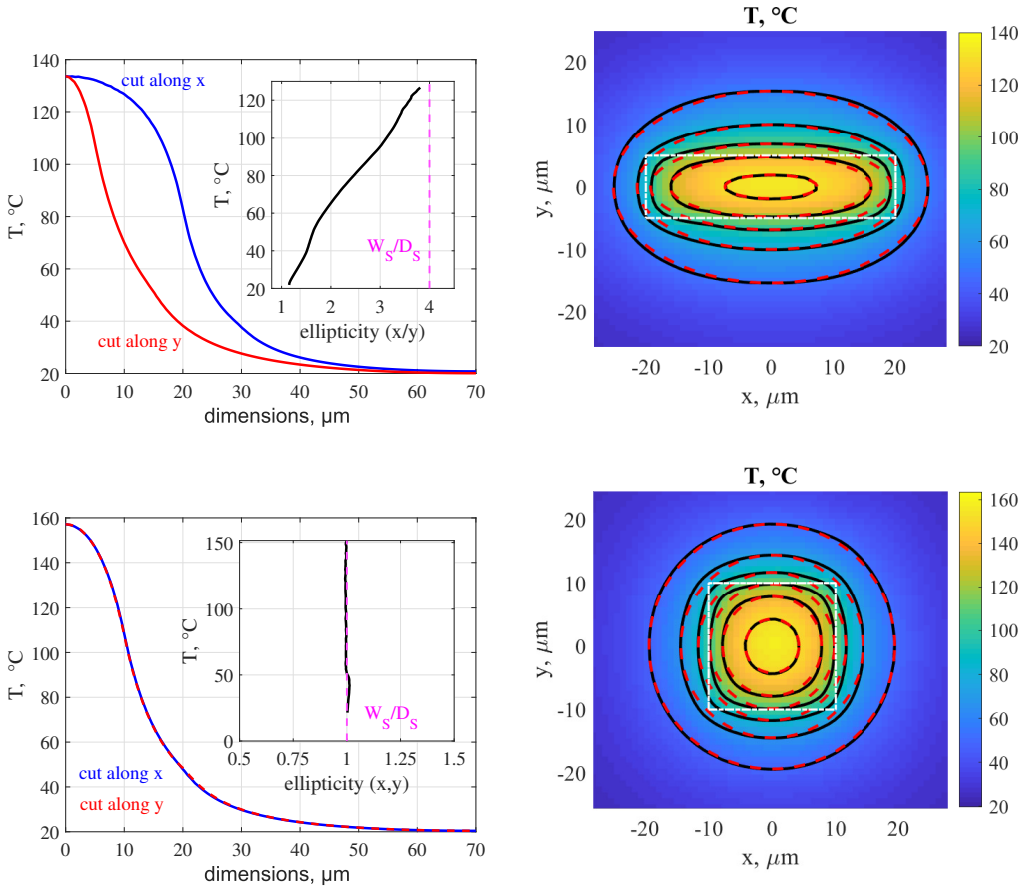

Fig. 4.12 Left column: self-heating temperature profile cuts at the QWs section along the x (blue) and y (red) directions. Insets represent the x-to-y ratios of such cuts, which can be interpreted as the ellipticity of isothermal contours. Magenta dashed lines represent the aspect ratio of the oxide aperture. Right column: color map and contour plot (black solid lines) of the self-heating temperature at the QWs section. Isothermal contour lines can be well approximated by ellipses (dashed red lines). White dashed lines represent the oxide aperture.

Dimension	Value
W	200 µm
H_{sub}	120 µm
W_S	26 µm
D_S	6 µm
H_S	0.5 µm
H_{DBR}	5.2 µm

Table 4.4 Geometrical parameters of the structure under investigation.

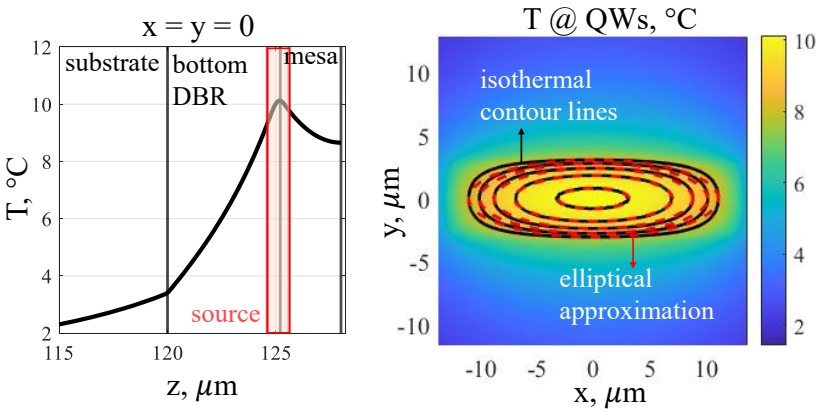

Fig. 4.13 Left: longitudinal self-heating temperature profile along the VCSEL symmetry axis. The different sections of the VCSEL are highlighted, from the substrate, to the bottom DBR and to the mesa. Red lines identify the region where the uniform simplified heat source is placed, in correspondence of the QW section. Right: transverse self-heating temperature profile at the QW section, highlighting how isothermal contour lines (black lines) can be well approximated by ellipses (dashed red lines).

corresponding temperature profile is only modified by a multiplicative factor, with the peak self-heating temperature that can be calculated as:

$$T_{\max} = \eta_{P\to T} P_{\text{loss}}, \tag{4.5}$$

where $\eta_{P\to T}$ represents a conversion factor, obtainable as $\eta_{P\to T} = 10.1°\text{C}/(5\,\text{mW}) \sim 2$ °C/mW.

Using (4.5) and the spatial profile reported in Fig. 4.13 we can modify the VCSEL refractive index and run optical simulations for any given P_{loss}, thus we can understand how optical modes are affected by increasing self-heating. To do so, let us recall that $T(\mathbf{r})$ represents the temperature rise with respect to the bottom of the VCSEL substrate, which can be set at the heat sink temperature T_{HS}. As a consequence, the absolute temperature profile reads:

$$T_{\text{tot}}(\mathbf{r}) = T_{\text{HS}} + T(\mathbf{r}). \tag{4.6}$$

The dependence of the VCSEL refractive index n on temperature can be linearized around T_{HS} [85] as:

$$n(T_{\text{tot}}) = n_{\text{HS}} + \frac{\mathrm{d}n}{\mathrm{d}T} T, \tag{4.7}$$

where $n_{\text{HS}} = n(T_{HS})$ and $\mathrm{d}n/\mathrm{d}T \sim 2\times 10^{-4}\,(°\text{C})^{-1}$, as discussed in Subsection 4.2.1. The refractive index variation can be converted into a the dielectric constant variation, needed for the calculation of the coupling operators, as:

$$\varepsilon = \varepsilon_0 \left(n_{\text{HS}} + \frac{\mathrm{d}n}{\mathrm{d}T} T \right)^2 \sim \varepsilon_{\text{HS}} + 2\varepsilon_0 n_{\text{HS}} \frac{\mathrm{d}n}{\mathrm{d}T} T, \tag{4.8}$$

where $\varepsilon_{\text{HS}} = \varepsilon_0 n_{\text{HS}}^2$ and the quadratic term in T is neglected as it represents a second order variation. This profile can now be plugged into the expressions in Fig. 2.6 to eventually determine the effect of temperature on the optical modes.

Starting with the rectangular VCSEL without any form of modal control, producing the modes reported in Fig. 4.1, we can see how the fundamental mode $(0,0)$ and the targeted mode $(4,0)$ evolve when applying a certain dissipated power. Results are shown in Fig. 4.14. One can notice how the effect of self-heating on the fundamental mode simply causes a shrinkage towards the middle part of the active area due to the thermal lensing. On the other hand, the effect on the superior mode $(4,0)$ is more

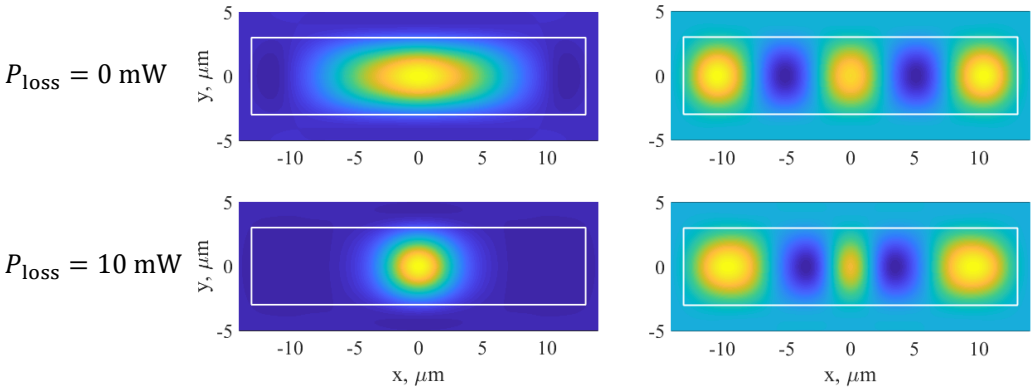

Fig. 4.14 Effect of self-heating on both the fundamental mode $(0,0)$ and the targeted mode $(4,0)$ (NF profiles).

complex, showing how the various NF peaks get distorted, varying both in shape and relative intensity.

A parametric investigation of this effect is presented in Fig. 4.15. Identifying the central peak and the two peaks on the right of mode $(4,0)$ as peaks 0, 1, and 2, respectively,[4] the plot on the left illustrates how the positions of peaks 1 and 2 evolve with the applied dissipated power. The position of peak 0 is not reported, as the problem is symmetrical and it always remains at the center of the active area. As expected, the field is compressed towards the center of the active area due to thermal lensing, yielding a reduction of positions of peaks 1 and 2, qualitatively confirming the experimental evidence in Fig. 4.9 (top left).

Conversely, the plot on the right shows how the peak intensity of peaks 0 and 1 varies with increasing dissipated power. Peak intensities are normalized with respect to the brightest peak, *i.e.*, peak 2. The results qualitatively agree with the experimental data in both Fig. 4.5 and Fig. 4.9, demonstrating that our combined thermal and optical model effectively captures the behavior of higher-order modes at different bias currents. Consequently, this model can be utilized to provide design guidelines when thermal lensing is considered. The transverse shape of a grating relief array equivalent to design B described in Subsection 4.1.2 can be optimized to have SM emission at low and high thermal lensing regime.

[4]The structure and the self-heating temperature profile are assumed to be entirely symmetrical, so that an equivalent behavior is expected for the peaks on the left.

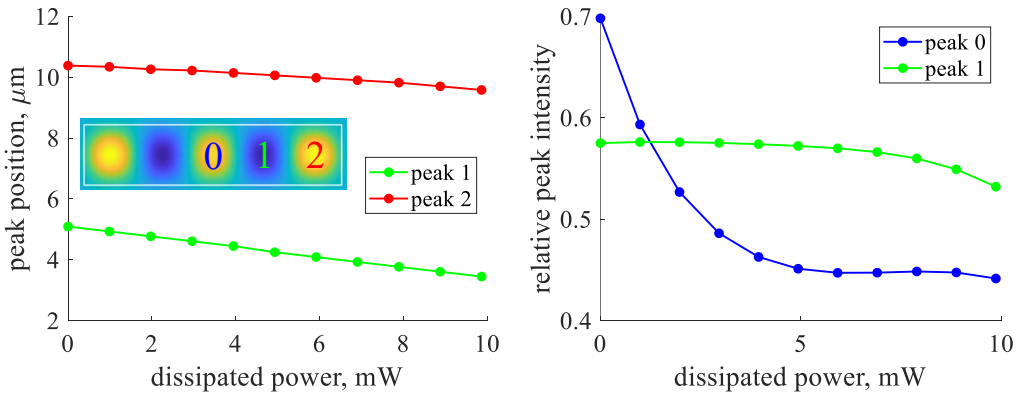

Fig. 4.15 Identifying the central peak and the peaks on the right of the active area as peaks 0, 1 and 2, respectively, the peak positions of peaks 1 and 2 (left) and the peak intensity of peaks 0 and 1, normalized with respect to peak 2 (right), are reported.

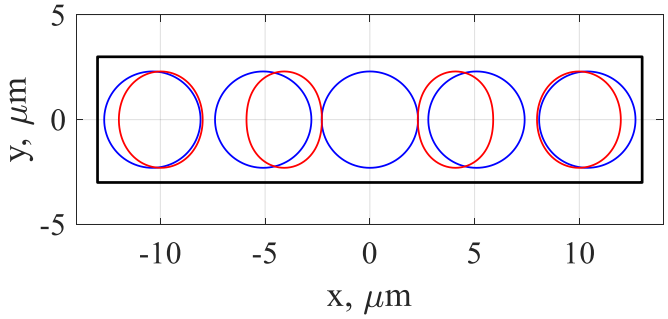

Fig. 4.16 Grating relief array design for low self-heating (blue), obtained through Fig. 4.15 using $P_{\text{loss}} = 0$, ad for high self-heating (ref), obtained through Fig. 4.15 using $P_{\text{loss}} = 5.9$ mW.

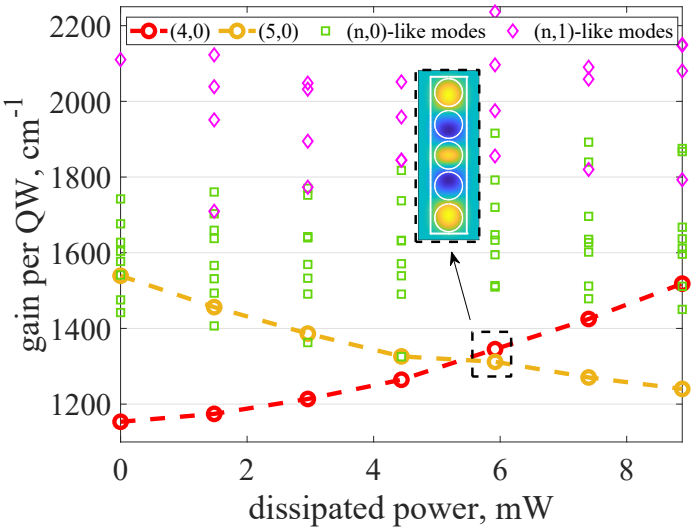

Fig. 4.17 Threshold gain of the transverse modes of the VCSEL featuring the low self-heating grating relief array design described in Fig. 4.16. The legend highlights the targeted mode $(4,0)$ and its competitor for higher dissipated powers, *i.e.*, mode $(5,0)$. All the other modes featuring either zero nodes or one node along the short direction of the active area are reported as $(n,0)$-like and $(n,1)$-like modes, respectively. $(n,1)$-like modes feature higher thresholds than $(n,0)$-like modes. The inset represents the $(4,0)$ modal field profile at the QW section together with the low self-heating relief design, highlighting a significant misalignment between reliefs and the field spots. In this plot, only the dominant polarization selected by the grating is reported.

This can be done analyzing the results in Fig. 4.15. Once a certain dissipated power is selected, reliefs should be aligned with the peak positions which can be determined using the left graph of 4.15. Similarly, the transverse area associated to the reliefs is influenced by the relative importance of the peaks. For instance, at high self-heating, the middle peak 0 becomes weak with respect to the others. Furthermore, from Fig. 4.14, one can notice how the fundamental mode is able to squeeze in a very narrow portion of the active area due to thermal lensing. Combining this information, one can infer that the central relief should be much smaller than the others for high self-heating regimes, or even absent, to avoid the involuntary selection of mode $(0,0)$. A possible design for low self-heating, *i.e.*, $P_{\text{loss}} = 0$ mW, is reported as the blue curve of Fig. 4.16.

The low self-heating design is tested in terms of modal threshold of all transverse modes supported by the VCSEL as a function of the dissipated power in Fig. 4.17, proving how mode $(4,0)$ is effectively selected for low values of P_{loss}. Efficient modal discrimination is lost at around $P_{\text{loss}} = 5.9$ mW, where the mode $(5,0)$ features

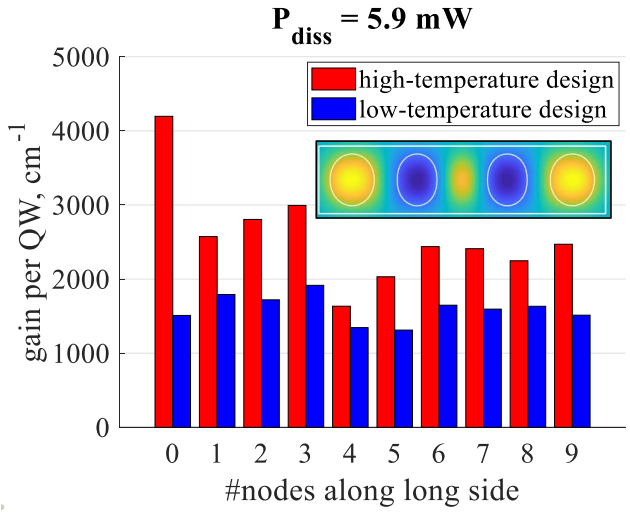

Fig. 4.18 Comparison between low and high self-heating designs at $P_{\text{loss}} = 5.9$ mW in terms of modal thresholds of modes $(0,0)$, $(1,0)$, …, $(9,0)$. The inset represents the $(4,0)$ mode of the high self-heating design at the QW section, displaying how well the field peaks align with the reliefs.

a similar threshold gain with respect to mode $(4,0)$. At higher dissipated powers, mode $(5,0)$ is selected instead of our targeted mode $(4,0)$. The inset at $P_{\text{loss}} = 5.9$ mW represents the targeted mode at the QW section, showing how the misalignment between the field spots and the reliefs become significant.

Aiming to maintain SM emission of mode $(4,0)$, a high self-heating design, obtained through Fig. 4.15 at $P_{\text{loss}} = 5.9$ mW, *i.e.* the power at which the low self-heating design loses its modal discrimination capabilities, is tested at exactly that dissipated power[5]. Its performances in terms of modal thresholds for all transverse modes are compared to the low self-heating design in Fig. 4.18, showing how the high self-heating design is able to retrieve a good enough modal discrimination to select mode $(4,0)$, also showcasing how the latter perfectly aligns with the new relief design. As a final remark, one can notice how the threshold of the fundamental mode $(0,0)$ is extremely high for the high self-heating design. This is due to the absence of the central relief, which, if present, would have dramatically lowered the

[5]The dissipated power range in both Fig 4.15 and Fig. 4.17 represents a case study. Indeed, the dissipated power in high-power VCSELs can also reach much higher values than 10 mW, depending on the active area of the rectangle itself. Of course, the longer the rectangle is, the more the intensity peaks will drift with self-heating temperature, making the overall relief design more challenging.

$(0,0)$ modal threshold, possibly competing with the targeted mode $(4,0)$, overall worsening the modal discrimination properties.

Chapter 5

Circularly polarized VCSELs

Part of the content of this chapter was published by our group in [37, 86, 87].

Chip-scale atomic devices, such as atomic clocks, quantum gyroscopes, and atomic magnetometers, require circularly polarized (CP) light for atomic pumping, which is essential for light-matter interaction [27]. The conventional non-monolithic approach to generate CP light relies on linearly polarized emitters, like the ones described in Chapter 4, followed by a quarter-wave plate, which can be bulky and hinders the miniaturization of such devices. In this chapter, we aim to develop emitters capable of directly generating elliptically polarized and CP light.

The dispute about the polarization state of the coherent light emitted by VCSELs dates back to their very origin. Due to their cylindrical rotational symmetry [88, 89] and their in-plane QW isotropic gain, an undetermined polarization was firstly expected. However, it has been recognized that several mechanisms break this rotational symmetry. The intrinsic semiconductor electro- and elasto-optic anisotropies [40] eventually lead to a linear polarization operation, although with a huge variety of dynamics and polarization switching instabilities [90–95]. The polarization issues are fully detrimental, especially for sensing applications. For that reason, many efforts finally resulted in a simple and effective technique to achieve polarization-stable VCSEL operation, *i.e.*, surface gratings aligned to the VCSEL crystalline axes, first proposed in [41] and soon after demonstrated by experimental and technological results [74, 75]. Since then, gratings have become the standard way of fixing VCSELs' polarization, with improved performance introduced by subwavelength gratings (SWGs) [96]. The latter eliminate any diffraction loss and

are today one of the most used technologies for stabilizing VCSELs' polarization. A suitable alternative is also represented by high-contrast gratings (HCG) [97] and high-contrast metastructures (HCM) [98, 99], which allow to replace part of the VCSEL DBRs with either a grating or a two-dimensional metastructure, which strongly contributes to the mirror reflectivity, achieving both polarization control and thinning of the device.

Besides chip-scale atomic devices [27], CP has recently become an enabling feature in many advanced quantum photonic applications [100], such as information storage and processing [36, 101, 102], communication by spin modulation [103], ellipsometry-based tomography [104, 105] or chirality-based microscopy [106], targeting an improved resolution in the biological chiral environments. In this context, various approaches have been explored to achieve well-controlled CP emission from VCSELs through a compact monolithic solution [107]. One possible approach is to inject spin-polarized electrons thus converting the electron spin into CP photons. This can be done either by applying spintronic contacts, which is still a difficult technology, or by optically pumping the VCSEL with a CP laser [108]. The latter approach is once again bulky and against the reasons VCSELs are used: small size and electrical injection.

To the best of our knowledge, two different compact solutions have been proposed so far, both based on introducing one single chiral component in the resonator. Namely, either a cholesteric liquid crystal [109–112, 31, 113] or a chiral metamaterial layer [36, 32]. In 2023, this approach was deployed in [34], with a novelty compared to previous implementations: the chiral structure also contributes to the reflectivity of the top mirror.

All the previous techniques present some drawbacks. The use of liquid crystals requires non-standard and non-monolithic technologies, which resulted in successful experimental validation only in a few cases [111, 112]. Similarly, the growth of chiral structures also requires non-standard VCSEL processes, not always ensuring the desired performance in terms of the degree of CP, for instance around 40% and 60% in [34].

Here we follow a different approach, investigating the condition that the resonator must fulfill in order to emit any given polarization state. The resonator chirality plays a key role [114, 115] here. The difference between previous approaches and ours lies in the fact that we move the focus from the chirality of a single component (for

instance a liquid crystal [31] or a high-contrast chiral patterned layer [34]) to the three-dimensional chirality of the whole resonator. This is achieved by considering anisotropic layers that are non-chiral when considered singularly but make the overall resonator chiral when their anisotropic axes are tilted against each other and interact via within the resonator roundtrip loop.

Having addressed the issue of single transverse mode selection in Chapter 4, in this chapter we analyze VCSELs featuring a single transverse mode, solely focusing on polarization properties. Before tackling the problem using our 1D vectorial analysis described in Section 3.2, we aim at understanding the basic working principle of resonator chirality. To do so, we generalize the Barkhousen criterion [7] to the vectorial case and we apply this model to a case study. Then, we analyze a real VCSEL structure, focusing on strategies aimed at optimizing its degree of CP and validating our modeling against experimental Stokes parameters.

5.1 Vectorial Barkhausen criterion and polarization equation

5.1.1 Description of polarization with a unique complex number and its representation on the Poincaré sphere

Considering normal incidence and recalling that we have defined z as the longitudinal propagation direction, the electric field phasor is contained entirely in the transverse plane, reading:

$$\mathbf{E} = E_x\hat{x} + E_y\hat{y} \in \mathbb{C}^2. \tag{5.1}$$

We can see how the electric field phasor is linked to the trajectory that the electric field $\mathscr{E}(t)$ follows in time domain, oscillating at the optical frequency ω, recalling their relation, *i.e.*,

$$\begin{aligned}\mathscr{E}(t) &= \Re\left\{\mathbf{E}e^{j\omega t}\right\} = \Re\left\{\left(E_x\hat{x} + E_y\hat{y}\right)e^{j\omega t}\right\} = \\ &= \Re\left\{\left(\hat{x}|E_x|e^{j\angle E_x} + \hat{y}|E_y|e^{j\angle E_y}\right)e^{j\omega t}\right\} \in \mathbb{R}^2.\end{aligned} \tag{5.2}$$

This trajectory determines the polarization of the considered field. Collecting E_y we obtain:

$$\begin{aligned}
&\mathscr{E}(t) = \Re\left\{|E_y|e^{j\angle E_y}\left[\frac{|E_x|}{|E_y|}e^{j(\angle E_x-\angle E_y)}\hat{x}+\hat{y}\right]e^{j\omega t}\right\} = \\
&= \Re\left\{|E_y|\left[\frac{|E_x|}{|E_y|}e^{j(\angle E_x-\angle E_y)}\hat{x}+\hat{y}\right]e^{j(\omega t+\angle E_y)}\right\} = \\
&= |E_y|\left\{\frac{|E_x|}{|E_y|}\cos\left[\omega t+\angle E_y+(\angle E_x-\angle E_y)\right]\hat{x}+\cos\left(\omega t+\angle E_y\right)\hat{y}\right\}. \qquad (5.3)
\end{aligned}$$

From (5.3) it can be seen how $\mathscr{E}:\mathbb{R}\to\mathbb{R}^2$ represents the parametrization of an ellipse in the real 2D plane. Such an ellipse completely determines the polarization properties and the optical power of the light. If we are not interested in quantifying the optical power, we can eliminate the multiplicative constant $|E_y|$ in front, which is the case for modal calculations, where fields are identified up to a multiplicative constant. From a geometrical standpoint, eliminating $|E_y|$ means that we do not care about the area of the ellipse, which would of course be scaled by $|E_y|$. Furthermore, we can notice how the image of $\mathscr{E}$ in the 2D real plane, *i.e.*, the actual elliptical shape, is independent on the constant phase shift $\angle E_y$, present in both cosines, which in turn can be eliminated since it does not affect polarization. Under these assumptions, (5.3) can be simplified as:

$$\mathscr{E}(t) = \frac{|E_x|}{|E_y|}\cos\left[\omega t+(\angle E_x-\angle E_y)\right]\hat{x}+\cos(\omega t)\hat{y}. \qquad (5.4)$$

Going back to the frequency domain, the electric field phasor can be simplified as well as the red term in (5.3), obtaining:

$$\mathbf{E} = \chi\hat{x}+\hat{y}, \qquad (5.5)$$

where we have defined the complex polarization index χ as:

$$\chi = \frac{E_x}{E_y}\in\mathbb{C}, \qquad (5.6)$$

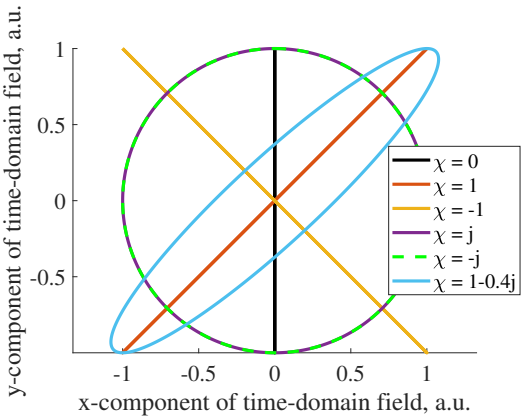

Fig. 5.1 Polarization ellipses according to (5.7) for different values of the complex polarization index χ. $\chi = 0$ corresponds to linear polarization along y, $\chi = \pm 1$ to linearly polarized light at $\pm 45°$, $\chi = \pm j$ to circularly polarized light and any other value to elliptically polarized light.

which completely determines the polarization state of the light[1]. Using (5.6), (5.4) can be rewritten as:

$$\mathscr{E}(t) = |\chi| \cos(\omega t + \angle\chi)\hat{x} + \cos(\omega t)\hat{y}. \tag{5.7}$$

The image of (5.7) for different values of χ is reported in Fig. 5.1.

In the literature, the light polarization state is generally characterized by the Stokes parameters [116–120], which can be defined as a function of the electric field phasor $\mathbf{E}$ as[2]:

$$S_0 = |E_x|^2 + |E_y|^2 > 0, \tag{5.8}$$

$$S_1 = \frac{|E_x|^2 - |E_y|^2}{S_0} \in [-1, 1], \tag{5.9}$$

$$S_2 = \frac{+2\Re\{E_y^* E_x\}}{S_0} \in [-1, 1], \tag{5.10}$$

$$S_3 = \frac{-2\Im\{E_y^* E_x\}}{S_0} \in [-1, 1]. \tag{5.11}$$

[1]Please notice that in this way it is not possible to describe linearly polarized light along x, since the coefficient of $\hat{y}$ is always 1 independently on the value of χ. This comes from the fact that in (5.3) we have arbitrarily collected E_y. Had we chosen to collect E_x we would end up with an equivalent situation, with the impossibility to represent perfectly linearly polarized light along y. This is not an issue, since the missing polarization states are represented asymptotically, for $|\chi| \to \infty$.

[2]In this work, we choose to define a normalized version of S_1, S_2 and S_3.

S_0 describes the optical power, while the upper and lower bounds of S_1, S_2 and S_3 have precise meanings:

- $S_1 = \pm 1$ describes light linearly polarized along either $\hat{x}$ or $\hat{y}$. Let us perform a consistency check with respect to our description in terms of χ. Considering (5.7), in order to have linearly polarized light along $\hat{y}$, we must have $\chi = 0$ (see Fig. 5.1), so that $\mathbf{E} = \hat{y}$. Using (5.8) and (5.9), we can calculate $S_1 = -1$, as expected, confirming the consistency between the two representations.
- $S_2 = \pm 1$ describes light linearly polarized along $\dfrac{\hat{x} \pm \hat{y}}{\sqrt{2}}$. A similar consistency check can be performed by selecting $\chi = \pm 1$, *i.e.*, $|\chi| = 1$ and $\angle\chi \in \{0, \pi\}$ (see Fig. 5.1).
- $S_3 = \pm 1$ describes circularly polarized light rotating either clockwise or counterclockwise. In our description, circular polarization requires $|\chi| = 1$ and $\angle\chi = \pm\pi/2$, *i.e.*, $\chi = \pm j$ (see Fig. 5.1). Assuming, for instance, $\chi = j$, we obtain:
$$S_3 = \frac{-2\Im\{j\}}{1+1} = -1,$$
which is consistent. Conversely, choosing $\chi = -j$ yields $S_3 = +1$.

The three Stokes parameters S_1, S_2 and S_3 are not independent, indeed, using their definition, we can evaluate:

$$S_1^2 + S_2^2 + S_3^2 = \frac{|E_x|^4 + |E_y|^4 - 2|E_x|^2|E_y|^2 + 4\Re\{E_y^* E_x\}^2 + 4\Im\{E_y^* E_x\}^2}{|E_x|^4 + |E_y|^4 + 2|E_x|^2|E_y|^2}. \quad (5.12)$$

Defining $\Delta = \angle E_x - \angle E_y$, we can calculate:

$$E_y^* E_x = |E_y| e^{-j\angle E_y} |E_x| e^{j\angle E_x} = |E_x||E_y| e^{j\Delta}, \quad (5.13)$$

from which

$$\Re\{E_y^* E_x\}^2 = |E_x|^2 |E_y|^2 \cos^2(\Delta), \quad (5.14)$$

$$\Im\{E_y^* E_x\}^2 = |E_x|^2 |E_y|^2 \sin^2(\Delta). \quad (5.15)$$

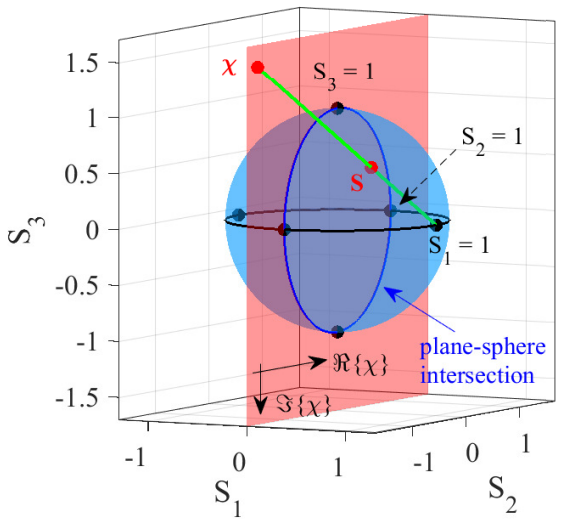

Fig. 5.2 Depiction of the stereographic projection of a point **S** of the Poincaré sphere (in blue) onto the complex χ plane for the representation of the polarization state (in red) and vice-versa. The case S_1=1, namely linear polarization along the x axis, can be only reached asymptotically for $|\chi| \to \infty$.

Substituting (5.14)–(5.15) into (5.12), we end up with:

$$\begin{aligned} & S_1^2 + S_2^2 + S_3^2 = \\ & = \frac{|E_x|^4 + |E_y|^4 - 2|E_x|^2|E_y|^2 + 4|E_x|^2|E_y|^2\cos^2(\Delta) + 4|E_x|^2|E_y|^2\sin^2(\Delta)}{|E_x|^4 + |E_y|^4 + 2|E_x|^2|E_y|^2} = \\ & = \frac{|E_x|^4 + |E_y|^4 - 2|E_x|^2|E_y|^2 + 4|E_x|^2|E_y|^2}{|E_x|^4 + |E_y|^4 + 2|E_x|^2|E_y|^2} = 1, \end{aligned} \tag{5.16}$$

yielding that the Stokes vector,

$$\mathbf{S} = \begin{bmatrix} S_1 \\ S_2 \\ S_3 \end{bmatrix}, \tag{5.17}$$

is a unitary vector which can be interpreted as a point of the unitary sphere $\mathbb{S}^2$, representing in this instance all possible light polarization states. Such a sphere is called the Poincaré sphere, where the equator ($S_3 = 0$, $S_1^2 + S_2^2 = 1$) represents linearly polarized light, the poles circularly polarized light ($S_3 = \pm 1$, $S_1 = S_2 = 0$), and all other points elliptically polarized light.

We have now seen how $\mathbf{S} \in \mathbb{S}^2$ and $\chi \in \mathbb{C}$ have the same number of degrees of freedom, *i.e.*, 2, however to explicitly understand their connection we must compute the Stokes parameters in (5.8)–(5.9)–(5.10)–(5.11) using the expression of the electric field phasor described in (5.5), yielding:

$$S_0 = |\chi|^2 + 1, \tag{5.18}$$

$$S_1 = \frac{|\chi|^2 - 1}{S_0}, \tag{5.19}$$

$$S_2 = \frac{+2\Re\{\chi\}}{S_0}, \tag{5.20}$$

$$S_3 = \frac{-2\Im\{\chi\}}{S_0}. \tag{5.21}$$

The latter equations (5.19)–(5.20)–(5.21) can be interpreted as a chart to go from the description of the polarization in the complex plane, relying the polarization index χ, to the description of the polarization onto the Poincaré sphere, relying on the Stokes vector $\mathbf{S}$. This transformation can be interpreted as a stereographic projection between the complex plane and the Poincaré sphere [121], which is visually represented in Fig. 5.2.

Practically speaking, one can imagine to place the Poincaré sphere at the origin of a 3D polarization space described the axes S_1, S_2 and S_3. Furthermore, one can identify the plane $S_1 = 0$ as the complex plane spanned by χ, where the axis $\Re\{\chi\}$ is oriented as the axis S_2, while the axis $\Im\{\chi\}$ is oriented as $-S_3$. At this point, if we select a specific χ on this plane, the corresponding $\mathbf{S}$ can be obtained as the intersection between the line connecting χ to the point $(1,0,0)$ and the Poincaré sphere itself. A similar procedure can be followed if one starts with a specifc $\mathbf{S}$ on the sphere to obtain the corresponding χ on the plane. Similar considerations for qubit states were done in [122].

Both representations are valid, however, we will see in the following how the polarization index χ is extremely useful to generalize the Barkhausen condition for a laser to the vectorial case and to obtain a simple method which provides threshold gain, emission wavelength and polarization states of the modes supported by a resonator. To do so, the polarization must be expressed in terms of χ, which can then be converted into $\mathbf{S}$ according to Fig. 5.2.

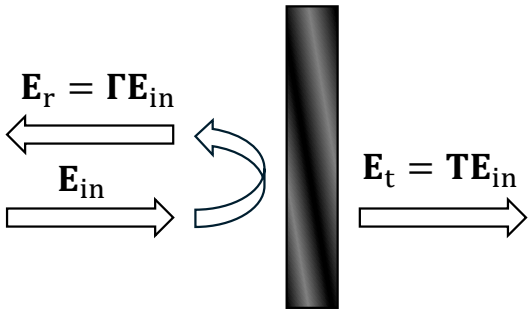

Fig. 5.3 Sketch of the relevant quantities when considering and input 2D electric field phasor impinging on a mirror, *e.g.*, one of the DBRs of a VCSEL.

5.1.2 Vectorial Barkhausen criterion: mirror and cavity chirality

If an input electric field phasor $\mathbf{E}_\mathrm{in} \in \mathbb{C}^2$ impinges on a mirror, which in general could be anisotropic or chiral as in the case of [34], with reflection and transmission matrices $\boldsymbol{\Gamma} \in \mathbb{C}^{2\times 2}$ and $\mathbf{T} \in \mathbb{C}^{2\times 2}$, it will produce a reflected and a transmitted electric field phasor, $\mathbf{E}_\mathrm{r}$ and $\mathbf{E}_\mathrm{t} \in \mathbb{C}^2$, respectively. The relations between $\mathbf{E}_\mathrm{in}$, $\mathbf{E}_\mathrm{r}$, $\mathbf{E}_\mathrm{t}$, $\boldsymbol{\Gamma}$ and $\mathbf{T}$ read:

$$\mathbf{E}_\mathrm{r} = \boldsymbol{\Gamma}\mathbf{E}_\mathrm{in}, \tag{5.22}$$

$$\mathbf{E}_\mathrm{t} = \mathbf{T}\mathbf{E}_\mathrm{in}, \tag{5.23}$$

and illustrated in Fig. 5.3. Notice how $\boldsymbol{\Gamma}$ and $\mathbf{T}$ represent a generalization of the scalar reflection and transmission coefficients of a standard isotropic mirror, that can be obtained using the coupled mode theory formulation from the scattering matrix defined in (3.22).

At this point, we can formally define the concept of chirality for a complex 2×2 matrix. Said matrix is said to be *non-chiral* if it can be diagonalized by means of real eigenvectors, defined up to a global complex multiplicative constant, reflected in the same phase factor for all the components of the eigenvectors. Conversely, a matrix is considered *chiral* if its diagonalization requires eigenvectors whose components have different phases, so that each eigenvector is always inherently complex independently of the arbitrary normalization constant.

In other words, a matrix is chiral if no real-space reference frame can render it diagonal, meaning that an inherently complex basis is necessary to express it in diagonal form. This definition is particularly useful in distinguishing between mirror chirality and resonator chirality, which are fundamentally different concepts.

A mirror can be described as chiral if its reflection matrix $\mathbf{\Gamma}$ exhibits chirality according to the aforementioned definition, which is the case of the top DBR in [34]. Geometrically, this is the same as the more common definition by which a 2D object and its reflection are not superimposable.

Moving on to resonators, consider an active optical cavity of thickness L_a, which can a field gain g_{field} and has a certain refractive index n[3]. The latter is embedded within two anisotropic mirrors on its left and right, described by their 2×2 reflection matrices $\mathbf{\Gamma}_l$ and $\mathbf{\Gamma}_r$. Consider and electric field phasor $\mathbf{E}$ in the cavity that is propagating towards to left, right before interacting with the left mirror. The field will:

1. be reflected off the left mirror,
2. propagate along the cavity towards the right,
3. be reflected off the right mirror,
4. propagate along the cavity towards the left, eventually reaching its starting position, completing a round trip.

Considering an optical wavelength λ and the corresponding propagation constant in the cavity, *i.e.*,

$$k = \frac{2\pi}{\lambda} n, \tag{5.24}$$

after a propagation in the cavity the field is multiplied by the scalar factor[4]:

$$P_{1/2} = e^{(g_{\text{field}} + jk)L_a}. \tag{5.25}$$

In order to have sustainable oscillations in the cavity, the field after a round trip must be equal to the field at the starting point. To obtain the field after a round trip, one must multiply the initial field $\mathbf{E}$ by the reflection matrix on the left $\mathbf{\Gamma}_l$, a

[3]Here we are considering the very general case of an active layer, called cavity, which can provide gain, embedded by two mirrors. In this view, when considering VCSELs, the part that provides the gain is the AR only, since the VCSEL cavity is much thicker. Everything that is not the AR must be included in the mirrors, thus they must include both the DBRs and parts of the VCSEL cavity other than the AR.

[4]If one were to consider the most general case of anisotropic gain, then a 2×2 matrix cavity propagator should be considered instead of the scalar factor in (5.25). This matrix is diagonal when expressed using the principal axes of the cavity, X and Y, as the reference frame. Along these axes one must consider two distinct gain values, g_X and g_Y. This is not the case of AlGaAs VCSELs.

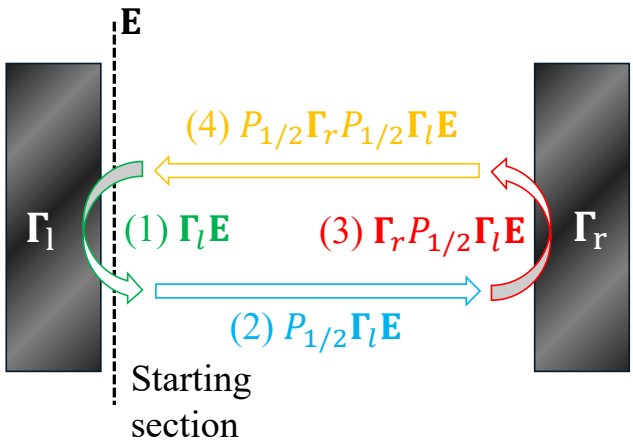

Fig. 5.4 Sketch of the vectorial Barkhause criterion, indicating how the electric field phasor evolves during the different phases of a round trip.

propagation factor throughout the cavity $P_{1/2}$, the reflection matrix and on the right $\mathbf{\Gamma}_r$ and again a propagation throughout the cavity $P_{1/2}$. This multiplication chains must be performed in this specific order, accounting for the fact that $\mathbf{\Gamma}_l$ and $\mathbf{\Gamma}_r$ are non-commuting matrices. Defining the round trip propagation factor as:

$$P = P_{1/2}^2 = e^{(g+2jk)L_a}, \tag{5.26}$$

where

$$g = 2g_{\text{field}}, \tag{5.27}$$

represents the power gain, the 2×2 vectorial Barkhausen round trip condition reads:

$$P\mathbf{\Gamma}_r\mathbf{\Gamma}_l\mathbf{E} = \mathbf{E}, \tag{5.28}$$

containing information regarding the modes ($\mathbf{E}$) supported by the cavity, determining the allowed polarizations, and the emission wavelength and threshold gain of the modes, contained in P. A sketch is reported in Fig. 5.4.

Defining the roto-reflection matrix $\mathbf{D}$ as:

$$\mathbf{D} = \mathbf{\Gamma}_r\mathbf{\Gamma}_l, \tag{5.29}$$

we can rewrite (5.28) as:

$$(P\mathbf{D} - \mathbf{I})\,\mathbf{E} = \mathbf{0}. \tag{5.30}$$

Notice how $P = P(\lambda, g)$ due to (5.26) and $\mathbf{D} = \mathbf{D}(\lambda)$ due to mirror dispersion. The unknowns in (5.30) are λ, g and $\mathbf{E}$, which can be determined with the following steps:

1. define the field generator matrix:

$$\mathbf{H} = P\mathbf{D} - \mathbf{I}, \tag{5.31}$$

   noticing how $\mathbf{H} = \mathbf{H}(\lambda, g)$;

2. scan the (λ, g) plane to determine the points $(\lambda_{\text{th}}, g_{\text{th}})$ for which $\det \mathbf{H} \neq 0$, implying a non-trivial solution of (5.30). The $(\lambda_{\text{th}}, g_{\text{th}})$ points represent the modal emission wavelengths and modal threshold gains of the resonator;

3. for each solution $(\lambda_{\text{th}}, g_{\text{th}})$, the associated electric field phasors are the ones belonging to $\ker \mathbf{H}(\lambda_{\text{th}}, g_{\text{th}})$.

From the latter point, one can see how a phasor which supports elliptical polarization can only be obtained for a chiral $\mathbf{H}$, implying in turn a chiral $\mathbf{D}$. In other words, the matrix that determines the chirality of the resonator is $\mathbf{D}$. A chiral $\mathbf{D}$ can result in elliptical polarization even if the mirrors are not chiral separately, which is the concept exploited in [37].

5.1.3 Polarization equation for dispersiveless mirrors

The procedure described in the previous subsection to solve the vectorial Barkhausen criterion expressed in (5.30) can only be carried out numerically. However, at this point, one could have directly employed a one-dimensional vectorial analysis, such as the one described in Section 3.2, which also provides access to a greater amount of information, including the longitudinal distribution of the phasors of the electric field. Therefore, in its current form, the vectorial Barkhausen criterion does not add new information and does not contribute to a better understanding of the physics of the polarizations supported by a resonator.

However, if we consider dispersiveless mirrors, *i.e.*, mirrors whose reflection and transmission matrices are independent of the optical wavelength, the vectorial Barkhausen criterion can be significantly simplified. This is particularly relevant for

VCSELs, as DBRs exhibit minimal dispersion, as shown in Fig. 3.3. The reflectivity profile remains remarkably flat over a spectral range of several tens of nanometers around the target wavelength. In contrast, the modal emission wavelengths vary by only about fractions of nanometers around the target wavelength as shown in Fig. 2.10, further confirming the negligible dispersion of DBRs.

Expressing the electric field phasor as a function of the polarization index χ, as done in (5.5), we can rewrite the vectorial Barkhausen criterion in (5.30) as:

$$P \begin{bmatrix} D_{11} & D_{12} \\ D_{21} & D_{22} \end{bmatrix} \begin{bmatrix} \chi \\ 1 \end{bmatrix} = \begin{bmatrix} \chi \\ 1 \end{bmatrix}, \tag{5.32}$$

resulting in

$$\begin{cases} PD_{11}\chi + PD_{12} = \chi \\ PD_{21}\chi + PD_{22} = 1 \end{cases}. \tag{5.33}$$

Multiplying the second equation by χ we get:

$$\begin{cases} PD_{11}\chi + PD_{12} = \chi \\ PD_{21}\chi^2 + PD_{22}\chi = \chi \end{cases} \tag{5.34}$$

and, equating the left-hand sides of both equations, we obtain:

$$PD_{11}\chi + PD_{12} = PD_{21}\chi^2 + PD_{22}\chi, \tag{5.35}$$

where the round trip propagation factor P, at this point the only one depending on λ and g having used the dispersionless hypothesis, cancels out. In this way, we were able to decouple the calculation of the modal threshold gain g_{th} and emission wavelength λ_{th} from the calculation of the modal polarization. Starting from (5.35), we can obtain the polarization equation, reading:

$$D_{21}\chi^2 + (D_{22} - D_{11})\chi - D_{12} = 0. \tag{5.36}$$

The latter represents a simple second degree polynomial equation in χ, allowing two possible solutions, $\chi^{(1)}$ and $\chi^{(2)}$, corresponding to the two allowed polarization modes of the resonator. Notice that, since $\mathbf{D}$ does not depend on λ, it is a completely known input of the problem, since it only depends on the reflection matrices of the left and right mirrors.

At this point, we can see how we can evaluate the threshold gain and emission wavelength associated to both modes, $g_{\text{th}}^{(1,2)}$ and $\lambda_{\text{th}}^{(1,2)}$ (linked to the modal propagation constants $k_{\text{th}}^{(1,2)}$ through (5.24)), starting from the knowledge of $\chi^{(1,2)}$. Consider the first equation of (5.33), from which the round trip propagation constant for both modes, $P^{(1,2)}$, can be calculated as:

$$P^{(1,2)} = \frac{\chi^{(1,2)}}{D_{11}\chi^{(1,2)} + D_{12}}. \tag{5.37}$$

Recalling (5.26), we can split (5.37) into an equation for the modulus and equation for the phase, yielding:

$$g_{\text{th}}^{(1,2)} = \frac{1}{L_a} \log \left| \frac{\chi^{(1,2)}}{D_{11}\chi^{(1,2)} + D_{12}} \right|, \tag{5.38}$$

$$k_{\text{th}}^{(1,2)} = \frac{1}{2L_a} \left[\angle \left(\frac{\chi^{(1,2)}}{D_{11}\chi^{(1,2)} + D_{12}} \right) + 2n\pi \right], \tag{5.39}$$

where n is an integer number. $n = 1$ for the fundamental longitudinal mode, which is the only longitudinal mode excited in VCSELs. The mode with the lowest threshold gain will be referred to as the lasing mode. Notice how from (5.38)–(5.39) we can obtain dichroism and birefringence, starting from knowledge of the roto-reflection matrix $\mathbf{D}$.

As a final remark, solutions $\chi^{(1,2)}$ represent the polarization states of the light within the active material. If one is interested in the polarization properties of light exiting for instance on the left, according to Fig. 5.4, we must use the transmission matrix of the left mirror $\mathbf{T}_l$, yielding:

$$\mathbf{E}_{\text{out}}^{(1,2)} = E_{\text{out},x}\hat{x} + E_{\text{out},y}\hat{y} = \mathbf{T}_l \begin{bmatrix} \chi^{(1,2)} \\ 1 \end{bmatrix}, \tag{5.40}$$

from which, using (5.6), we end up with the polarization index of the exiting light for both modes:

$$\chi_{\text{out}}^{(1,2)} = \frac{E_{\text{out},x}}{E_{\text{out},y}}. \tag{5.41}$$

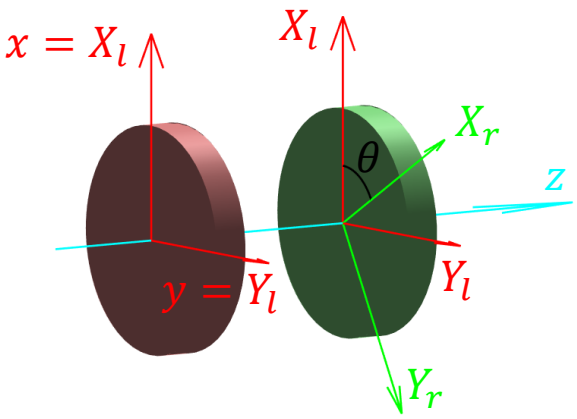

Fig. 5.5 Sketch of a cavity embedded in two anisotropic mirrors featuring a different set of principal axes, (X_l, Y_l) for the left mirror and (X_r, Y_r) for the right mirror, tilted by an angle θ.

5.1.4 Non-chiral dispersiveless anisotropic mirrors with tilted principal axes

The equations analyzed in Subsection 5.1.3 hold for any kind of dispersiveless mirror, even if chiral, provided its reflection and transmission matrices. Even though this is quite general, these matrices are easily computable when considering at most an anisotropic mirror, *e.g.*, an anisotropic DBR with electro-, elasto-optic effect or SWG. Indeed, the reflection and transmission matrices can be obtained along the principal axes of the mirror (X, Y) as:

$$\mathbf{\Gamma}_p = \begin{bmatrix} \Gamma^{XX} & 0 \\ 0 & \Gamma^{YY} \end{bmatrix}, \tag{5.42}$$

$$\mathbf{T}_p = \begin{bmatrix} T^{XX} & 0 \\ 0 & T^{YY} \end{bmatrix}. \tag{5.43}$$

Γ^{XX} and Γ^{YY} are the scalar reflection coefficients of the mirror obtained through two separate 1D calculations as the one in Subsection 3.1.1 from the 2×2 scattering matrix $\mathbf{S}$, using as longitudinal dielectric constant profile either $\varepsilon_{XX}(z)$ or $\varepsilon_{YY}(z)$, respectively, in place of what appears in Fig. 3.3 (top). The same applies to the transmission coefficients T^{XX} and T^{YY}. The subscript "p" in (5.42)–(5.43) refers to the fact that the matrices are evaluated along the mirror principal axes (X, Y).

In this view, consider a resonator embedded within two non-chiral anisotropic mirrors whose principal axes are tilted. The goal is to achieve resonator chirality without necessarily relying on chiral mirrors, but only on tilted optical anisotropies. As sketched in Fig. 5.5, let us choose our reference (x,y) frame to be aligned with the principal axes of the left mirror, so that its reflection and transmission matrices of the left mirror are diagonal:

$$\mathbf{\Gamma}_l = \mathbf{\Gamma}_{p,l} = \begin{bmatrix} \Gamma_l^{XX} & 0 \\ 0 & \Gamma_l^{YY} \end{bmatrix}, \tag{5.44}$$

$$\mathbf{T}_l = \mathbf{T}_{p,l} = \begin{bmatrix} T_l^{XX} & 0 \\ 0 & T_l^{YY} \end{bmatrix}. \tag{5.45}$$

On the other hand, we will consider the principal axes of the right mirror to be rotated by an angle θ with respect to our reference frame. If we know the reflection matrix of the right mirror expressed in its principal axes, namely:

$$\mathbf{\Gamma}_{p,r} = \begin{bmatrix} \Gamma_r^{XX} & 0 \\ 0 & \Gamma_r^{YY} \end{bmatrix}, \tag{5.46}$$

we can use it to calculate the reflection matrix of the right mirror $\mathbf{\Gamma}_r$ in our reference frame considering that an impinging field must be rotated by θ, multiplied by $\mathbf{\Gamma}_{p,r}$, and then rotated back to our reference frame. This reads:

$$\mathbf{\Gamma}_r = \mathbf{R}^{-1}\mathbf{\Gamma}_{p,r}\mathbf{R}, \tag{5.47}$$

where $\mathbf{R}$ is the 2D rotation matrix:

$$\mathbf{R} = \begin{bmatrix} \cos\theta & -\sin\theta \\ \sin\theta & \cos\theta \end{bmatrix}. \tag{5.48}$$

In this context, knowing Γ_l^{XX}, Γ_l^{YY}, Γ_r^{XX}, Γ_r^{YY} and θ we can determine the roto-reflection matrix as:

$$\mathbf{D} = \mathbf{R}^{-1}\mathbf{\Gamma}_r\mathbf{R}\mathbf{\Gamma}_l. \tag{5.49}$$

Being $\mathbf{D}$ the product of two matrices, $\mathbf{\Gamma}_l$ and $\mathbf{\Gamma}_l$, that cannot be simultaneously diagonalized by the same real reference frame, $\mathbf{D}$ is chiral, thus a cavity featuring misaligned optical anisotropies can support elliptically polarized modes.

In this specific case, the electric field phasor exiting the resonator on the left, $\mathbf{E}_{\text{out}}^{(1,2)}$, expressed in (5.40) reads:

$$\mathbf{E}_{\text{out}}^{(1,2)} = \begin{bmatrix} T_l^{XX} & 0 \\ 0 & T_l^{YY} \end{bmatrix} \begin{bmatrix} \chi^{(1,2)} \\ 1 \end{bmatrix} = \begin{bmatrix} T_l^{XX}\chi^{(1,2)} \\ T_l^{YY} \end{bmatrix}. \tag{5.50}$$

Using (5.41), $\chi_{\text{out}}^{(1,2)}$ simply becomes proportional to the polarization index inside the cavity:

$$\chi_{\text{out}}^{(1,2)} = \frac{T_l^{XX}}{T_l^{YY}}\chi^{(1,2)}. \tag{5.51}$$

It is also possible to obtain an analytical behavior for $\chi^{(1,2)}$ for small values of tilting angle. Indeed, solving the polarization equation in (5.36) we obtain:

$$\chi^{(1,2)} = \frac{D_{11} - D_{22} \pm \sqrt{(D_{11} - D_{22})^2 + 4D_{12}D_{21}}}{2D_{21}}, \tag{5.52}$$

where, explicitly calculating $\mathbf{D}$ in (5.49), we have:

$$\mathbf{D} = \begin{bmatrix} \cos^2(\theta)\Gamma_r^{XX}\Gamma_l^{XX} + \sin^2(\theta)\Gamma_r^{YY}\Gamma_l^{XX} & \cos(\theta)\sin(\theta)\left(\Gamma_r^{YY}\Gamma_l^{YY} - \Gamma_r^{XX}\Gamma_l^{YY}\right) \\ \cos(\theta)\sin(\theta)\left(\Gamma_r^{YY}\Gamma_l^{XX} - \Gamma_r^{XX}\Gamma_l^{XX}\right) & \sin^2(\theta)\Gamma_r^{XX}\Gamma_l^{YY} + \cos^2(\theta)\Gamma_r^{YY}\Gamma_l^{YY} \end{bmatrix}. \tag{5.53}$$

Equation (5.52) can be numerically calculated for any angle θ, however, it is possible to extract an analytic dependency for small angles by evaluating the asymptotic behavior of $\chi^{(1,2)}$ for $\theta \to 0$. Denoting $\chi^{(1)}$ and $\chi^{(2)}$ as the solutions of (5.52) with plus and minus signs, respectively, it is possible to obtain:

$$\chi^{(1)}(\theta) = -\frac{\Gamma_r^{YY}\Gamma_l^{YY} - \Gamma_r^{XX}\Gamma_l^{YY}}{\Gamma_r^{XX}\Gamma_l^{XX} - \Gamma_r^{YY}\Gamma_l^{YY}}\theta + o(\theta), \quad \theta \to 0, \tag{5.54}$$

$$\chi^{(2)}(\theta) = \frac{\Gamma_r^{XX}\Gamma_l^{XX} - \Gamma_r^{YY}\Gamma_l^{YY}}{\Gamma_r^{YY}\Gamma_l^{XX} - \Gamma_r^{XX}\Gamma_l^{XX}}\frac{1}{\theta} + o\left(\frac{1}{\theta}\right), \quad \theta \to 0, \tag{5.55}$$

with $o(\theta)$ and $o(1/\theta)$ representing negligible quantities with respect to θ and $1/\theta$, when $\theta \to 0$.

A numerical example for a VCSEL having two DBRs terminated by two tilted SWGs, featuring $\Gamma_l^{XX} = 0.9978 + 1.53 \times 10^{-4} j$, $\Gamma_l^{YY} = 0.9988 - 1.19 \times 10^{-4} j$, $\Gamma_r^{XX} = 0.9985 - 4.57 \times 10^{-4} j$ and $\Gamma_r^{YY} = 0.994 - 0.003 j$ is reported in Fig. 5.6.

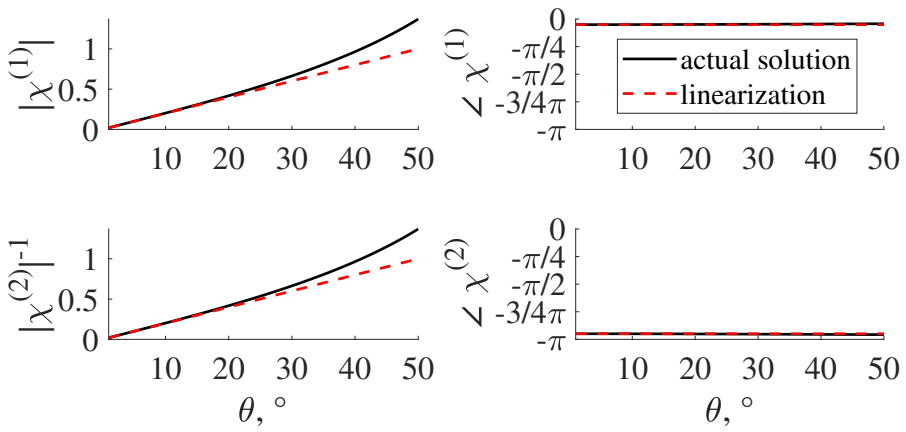

Fig. 5.6 Example of behavior of the polarization indices of the modes supported by a cavity with the tilting angle between the principal axes of the embedding anisotropic mirrors. Results show both (5.52) and the approximated formulae for small tilting angles (5.54)–(5.55).

5.2 Case study: isotropic VCSEL with two tilted sub-wavelength gratings

To investigate the concept presented in Subsection 5.1.4 at the most basic level, we propose the test structure reported in Fig. 5.7. The VCSEL designed for a wavelength of 850 nm features a λ-cavity and two symmetric 20-pairs $\lambda/4$ DBRs terminated by SWGs. The high and low values of refractive index in the DBRs are chosen to be $n_H = 3.5$ and $n_L = 3$, respectively. The SWG bars feature alternating refractive indices of $n_{\text{fill}} = n_H = 3.5$ and $n_{\text{other}} = 1$, with a spatial duty cycle of $\eta_{\text{DC}} = 0.5$, using the same nomenclature as Subsection 3.3.2. SWGs are treated as homogeneous anisotropic media through the Born-Wolf formulae (3.45)–(3.46), from which $n_\perp = 1.3$ and $n_\parallel = 2.57$.

We choose our reference frame (x,y) to be aligned with the principal axes of the left SWG, x corresponding to the direction orthogonal to the grating bars and y to the direction parallel to the bars. On the other hand, the principal axes of the right SWG are rotated by an angle θ_R, similarly to what is described in Subsection 5.1.4. In an attempt to understand the basic principle of resonator chirality, we neglect electro- and elasto-optic effects in the DBRs, leaving the SWGs as the only source of optical anisotropy of the left and right mirrors. Our goal is to understand how the output polarization index for the lasing mode, χ_{out}, and the corresponding

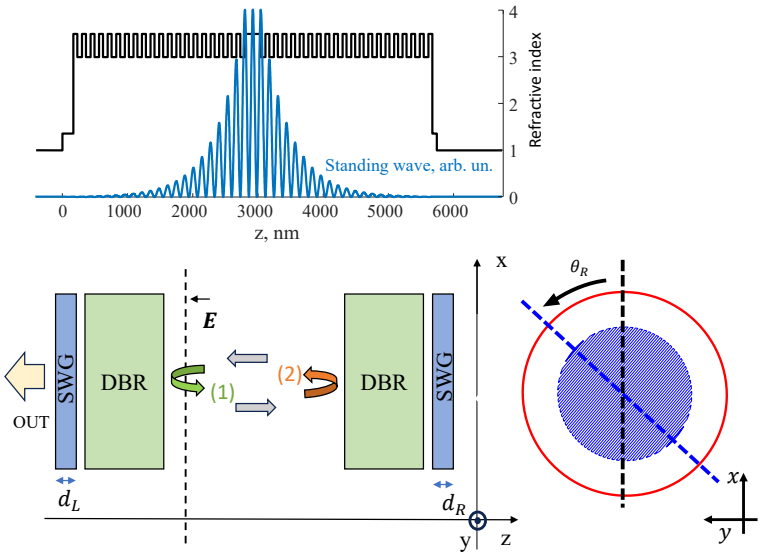

Fig. 5.7 Top: Refractive index and standing wave profile of the investigated VCSEL test structure. The indices of the SWGs in the refractive index profile are effective indices obtained with the Born-Wolf formula (3.45). Bottom: Schematics of the cavity to be investigated within the Barkhausen round-trip cavity framework with the orientation of the tilted gratings (right).

Stokes parameters S_1, S_3 and S_3 are affected by the SWG parameters, namely their thicknesses d_L and d_R and the tilting angle θ_R, affecting the roto-reflection matrix $\mathbf{D}$ and therefore the supported polarizations.

As a first investigation, the output polarization index χ_{out} and its projection onto the Poincaré sphere according to (5.19)–(5.20)–(5.21) was determined for a wide range of grating parameters, namely $\theta_R \in [1,179]^\circ$, $d_L \in [20,400]$ nm and $d_R \in [50,130]$ nm. As a key result, the whole Poincaré sphere was accessed, showing how any polarization can be obtained on demand depending on the SWG parameters, as depicted in Fig. 5.8.

We now focus our attention on circularly polarized light, a case of particular interest in several applications. To this end, we select a fixed right grating thickness $d_R = 70$ nm and vary the other two parameters d_L and θ_R, resulting in the map depicted in Fig. 5.9 (left). The map displays the values of S_3, showing a wide range for which it approaches the desired value of 1. For a more quantitative visualization, Fig. 5.9 (right) reports cuts of the previous map at the value of d_L associated with the maximum S_3. This is reported not only for $d_R = 70$ nm, but also for two additional

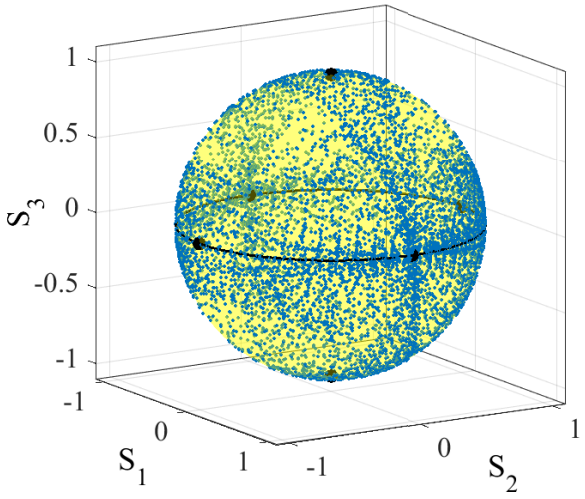

Fig. 5.8 Graphical depiction of accessing all polarization states on the full Poincaré sphere by spanning $\theta_R \in [0, 180]^\circ$, $d_L \in [20, 400]$ nm and $d_R \in [50, 70, 100, 130]$ nm.

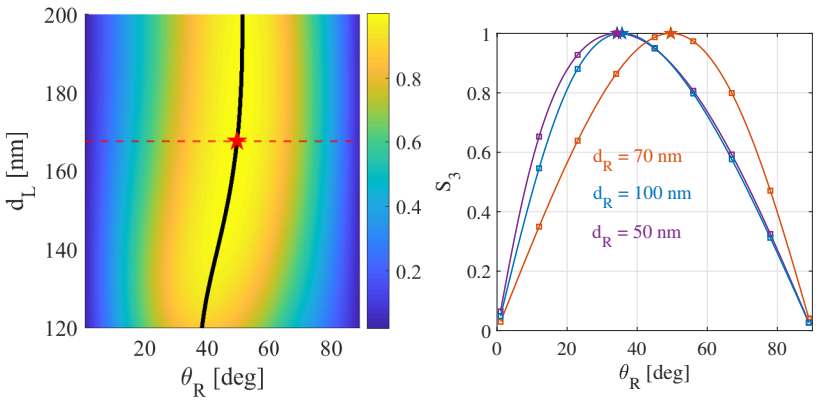

Fig. 5.9 Left: Color density plot of S_3 vs. d_L and θ_R for d_R=70 nm. The red dashed line is the cut at $d_L = 167$ nm, ensuring S_3=1 ($S_3 = 1$ at the star). The black solid line represents the curve along which S_3 is maximum for each fixed d_L value. Right: S_3 vs. θ_R for three values d_R =50, 70 and 100 nm. The d_L values are fixed to ensure $S_3 = 1$. For the red curve ($d_R = 70$ nm) we have that d_L =167 nm (cut along the dashed red line in the left map). Similarly, for the curves corresponding to d_R=50 and 100 nm, d_L=141 and 199 nm, respectively. The squares represent the values obtained with one-dimensional vectorial simulations as those described in Section 3.2.

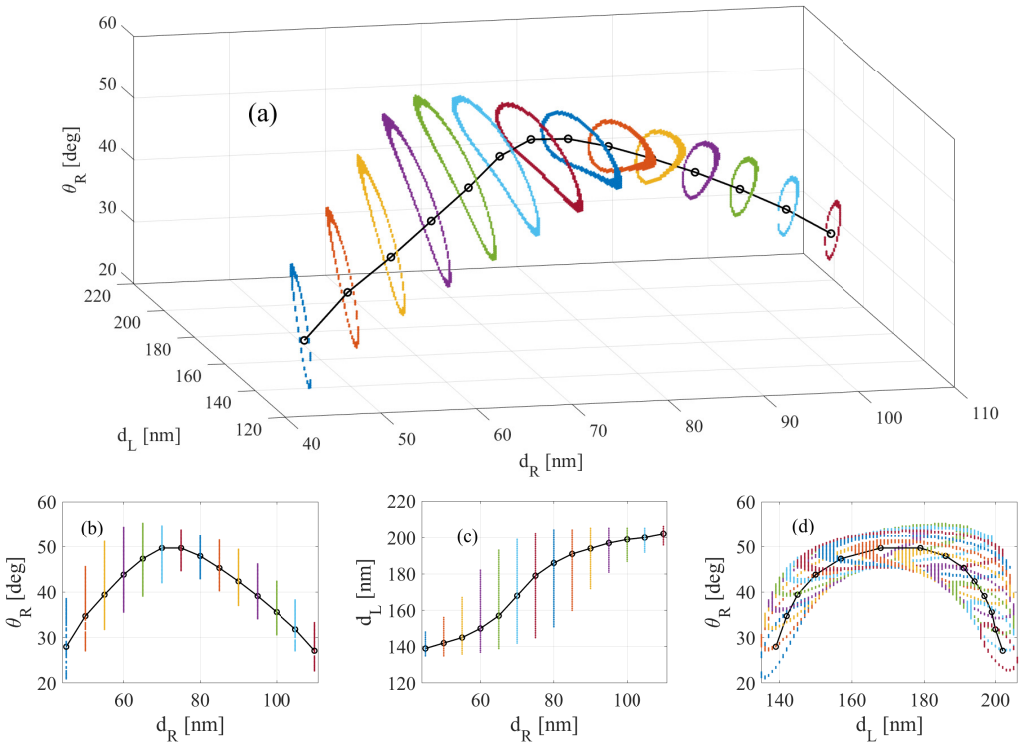

Fig. 5.10 Circular polarization design chart for the VCSEL of Fig. 5.7. Top: S_3=1 trajectory in the 3D parameter space and the regions featuring S_3>0.99 within the colored lines. Bottom (b to d): the 2-D projections visualize in a more readable form the corresponding d_R, d_L, and θ_R values. Altogether, the full trajectory and the projections (b), (c), and (d) provide all needed information regarding the design sensitivity to the relevant parameters.

thicknesses of the right grating, demonstrating that it is still possible to reach $S_3 = 1$ even with different d_R values. The same results are also calculated using the vectorial one-dimensional formalism described in Section 3.2 for comparison, reported with squares in Fig. 5.9 (right). The perfect agreement validates the soundness of the dispersionless approximation, not assumed in vectorial one-dimensional simulations.

In Fig. 5.10 we provide a complete investigation of the parameter space. The black curve in the 3D space of grating thicknesses and relative angle (d_L, d_R, θ_R) shows the trajectory where $S_3 = 1$, while the colored dots around it define the boundaries of the region for which $S_3 \geq 0.99$. In general, we can see that the tolerance for θ_R is always at least $\pm 5^\circ$. Moreover, we observe a large insensitivity to d_L, maximum for $d_R = 70$ nm, but pretty much the same in the whole range $60 < d_R < 80$ nm. In summary, we can achieve $S_3 = 1$ in a very broad range of grating thicknesses: $40 < d_R < 100$ nm and $130 < d_L < 210$ nm, with tilting angles

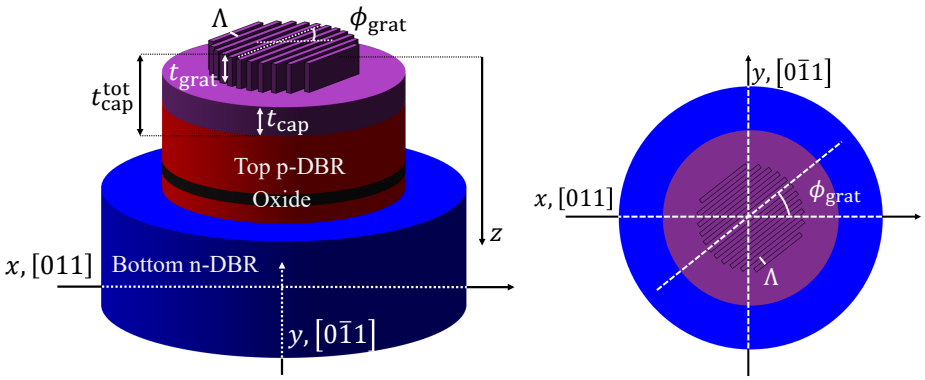

Fig. 5.11 Sketch of the investigated VCSEL structure, together with the reference system and the definition of the most relevant dimensions.

from 25 to 50°. The better performance in terms of parameter insensitivity is at the center of those intervals, where the tilting angle is around 45°. $S_3 = -1$ can be achieved using the same grating parameters as those in Fig. 5.10, but with opposite tilting angle θ_R. In this way, one might have on the same chip, close to each other, two VCSELs emitting $S_3 = \pm 1$.

5.3 Elliptically and circularly polarized VCSEL with a single tilted grating

5.3.1 Investigated VCSEL structure and fabrication process

Having demonstrated that tilted optical anisotropies can generate elliptically and circularly polarized light on the test structure defined in Section 5.2, we now apply the same concept to a real VCSEL. In this case, however, cavity chirality arises from the interaction between a SWG tilted with respect to the crystalline axes and the intrinsic semiconductor optical anisotropies, namely electro-optic and elasto-optic effects. This analysis is conducted both experimentally and theoretically, with the theoretical framework serving both to interpret the experimental data and, in a subsequent step, to optimize the structure towards a CP-VCSEL fully compatible with standard grating VCSEL fabrication processes.

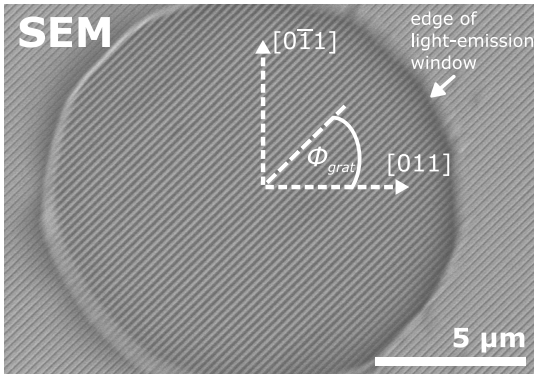

Fig. 5.12 SEM picture of the light-emission window of a VCSEL. The SWG is tilted by the angle ϕ_{grat}.

The considered AlGaAs-VCSEL, sketched in Fig. 5.11 and emitting at $\lambda = 850$ nm, is grown epitaxially by metal-organic vapor-phase epitaxy (MOVPE) on an n-doped GaAs substrate with a donor concentration of $N_{\text{D}} = 2 \times 10^{18}\,\text{cm}^{-3}$. The bottom n-doped ($N_{\text{D}} = 1.5 \times 10^{18}\,\text{cm}^{-3}$) DBR comprises 30 pairs of

$$\text{Al}_{0.10}\text{Ga}_{0.90}\text{As:Si}/\text{Al}_{0.95}\text{Ga}_{0.05}\text{As:Si}$$

layers. Each layer has a thickness of $\lambda/(4n_r)$, where n_r is its refractive index as if it is unaffected by optical anisotropies. Above the bottom DBR, an intrinsic λ-cavity made of $\text{Al}_{0.50}\text{Ga}_{0.50}\text{As}$ embeds the active region (AR), which provides optical gain to support lasing. The top p-doped ($N_{\text{A}} = 1.5 \times 10^{18}\,\text{cm}^{-3}$) DBR consists of 19.5 pairs of

$$\text{Al}_{0.20}\text{Ga}_{0.80}\text{As:Zn}/\text{Al}_{0.95}\text{Ga}_{0.05}\text{As:Zn}$$

layers, connected by a linear molar fraction grading of 26 nm[5]. Following the cavity, a high aluminum content layer ($\text{Al}_{0.98}\text{Ga}_{0.02}\text{As}$) is introduced for oxidation, allowing the transverse definition of the oxide aperture, which confines both carriers and light.

The out-of-phase top DBR is turned in-phase by a heavily p-doped GaAs cap layer with an acceptor concentration of $N_{\text{A}} = 1 \times 10^{19}\,\text{cm}^{-3}$ and a total thickness of $t_{\text{cap}}^{\text{tot}} = 3\lambda/(4n_r) = 175$ nm, which also serves as contact layer.

To enable polarization control, a SWG is defined in a first processing step by electron-beam lithography and subsequently etched into the cap layer with a spatial

[5]It is important to note that, in this structure, the cap layer is treated as a separate layer and not as an integral part of the top DBR. In other words, it is described independently rather than being grouped within the top DBR stack.

period $\Lambda = 200$ nm by inductively-coupled plasma (ICP)-etching. The grating extends to a depth of $t_{\text{grat}} = \lambda/(2n_r) = 116$ nm, leaving a residual cap layer thickness of $t_{\text{cap}} = t_{\text{cap}}^{\text{tot}} - t_{\text{grat}} = 59$ nm. In Fig. 5.12, we show a scanning electron microscope (SEM) image of the resulting SWG.

The reference coordinate system (x,y) is aligned to the crystal directions, *i.e.*, $x = X = [011]$, $y = Y = [0\bar{1}1]$, where X and Y represent the principal axes of the semiconductor optical anisotropies according to Subsection 3.3.1. The longitudinal z-axis is defined as opposite to the growth direction. The subsequent device fabrication follows a standard VCSEL process. Mesas are defined by a combination of photolithography and ICP-etching. The current confining oxide aperture is formed by wet-thermal oxidation of the $Al_{0.98}GaAs$:Zn layer in an oxidation oven. Thereon, a 4 µm BCB isolation layer is spun on the sample and structured via UV-lithography. In the last processing steps the p-contact is defined by photolithography and deposited by electron beam evaporation, before evaporation of the n-contact completes the fabrication process.

5.3.2 Characterization of anisotropies: drift-diffusion simulations for the electro-optic effect

To investigate the effect of the tilting angle ϕ_{grat} (displayed in Fig. 5.11) between the crystal axes and the grating bars, many identical samples with different ϕ_{grat} values ranging from 0° to 180° in steps of 5° are manufactured and analyzed, both experimentally and through simulations. This comprehensive approach ensures that the polarization features are thoroughly understood in all conditions.

As the device operates in a single transverse mode, a one-dimensional electro-optical simulation along the z-axis is sufficient to capture its polarization characteristics. Since in this case the top mirror features both the semiconductor anisotropies and the tilted anisotropy introduced by the SWG, we adopt the one-dimensional vectorial analysis of Section 3.2 instead of the vectorial Barkhausen criterion.

If we do not apply any strain, two anisotropies are present: the tilted SWG and the electro-optic effect (EOE). The SWG transmission matrix is computed directly by rigorous coupled wave analysis [50, 51], without performing the homogenization of Subsection 3.3.2. On the other hand, according to Subsection 3.3.1, the anisotropy arising from the EOE can be evaluated in terms of the semi-difference of the relative

dielectric constants along x, ε_{XX}, and y, ε_{YY}, as (3.42)–(3.43)

$$\Delta\varepsilon_{\mathrm{EOE}}(z) = \frac{\varepsilon_{XX} - \varepsilon_{YY}}{2\varepsilon_0} = n_r^4(z) r_{41}(z) E(z), \tag{5.56}$$

as it is needed in (A.21). In the latter, $n_r(z)$ is the refractive index profile in the absence of the optical anisotropies induced by the electro-optic and elasto-optic effects[6], $E(z)$ is the z-component of the electrostatic field profile and $r_{41} = 1.6$ pm/V for GaAs [72], and 0.78 pm/V for AlAs [73], with a linear interpolation for intermediate aluminum molar fractions, as stated in Subsection 3.3.1.

The electrostatic field profile is obtained with our in-house 1D drift-diffusion (DD) code [45]. The model includes the Poisson's equation (5.57a) for the electrostatics and the continuity equations for the carriers (5.57b)–(5.57c) with their corresponding constitutive relations (5.57d)–(5.57e):

$$\partial_z^2 \phi(z) = -q/\varepsilon_{\mathrm{st}} \left[N_{\mathrm{D}}^+(z) - N_{\mathrm{A}}^-(z) + p(z) - n(z) \right], \tag{5.57a}$$

$$\partial_z J_n(z) = q U_n(z), \tag{5.57b}$$

$$\partial_z J_p(z) = -q U_p(z), \tag{5.57c}$$

$$J_n(z) = -q\mu_n n(z) \partial_z \phi(z) + k_B T \mu_n \partial_z n(z), \tag{5.57d}$$

$$J_p(z) = -q\mu_p p(z) \partial_z \phi(z) - k_B T \mu_p \partial_z p(z). \tag{5.57e}$$

where q is the elementary charge, k_B is the Boltzmann constant, T is the temperature, μ_n and μ_p are the mobilities, $\varepsilon_{\mathrm{st}}$ is the static dielectric constant, ϕ is the electrostatic potential profile and J_n, J_p are the densities of current of electrons and holes, respectively. U_n and U_p represent the net recombination rates, including Shockley-Read-Hall (SRH), Auger and radiative recombinations, with the same AlGaAs parameters used in [45]. The spatial distribution of the electrostatic field under the application of a direct bias is mainly governed by the doped heterostructures of the DBRs. Once the system is solved, the electrostatic field distribution can be calculated from the electrostatic potential as

$$E(z) = -\frac{\partial \phi(z)}{\partial z}. \tag{5.58}$$

[6] This corresponds to the quantity n_{iso} used in Subsection 3.3.1.

Finally, if a uniform longitudinal strain σ (adimensional) is mechanically applied along $Y = [1\bar{1}0]$, an additional anisotropy results as consequence of the elasto-optic effect. The equivalent of (5.56) for the elasto-optic effect reads (3.40)–(3.41)[7]

$$\Delta\varepsilon_\sigma = n_r^4(z)\, p_{44}\frac{\sigma}{2}, \tag{5.59}$$

where $p_{44} = 0.072$ [69]. The overall anisotropy $\Delta\varepsilon = \Delta\varepsilon_{\mathrm{EOE}} + \Delta\varepsilon_\sigma$ can be evaluated as the sum of the two effects.

5.3.3 Experimental measurement of the Stokes parameters

The VCSEL characterization setup features a temperature-cooled copper plate that also serves as the n-electrode on which the device under investigation is placed. The p-side of the VCSEL is contacted via a probe needle controlled by a micromanipulator. The setup further uses an optical telescope arrangement consisting of three lenses for collimating and guiding the VCSEL emission towards the measurement head of a Newport 1830-C powermeter. In order to determine the Stokes parameters, the method of the rotating quarter wave-plate is applied [120, 123]. For this purpose a quarter wave-plate on an automatized rotation mount and a linear polarizer are inserted into the optical path in front of the powermeter head. A mechanical stop is used to ensure a fixed orientation of the VCSEL chip for all measurements. While the polarizer is kept fixed, the quarter wave-plate is rotated and the intensity on the powermeter head detected. The intensity detected on the powermeter head in dependence of the quarter wave-plate rotation angle θ follows

$$I = \frac{1}{2}\left(A + B\sin(2\theta) + C\cos(4\theta) + D\sin(4\theta)\right), \tag{5.60}$$

where the experimental Stokes parameters S_0, S_1, S_2 and S_3 are obtained from according to

$$S_0 = A - C,\ S_1 = 2C,\ S_2 = 2D,\ S_3 = B. \tag{5.61}$$

[7] Notice the sign flip in (3.40)–(3.41) due to the fact that σ is a longitudinal strain applied along Y and X.

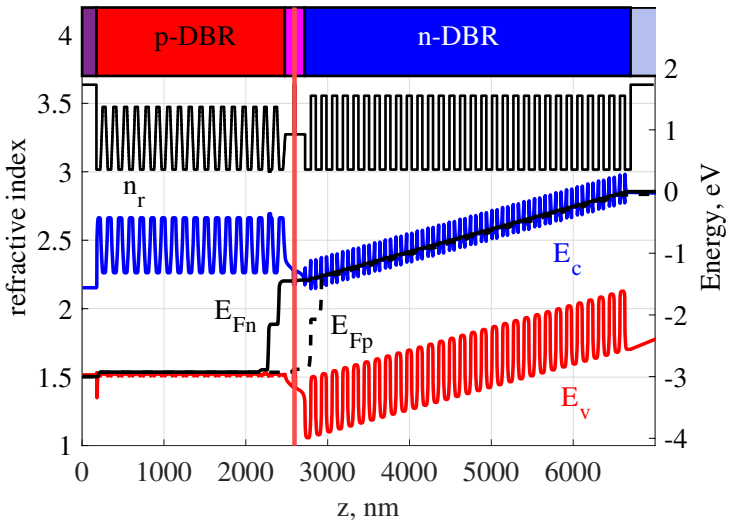

Fig. 5.13 Band diagram of the VCSEL together with the refractive index profile. The refractive index curve is read on the left axis, while all energies are read on the right axis. The vertical red line highlights the active region.

5.3.4 Experimental validation of elliptical polarization and theoretical optimization for circular polarization

The structure reported in Fig. 5.11 is simulated by means of our DD model. The band diagram of the device at the applied direct bias voltage of 3 V is reported in Fig. 5.13. We sketch with different colors the longitudinal extension of the cap layer, the p-DBR, the cavity, the n-DBR and the substrate, from left to right.

Applying (5.58), it is possible to determine the electrostatic field distribution $E(z)$ reported in Fig. 5.14 (top). Strong peaks arise in the DBR regions due to the presence of hetero-interfaces. However, such peaks are mitigated in the top p-DBR by the compositional grading, as highlighted in the insets. This profile induces an EOE anisotropy, that is independent from the applied voltage as shown in Fig. 5.14 (bottom). It depends solely on the aluminum molar fraction and doping profiles. As a result, the emitted polarization is unaffected by the DC bias point.

At this stage, optical simulations can be carried out. Before incorporating the grating effects, we focus exclusively on the EOE using (5.56). The resulting SW can be superimposed with the anisotropy profile, $\Delta\varepsilon_{\mathrm{EOE}}$, as shown in Fig. 5.15.

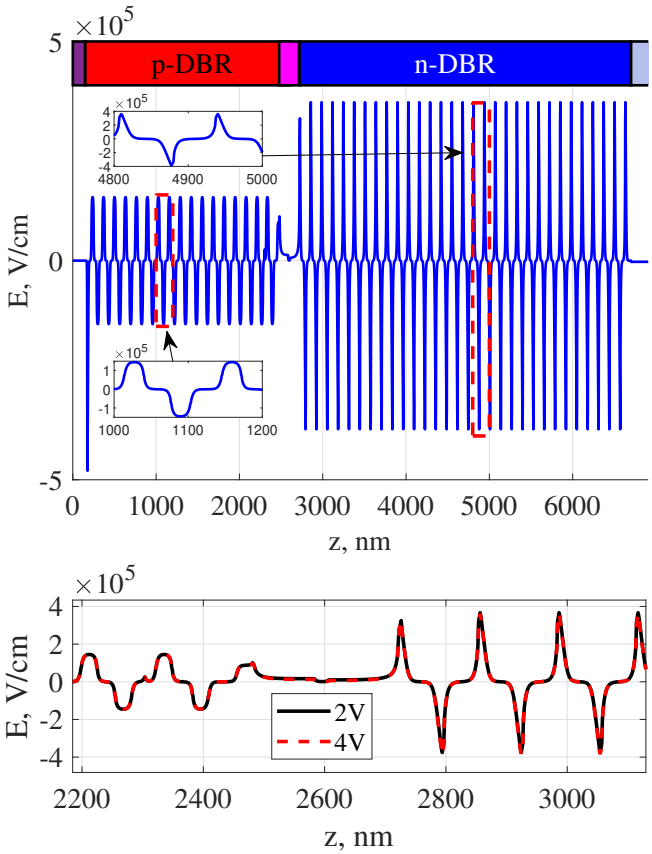

Fig. 5.14 Top: electrostatic field distribution along the longitudinal direction of the VCSEL at 3 V of bias voltage. Insets represent zooms of the profile in the p- and n-DBRs. Bottom: impact of the bias voltage on the electrostatic field profile.

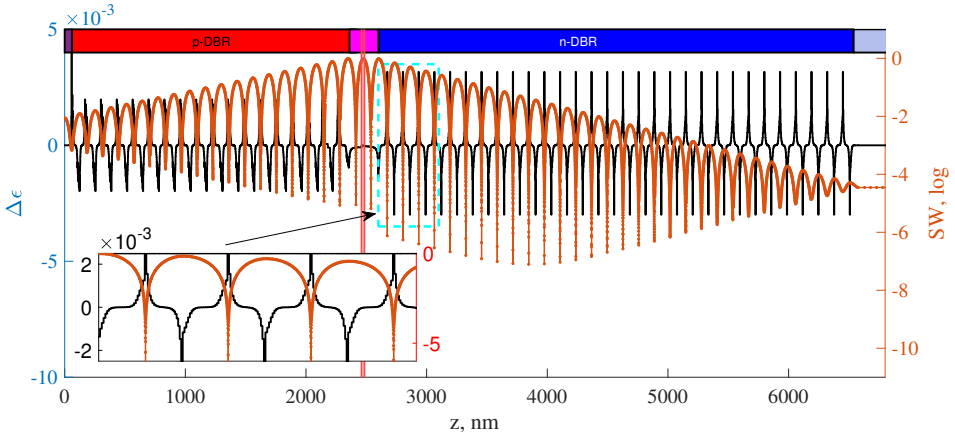

Fig. 5.15 SW and anisotropy profile resulting from the EOE. The inset highlights how only negative peaks of $\Delta\varepsilon$ are relevant to the optical mode.

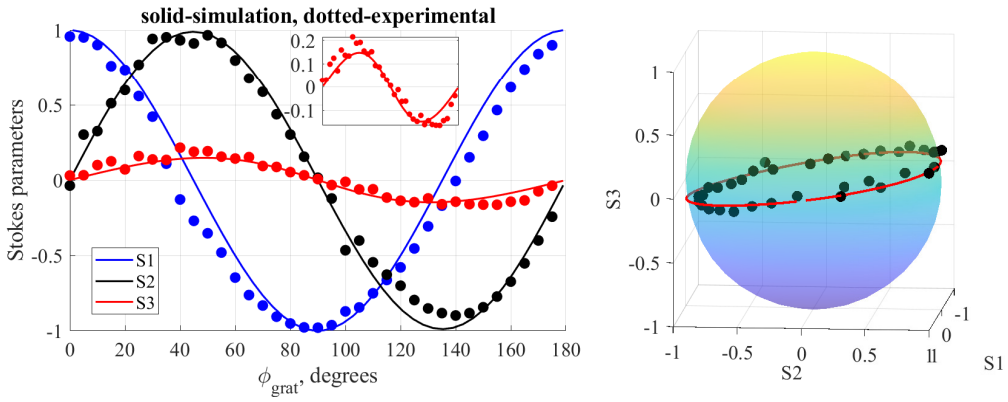

Fig. 5.16 Stokes parameters as function of the tilting grating angle ϕ_{grat} (left), also represented on the Poincaré Sphere.

This analysis is important for understanding the significant impact of the EOE on device performance. Despite the null average of $E(z)$, the positive peaks within the DBRs are aligned with the nodes of the SW and, consequently, minimally interact with the optical mode. Conversely, negative peaks coincide with the antinodes of the SW, resulting in an averaged anisotropy calculated as:

$$\langle \Delta\varepsilon_{\text{EOE}} \rangle = \frac{\int dz \Delta\varepsilon_{\text{EOE}}(z) \cdot \text{SW}(z)}{\int dz \, \text{SW}(z)}, \tag{5.62}$$

amounting for this structure to -3.55×10^{-4}. This anisotropy is aligned with the crystal axes defined in Fig. 5.11 and can interact with the misaligned anisotropy of the grating, effectively forming a 3D chiral cavity that induces elliptical polarization [37]. This phenomenon is confirmed by analyzing the calculated output Stokes parameters of the lasing polarization, and comparing them with measurements obtained for varying tilting angles ϕ_{grat}, as shown in Fig. 5.16.

When $\phi_{\text{grat}} = 0°, 90°, 180°$, $S_3 = 0$ so the polarization is purely linear, as all anisotropies are aligned with crystal axes, while for intermediate angles polarization is elliptical.

The excellent agreement between computed and experimental Stokes parameters proves that VCSELs with SWG tilted to the crystal axes can emit elliptical polarization without modifying the state-of-the-art manufacturing processes. When strain is applied, the averaged anisotropy in (5.62) is modified and it is possible to obtain a

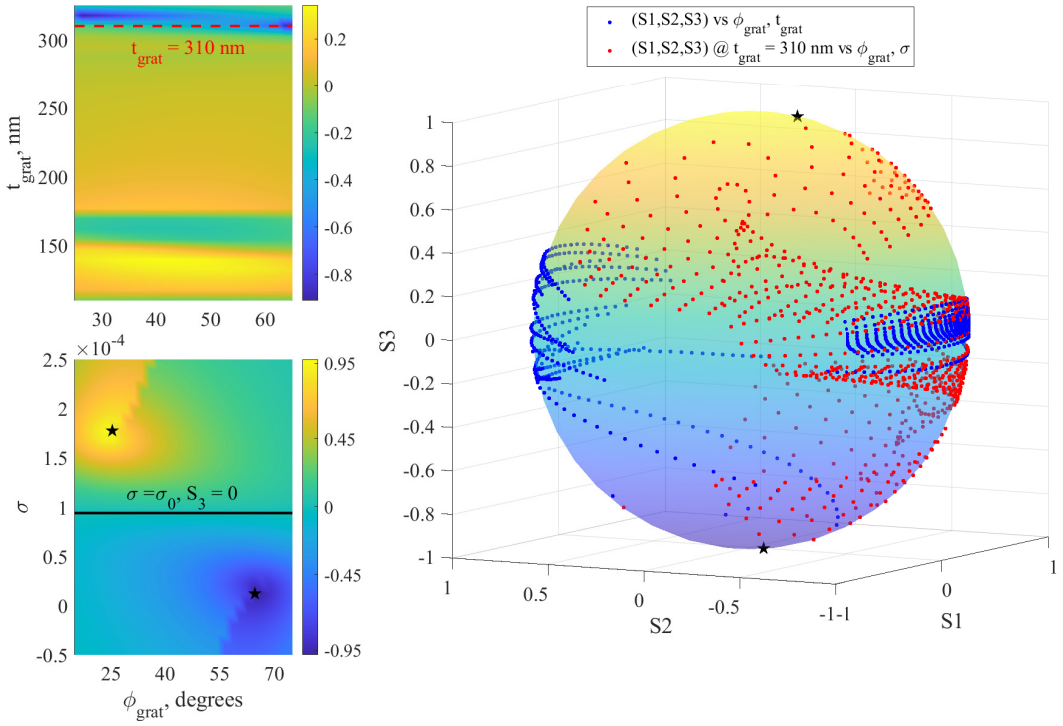

Fig. 5.17 Top left: S_3 component of the lasing output polarization varying t_{grat} and ϕ_{grat}, the red dashed line is the one associated to the grating thickness for which S3 is largest in magnitude. Bottom Left: S_3 component of the output polarization varying σ and ϕ_{grat} keeping $t_{\text{grat}} = 310$ nm, the black solid line is associated to σ_0 and linear output polarization. Right: Stokes parameters obtained from the parametric campaigns, black stars highlight $S_3 \simeq \pm 1$.

linear dependence as[8]:

$$\langle \Delta\varepsilon \rangle = \frac{\int dz\, (\Delta\varepsilon_{\text{EOE}}(z) + \Delta\varepsilon_{\sigma}(z)) \cdot \text{SW}(z)}{\int dz\, \text{SW}(z)} = \langle \Delta\varepsilon_{\text{EOE}} \rangle + \sigma \left(\frac{p_{44}}{2} \frac{\int dz\, n_r^4(z) \text{SW}(z)}{\int dz\, \text{SW}(z)} \right). \tag{5.63}$$

For the device under study, it holds $\langle \Delta\varepsilon \rangle = -3.55 \times 10^{-4} + 3.77\sigma$. This formula implies that the overall averaged intrinsic anisotropy can be zero when an external strain $\sigma_0 = 9.4 \times 10^{-5}$ is applied, thus eliminating the competition between the tilted grating anisotropy and the intrinsic ones. In this special case, the output polarization is always linear and oriented according to ϕ_{grat}.

[8]This is possible since the SW is nearly independent on the applied strain.

Our model, as proved by the excellent comparison with the experimental results, allows to understand how lasing polarization depends on geometrical parameters such as ϕ_{grat}, t_{grat} and mechanically applied strain σ [124]. A simulation campaign is reported in Fig. 5.17. On the top-left map the Stokes parameter S_3 is reported as a function of ϕ_{grat} and t_{grat}, reaching a large negative value[9] for $t_{\text{grat}} \simeq 310$ nm. Fixing this value, the bottom left map displays the behavior of S_3 for varying ϕ_{grat} and σ, showing how a complete custom polarization control is possible in real-world standard grating VCSELs. This is better evidenced in the right-hand side plot, displaying all simulation results on the Poincaré Sphere, that is covered for the most part and includes also cases of pure circular polarization ($S_3 = \pm 1$). As expected from (5.63), when $\sigma = \sigma_0$, $S_3 = 0$ allowing for linear polarization control oriented along the grating angle, suitable for quantum key distribution applications [77].

In this chapter, we theoretically and experimentally demonstrated how the interaction between tilted optical anisotropies enable VCSELs custom polarization states. Our results highlight the value of fast and efficient simulation campaigns in understanding how polarization depends on geometric and technological parameters, paving the way for the design of CP VCSELs. A key advantage of the approach of this section over the solution of using inherently chiral layers is its reliance on well-established grating VCSEL technology, ensuring compatibility with existing fabrication processes.

[9] In this design, the maximum S_3 value achievable by varying only the grating parameters, *i.e.*, the thickness and the grating angle, is approximately -0.9. This specific structure was chosen because experimental data were available for validating the model (see Fig. 5.16). However, for other structures investigated only through simulations, it is possible to achieve fully circular polarization even without applying external strain, which is required in this case. This suggests that circular polarization can be obtained by modifying only the epitaxial structure and the grating parameters. Such modifications were not explored here, as the epitaxial structure was fixed by the experimentally fabricated device.

Chapter 6

Conclusions

In this thesis, we developed a comprehensive mathematical framework for the investigation of the electromagnetic modal properties of VCSELs, based on coupled mode theory. This framework spans from full three-dimensional full-wave simulations to reduced one-dimensional scalar and vectorial models, as well as analytical approaches. Such a multifaceted formulation enables the selection of the most appropriate methodology based on the specific objectives of the analysis.

From an implementation standpoint, these methodologies can be viewed as a simulation suite for the electromagnetic modeling of VCSELs, hence the name **V**CSEL **EL**ectro**M**agnetic **S**uite (VELMS).

Depending on the desired level of detail, users can choose the most suitable approach. For instance, the full 3D vectorial formulation is ideal for studying the general behavior of multimode VCSELs, including distinct transverse modes, their polarization characteristics, threshold gains, and resonant emission wavelengths. Alternatively, for single-mode VCSELs, either due to small oxide apertures or the presence of surface reliefs, simplified 1D scalar or vectorial models can be employed. The scalar formulation is particularly useful for investigating how the epitaxial structure affects global device characteristics such as 1D threshold gain, 1D emission wavelength, and standing wave distribution. The vectorial model, while retaining all these capabilities, further enables the analysis of polarization-related effects, such as birefringence, dichroism, and the behavior of Stokes parameters, thus providing a more complete picture when polarization plays a significant role in device performance.

Although the 3D approach was originally proposed in earlier works, this thesis provides a rigorous mathematical derivation of the method, starting from Maxwell's equations. This demonstrates that the method is firmly rooted in physical principles, relying solely on the geometrical structure and refractive index distribution of the VCSEL, with no fitting parameters or phenomenological assumptions.

Moreover, the mathematical formalism has been generalized beyond the original cylindrical wave expansion used in [39], allowing for the use of any suitable basis to represent the field inside the VCSEL. While the cylindrical wave basis remains computationally efficient, requiring fewer basis functions compared to plane waves, this generalization enhances the adaptability of the framework.

Another improvement over previously published work concerns the computation of the coupling matrices. In earlier implementations, these matrices were derived analytically or semi-analytically by evaluating the required double integrals through explicit parametrization in polar coordinates of any transverse shape, *e.g.*, the oxide aperture. While this approach could offer a slight speedup in code execution, it demanded considerable effort whenever a new shape had to be analyzed. In contrast, the methodology presented in this thesis adopts a fully numerical evaluation of the double integrals involved in the coupling matrices. This allows for the rapid and flexible analysis of arbitrary transverse profile, with only a modest computational cost when executed on a standard modern personal computer. As a result, it becomes possible to simulate VCSELs with oxide apertures and self-heating temperature distributions of any shape, *e.g.*, rectangular oxide apertures with elliptical self-heating temperature contour lines.

Although the 1D VELM scalar formulation has been employed in prior studies, in this thesis we present its formal derivation. Furthermore, the vectorial generalization and the derivation of the polarization equation for the analysis of cavity chirality are novel contributions of this work. These additions further enhance the versatility of the simulation suite, enabling extensive parametric sweeps thanks to the exceptional computational efficiency of the 1D algorithms.

An overview of the available methodologies applicable to VCSEL modeling is provided in Fig. 6.1.

From a device perspective, the developed model has been applied to two classes of VCSELs: large-area single-mode devices and elliptically polarized VCSELs, with particular emphasis on circular polarization. These classes are particularly suitable

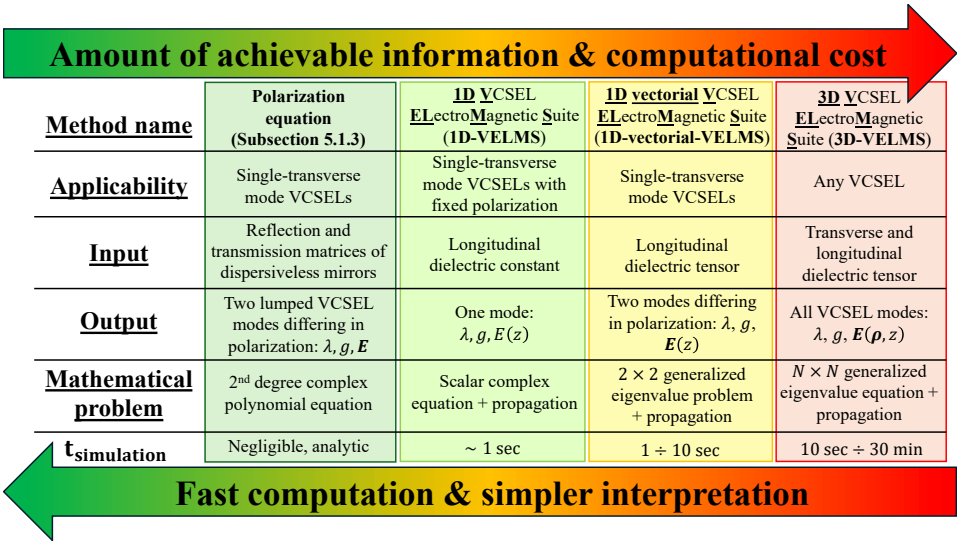

Fig. 6.1 Comparison of the different methodologies analyzed throughout the thesis. From left to right: the polarization equation approach (Subsection 5.1.3), the 1D scalar VELMS (Section 3.1), the 1D vectorial VELMS (Section 3.2), and the full-wave 3D VELMS (Section 2.6). For each methodology, the figure reports its applicability range, required input parameters, obtainable outputs, a brief description of the underlying mathematical problem, and an estimated simulation time on a standard personal computer.

for applications such as atomic clocks, quantum gyroscopes, and atomic magnetometers, all based on optical atomic pumping. To achieve chip-scale miniaturization of such systems, VCSELs have been recently considered as promising light sources due to their compactness. In this context, requirements include high output power for efficient pumping, single-mode emission to selectively excite atomic transitions, and circular polarization to satisfy light–matter interaction rules.

To increase output power, VCSELs with large rectangular active areas have been investigated. Compared to circular or square geometries of equivalent area, the rectangular shape was chosen for its superior thermal dissipation properties. However, increasing the transverse active area leads to multimode operation. Using our simulation tool, we explored several strategies to maintain single-mode behavior, primarily through surface patterning of the outcoupling facet. The most effective solution consists of introducing an array of surface grating reliefs, etched so that their positions match the intensity peaks of the desired mode. This design enables single-mode operation with stable linear polarization in large-area VCSELs. Simulation results were validated against experimental measurements, demonstrating single-mode output powers exceeding 20 mW.

The simulator was also employed to shape the far-field emission profile of the selected mode. Indeed, it features a low intensity along the VCSEL symmetry axis due to destructive interference between out-of-phase lobes in the near field. This occurs since the selected mode is not the fundamental one, and the spatial distribution of its field exhibits multiple lobes with alternating phase. To recover significant axial far-field intensity, two design strategies were explored. The first consists in selectively blocking all the near-field lobes with identical phase using metallic masks, allowing only the remaining in-phase lobes to radiate, thereby reducing destructive interference. The second strategy makes use of dielectric pillars placed over the same-phase lobes, introducing a dephasing that mitigates the interference effect. Both methods proved effective in restoring substantial far-field intensity along the VCSEL symmetry axis, particularly useful for fiber coupling.

We further investigated the behavior of such rectangular VCSELs with grating arrays under increasing self-heating conditions and therefore operating current. Thermal lensing distorts the transverse mode profile, as evidenced by experimental data, and misaligns it with respect the grating relief array, thus degrading modal selectivity. Our simulations revealed the evolution of the optical modes as a function of operating point. Based on these insights, we proposed design guidelines for the grating arrays to ensure robust single-mode operation even at elevated self-heating temperatures and high current levels.

This results in VCSELs capable of emitting high-power, single-mode light with stable linear polarization, enabled by the grating reliefs. In chip-scale atomic systems, however, a quarter-wave plate is then required to convert linear polarization into circular, introducing bulky optical components that limit device miniaturization. Therefore, we investigated strategies to design VCSELs that emit natively elliptically or circularly polarized light, eliminating the need for external polarization converters.

Unlike previous approaches in the literature, which rely on a single chiral layer within the epitaxial structure, we focused on the necessary conditions for a resonator to support elliptical polarization, *i.e.*, a 3D resonator chirality. This can be achieved either by introducing a chiral layer or through misaligned optical anisotropies. After establishing the working principle using a VCSEL featuring two tilted gratings as a case study, we applied this theory to an experimentally fabricated device. In this case, the optical anisotropies arise from the electro-optic effect aligned with the crystallographic axes and a surface grating rotated with respect to them. The device

emits elliptically polarized light, and the degree of circular polarization depends on the grating tilting angle. Simulations and measurements of the Stokes parameters were in excellent agreement, validating the model. We then performed parametric optimization of the grating configuration to maximize circular polarization and also investigated the role of strain, which introduces additional anisotropies through the elasto-optic effect.

In future developments, the concepts of high-power single-mode operation and native circular polarization could be merged. Experimental prototyping campaigns, guided by fast and efficient optical simulations, could lead to the realization of compact, coherent light sources tailored for chip-scale atomic devices.

Beyond these applications, the versatility of the model allows it to be applied to a wide range of VCSEL designs, operating at different wavelengths and based on various material systems, as long as the refractive index distribution is known. Its ability to capture both modal and polarization characteristics makes it suitable for analyzing virtually any VCSEL geometry.

Appendix A

Anisotropic coupling operator

Dielectric tensor and principal axes

If one chooses the (x,y,z) Cartesian reference system to coincide with the principal axes of the considered medium, (X,Y,Z), then the dielectric tensor $\boldsymbol{\varepsilon}$ in (2.11) becomes diagonal, namely:

$$\boldsymbol{\varepsilon}_p = \begin{bmatrix} \varepsilon_{XX} & 0 & 0 \\ 0 & \varepsilon_{YY} & 0 \\ 0 & 0 & \varepsilon_{ZZ} \end{bmatrix}, \tag{A.1}$$

which corresponds to the case studied in [69]. In our analysis, aiming to investigate multiple optical anisotropies, each tilted with respect to the other in the transverse plane, we must compute the coupling operator in the case where our reference

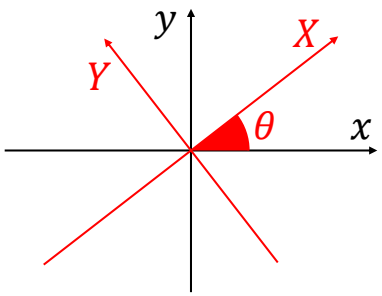

Fig. A.1 Definition of the rotation angle θ between the material principal axes (X,Y) in the transverse plane and our arbitrary choice of reference system in the transverse plane (x,y).

transverse system, (x,y), is rotated by an angle θ relative to the material's principal axes (X,Y), while still considering $z = Z$ as the VCSEL growth direction. The rotation in the transverse plane is visualized in Fig. A.1.

The dielectric tensor allows the evaluation of the dielectric displacement vector given a certain input electric field. With our tilted reference system, in order to apply the simple diagonal expression in (A.1), we must:

1. rotate the field components, expressing them with respect to the principal axes,
2. apply the diagonal dielectric tensor,
3. rotate the result back to the original reference system.

Defining $c = \cos(\theta)$ and $s = \sin(\theta)$ for sake of compactness and

$$\mathbf{R}_t = \begin{bmatrix} c & s & 0 \\ -s & c & 0 \\ 0 & 0 & 1 \end{bmatrix} \tag{A.2}$$

as the rotation matrix acting on the transverse plane, then the dielectric tensor in this general framework reads:

$$\boldsymbol{\varepsilon} = \mathbf{R}_t^{-1} \boldsymbol{\varepsilon}_p \mathbf{R}_t = \begin{bmatrix} c^2\varepsilon_{XX} + s^2\varepsilon_{YY} & cs\,(\varepsilon_{XX} - \varepsilon_{YY}) & 0 \\ cs\,(\varepsilon_{XX} - \varepsilon_{YY}) & c^2\varepsilon_{YY} + s^2\varepsilon_{XX} & 0 \\ 0 & 0 & \varepsilon_{ZZ} \end{bmatrix}, \tag{A.3}$$

from which

$$\Delta\boldsymbol{\varepsilon} = \boldsymbol{\varepsilon} - \varepsilon_{\text{ref}}\mathbf{I} = \begin{bmatrix} c^2\varepsilon_{XX} + s^2\varepsilon_{YY} - \varepsilon_{\text{ref}} & cs\,(\varepsilon_{XX} - \varepsilon_{YY}) & 0 \\ cs\,(\varepsilon_{XX} - \varepsilon_{YY}) & c^2\varepsilon_{YY} + s^2\varepsilon_{XX} - \varepsilon_{\text{ref}} & 0 \\ 0 & 0 & \varepsilon_{ZZ} - \varepsilon_{\text{ref}} \end{bmatrix} =$$

$$= \begin{bmatrix} \Delta\varepsilon_{xx} & \Delta\varepsilon_{xy} & 0 \\ \Delta\varepsilon_{yx} & \Delta\varepsilon_{yy} & 0 \\ 0 & 0 & \Delta\varepsilon_{zz} \end{bmatrix}. \tag{A.4}$$

Coupling operator of an anisotropic layer

At this point, we can attack the general expression of the coupling operator in (2.89) considering that $\Delta\boldsymbol{\varepsilon}_{t,z} = \mathbf{0}$. It is useful to perform the following preliminary calculation:

$$\begin{aligned}
\Delta\boldsymbol{\varepsilon}\mathbf{e}_{\boldsymbol{\nu}}^{\text{tot}} &= \begin{bmatrix} \Delta\varepsilon_{xx} & \Delta\varepsilon_{xy} & 0 \\ \Delta\varepsilon_{yx} & \Delta\varepsilon_{yy} & 0 \\ 0 & 0 & \Delta\varepsilon_{zz} \end{bmatrix} \begin{bmatrix} e_{x,\boldsymbol{\nu}} \\ e_{y,\boldsymbol{\nu}} \\ e_{z,\boldsymbol{\nu}} \end{bmatrix} = \\
&= \begin{bmatrix} \Delta\varepsilon_{xx}e_{x,\boldsymbol{\nu}} + \Delta\varepsilon_{xy}e_{y,\boldsymbol{\nu}} \\ \Delta\varepsilon_{yx}e_{x,\boldsymbol{\nu}} + \Delta\varepsilon_{yy}e_{y,\boldsymbol{\nu}} \\ \Delta\varepsilon_{zz}e_{z,\boldsymbol{\nu}} \end{bmatrix} = \\
&= \begin{bmatrix} \Delta\varepsilon_{xx}e_{x,\boldsymbol{\nu}} + \Delta\varepsilon_{xy}e_{y,\boldsymbol{\nu}} \\ \Delta\varepsilon_{yx}e_{x,\boldsymbol{\nu}} + \Delta\varepsilon_{yy}e_{y,\boldsymbol{\nu}} \\ 0 \end{bmatrix} + \begin{bmatrix} 0 \\ 0 \\ \Delta\varepsilon_{zz}e_{z,\boldsymbol{\nu}} \end{bmatrix} = \left(\Delta\boldsymbol{\varepsilon}\mathbf{e}_{\boldsymbol{\nu}}^{\text{tot}}\right)_t + \left(\Delta\boldsymbol{\varepsilon}\mathbf{e}_{\boldsymbol{\nu}}^{\text{tot}}\right)_z \hat{z}.
\end{aligned} \tag{A.5}$$

At this point, the argument of the double integral in (2.89) can be rewritten using (2.36)–(2.37) as

$$\mathbf{e}_{\boldsymbol{\mu}} \cdot \left(\Delta\boldsymbol{\varepsilon}\mathbf{e}_{\boldsymbol{\nu}}^{\text{tot}}\right)_t - \frac{\varepsilon_{\text{ref}}\Delta\varepsilon_{zz}}{\varepsilon_{\text{ref}} + \Delta\varepsilon_{zz}} e_{z,\boldsymbol{\mu}} e_{z,\boldsymbol{\nu}}. \tag{A.6}$$

This means that the expression for $\mathbf{K}^z$ remains exactly the same as the isotropic case, with the replacement of $\Delta\varepsilon$ with $\Delta\varepsilon_{zz} = \varepsilon_{ZZ} - \varepsilon_{\text{ref}}$. The only additional calculations we need to carry out retain to $\mathbf{K}^t$, however the properties in (2.109) still hold, since the first term in (A.6) does not depend on the z-components of the basis fields, thus the sign is entirely determined by the power normalization constant $C_{\boldsymbol{\mu}}$ in front of (2.89).

Further developing the first term in (A.6), impacting on the transverse coupling operator, we get:

$$\begin{aligned}
\mathbf{e}_{\boldsymbol{\mu}} \cdot \left(\Delta\boldsymbol{\varepsilon}\mathbf{e}_{\boldsymbol{\nu}}^{\text{tot}}\right)_t &= \begin{bmatrix} e_{x,\boldsymbol{\mu}} \\ e_{y,\boldsymbol{\mu}} \\ 0 \end{bmatrix} \cdot \begin{bmatrix} \Delta\varepsilon_{xx}e_{x,\boldsymbol{\nu}} + \Delta\varepsilon_{xy}e_{y,\boldsymbol{\nu}} \\ \Delta\varepsilon_{yx}e_{x,\boldsymbol{\nu}} + \Delta\varepsilon_{yy}e_{y,\boldsymbol{\nu}} \\ 0 \end{bmatrix} = \\
&= \Delta\varepsilon_{xx}e_{x,\boldsymbol{\mu}}e_{x,\boldsymbol{\nu}} + \Delta\varepsilon_{xy}e_{x,\boldsymbol{\mu}}e_{y,\boldsymbol{\nu}} + \Delta\varepsilon_{yx}e_{y,\boldsymbol{\mu}}e_{x,\boldsymbol{\nu}} + \Delta\varepsilon_{yy}e_{y,\boldsymbol{\mu}}e_{y,\boldsymbol{\nu}}.
\end{aligned} \tag{A.7}$$

In this way, $K^t_{\boldsymbol{\mu\nu}}$ reads:

$$\begin{aligned}
K^t_{\boldsymbol{\mu\nu}} &= -\frac{j\omega}{C_{\boldsymbol{\mu}}}\int_{\mathbb{R}^2}\Delta\varepsilon_{xx}e_{x,\boldsymbol{\mu}}e_{x,\boldsymbol{\nu}}\,d^2\rho+\\
&-\frac{j\omega}{C_{\boldsymbol{\mu}}}\int_{\mathbb{R}^2}\Delta\varepsilon_{xy}e_{x,\boldsymbol{\mu}}e_{y,\boldsymbol{\nu}}\,d^2\rho+\\
&-\frac{j\omega}{C_{\boldsymbol{\mu}}}\int_{\mathbb{R}^2}\Delta\varepsilon_{yx}e_{y,\boldsymbol{\mu}}e_{x,\boldsymbol{\nu}}\,d^2\rho+\\
&-\frac{j\omega}{C_{\boldsymbol{\mu}}}\int_{\mathbb{R}^2}\Delta\varepsilon_{yy}e_{y,\boldsymbol{\mu}}e_{y,\boldsymbol{\nu}}\,d^2\rho=\\
&=\left(K^t_{xx}\right)_{\boldsymbol{\mu\nu}}+\left(K^t_{xy}\right)_{\boldsymbol{\mu\nu}}+\left(K^t_{yx}\right)_{\boldsymbol{\mu\nu}}+\left(K^t_{yy}\right)_{\boldsymbol{\mu\nu}}=\sum_{i\in\{x,y\}}\sum_{j\in\{x,y\}}\left(K^t_{ij}\right)_{\boldsymbol{\mu\nu}}.
\end{aligned}\tag{A.8}$$

More explicitly, using the expressions for $\Delta\varepsilon_{ij}$ in (A.4), with $i,j\in\{x,y\}$, considering that $\Delta\varepsilon_{xy}=\Delta\varepsilon_{yx}=cs\,(\varepsilon_{XX}-\varepsilon_{YY})$, $K^t_{\boldsymbol{\mu\nu}}$ becomes:

$$\begin{aligned}
K^t_{\boldsymbol{\mu\nu}} &= -\frac{j\omega}{C_{\boldsymbol{\mu}}}\int_{\mathbb{R}^2}\left(c^2\varepsilon_{XX}+s^2\varepsilon_{YY}-\varepsilon_{\text{ref}}\right)e_{x,\boldsymbol{\mu}}e_{x,\boldsymbol{\nu}}\,d^2\rho+\\
&-\frac{j\omega}{C_{\boldsymbol{\mu}}}\int_{\mathbb{R}^2}cs\,(\varepsilon_{XX}-\varepsilon_{YY})\left(e_{x,\boldsymbol{\mu}}e_{y,\boldsymbol{\nu}}+e_{y,\boldsymbol{\mu}}e_{x,\boldsymbol{\nu}}\right)d^2\rho+\\
&-\frac{j\omega}{C_{\boldsymbol{\mu}}}\int_{\mathbb{R}^2}\left(c^2\varepsilon_{YY}+s^2\varepsilon_{XX}-\varepsilon_{\text{ref}}\right)e_{y,\boldsymbol{\mu}}e_{y,\boldsymbol{\nu}}\,d^2\rho.
\end{aligned}\tag{A.9}$$

Introduction of transverse variations with respect to a background

Consider now the specific case of an anisotropic layer featuring transverse variations, localized within a certain area, with a background medium all around. The quantities that vary over the transverse plane, entering the double integral for the transverse coupling operator, are $\varepsilon_{XX}(\boldsymbol{\rho})$, $\varepsilon_{YY}(\boldsymbol{\rho})$ and $\theta(\boldsymbol{\rho})$. Suppose that the domains where each of these quantities differ from the background values $\varepsilon_{b,XX}$, $\varepsilon_{b,YY}$ and θ_b are D_X, D_Y and $D_\theta\subset\mathbb{R}^2$, respectively. This means that:

$$\begin{cases}
\varepsilon_{XX}(\boldsymbol{\rho})=\varepsilon_{b,XX}, & \text{if } \boldsymbol{\rho}\in\mathbb{R}^2\setminus D_X,\\
\varepsilon_{YY}(\boldsymbol{\rho})=\varepsilon_{b,YY}, & \text{if } \boldsymbol{\rho}\in\mathbb{R}^2\setminus D_Y,\\
\theta(\boldsymbol{\rho})=\theta_b, & \text{if } \boldsymbol{\rho}\in\mathbb{R}^2\setminus D_\theta.
\end{cases}\tag{A.10}$$

Defining the maximum variation domain as

$$D_{\cup} = D_X \cup D_Y \cup D_{\theta}, \tag{A.11}$$

then we can define, for instance,

$$\Delta\varepsilon_{xx}(\boldsymbol{\rho}) = \Delta\varepsilon_{b,xx} + \delta\varepsilon_{xx}(\boldsymbol{\rho}), \tag{A.12}$$

where

$$\Delta\varepsilon_{b,xx} = \cos^2(\theta_b)\varepsilon_{b,XX} + \sin^2(\theta_b)\varepsilon_{b,YY} - \varepsilon_{\text{ref}} \tag{A.13}$$

and

$$\begin{aligned}\delta\varepsilon_{xx}(\boldsymbol{\rho}) = &\left\{\cos^2[\theta(\boldsymbol{\rho})]\varepsilon_{XX}(\boldsymbol{\rho}) + \sin^2[\theta(\boldsymbol{\rho})]\varepsilon_{YY}(\boldsymbol{\rho})\right\} + \\ &- \left[\cos^2(\theta_b)\varepsilon_{b,XX} + \sin^2(\theta_b)\varepsilon_{b,YY}\right],\end{aligned} \tag{A.14}$$

which is identically zero outside of $D_{\cup}$[1]. A similar definition holds for $\Delta\varepsilon_{yy}(\boldsymbol{\rho})$, $\Delta\varepsilon_{b,yy}$ and $\delta\varepsilon_{yy}(\boldsymbol{\rho})$. For the cross terms, we can write

$$\Delta\varepsilon_{xy}(\boldsymbol{\rho}) = \Delta\varepsilon_{yx}(\boldsymbol{\rho}) = \Delta\varepsilon_{b,xy} + \delta\varepsilon_{xy}(\boldsymbol{\rho}), \tag{A.15}$$

where

$$\Delta\varepsilon_{b,xy} = \Delta\varepsilon_{b,yx} = \cos(\theta_b)\sin(\theta_b)\left(\varepsilon_{b,XX} - \varepsilon_{b,YY}\right), \tag{A.16}$$

and

$$\delta\varepsilon_{xy}(\boldsymbol{\rho}) = \delta\varepsilon_{yx}(\boldsymbol{\rho}) = \{\cos[\theta(\boldsymbol{\rho})]\sin[\theta(\boldsymbol{\rho})]\left(\varepsilon_{XX}(\boldsymbol{\rho}) + \varepsilon_{YY}(\boldsymbol{\rho})\right)\} + \tag{A.17}$$

$$- \left[\cos(\theta_b)\sin(\theta_b)\left(\varepsilon_{b,XX} - \varepsilon_{b,YY}\right)\right], \tag{A.18}$$

also identically zero outside of $D_{\cup}$. In this way, each term composing the transverse coupling operator defined in (A.8) can be split as:

$$\left(K^t_{ij}\right)_{\boldsymbol{\mu}\boldsymbol{\nu}} = -\frac{j\omega\Delta\varepsilon_{b,ij}}{C_{\boldsymbol{\mu}}}\int_{\mathbb{R}^2} e_{i,\boldsymbol{\mu}}e_{j,\boldsymbol{\nu}}\,d^2\rho - \frac{j\omega}{C_{\boldsymbol{\mu}}}\int_{D_{\cup}} \delta\varepsilon_{ij}(\boldsymbol{\rho})e_{i,\boldsymbol{\mu}}e_{j,\boldsymbol{\nu}}\,d^2\rho, \quad i,j \in \{x,y\}, \tag{A.19}$$

where the first integral is part of the transverse coupling operator associated with the uniform anisotropic background, still to be determined, while the second finite

[1]Notice that one could write $\delta\varepsilon_{xx}(\boldsymbol{\rho}) = (\delta\varepsilon_{xx})_{\max} S_{xx}(\boldsymbol{\rho})$, $S_{xx}(\boldsymbol{\rho})$ representing an adimensional normalized shape function, to retrieve a definition similar to (2.110).

integral[2] represents anisotropic transverse variations with respect to the background, which can be calculated numerically for all combinations *xx*, *xy*, *yx* and *yy*.

Alternative expression: anisotropic transverse coupling operator as a correction of the isotropic one

Starting from (A.4) and defining

$$\varepsilon_{\text{iso}} = \frac{\varepsilon_{XX} + \varepsilon_{YY}}{2}, \tag{A.20}$$

$$\varepsilon_{\text{ani}} = \frac{\varepsilon_{XX} - \varepsilon_{YY}}{2}, \tag{A.21}$$

we can rewrite

$$\Delta\varepsilon_{xx} = (\varepsilon_{\text{iso}} - \varepsilon_{\text{ref}}) + \varepsilon_{\text{ani}} \cos(2\theta), \tag{A.22}$$

$$\Delta\varepsilon_{yy} = (\varepsilon_{\text{iso}} - \varepsilon_{\text{ref}}) - \varepsilon_{\text{ani}} \cos(2\theta), \tag{A.23}$$

$$\Delta\varepsilon_{xy} = \Delta\varepsilon_{yx} = \varepsilon_{\text{ani}} \sin(2\theta). \tag{A.24}$$

In this view, (A.7) becomes

$$\begin{aligned}
&\mathbf{e}_{\boldsymbol{\mu}} \cdot \left(\Delta\boldsymbol{\varepsilon}\, \mathbf{e}_{\boldsymbol{\nu}}^{\text{tot}}\right)_t = (\varepsilon_{\text{iso}} - \varepsilon_{\text{ref}})\, e_{x,\boldsymbol{\mu}} e_{x,\boldsymbol{\nu}} + \varepsilon_{\text{ani}} \cos(2\theta) e_{x,\boldsymbol{\mu}} e_{x,\boldsymbol{\nu}} + \\
&+ (\varepsilon_{\text{iso}} - \varepsilon_{\text{ref}})\, e_{y,\boldsymbol{\mu}} e_{y,\boldsymbol{\nu}} - \varepsilon_{\text{ani}} \cos(2\theta) e_{y,\boldsymbol{\mu}} e_{y,\boldsymbol{\nu}} + \\
&+ \varepsilon_{\text{ani}} \sin(2\theta) \left(e_{x,\boldsymbol{\mu}} e_{y,\boldsymbol{\nu}} + e_{y,\boldsymbol{\mu}} e_{x,\boldsymbol{\nu}}\right) = \\
&= (\varepsilon_{\text{iso}} - \varepsilon_{\text{ref}}) \left(e_{x,\boldsymbol{\mu}} e_{x,\boldsymbol{\nu}} + e_{y,\boldsymbol{\mu}} e_{y,\boldsymbol{\nu}}\right) + \\
&+ \varepsilon_{\text{ani}} \cos(2\theta) \left(e_{x,\boldsymbol{\mu}} e_{x,\boldsymbol{\nu}} - e_{y,\boldsymbol{\mu}} e_{y,\boldsymbol{\nu}}\right) + \\
&+ \varepsilon_{\text{ani}} \sin(2\theta) \left(e_{x,\boldsymbol{\mu}} e_{y,\boldsymbol{\nu}} + e_{y,\boldsymbol{\mu}} e_{x,\boldsymbol{\nu}}\right).
\end{aligned} \tag{A.25}$$

[2]This integral, being finite, must be multiplied by the spacings associated to the discretization of continuous labels (Δk_t for cylindrical waves).

The transverse coupling operator can then be rewritten as:

$$K^t_{\boldsymbol{\mu}\boldsymbol{\nu}} = -\frac{j\omega}{C_{\boldsymbol{\mu}}}\int_{\mathbb{R}^2}(\varepsilon_{\text{iso}}-\varepsilon_{\text{ref}})\left(e_{x,\boldsymbol{\mu}}e_{x,\boldsymbol{\nu}}+e_{y,\boldsymbol{\mu}}e_{y,\boldsymbol{\nu}}\right)d^2\rho+$$
$$-\frac{j\omega}{C_{\boldsymbol{\mu}}}\int_{\mathbb{R}^2}\varepsilon_{\text{ani}}\cos(2\theta)\left(e_{x,\boldsymbol{\mu}}e_{x,\boldsymbol{\nu}}-e_{y,\boldsymbol{\mu}}e_{y,\boldsymbol{\nu}}\right)d^2\rho+$$
$$-\frac{j\omega}{C_{\boldsymbol{\mu}}}\int_{\mathbb{R}^2}\varepsilon_{\text{ani}}\sin(2\theta)\left(e_{x,\boldsymbol{\mu}}e_{y,\boldsymbol{\nu}}+e_{y,\boldsymbol{\mu}}e_{x,\boldsymbol{\nu}}\right)d^2\rho. \tag{A.26}$$

Notice that the first term is exactly the same as the coupling operator associated to a uniform layer with a dielectric constant profile described by ε_{iso}. The two additional terms represent a correction that vanishes for $\varepsilon_{XX}=\varepsilon_{YY}$, *i.e.*, $\varepsilon_{\text{ani}}=0$.

Transverse coupling operator of a uniform anisotropic layer

In this section we give a methodology to evaluate the transverse coupling operator for a uniform anisotropic layer using the cylindrical waves basis defined in Tab. 2.2. The x and y component of the electric field with labels $\boldsymbol{\mu}=[k_t,m,p,l,\alpha]^T$ can be compactly written as:

$$e_{i,\boldsymbol{\mu}} = s_i J_+\varphi_+ + s_p J_-\varphi_-, \quad i\in\{x,y\} \tag{A.27}$$

where

$$s_i = \begin{cases} +1, & i=x, \\ -1, & i=y, \end{cases} \tag{A.28}$$

$$\varphi_\pm = \begin{cases} f_\pm, & i=x, \\ g_\pm, & i=y, \end{cases} \tag{A.29}$$

$$s_p = \begin{cases} +1, & p=\text{TE}, \\ -1, & p=\text{TM}, \end{cases} \tag{A.30}$$

with $J_\pm$, $f_\pm$ and $g_\pm$ being the same defined in (2.63). For the mode identified by $\boldsymbol{\nu} = [k_t', m', p', l', \alpha']$ we have an equivalent expression:

$$e_{i,\boldsymbol{\nu}} = s_i J_+' \varphi_+' + s_{p'} J_-' \varphi_-', \quad i \in \{x, y\}. \tag{A.31}$$

With this notation, (A.7) can be written as

$$\begin{aligned}
\mathbf{e}_{\boldsymbol{\mu}} \cdot \left(\Delta\boldsymbol{\varepsilon}\, \mathbf{e}_{\boldsymbol{\nu}}^{\text{tot}}\right)_t = {} & \Delta\varepsilon_{xx} \left[\left(J_+ f_+ + s_p J_- f_-\right)\left(J_+' f_+' + s_{p'} J_-' f_-'\right)\right] \\
& + \Delta\varepsilon_{xy} \left[\left(J_+ f_+ + s_p J_- f_-\right)\left(-J_+' g_+' + s_{p'} J_-' g_-'\right)\right] \\
& + \Delta\varepsilon_{yx} \left[\left(-J_+ g_+ + s_p J_- g_-\right)\left(J_+' f_+' + s_{p'} J_-' f_-'\right)\right] \\
& + \Delta\varepsilon_{yy} \left[\left(-J_+ g_+ + s_p J_- g_-\right)\left(-J_+' g_+' + s_{p'} J_-' g_-'\right)\right].
\end{aligned} \tag{A.32}$$

The red and blue terms can be compactly rewritten as:

$$\beta_i = s_p s_{p'} J_- J_-' \varphi_- \varphi_-' + J_+ J_+' \varphi_+ \varphi_+' + \tag{A.33}$$

$$+ s_i \left(s_p J_- J_+' \varphi_- \varphi_+' + J_+ s_{p'} J_-' \varphi_+ \varphi_-'\right), \quad i \in \{x, y\}. \tag{A.34}$$

Defining

$$\psi_\pm = \begin{cases} g_\pm, & i = x, \\ f_\pm, & i = y, \end{cases} \tag{A.35}$$

the green and magenta terms can be compactly rewritten as:

$$\gamma_i = s_p s_{p'} J_- J_-' \varphi_- \psi_-' - J_+ J_+' \varphi_+ \psi_+' + \tag{A.36}$$

$$+ s_i \left(-s_p J_- J_+' \varphi_- \psi_+' + J_+ s_{p'} J_-' \varphi_+ \psi_-'\right), \quad i \in \{x, y\}. \tag{A.37}$$

In this way, (A.32) can be cast into:

$$\begin{aligned}
\mathbf{e}_{\boldsymbol{\mu}} \cdot \left(\Delta\boldsymbol{\varepsilon}\, \mathbf{e}_{\boldsymbol{\nu}}^{\text{tot}}\right)_t &= \Delta\varepsilon_{xx}\beta_x + \Delta\varepsilon_{yy}\beta_y + \Delta\varepsilon_{xy}\gamma_x + \Delta\varepsilon_{yx}\gamma_y = \\
&= \Delta\varepsilon_{xx}\beta_x + \Delta\varepsilon_{yy}\beta_y + \Delta\varepsilon_{xy}\left(\gamma_x + \gamma_y\right),
\end{aligned} \tag{A.38}$$

The same notation can be applied to (A.25), which becomes:

$$\mathbf{e}_{\boldsymbol{\mu}} \cdot \left(\Delta\boldsymbol{\varepsilon}\, \mathbf{e}_{\boldsymbol{\nu}}^{\text{tot}}\right)_t = \left(\varepsilon_{\text{iso}} - \varepsilon_{\text{ref}}\right)\left(\beta_x + \beta_y\right) + \varepsilon_{\text{ani}} \cos(2\theta)\left(\beta_x - \beta_y\right) + \varepsilon_{\text{ani}} \sin(2\theta)\left(\gamma_x + \gamma_y\right). \tag{A.39}$$

To evaluate entirely the coupling operator we need to integrate over the transverse plane three different contributions: $\beta_x+\beta_y$, $\beta_x-\beta_y$ and $\gamma_x+\gamma_y$. Further defining

$$\Psi_1 = \varphi_- \varphi'_-, \tag{A.40}$$

$$\Psi_2 = \varphi_+ \varphi'_+, \tag{A.41}$$

$$\Psi_3 = \varphi_- \varphi'_+, \tag{A.42}$$

$$\Psi_4 = \varphi_+ \varphi'_-, \tag{A.43}$$

$$\bar{\Psi}_1 = \varphi_- \psi'_-, \tag{A.44}$$

$$\bar{\Psi}_2 = \varphi_+ \psi'_+, \tag{A.45}$$

$$\bar{\Psi}_3 = \varphi_- \psi'_+, \tag{A.46}$$

$$\bar{\Psi}_4 = \varphi_+ \psi'_-, \tag{A.47}$$

$$\mathscr{J}_1 = J_- J'_-, \tag{A.48}$$

$$\mathscr{J}_2 = J_+ J'_+, \tag{A.49}$$

$$\mathscr{J}_3 = J_- J'_+, \tag{A.50}$$

$$\mathscr{J}_4 = J_+ J'_-, \tag{A.51}$$

we have that

$$\beta_i = s_p s_{p'} \mathscr{J}_1 \Psi_1 + \mathscr{J}_2 \Psi_2 + s_i \left(s_p \mathscr{J}_3 \Psi_3 + s_{p'} \mathscr{J}_4 \Psi_4 \right), \quad i \in \{x,y\}, \tag{A.52}$$

$$\gamma_i = s_p s_{p'} \mathscr{J}_1 \bar{\Psi}_1 - \mathscr{J}_2 \bar{\Psi}_2 + s_i \left(-s_p \mathscr{J}_3 \bar{\Psi}_3 + s_{p'} \mathscr{J}_4 \bar{\Psi}_4 \right), \quad i \in \{x,y\}. \tag{A.53}$$

Notice that the angular functions depend on $i \in \{x,y\}$, $l \in \{\text{even, odd}\}$, and $l' \in \{\text{even, odd}\}$. The various cases can be explicitly analyzed employing the trigonometric Werner formulae to the angular functions. Naturally, since we are using a basis of cylindrical waves, it is convenient to describe the transverse plane in polar coordinates, with ρ as the radial variable and ϕ as the angular variable. After some algebraic manipulations, we obtain the following results, distinguishing between the four possible even and odd combinations.

Case: $l = \text{even}$, $l' = \text{even}$

$$\begin{aligned}\beta_x = &\frac{\mathscr{J}_2}{2}\left[\cos((m-m')\phi)+\cos((m+m'+2)\phi)\right]+\\
&+\frac{s_p\mathscr{J}_3}{2}\left[\cos((m+m')\phi)+\cos((m-m'-2)\phi)\right]+\\
&+\frac{s_{p'}\mathscr{J}_4}{2}\left[\cos((m+m')\phi)+\cos((m-m'+2)\phi)\right]+\\
&+\frac{s_p s_{p'}\mathscr{J}_1}{2}\left[\cos((m-m')\phi)+\cos((m+m'-2)\phi)\right].\end{aligned} \tag{A.54}$$

$$\begin{aligned}\beta_y = &\frac{\mathscr{J}_2}{2}\left[\cos((m-m')\phi)-\cos((m+m'+2)\phi)\right]+\\
&+\frac{s_p\mathscr{J}_3}{2}\left[\cos((m+m')\phi)-\cos((m-m'-2)\phi)\right]+\\
&+\frac{s_{p'}\mathscr{J}_4}{2}\left[\cos((m+m')\phi)-\cos((m-m'+2)\phi)\right]+\\
&+\frac{s_p s_{p'}\mathscr{J}_1}{2}\left[\cos((m-m')\phi)-\cos((m+m'-2)\phi)\right].\end{aligned} \tag{A.55}$$

$$\begin{aligned}\gamma_x = &\frac{\mathscr{J}_2}{2}\left[\sin((m-m')\phi)+\sin((m+m'+2)\phi)\right]+\\
&+\frac{s_p\mathscr{J}_3}{2}\left[\sin((m+m')\phi)+\sin((m-m'-2)\phi)\right]-\\
&-\frac{s_{p'}\mathscr{J}_4}{2}\left[\sin((m+m')\phi)+\sin((m-m'+2)\phi)\right]-\\
&-\frac{s_p s_{p'}\mathscr{J}_1}{2}\left[\sin((m-m')\phi)+\sin((m+m'-2)\phi)\right].\end{aligned} \tag{A.56}$$

$$\begin{aligned}\gamma_y = &\frac{\mathscr{J}_2}{2}\left[\sin((m-m')\phi)+\sin((m+m'+2)\phi)\right]-\\
&-\frac{s_p\mathscr{J}_3}{2}\left[\sin((m+m')\phi)+\sin((m-m'-2)\phi)\right]+\\
&+\frac{s_{p'}\mathscr{J}_4}{2}\left[\sin((m+m')\phi)+\sin((m-m'+2)\phi)\right]-\\
&-\frac{s_p s_{p'}\mathscr{J}_1}{2}\left[\sin((m-m')\phi)+\sin((m+m'-2)\phi)\right].\end{aligned} \tag{A.57}$$

$$\beta_x+\beta_y=\mathscr{J}_2\cos((m-m')\phi)+s_p\mathscr{J}_3\cos((m+m')\phi)+ \\ +s_{p'}\mathscr{J}_4\cos((m+m')\phi)+s_ps_{p'}\mathscr{J}_1\cos((m-m')\phi). \tag{A.58}$$

$$\beta_x-\beta_y=\mathscr{J}_2\cos((m+m'+2)\phi)+s_p\mathscr{J}_3\cos((m-m'-2)\phi)+ \\ +s_{p'}\mathscr{J}_4\cos((m-m'+2)\phi)+s_ps_{p'}\mathscr{J}_1\cos((m+m'-2)\phi). \tag{A.59}$$

$$\gamma_x+\gamma_y=\mathscr{J}_2\left[\sin((m-m')\phi)+\sin((m+m'+2)\phi)\right]+ \\ -s_ps_{p'}\mathscr{J}_1\left[\sin((m-m')\phi)+\sin((m+m'-2)\phi)\right]. \tag{A.60}$$

At this point, following (A.26), for the transmission operator of an anisotropic layer, we need to integrate $\beta_x\pm\beta_y$ and $\gamma_x+\gamma_y$ over the transverse plane, to obtain all the contributions. Starting with $\beta_x+\beta_y$, focus on the first term with $\mathscr{J}_2$. The angular integral is different from zero only if $m=m'$. In that specific case, the cosinusoidal function is identically 1, giving rise to a factor of 2π when integrated, while $\mathscr{J}_1=J_{m+1}(k_t\rho)J_{m+1}(k_t'\rho)$, which becomes $\delta(k_t-k_t')/k_t$ when integrated. The term $\mathscr{J}_1\cos((m-m')\phi)$ gives the same result when integrated, yielding:

$$\int_0^\infty\rho d\rho\int_0^{2\pi}d\phi\left(\mathscr{J}_2\cos((m-m')\phi)+s_ps_{p'}\mathscr{J}_1\cos((m-m')\phi)\right)= \\ =\frac{4\pi\delta(k_t-k_t')}{k}\delta_{mm'}\delta_{pp'}. \tag{A.61}$$

Furthermore, the term $\mathscr{J}_3\cos((m+m')\phi)$ forces $m'=-m$, which is not considered in the modal basis. Similarly for the term $\mathscr{J}_4\cos((m+m')\phi)$. These two terms only give an additional contribution in the case $m=m'=0$, turning the factor in front of $\beta_x+\beta_y$ from 4π, resulting from $\mathscr{J}_2\cos((m-m')\phi)+s_ps_{p'}\mathscr{J}_1\cos((m-m')\phi)$, to 8π when $s_p=s_{p'}=1$. This is in agreement with the isotropic coupling operator of a uniform layer expressed in Fig. 2.6. With this methodology, one can estimate all the other non-vanishing terms, first determining which azimuthal orders can interact

on the result, then evaluating the integral of the Bessel functions. For the remaining cases, the integrand functions $\beta_x \pm \beta_y$ and $\gamma_x + \gamma_y$ are reported for completeness.

Case: $l =$ even, $l' =$ odd

$$\begin{aligned}\beta_x = &\frac{\mathscr{J}_2}{2}\left[\sin((m-m')\phi)+\sin((m+m'+2)\phi)\right]+\\ &+\frac{s_p\mathscr{J}_3}{2}\left[\sin((m+m')\phi)+\sin((m-m'-2)\phi)\right]+\\ &+\frac{s_{p'}\mathscr{J}_4}{2}\left[\sin((m+m')\phi)+\sin((m-m'+2)\phi)\right]+\\ &+\frac{s_p s_{p'}\mathscr{J}_1}{2}\left[\sin((m-m')\phi)+\sin((m+m'-2)\phi)\right].\end{aligned} \tag{A.62}$$

$$\begin{aligned}\beta_y = &\frac{s_p\mathscr{J}_3}{2}\left[\sin((m+m')\phi)+\sin((m-m'-2)\phi)\right]-\\ &-\frac{\mathscr{J}_2}{2}\left[\sin((m-m')\phi)+\sin((m+m'+2)\phi)\right]+\\ &+\frac{s_{p'}\mathscr{J}_4}{2}\left[\sin((m+m')\phi)+\sin((m-m'+2)\phi)\right]-\\ &-\frac{s_p s_{p'}\mathscr{J}_1}{2}\left[\sin((m-m')\phi)+\sin((m+m'-2)\phi)\right].\end{aligned} \tag{A.63}$$

$$\begin{aligned}\gamma_x = &\frac{s_{p'}\mathscr{J}_4}{2}\left[\cos((m+m')\phi)+\cos((m-m'+2)\phi)\right]-\\ &-\frac{s_p\mathscr{J}_3}{2}\left[\cos((m+m')\phi)+\cos((m-m'-2)\phi)\right]-\\ &-\frac{\mathscr{J}_2}{2}\left[\cos((m-m')\phi)+\cos((m+m'+2)\phi)\right]+\\ &+\frac{s_p s_{p'}\mathscr{J}_1}{2}\left[\cos((m-m')\phi)+\cos((m+m'-2)\phi)\right].\end{aligned} \tag{A.64}$$

$$\begin{aligned}\gamma_y = &\frac{\mathscr{J}_2}{2}\left[\cos((m-m')\phi)-\cos((m+m'+2)\phi)\right]+\\ &+\frac{s_p\mathscr{J}_3}{2}\left[\cos((m+m')\phi)-\cos((m-m'-2)\phi)\right]-\\ &-\frac{s_{p'}\mathscr{J}_4}{2}\left[\cos((m+m')\phi)-\cos((m-m'+2)\phi)\right]-\\ &-\frac{s_p s_{p'}\mathscr{J}_1}{2}\left[\cos((m-m')\phi)-\cos((m+m'-2)\phi)\right].\end{aligned} \tag{A.65}$$

Both $\beta_x+\beta_y$ and $\beta_x-\beta_y$ only depend on the sinusoid function in ϕ, yielding a zero integral over the transverse plane no matter the values of m and m'. Conversely,

$$\gamma_x+\gamma_y = s_{p'}\mathscr{J}_4\cos((m-m'+2)\phi) - s_p\mathscr{J}_3\cos((m-m'-2)\phi) + \\ -\mathscr{J}_2\cos((m+m'+2)\phi) + s_p s_{p'}\mathscr{J}_1\cos((m+m'-2)\phi). \tag{A.66}$$

Case: $l=$ odd, $l'=$ even

$$\beta_x = \frac{\mathscr{J}_2}{2}\left[\sin((m-m')\phi)+\sin((m+m'+2)\phi)\right] + \\ +\frac{s_p\mathscr{J}_3}{2}\left[\sin((m+m')\phi)+\sin((m-m'-2)\phi)\right] + \\ +\frac{s_{p'}\mathscr{J}_4}{2}\left[\sin((m+m')\phi)+\sin((m-m'+2)\phi)\right] + \\ +\frac{s_p s_{p'}\mathscr{J}_1}{2}\left[\sin((m-m')\phi)+\sin((m+m'-2)\phi)\right]. \tag{A.67}$$

$$\beta_y = \frac{s_p\mathscr{J}_3}{2}\left[\sin((m+m')\phi)+\sin((m-m'-2)\phi)\right] - \\ -\frac{\mathscr{J}_2}{2}\left[\sin((m-m')\phi)+\sin((m+m'+2)\phi)\right] + \\ +\frac{s_{p'}\mathscr{J}_4}{2}\left[\sin((m+m')\phi)+\sin((m-m'+2)\phi)\right] - \\ -\frac{s_p s_{p'}\mathscr{J}_1}{2}\left[\sin((m-m')\phi)+\sin((m+m'-2)\phi)\right]. \tag{A.68}$$

$$\gamma_x = \frac{\mathscr{J}_2}{2}\left[\cos((m-m')\phi)-\cos((m+m'+2)\phi)\right] - \\ -\frac{s_p\mathscr{J}_3}{2}\left[\cos((m+m')\phi)-\cos((m-m'-2)\phi)\right] + \\ +\frac{s_{p'}\mathscr{J}_4}{2}\left[\cos((m+m')\phi)-\cos((m-m'+2)\phi)\right] - \\ -\frac{s_p s_{p'}\mathscr{J}_1}{2}\left[\cos((m-m')\phi)-\cos((m+m'-2)\phi)\right]. \tag{A.69}$$

$$\gamma_y = \frac{s_p \mathscr{J}_3}{2}\left[\cos((m+m')\phi)+\cos((m-m'-2)\phi)\right] -$$
$$-\frac{\mathscr{J}_2}{2}\left[\cos((m-m')\phi)+\cos((m+m'+2)\phi)\right] -$$
$$-\frac{s_{p'} \mathscr{J}_4}{2}\left[\cos((m+m')\phi)+\cos((m-m'+2)\phi)\right] +$$
$$+\frac{s_p s_{p'} \mathscr{J}_1}{2}\left[\cos((m-m')\phi)+\cos((m+m'-2)\phi)\right]. \tag{A.70}$$

Also in this case, $\beta_x \pm \beta_y$ vanish when integrated for each (m,m') combination, and the only relevant term is

$$\gamma_x+\gamma_y = -\mathscr{J}_2\cos((m+m'+2)\phi)+s_p\mathscr{J}_3\cos((m-m'-2)\phi)+$$
$$-s_{p'}\mathscr{J}_4\cos((m-m'+2)\phi)+s_p s_{p'}\mathscr{J}_1\cos((m+m'-2)\phi). \tag{A.71}$$

Case: $l = \text{odd}$, $l' = \text{odd}$

$$\beta_x = \frac{\mathscr{J}_2}{2}\left[\cos((m-m')\phi)-\cos((m+m'+2)\phi)\right] -$$
$$-\frac{s_p \mathscr{J}_3}{2}\left[\cos((m+m')\phi)-\cos((m-m'-2)\phi)\right] -$$
$$-\frac{s_{p'} \mathscr{J}_4}{2}\left[\cos((m+m')\phi)-\cos((m-m'+2)\phi)\right] +$$
$$+\frac{s_p s_{p'} \mathscr{J}_1}{2}\left[\cos((m-m')\phi)-\cos((m+m'-2)\phi)\right]. \tag{A.72}$$

$$\beta_y = \frac{\mathscr{J}_2}{2}\left[\cos((m-m')\phi)+\cos((m+m'+2)\phi)\right] -$$
$$-\frac{s_p \mathscr{J}_3}{2}\left[\cos((m+m')\phi)+\cos((m-m'-2)\phi)\right] -$$
$$-\frac{s_{p'} \mathscr{J}_4}{2}\left[\cos((m+m')\phi)+\cos((m-m'+2)\phi)\right] +$$
$$+\frac{s_p s_{p'} \mathscr{J}_1}{2}\left[\cos((m-m')\phi)+\cos((m+m'-2)\phi)\right]. \tag{A.73}$$

$$\gamma_x = \frac{s_{p'}\mathscr{J}_4}{2}\left[\sin((m+m')\phi)+\sin((m-m'+2)\phi)\right] - \\ -\frac{s_p\mathscr{J}_3}{2}\left[\sin((m+m')\phi)+\sin((m-m'-2)\phi)\right] - \\ -\frac{\mathscr{J}_2}{2}\left[\sin((m-m')\phi)+\sin((m+m'+2)\phi)\right] + \\ +\frac{s_p s_{p'}\mathscr{J}_1}{2}\left[\sin((m-m')\phi)+\sin((m+m'-2)\phi)\right]. \tag{A.74}$$

$$\gamma_y = \frac{s_p\mathscr{J}_3}{2}\left[\sin((m+m')\phi)+\sin((m-m'-2)\phi)\right] - \\ -\frac{\mathscr{J}_2}{2}\left[\sin((m-m')\phi)+\sin((m+m'+2)\phi)\right] - \\ -\frac{s_{p'}\mathscr{J}_4}{2}\left[\sin((m+m')\phi)+\sin((m-m'+2)\phi)\right] + \\ +\frac{s_p s_{p'}\mathscr{J}_1}{2}\left[\sin((m-m')\phi)+\sin((m+m'-2)\phi)\right]. \tag{A.75}$$

$$\beta_x+\beta_y = \mathscr{J}_2\cos((m-m')\phi) - s_p\mathscr{J}_3\cos((m+m')\phi) + \\ -s_{p'}\mathscr{J}_4\cos((m+m')\phi) + s_p s_{p'}\mathscr{J}_1\cos((m-m')\phi). \tag{A.76}$$

$$\beta_x-\beta_y = -\mathscr{J}_2\cos((m+m'+2)\phi) + s_p\mathscr{J}_3\cos((m-m'-2)\phi) + \\ +s_{p'}\mathscr{J}_4\cos((m-m'+2)\phi) - s_p s_{p'}\mathscr{J}_1\cos((m+m'-2)\phi). \tag{A.77}$$

On the other hand, $\gamma_x+\gamma_y$ vanishes when integrated over the transverse plane. As expected from the theory of an isotropic layer, the integral of $\beta_x+\beta_y$ gives the same result as the even-even case.

As a final comment, it is clear that:

$$\int_{\mathbb{R}^2}(\beta_x \pm \beta_y)\, d^2\rho \propto \delta_{ll'}, \tag{A.78}$$

in agreement with the coupling operator of an isotropic uniform layer, represented by $\beta_x+\beta_y$, while

$$\int_{\mathbb{R}^2}(\gamma_x+\gamma_y)\, d^2\rho \propto 1-\delta_{ll'}, \tag{A.79}$$

coupling even and odd modes together.

Appendix B

Linearizing the transmission operator of the active layer

Zassenhaus formula: exponentiation of the sum of non-commuting operators

The linearization of the active layer transmission operator $\mathbf{T}_a$, reported in (2.141), requires particular attention. Indeed, it requires the exponentiation of non-commutative operators.

Given an operator $\mathbf{X}$, its exponential is defined through its Taylor expansion as:

$$e^{\mathbf{X}} = \frac{1}{k!}\sum_{k=0}^{\infty}\mathbf{X}^k. \tag{B.1}$$

As a consequence, if λ is an arbitrarily small scalar quantity, then the Taylor expansion at the first order of $e^{\lambda\mathbf{X}}$ reads:

$$e^{\lambda\mathbf{X}} = \frac{1}{k!}\sum_{k=0}^{\infty}\lambda^k\mathbf{X}^k = \mathbf{I} + \lambda\mathbf{X} + o(\lambda), \tag{B.2}$$

where $\mathbf{I}$ is the identity operator and $o(\lambda)$ represents negligible quantities with respect to λ.

Furthermore, considering now two non-commuting operators, $\mathbf{X}$ and $\mathbf{Y}$, the Baker-Cambell-Hausdorff (BCH) formula [125] holds:

$$e^{\mathbf{X}}e^{\mathbf{Y}} = e^{\mathbf{Z}}, \tag{B.3}$$

where

$$\mathbf{Z} = \mathbf{X} + \mathbf{Y} + \frac{1}{2}[\mathbf{X},\mathbf{Y}] + \frac{1}{12}[\mathbf{X},[\mathbf{X},\mathbf{Y}]] - \frac{1}{12}[\mathbf{Y},[\mathbf{X},\mathbf{Y}]] + \ldots, \tag{B.4}$$

with the square brackets representing the commutator between two operators, namely:

$$[\mathbf{X},\mathbf{Y}] = \mathbf{X}\mathbf{Y} - \mathbf{Y}\mathbf{X}. \tag{B.5}$$

As a consequence of the BCA formula (B.3)–(B.4), the Zassenhaus formula holds [126], stating how to evaluate the exponential of the sum of two non-commuting operators

$$e^{\mathbf{X}+\mathbf{Y}} = e^{\mathbf{X}}e^{\mathbf{Y}}\exp\left(-\frac{1}{2}[\mathbf{X},\mathbf{Y}]\right)\exp\left(\frac{1}{6}\left(2[\mathbf{Y},[\mathbf{X},\mathbf{Y}]] + [\mathbf{X},[\mathbf{X},\mathbf{Y}]]\right)\right)\ldots \tag{B.6}$$

where the dots at the end represent terms with increasingly more nested commutators. This formula represents the starting point for the linearization of the active layer transmission operator.

Linearization of the exponentiation of a sum of operators with different magnitudes

The expression to be linearized in (2.141) can be cast into the following form:

$$e^{\mathbf{U}+\lambda\mathbf{V}}, \tag{B.7}$$

where λ is a small scalar quantity. At this point, we can apply the Zassenhaus formula (B.6) identifying $\mathbf{X} = \mathbf{U}$ and $\mathbf{Y} = \lambda\mathbf{V}$ and only keeping linear terms in λ. To do so, the first three exponentials of the product in (B.6) must be considered, since the argument of the first is not dependent on λ, while the arguments of the second and third ones are linear in λ. The fourth term features two commutators; the first one contains $\mathbf{Y} = \lambda\mathbf{V}$ twice, which is proportional to λ^2 and thus must

be neglected. On the other hand, the second commutator contains $\mathbf{Y}$ only once, thus being proportional to λ, so it must be kept. All other nested commutators in the subsequent exponential are proportional to higher powers in λ, so they can be neglected and all of those exponentials simply give rise to the identity operator. In this view, it holds that:

$$e^{\mathbf{U}+\lambda\mathbf{V}} \sim e^{\mathbf{U}} e^{\lambda\mathbf{V}} e^{-\frac{1}{2}[\mathbf{U},\lambda\mathbf{V}]} e^{\frac{1}{6}[\mathbf{U},[\mathbf{U},\lambda\mathbf{V}]]}. \tag{B.8}$$

We can calculate separately the only nested commutator, reading:

$$\begin{aligned}[\mathbf{U},[\mathbf{U},\lambda\mathbf{V}]] &= \mathbf{U}[\mathbf{U},\lambda\mathbf{V}] - [\mathbf{U},\lambda\mathbf{V}]\mathbf{U} = \mathbf{U}(\lambda\mathbf{U}\mathbf{V} - \lambda\mathbf{V}\mathbf{U}) - (\lambda\mathbf{U}\mathbf{V} - \lambda\mathbf{V}\mathbf{U})\mathbf{U} = \\ &= \lambda\mathbf{U}^2\mathbf{V} - \lambda\mathbf{U}\mathbf{V}\mathbf{U} - \lambda\mathbf{U}\mathbf{V}\mathbf{U} + \lambda\mathbf{V}\mathbf{U}^2 = \lambda\left(\mathbf{U}^2\mathbf{V} + \mathbf{V}\mathbf{U}^2 - 2\mathbf{U}\mathbf{V}\mathbf{U}\right).\end{aligned} \tag{B.9}$$

Plugging (B.9) into (B.8) one gets:

$$e^{\mathbf{U}+\lambda\mathbf{V}} \sim e^{\mathbf{U}} e^{\lambda\mathbf{V}} e^{-\frac{\lambda}{2}(\mathbf{U}\mathbf{V}-\mathbf{V}\mathbf{U})} e^{\frac{\lambda}{6}\left(\mathbf{U}^2\mathbf{V}+\mathbf{V}\mathbf{U}^2-2\mathbf{U}\mathbf{V}\mathbf{U}\right)}. \tag{B.10}$$

We can now apply a first order Taylor expansion (B.2) to the second, third and fourth terms:

$$e^{\mathbf{U}+\lambda\mathbf{V}} \sim e^{\mathbf{U}}(\mathbf{I}+\lambda\mathbf{V})\left[\mathbf{I} - \frac{\lambda}{2}(\mathbf{U}\mathbf{V}-\mathbf{V}\mathbf{U})\right]\left[\mathbf{I} + \frac{\lambda}{6}\left(\mathbf{U}^2\mathbf{V}+\mathbf{V}\mathbf{U}^2-2\mathbf{U}\mathbf{V}\mathbf{U}\right)\right]. \tag{B.11}$$

Computing all the products and neglecting the terms in λ^2 and λ^3 we eventually obtain the final expression:

$$\begin{aligned}&e^{\mathbf{U}+\lambda\mathbf{V}} \sim \\ &\sim e^{\mathbf{U}} + \lambda e^{\mathbf{U}}\left(\mathbf{V} - \frac{1}{2}\mathbf{U}\mathbf{V} + \frac{1}{2}\mathbf{V}\mathbf{U} + \frac{1}{6}\mathbf{U}^2\mathbf{V} + \frac{1}{6}\mathbf{V}\mathbf{U}^2 - \frac{1}{3}\mathbf{U}\mathbf{V}\mathbf{U}\right).\end{aligned} \tag{B.12}$$

Recall now (2.141), here reported for clarity:

$$\mathbf{T}_a = \exp\left[\left(\mathbf{B} + \mathbf{K}_a^{(0)} + \frac{\Delta\tilde{\varepsilon}_a}{\varepsilon_{\text{ref}}}\Delta\mathbf{K}_a\right)L_a\right]. \tag{B.13}$$

We can linearize this expression using (B.12) by identifying

$$\mathbf{U} = \left(\mathbf{B} + \mathbf{K}_a^{(0)}\right)L_a, \tag{B.14}$$

$$\mathbf{V} = \Delta \mathbf{K}_a L_a \tag{B.15}$$

$$\lambda = \frac{\Delta \tilde{\varepsilon}_a}{\varepsilon_{\text{ref}}}. \tag{B.16}$$

Notice that $\mathbf{U} \propto L_a$ and $\mathbf{V} \propto L_a$, therefore, in the bracket of (B.12), we have that

$$\mathbf{V} \propto L_a, \tag{B.17}$$

$$-\frac{1}{2}\mathbf{UV} + \frac{1}{2}\mathbf{VU} \propto L_a^2 \tag{B.18}$$

and

$$\frac{1}{6}\mathbf{U}^2\mathbf{V} + \frac{1}{6}\mathbf{VU}^2 - \frac{1}{3}\mathbf{UVU} \propto L_a^3, \tag{B.19}$$

implying that only the first term $\mathbf{V}$ remains relevant when a small active layer is considered. This is the case analyzed in (2.142).

List of Figures

List of Tables

References

[1] Fumio Koyama. VCSELs: their 30 years history and new challenges. In Yi Luo, Jens Buus, Fumio Koyama, and Yu-Hwa Lo, editors, *Optoelectronic Materials and Devices III*, volume 7135, page 71350J. International Society for Optics and Photonics, SPIE, 2008.

[2] Hao-Tien Cheng, Yun-Cheng Yang, Te-Hua Liu, and Chao-Hsin Wu. Recent advances in 850 nm vcsels for high-speed interconnects. *Photonics*, 9(2), 2022.

[3] G. K. Veerabathran, S. Sprengel, A. Andrejew, and M.-C. Amann. Room-temperature vertical-cavity surface-emitting lasers at 4 μm with GaSb-based type-II quantum wells. *Appl. Phys. Lett.*, 110:071104–1–5, 2017.

[4] M. Dummer, K. Johnson, S. Rothwell, K. Tatah, and M. Hibbs-Brenner. The role of VCSELs in 3D sensing and LiDAR. In Henning Schröder and Ray T. Chen, editors, *Optical Interconnects XXI*, volume 11692, page 116920C. International Society for Optics and Photonics, SPIE, 2021.

[5] Dong Liang, Cheng Zhang, Pengfei Zhang, Song Liu, Huijie Li, Shouzhu Niu, Ryan Z Rao, Li Zhao, Xiaochi Chen, Hanxuan Li, et al. Evolution of laser technology for automotive lidar, an industrial viewpoint. *nature communications*, 15(1):7660, 2024.

[6] Leonardo Minelli, Fabrizio Forghieri, Antonino Nespola, Stefano Straullu, and Roberto Gaudino. A multi-rate approach for nonlinear pre-distortion using end-to-end deep learning in im-dd systems. *Journal of Lightwave Technology*, 41(2):420–431, 2023.

[7] L. A. Coldren and S. W. Corzine. *Diode Lasers and Photonic Integrated Circuits*. John Wiley & Sons, New York, 1995.

[8] Hamed Dalir and Fumio Koyama. 29 ghz directly modulated 980 nm vertical-cavity surface emitting lasers with bow-tie shape transverse coupled cavity. *Applied Physics Letters*, 103(9), 2013.

[9] Hamed Dalir and Fumio Koyama. High-speed operation of bow-tie-shaped oxide aperture vcsels with photon–photon resonance. *Applied physics express*, 7(2):022102, 2014.

[10] Harshil Dave, Zihe Gao, Stewart Thomas McKee Fryslie, Bradley J. Thompson, and Kent D. Choquette. Static and dynamic properties of coherently-coupled photonic-crystal vertical-cavity surface-emitting laser arrays. *IEEE Journal of Selected Topics in Quantum Electronics*, 25(6):1–8, 2019.

[11] M. Lindemann, N. C. Gerhardt, M.R. Hofmann, N. Ledentsov, V. A. Shchukin, N. N. Ledentsov, O. Yu. Makarov, Ł. Chorchos, and J. P. Turkiewicz. Coupled aperture vcsels suitable for 100 ghz intensity modulation. In *2023 23rd International Conference on Transparent Optical Networks (ICTON)*, pages 1–4, 2023.

[12] N. Ledentsov Jr., V. A. Shchukin, Ł. Chorchos, O. Yu. Makarov, J.-R. Kropp, I. E. Titkov, V. P. Kalosha, V. Zerova, M. Lindemann, N. C. Gerhardt, M. D'Alessandro, V. Torrelli, P. Debernardi, A. Tibaldi, M. R. Hofmann, and N. N. Ledentsov. Analysis of laterally-coupled-cavity VCSELs for ultra-high-frequency photon-photon resonance modulation. In Chun Lei and Kent D. Choquette, editors, *Vertical-Cavity Surface-Emitting Lasers XXVIII*, volume 12904, page 1290405. International Society for Optics and Photonics, SPIE, 2024.

[13] Martino D'Alessandro, Valerio Torrelli, Francesco Bertazzi, Michele Goano, Nikolay N. Ledentsov, Markus Lindemann, Mariangela Gioannini, Pierluigi Debernardi, and Alberto Tibaldi. Transverse coupled cavity vcsels: Bridging ultrabroadband dynamics to optical supermodes. *IEEE Photonics Journal*, 16(2):1–7, 2024.

[14] P. Debernardi, G. P. Bava, F. Monti di Sopra, and M. B. Willemsen. Features of vectorial modes in phase-coupled VCSEL arrays: experiments and theory. *IEEE J. Quantum Electron.*, 39(1):109–119, January 2003.

[15] S. Gronenborn, J. Pollmann-Retsch, P. Pekarski, M. Miller, M. Strösser, J. Kolb, H. Mönch, and P. Loosen. High-power VCSELs with a rectangular aperture. *Appl. Phys. B*, 105:783–792, 2011.

[16] Stephan Gronenborn, Thomas Schwarz, Pavel Pekarski, Michael Miller, Holger Mönch, and Peter Loosen. Optical modes in a rectangular VCSEL resonator with properties of both Gaussian and Fourier modes. *IEEE J. Quantum Electron.*, 48(8):1040–1044, August 2012.

[17] Guanzhong Pan, Meng Xun, Xiaoli Zhou, Yun Sun, Yibo Dong, and Dexin Wu. Harnessing the capabilities of vcsels: unlocking the potential for advanced integrated photonic devices and systems. *Light: Science & Applications*, 13(1):229, 2024.

[18] Meng Xun, Guanzhong Pan, Zhuang Zhuang Zhao, Yun Sun, Weichao Wu, Wenjing Jiang, Runze Zhang, and Dexin Wu. High single fundamental-mode output power from 795 nm VCSELs with a long monolithic cavity. *IEEE Electron Device Lett.*, 44(7):1144–1147, July 2023.

[19] M. Huang, D. K. Serkland, and J. Camparo. A narrow-linewidth three-mirror VCSEL for atomic devices. *Appl. Phys. Lett.*, 121(11):114002, 2022.

[20] Yinli Zhou, Yuchen Jia, Xing Zhang, Jianwei Zhang, Zhanchao Liu, Yongqiang Ning, and Lijun Wang. Large-aperture single-mode 795 nm VCSEL for chip-scale nuclear magnetic resonance gyroscope with an output power of 4.1 mW at 80°c. *Opt. Express*, 30(6):8991–8999, March 2022.

[21] Kai Jin, Xuxing Geng, Zhi Liang, Wangwang Tang, Jianfeng Xiao, Heng Hu, Guangming Huang, Gaoxiang Li, Guoqing Yang, and Shangqing Liang. Design of portable self-oscillating VCSEL-pumped cesium atomic magnetometer. *MDPI Electron.*, 11(22):3666, November 2022.

[22] Quanpu Liu, Zhen Chai, Jixi Lu, Kaifeng Yin, and Jianli Li. Development of non-magnetic VCSEL module for compact atomic magnetometer. In *Proc. SPIE 12311*, page 123110U, December 2022.

[23] Yinli Zhou, Xing Zhang, Jianwei Zhang, Jinjiang Cui, Yongqiang Ning, Yugang Zeng, and Lijun Wang. Wavelength tuning robustness optimization for a high-temperature single-mode VCSEL used in chip-scale atomic sensing systems. *Appl. Opt.*, 61(9):2417–2423, March 2022.

[24] Lele Bai, Xin Wen, Yulin Yang, Lulu Zhang, Jun He, Yanhua Wang, and Junmin Wang. Quantum-enhanced rubidium atomic magnetometer based on Faraday rotation via 795 nm Stokes operator squeezed light. *J. Opt.*, 23(8):085202, August 2021.

[25] M. A. Bobrov, S. A. Blokhin, N. A. Maleev, A. A. Blokhin, A. P. Vasyl'ev, A. G. Kuzmenkov, A. S. Pazgalev, M. V. Petrenko, S. P. Dmitriev, A. K. Vershovskii, V. M. Ustinov, I. I. Novikov, and L. Ya Karachinskii. Optically pumped non-zero field magnetometric sensor for the magnetoencephalographic systems using intra-cavity contacted VCSELs with rhomboidal oxide current aperture. *J. Phys. Conf. Ser.*, 1697(1):012175, October 2020.

[26] N. A. Maleev, S. A. Blokhin, M. A. Bobrov, A. G. Kuz'menkov, M. M. Kulagina, and V. M. Ustinov. Laser source for a compact nuclear magnetic resonance gyroscope. *Gyroscopy Navig.*, 9(3):177–182, 2018.

[27] John Kitching. Chip-scale atomic devices. *Applied Physics Reviews*, 5(3), 2018.

[28] L. S. Watkins, C. Ghosh, J.-F. Seurin, D. Zhou, G. Xu, B. Xu, and A. Miglo. High power VCSEL devices for atomic clock applications. *Proc. SPIE 9616*, page 96160J, September 2015.

[29] Valerio Torrelli, Alberto Gullino, Alberto Tibaldi, Francesco Bertazzi, Michele Goano, and Pierluigi Debernardi. High-power emission via large-area vcsels with single high-order mode operation. *IEEE Photonics Journal*, 16(2):1–7, 2024.

[30] Markus Lindemann, Gaofeng Xu, Tobias Pusch, Rainer Michalzik, Martin R Hofmann, Igor Žutić, and Nils C Gerhardt. Ultrafast spin-lasers. *Nature*, 568(7751):212–215, 2019.

[31] Xiuqin Zhan, Fa-Feng Xu, Zhonghao Zhou, Yongli Yan, Jiannian Yao, and Yong Sheng Zhao. 3d laser displays based on circularly polarized lasing from cholesteric liquid crystal arrays. *Advanced Materials*, 33(37), August 2021.

[32] Ming Kang and Jing Chen. Pseudo coherent-perfect-absorption approach toward perfect polarization conversion. *Optics Express*, 32(8):13357, March 2024.

[33] Zhiyi Yuan, Shih-Hsiu Huang, Zhen Qiao, Pin Chieh Wu, and Yu-Cheng Chen. Metasurface-tunable lasing polarizations in a microcavity. *Optica*, 10(2):269–278, Feb 2023.

[34] Xiangli Jia, Jonas Kapraun, Jiaxing Wang, Jipeng Qi, Yipeng Ji, and Connie Chang-Hasnain. Metasurface reflector enables room-temperature circularly polarized emission from VCSEL. *Optica*, 10(8):1093, August 2023.

[35] Kirill Voronin, Alexey S. Taradin, Maxim V. Gorkunov, and Denis G. Baranov. Single-handedness chiral optical cavities. *ACS Photonics*, 9(8):2652–2659, 2022.

[36] YiMing Zhu, Fan Zhang, GuanJun You, Jie Liu, John D. Zhang, Akhlesh Lakhtakia, and Jian Xu. Stable circularly polarized emission from a vertical-cavity surface-emitting laser with a chiral reflector. *Applied Physics Express*, 5(3):032102, February 2012.

[37] Valerio Torrelli, Martino D'Alessandro, Wolfgang Elsäßer, and Pierluigi Debernardi. On-demand polarization by a vertical-cavity surface-emitting laser with two tilted sub-wavelength gratings. *Opt. Lett.*, 49(13):3773–3776, Jul 2024.

[38] Julian Lindner, Tobias Pusch, Stephan Gronenborn, Jochen Reichel, Ulrich Weichmann, Markus Herper, Alexander van der Lee, Susanne Weidenfeld, Cynthia Klett, Holger Moench, and Roman Alexander Koerner. Compact VCSEL chips for diverse applications (795nm to 850nm). In Kent D. Choquette and Luke A. Graham, editors, *Vertical-Cavity Surface-Emitting Lasers XXIX*, volume 13384, page 133840A. International Society for Optics and Photonics, SPIE, 2025.

[39] G. P. Bava, P. Debernardi, and L. Fratta. Three-dimensional model for vectorial fields in vertical-cavity surface-emitting lasers. *Phys. Rev. A*, 63(2):23816, 2001.

[40] P. Debernardi, G. P. Bava, C. Degen, I. Fischer, and W. Elsäßer. Influence of anisotropies on transverse modes in oxide-confined VCSELs. *IEEE J. Quantum Electron.*, 38(1):73–84, January 2002.

[41] P. Debernardi and G. P. Bava. Coupled mode theory: a powerful tool for analyzing complex VCSELs and designing advanced devices features. *IEEE J. Select. Topics Quantum Electron.*, 9(3):905–917, May/June 2003.

[42] P. Debernardi, J. M. Ostermann, M. Sondermann, T. Ackemann, G. P. Bava, and R. Michalzik. Theoretical-experimental study of the vectorial modal properties of polarization-stable multimode grating VCSELs. *IEEE J. Select. Topics Quantum Electron.*, 13(5):1340–1348, September/October 2007.

[43] P. Debernardi, A. Kroner, F. Rinaldi, and R. Michalzik. Surface relief versus standard VCSELs: a comparison between experimental and hot-cavity model results. *IEEE J. Select. Topics Quantum Electron.*, 15(3):828–837, May/June 2009.

[44] P. Debernardi. HOT-VELM: a comprehensive and efficient code for fully vectorial and 3-D hot-cavity VCSEL simulation. *IEEE J. Quantum Electron.*, 45(8):979–992, August 2009.

[45] Alberto Tibaldi, Francesco Bertazzi, Michele Goano, Rainer Michalzik, and Pierluigi Debernardi. VENUS: a Vertical-cavity surface-emitting laser Electro-opto-thermal NUmerical Simulator. *IEEE J. Select. Topics Quantum Electron.*, 25(6):1500212, November/December 2019.

[46] P. Debernardi, A. Tibaldi, P. Gerlach, P. Martelli, P. Boffi, M. Martinelli, D. Coviello, and R. Orta. Modal performance of spiral phase plate VCSELs. *IEEE J. Quantum Electron.*, 52(5):2400108–1–8, May 2016.

[47] D.I. Babic and S.W. Corzine. Analytic expressions for the reflection delay, penetration depth, and absorptance of quarter-wave dielectric mirrors. *IEEE Journal of Quantum Electronics*, 28(2):514–524, 1992.

[48] Martin A. Afromowitz. Refractive index of $Ga_{1-x}Al_xAs$. *Solid State Commun.*, 15:59–63, February 1974.

[49] Max Born and Emil Wolf. *Principles of Optics: 60th Anniversary Edition*. Cambridge University Press, December 2019.

[50] M. G. Moharam and T. K. Gaylord. Rigorous coupled-wave analysis of planar-grating diffraction. *Journal of the Optical Society of America*, 71(7):811, July 1981.

[51] Lifeng Li. Use of fourier series in the analysis of discontinuous periodic structures. *Journal of the Optical Society of America A*, 13(9):1870, September 1996.

[52] Maciej Dems. Convergence analysis of various factorization rules in the fourier-bessel basis for solving maxwell equations using modal methods. *Opt. Express*, 29(3):4378–4391, Feb 2021.

[53] Jingxiao Xu, Douglas McCulloch, and Martin DB Charlton. Modeling full pcsels and vcsels using modified rigorous coupled-wave analysis. *Optics Express*, 32(13):22169–22180, 2024.

[54] Maciej Dems, Tomasz Czyszanowski, and Krassimir Panajotov. Plane-wave and cylindrical-wave admittance method for simulation of classical and photonic-crystal-based vcsels. In *Photonic Crystal Materials and Devices III (ie V)*, volume 6182, pages 256–263. SPIE, 2006.

[55] Tomasz Czyszanowski, Maciej Dems, Hugo Thienpont, and Krassimir Panajotov. Full vectorial electromagnetic modeling of vertical-cavity surface-emitting diode lasers by the plane wave admittance method. In *Micro-Optics, VCSELs, and Photonic Interconnects II: Fabrication, Packaging, and Integration*, volume 6185, pages 290–298. SPIE, 2006.

[56] Tomasz Czyszanowski, Maciej Dems, Hugo Thienpont, and Krassimir Panajotov. Modal behavior of photonic-crystal vertical-cavity surface-emitting diode laser analyzed with plane wave admittance method. *Optical and quantum electronics*, 39:427–433, 2007.

[57] E Ahlers, SF Helfert, and R Pregla. Modelling of vcsels by the method of lines. In *Integrated Photonics Research*, page ITuE5. Optica Publishing Group, 1996.

[58] Jan Pomplun, Sven Burger, Maria Rozova, Lin Zschiedrich, and Frank Schmidt. Finite element simulation of optical modes in vcsels. In *2011 Numerical Simulation of Optoelectronic Devices*, pages 119–120, 2011.

[59] AD Bresler. *Operator methods in electromagnetic field theory*, volume 57. Microwave Research Institute, Polytechnic Institute of Brooklyn, 1957.

[60] Leopold B Felsen and Nathan Marcuvitz. *Radiation and scattering of waves*. John Wiley & Sons, 1994.

[61] Allan W Snyder, John D Love, et al. *Optical waveguide theory*, volume 175. Chapman and hall London, 1983.

[62] Frank Bowman. *Introduction to Bessel functions*. Courier Corporation, 2012.

[63] Frank WJ Olver and Leonard C Maximon. *Bessel functions*. Cambridge University Press Cambridge, 1960.

[64] Maciej Dems. Convergence of factorization rules for modal methods in fourier-bessel basis. is the inverse rule really the best? In *2023 International Conference on Numerical Simulation of Optoelectronic Devices (NUSOD)*, pages 31–32, 2023.

[65] Renato Orta. Lecture notes on transmission line theory. *Online. http://personal. delen. polito. it/Renato. Orta*, 2012.

[66] P. Debernardi and R. Orta. Mastering lateral radiation losses in tunable VCSELs. *IEEE J. Quantum Electron.*, 55(1):2400108, 2019.

[67] Teppo Häyrynen, Jakob Rosenkrantz de Lasson, and Niels Gregersen. Open-geometry fourier modal method: modeling nanophotonic structures in infinite domains. *J. Opt. Soc. Am. A*, 33(7):1298–1306, Jul 2016.

[68] David M Pozar. *Microwave engineering: theory and techniques*. John wiley & sons, 2021.

[69] P. Debernardi and G. P. Bava. Effects of anisotropies on vectorial modes of vertical-cavity surface-emitting lasers. *Phys. Status Solidi A*, 188(3):967–977, 2001.

[70] Tobias Pusch, Markus Lindemann, Natalie Jung, Nils C. Gerhardt, Martin R. Hofmann, and Rainer Michalzik. Manipulation of birefringence in spin-VCSELs. In Henri-Jean M. Drouhin, Jean-Eric Wegrowe, and Manijeh Razeghi, editors, *Spintronics XIII*, volume 11470, page 114702K. International Society for Optics and Photonics, SPIE, 2020.

[71] M. San Miguel, Q. Feng, and J. V. Moloney. Light-polarization dynamics in surface-emitting semiconductor lasers. *Phys. Rev. A*, 52:1728–1739, Aug 1995.

[72] Georgios Sinatkas, Thomas Christopoulos, Odysseas Tsilipakos, and Emmanouil E. Kriezis. Electro-optic modulation in integrated photonics. *J. Appl. Phys.*, 130(1):010901, 2021.

[73] S. Adachi, editor. *Properties of Aluminium Gallium Arsenide*. EMIS Datareviews Series. INSPEC, London, 1993.

[74] Johannes M. Ostermann, Pierluigi Debernardi, Christof Jalics, Andrea Kroner, Martin Feneberg, Michael C. Riedl, and Rainer Michalzik. Monolithic polarization control of multimode VCSELs by a dielectric surface grating. *Vertical-Cavity Surface-Emitting Lasers VIII, Proc. SPIE 5364*, June 2004.

[75] P. Debernardi, J.M. Ostermann, M. Feneberg, C. Jalics, and R. Michalzik. Reliable polarization control of VCSELs through monolithically integrated surface gratings: a comparative theoretical and experimental study. *IEEE Journal of Selected Topics in Quantum Electronics*, 11(1):107–116, January 2005.

[76] Pierluigi Debernardi, Johannes Michael Ostermann, Markus Sondermann, Thorsten Ackemann, Gian Paolo Bava, and Rainer Michalzik. Theoretical-experimental study of the vectorial modal properties of polarization-stable multimode grating vcsels. *IEEE Journal of Selected Topics in Quantum Electronics*, 13(5):1340–1348, 2007.

[77] Michael Zimmer, Moritz Birkhold, Michael Jetter, and Peter Michler. Monolithic 850 nm VCSEL array for quantum key distribution via the BB84 and decoy state protocol. In Chun Lei and Kent D. Choquette, editors, *Vertical-Cavity Surface-Emitting Lasers XXVIII*, volume PC12904, page PC1290402. International Society for Optics and Photonics, SPIE, 2024.

[78] Å. Haglund, J. S. Gustavsson, J. Vukusic, P. Modh, and A. Larsson. Single fundamental-mode output power exceeding 6 mW from VCSELs with a shallow surface relief. *IEEE Photon. Technol. Lett.*, 16(2):368–370, February 2004.

[79] M. C. G. Alasio, V. Torrelli, S. Albano, L. Miri, A. Gullino, M. Goano, and P. Debernardi. Modeling self-heating in high-power non-circular vcsels. In *2024 IEEE Photonics Conference (IPC)*, pages 1–2, 2024.

[80] Kent D Choquette, DA Richie, and RE Leibenguth. Temperature dependence of gain-guided vertical-cavity surface emitting laser polarization. *Applied physics letters*, 64(16):2062–2064, 1994.

[81] Valerio Torrelli, Alberto Tibaldi, Francesco Bertazzi, Michele Goano, and Pierluigi Debernardi. Modeling of single-mode high-power vcsel arrays. In *2023 International Conference on Numerical Simulation of Optoelectronic Devices (NUSOD)*, pages 93–94, 2023.

[82] A. J. A. Carvalho, R. S. N. Moreira, J. Ferraz, S. S. Vianna, L. H. Acioli, and D. Felinto. Enhanced absorption of weak ultrashort light pulses by a narrowband atomic medium. *Phys. Rev. A*, 101:053426, May 2020.

[83] Thomas Knodl, Matthias Golling, Axel Straub, R Jager, Rainer Michalzik, and Karl Joachim Ebeling. Multistage bipolar cascade vertical-cavity surface-emitting lasers: Theory and experiment. *IEEE Journal of selected topics in quantum electronics*, 9(5):1406–1414, 2003.

[84] Cort Johnson, Peter D. D. Schwindt, and Michael Weisend. Magnetoencephalography with a two-color pump-probe, fiber-coupled atomic magnetometer. *Appl. Phys. Lett.*, 97(24):243703, December 2010.

[85] Pierluigi Debernardi, Alberto Tibaldi, Markus Daubenschüz, Rainer Michalzik, Michele Goano, and Francesco Bertazzi. Probing thermal effects in VCSELs by experiment-driven multiphysics modeling. *IEEE J. Select. Topics Quantum Electron.*, 25(6):1700914, November/December 2019.

[86] Valerio Torrelli, Martino D'Alessandro, Lorenzo Miri, Alberto Gullino, Wolfgang Elsässer, Alberto Tibaldi, and Pierluigi Debernardi. Mastering VCSEL polarization from linear to circular using subwavelength gratings. In Kent D. Choquette and Luke A. Graham, editors, *Vertical-Cavity Surface-Emitting Lasers XXIX*, volume PC13384, page PC1338407. International Society for Optics and Photonics, SPIE, 2025.

[87] Valerio Torrelli, Lorenzo Miri, Martino D'Alessandro, Alberto Gullino, Michael Zimmer, Katharina Dahler, Michael Jetter, Peter Michler, Wolfgang Elsäßer, Francesco Bertazzi, Alberto Tibaldi, and Pierluigi Debernardi. Elliptical polarization in vcsels via joint interaction of a tilted sub-wavelength grating and intrinsic semiconductor anisotropies. *Opt. Lett.*, 50(9):3082–3085, May 2025.

[88] D Lenstra. On the theory of polarization effects in gas lasers. *Physics Reports*, 59(3):299–373, March 1980.

[89] A.K Jansen van Doorn, M.P van Exter, M Travagnin, and J.P Woerdman. Polarization behavior of surface-emitting semiconductor lasers in an axial magnetic field. *Optics Communications*, 133(1–6):252–258, January 1997.

[90] M. San Miguel, Q. Feng, and J. V. Moloney. Light-polarization dynamics in surface-emitting semiconductor lasers. *Physical Review A*, 52(2):1728–1739, August 1995.

[91] J. Martin-Regalado, F. Prati, M. San Miguel, and N.B. Abraham. Polarization properties of vertical-cavity surface-emitting lasers. *IEEE Journal of Quantum Electronics*, 33(5):765–783, May 1997.

[92] Krassimir Panajotov and Franco Prati. Polarization dynamics of VCSELs. In *Springer Series in Optical Sciences*, SPringer series in optical sciences, pages 181–231. Springer Berlin Heidelberg, Berlin, Heidelberg, 2013.

[93] F. Prati, L. Fratta, and M. Travagnin. Band model for light-polarization selection in unstrained quantum-well vertical-cavity surface-emitting lasers. *Physical Review A*, 62(3), August 2000.

[94] M. B. Willemsen, M. P. van Exter, and J. P. Woerdman. Anatomy of a polarization switch of a vertical-cavity semiconductor laser. *Physical Review Letters*, 84(19):4337–4340, May 2000.

[95] M.B. Willemsen, M.P. van Exter, and J.P. Woerdman. Polarization loxodrome of a vertical-cavity semiconductor laser. *Optics Communications*, 199(1–4):167–173, November 2001.

[96] A. Haglund, J.S. Gustavsson, J. Bengtsson, P. Jedrasik, and A. Larsson. Design and evaluation of fundamental-mode and polarization-stabilized VCSELs with a subwavelength surface grating. *IEEE Journal of Quantum Electronics*, 42(3):231–240, March 2006.

[97] Connie J Chang-Hasnain, Ye Zhou, Michael CY Huang, and Christopher Chase. High-contrast grating vcsels. *IEEE Journal of Selected Topics in Quantum Electronics*, 15(3):869–878, 2009.

[98] Kun Li, Yi Rao, Chris Chase, Weijian Yang, and Connie J Chang-Hasnain. Monolithic high-contrast metastructure for beam-shaping vcsels. *Optica*, 5(1):10–13, 2018.

[99] Yao Cui, Huawen Hu, Yipeng Ji, Jonas Kapraun, Jiaxing Wang, Xuanlun Huang, and Connie J Chang-Hasnain. Single-mode chirped high-contrast metastructure vcsel for 106 gbps pam4 transmission. *Optica*, 11(11):1567–1574, 2024.

[100] Aaron Z. Goldberg, Pablo de la Hoz, Gunnar Björk, Andrei B. Klimov, Markus Grassl, Gerd Leuchs, and Luis L. Sánchez-Soto. Quantum concepts in optical polarization. *Advances in Optics and Photonics*, 13(1):1, March 2021.

[101] Jacob F Sherson, Hanna Krauter, Rasmus K Olsson, Brian Julsgaard, Klemens Hammerer, Ignacio Cirac, and Eugene S Polzik. Quantum teleportation between light and matter. *Nature*, 443(7111):557–560, 2006.

[102] Claudia Wagenknecht, Che-Ming Li, Andreas Reingruber, Xiao-Hui Bao, Alexander Goebel, Yu-Ao Chen, Qiang Zhang, Kai Chen, and Jian-Wei Pan. Experimental demonstration of a heralded entanglement source. *Nature Photonics*, 4(8):549–552, 2010.

[103] Rouin Farshchi, M Ramsteiner, J Herfort, A Tahraoui, and HT Grahn. Optical communication of spin information between light emitting diodes. *Applied Physics Letters*, 98(16), 2011.

[104] Chia-Ming Jan, Yu-Hsun Lee, Kuang-Chong Wu, and Chih-Kung Lee. Integrating fault tolerance algorithm and circularly polarized ellipsometer for point-of-care applications. *Optics Express*, 19(6):5431–5441, 2011.

[105] Chih-Jen Yu, Chu-En Lin, Li-Ping Yu, and Chien Chou. Paired circularly polarized heterodyne ellipsometer. *Applied Optics*, 48(4):758–764, 2009.

[106] Hiroyuki Tsumatori, Takashi Harada, Junpei Yuasa, Yasuchika Hasegawa, and Tsuyoshi Kawai. Circularly polarized light from chiral lanthanide (iii) complexes in single crystals. *Applied Physics Express*, 4(1):011601, 2011.

[107] A.A. Maksimov, E.V. Filatov, I. I. Tartakovskii, V.D. Kulakovskii, S.G. Tikhodeev, C. Schneider, and S. Höfling. Circularly polarized laser emission from an electrically pumped chiral microcavity. *Physical Review Applied*, 17(2), February 2022.

[108] Markus Lindemann, Gaofeng Xu, Tobias Pusch, Rainer Michalzik, Martin R. Hofmann, Igor Žutić, and Nils C. Gerhardt. Ultrafast spin-lasers. *Nature*, 568(7751):212–215, April 2019.

[109] Yosuke Tanaka, Hiroyuki Takano, and Takashi Kurokawa. Circular polarization resonator based on cholesteric liquid crystal. *Japanese Journal of Applied Physics*, 43(3R):1062, March 2004.

[110] Chun-Ta Wang and Tsung-Hsien Lin. Polarization-tunable chiral nematic liquid crystal lasing. *Journal of Applied Physics*, 107(12), June 2010.

[111] Yi Xie, Jeroen Beeckman, Krassimir Panajotov, and Kristiaan Neyts. Vertical-cavity surface-emitting laser with a chiral nematic liquid crystal overlay. *IEEE Photonics Journal*, 6(1):1–10, 2013.

[112] B. Boisnard, C. Levallois, C. Paranthoen, S. Pes, T. Camps, B. Sadani, K. Tavernier, S. Bouchoule, L. Dupont, M. Alouini, P. Debernardi, and V. Bardinal. CW operation of a tunable 1550-nm VCSEL integrating liquid-crystal microcells. *IEEE Photonics Technology Letters*, 32(7):391–394, April 2020.

[113] Krassimir Panajotov and Mustapha Tlidi. Liquid crystal resonator as a nonlinear reflector for passive q-switching and mode locking. *Optics Communications*, 549:129872, 2023.

[114] Luis Cerdán, Sara García-Moreno, Angel Costela, Inmaculada García-Moreno, and Santiago de la Moya. Circularly polarized laser emission induced in isotropic and achiral dye systems. *Scientific Reports*, 6(1), June 2016.

[115] Yong Wang, Jun Xu, Yawen Wang, and Hongyu Chen. Emerging chirality in nanoscience. *Chemical Society Reviews*, 42(7):2930–2962, 2013.

[116] G. G. Stokes. On the composition and resolution of streams of polarized light from different sources. *Trans. Cambridge Philos. Soc.*, 9:399–416, 1852. Reprinted in Mathematical and Physical Papers by Cambridge University Press (2009).

[117] E. Collett. *Polarized Light: Fundamentals and Applications*. Marcel Dekker, 1993.

[118] W.A. Shurcliff and S.S. Stanley. *Polarized Light*. Harvard University, 1964.

[119] H. G. Berry, G. Gabrielse, and A. E. Livingston. Measurement of the Stokes parameters of light. *Applied Optics*, 16(12):3200, December 1977.

[120] Beth Schaefer, Edward Collett, Robert Smyth, Daniel Barrett, and Beth Fraher. Measuring the Stokes polarization parameters. *American Journal of Physics*, 75(2):163–168, February 2007.

[121] James R Munkres and James W Munkres. *Elements of algebraic topology*. CRC press, 2018.

[122] Hirokazu Kobayashi, Koji Nonaka, and Yutaka Shikano. Stereographical visualization of a polarization state using weak measurements with an optical-vortex beam. *Physical Review A*, 89(5), May 2014.

[123] Andreas Molitor, Sébastien Hartmann, and Wolfgang Elsässer. Stokes vector characterization of the polarization behavior of vertical-cavity surface-emitting lasers. *Optics Letters*, 37(22):4799, November 2012.

[124] T. Pusch, M. Lindemann, N.C. Gerhardt, M.R. Hofmann, and R. Michalzik. Impact of in-plane anisotropic strain on the polarization behavior of vertical-cavity surface-emitting lasers. *Electron. Lett.*, 51(20):1600–1602, 2015.

[125] Wulf Rossmann. *Lie groups: an introduction through linear groups*, volume 5. OUP Oxford, 2006.

[126] Fernando Casas, Ander Murua, and Mladen Nadinic. Efficient computation of the zassenhaus formula. *Computer Physics Communications*, 183(11):2386–2391, 2012.